

University of Nottingham
UK | CHINA | MALAYSIA

Investigation of synthesis methods of ZIF-8 membranes for CO_2/CH_4 separation

Qasim M Mushtaq

Thesis submitted to the University of Nottingham for the degree of Doctor of Philosophy (PhD)

April 2021

Abstract

Although there has been a rapid expansion into renewable energies such as (bio)methane, hydrogen, solar PV and wind power, fossil fuels still account for approximately 80% of the total primary energy demand. Methane, whether produced via anaerobic digestion or taken from gas wells, is one of the cleanest of all fossil-derived fuels. However, the contaminant, CO_2, creates challenges with production, e.g. pipeline corrosion where CO_2 makes the stream acidic in the presence of water increasing operational costs.

Membranes are a preferred method for separating gas mixtures since they are up to 50% more energy-efficient than conventional separation technologies e.g., absorption and distillation. The technology can be retrofitted to existing unit operations since membranes are very simple, compact, and easy to operate and control. However, commercially, amine absorption is the more dominant form of separation for the CO_2/CH_4 mixture due to amines high selectivity towards CO_2. There are a few commercial polymeric membranes. However, the CO_2 content (up to 75%) of the natural gas and the pressure of the separation (up to 50 bar) make polymer structure susceptible to plasticisation, which reduces the polymers lifespan and durability when in use, impeding selectivity leading to poor separation performance. For this reason, the research community has been actively investigated the alternative materials to polymers for membranes.

An alternative to polymers is the hybrid structure of metal organic frameworks (MOFs), which are metal centres connected by organic linkers forming 'net' like structures. An advantage of MOFs is the tailorability of their structure, by changing the metal centre or organic linker, an infinite combination of structures can be developed and created for the designated gas mixture and processing condition. Another key advantage is their large surface to volume ratios, more than 6000 m^2/g.

ZIF-8 belongs to the zeolitic imidazolate frameworks (ZIFs) family, a subclass of MOFs with similar topology to the inorganic structure zeolite. ZIF-8 is of interest

because of its high surface to volume ratio, chemical and thermal stability, hydrophobic nature, and ideal pore structure to exclude CH_4 and natural affinity to CO_2. However, there are challenges with synthesising continuous and dense ZIF-8 membranes onto substrates. For example, literature reiterates the difficulty with repeatability and reproducibility when growing the films onto substrates to form membranes. Production costs and scalability are issues too.

This thesis explored the heterogeneous growth of ZIF-8 membranes onto tubular alumina substrates in batch systems using microwave and conventional heating, and deposition of MOFs onto flat substrates using spray coating. The batch systems investigated the role of precursor concentrations and ratios, conjugate base, and synthesis time on the heterogenous growth of ZIF-8 under their respective heating mechanisms. The batch systems also investigated the same parameters with the precursors isolated. The dynamic cold spray coating chapter studied the efficient deposition of MOFs onto flat substrates by optimising the atomisation of the slurry.

Characterisation of the samples were conducted using X-ray diffraction to determine the formation and the crystallinity of the structures. Scanning electron microscopy was used to investigate the morphology, membrane thickness and surface coverage.

The batch production results under conventional heating support other researchers' findings on the difficulty of achieving heterogeneous growth of ZIF-8 onto substrates since ZIF-8 is a predominantly homogenous nucleation process and some form of surface modification is needed to promote growth onto the substrate, particularly tubular substrates. The difficulty with tubular substrates is the low mass transfer efficiency inside the tubular substrate’s lumen. The results also showed how the synthesis conditions controlled the level of growth onto the substrate with low precursor concentrations delivering a weaker level of continuity of film growth onto the substrate, smaller linker/metal ratios forming larger crystals and thicker membranes, and longer synthesis times delivering more evolved crystals whilst no increase in the level of continuity of film growth.

The novel metal-linker isolation work studied the formation of ZIF-8 by analysing the reaction and diffusion effects at the substrate's surface. The work emphasises the homogenous nature of ZIF-8, the work also suggested that the respective precursor location can control the crystal morphology and size (inside or outside of substrate), even when at the same linker/metal ratio.

The synthesis of ZIF-8 onto tubular substrates under microwave heating showed how volumetric heating affects heterogenous growth since the microwave system achieved crystal growth on the tubular substrate in a 1 hour synthesis. A more robust level of heterogenous growth of ZIF-8 was also achieved in the microwave system by increasing solvent volume to 16 ml from 4 ml to accommodate the microwave chemistry.

The cold spray coating enhanced particle attachment by optimising the mechanical parameters when designing the atomiser for the coating of MOFs onto substrates. The result indicates that the optimum mechanical conditions for pressure, stand of distance (SOD), the number of passes and angle of injection are 2 bar, 300 mm, two passes, and 90 °, respectively. The novel design of the atomiser can be applied to temperature-sensitive MOF/ZIF structures.

Acknowledgements

I would like to thank my supervisors Dr. Begum Tokay and Prof. Ed Lester, for their guidance, suggestions, and invaluable input into my PhD research. I am also very appreciative of their much-needed support, compassion, and patience when faced with the sudden decline in my health.

I would also like to thank Prof. Ed Lester for meeting weekly alongside Begum in which he provided lots of encouragement to try new things, introducing me to other academics in their respective fields, making the PhD journey a very rewarding experience. I gained lots of scientific knowledge, building a wealth of experience.

I want to thank the academics Dr. Andrea Laybourn and Dr. Tanvir Hussain for access to their laboratories and the guidance given in their respective fields. I am very appreciative of this.

I want to thank the Faculty of Engineering for the scholarship they provided me with, without which I would not have been able to be a part of the AMRG at the University of Nottingham.

Thank you to the NMRC and Wolfson technical staff for their assistance with SEM and XRD instruments: Nigel Neate, Beth Steer, Martin Roe, and Hannah Constantin. Technicians John and Rory, for help with the cold spray work set up. Safety staff, Aled Jones and Mark Rose for their role in helping with workplace adjustments, and Chris Booker support from infrastructure when requesting movement of offices.

I want to thank Dr. James Campbell, when I arrived at the university, he was a great mentor, it is great having you as a mentor and friend.

I want to thank my colleagues (Jan, Athil, Frank, and Zaid) in the L4 lab for the lovely conversations we would have. Thank you to the Thermofluids group for keeping me part of their research family too, invitations to their weekly social lunches and annual Christmas dinners were very friendly. These are lovely memories I will take away with me.

Special thanks go to my family, I appreciate their much needed emotional and financial support during the PhD. Especially towards the end of the PhD, regular visits to ensure I was keeping well and delivering healthy meals helped me remain focused on the PhD.

Contents

Abstract i
Acknowledgements iv
List of figures ix
List of tables xx
1. Introduction 1
1.1 General background 1
1.2 Aims, objectives and novelty. 4
1.3 Chapter outlines 6
1.4 Planned publications 6
1.5 Research work presented at conferences 7
2. Literature review 8
2.1 Membranes 8
2.2 Gas separation with membranes 12
2.3 Membrane materials for CO_2/CH_4 separation 15
2.4 Growth of ZIF-8 crystals 20
2.5 Synthesis of ZIF-8 membranes and films 23
2.5.1 Substrate modification 23
2.5.2 Synthesis methodologies 29
2.5.3 Gas separation Performance of ZIF-8 Membranes 42
2.6 ZIF-8 Membrane Synthesis using Microwave Heating 46
2.7 Dynamic cold spray coating of MOFs 54
3. Experimental Methods 58
3.1 Materials 58
3.3 Batch synthesis system 59
3.4 Continuous Spray Coating 62
3.5 Characterisation of MOF seeds and membranes 64
3.5.3 Energy Dispersive Spectroscopy (EDS) 72
3.5.4 Gas separation system 73
4. Batch synthesis of ZIF-8 membranes using mixed precursors under conventional heating 75
4.1 Introduction 75
4.2 Experimental procedure 75
4.2.1 Substrate preparation 75
4.2.2 Seed synthesis 76
4.2.3 Membrane synthesis using mixed precursors. 76
4.2.5 Particle size and surface area measurement 78
4.3 Results 78

4.3.1 Seed Synthesis 78
4.3.2 Membrane synthesis using mixed precursors. 79
4.4 Conclusion 99
4.5 Appendix 102
5. Batch synthesis of ZIF-8 membranes using isolated precursors under conventional heating 110
5.1 Introduction 110
5.2 Experimental procedure 110
5.2.1 Membrane synthesis with precursor isolation 110
5.2.2 Particle size and surface area measurement 113
5.3 Results 113
5.4 Conclusion 135
5.5 Appendix 138
6. Synthesising ZIF-8 onto tubular substrates using microwave heating. 142
6.1 Introduction 142
6.2 Experimental procedures 143
6.3 Results 146
6.3.1 Membrane synthesis using mixed precursors with microwave heating. 146
6.3.2 Membranes synthesis using isolated precursors with microwave heating. 168
6.4 Conclusions 182
7. Dynamic cold spraying of MOFs onto substrates 185
7.1 Introduction 185
7.2 Experimental procedure 186
7.3 Results 189
7.3.2 Pressure 189
7.3.3 Stand of distance (SOD) 193
7.3.4 Number of Passes 195
7.3.5 Angle of injection 198
7.3.6 High speed camera 201
7.4 Conclusions 206
8. Gas separation testing 207
8.1 Introduction 207
8.2 Experimental procedure 207
8.3 Results 209
8.4 Conclusions 218
9. Conclusions and Future Work 219
9.1 Conclusions 219

9.2 Future work 221
9.2.1 Conventionally heated batch system 221
9.2.2 Microwave heated batch system 222
9.2.3 Cold spray coating 222
10. References 223

List of figures

Figure 2- 1: Schematic of the separation of gas mixture moving across a porous membrane with pressure as the driving force for separation. 8
Figure 2- 2: Schematics representing the cross section of membranes. Non-porous membrane (a), symmetrical porous structure (b), asymmetrical porous structure (c) and composite structure (d). Schematics adapted from Terry et al. (Terry, 2004). Reproduced with permission from Terry et al. 2004. 10
Figure 2- 3: Schematic of membrane modules: (a) plate and frame membrane module, where two endplates enclose membranes, feed and product spacers (Baker, 2012). (b) exploded view of a spiral module, where the membranes and spacers wrapped around the central permeate collection channel (Baker, 2012). (c) tubular modules, a cluster of tubes housed in a single, larger tube acting as the pressure vessel (Uragami, 2017). (d) Hollow fibre module, schematic of shell side, feed passes through the shell side, and permeate passes through the fibre walls exiting the module via the fibre ends (Baker, 2012). Reproduced with permission from Baker et al. 2012 and Uragami et al. 2017.. 11
Figure 2- 4: Schematics of diffusion mechanisms, Knudsen (a), surface diffusion (b) molecular sieving (c) and solution diffusion (d). Some membranes may have a combination of the three separations mechanism (a-c) depending on material structure. Adapted from Terry et al. 2004 and Prasetya et al. 2020 (Terry, 2004) and (Prasetya et al., 2020). Reproduced with permission from Terry et al. 2004 and Prasetya et al. 2020. 13
Figure 2- 5: The Robeson plot shows two upper bounds from the years 1991 and 2008. The plot shows the different regions the different materials' performance can reach depending on materials derived from. 14
Figure 2- 6: Schematic of dispersed inorganic species in an ideal mixed matrix membrane (a), and an interfacial void between inorganic particle and polymer matrix (b). 17
Figure 2- 7: Schematic of metal organic frameworks self-assembly from metal ion and organic linker. 18
Figure 2- 8: Typical ZIF-8 cage with the yellow sphere representing free volume within the framework (Morris et al., 2012) (a) and rhombic shape representing the equilibrium shape of ZIF-8 (Linder-Patton et al., 2018) (b). Reproduced with permission from Morris et al. 2012 and Linder-Patton et al. 2018. 19
Figure 2- 9: Breathing (a) and linker rotation (b) are two types of structural behaviours of flexible MOF structures. (Qian et al., 2020). Reproduced with permission from Qian et al. 2020. 20
Figure 2- 10: Transmission electron microscopy images of ZIF-8 as a function of synthesis time 10 mins (a), 30 mins (b), 40 mins (c), 60 mins (d), 12 h (e) and 24 h(f). (Venna et al., 2010). Reproduced with permission from Venna et al. 2010. 22
Figure 2- 11: ZIF-8 growth on flat alumina substrates using suspension with PEI with (a) and without (b) seed (Bux et al., 2011). Reproduced with permission from Bux et al. 2011. 26
Figure 2- 12: Schematic of the growth between the hydroxyl group on the alumina substrate and the imidazoline group of the ZIF-8 structure (Tanaka et al., 2014b). Reproduced with permission from Tanaka et al. 2014. 27
Figure 2- 13: The surface image of two cycle synthesis of ZIF-8 including the APTES treatment stage (a), and surface image of two cycle synthesis on unmodified substrate with no APTES treatment. Synthesis conditions were microwave heating at 105 °C for 3 hours per cycle growth using zinc chloride (Zhu et al., 2016). Reproduced with permission from Zhu et al. 2016. 28

Figure 2- 14: Surface and cross-sectional SEM images of ZIF-8 membranes synthesized from zinc acetate dihydrate at room temperature and synthesis time of 24 hours. Synthesised at linker/metal ratios of 30, 40, and 60 (Tanaka et al., 2014a). Scale bar 2 µm. Reproduced with permission from Tanaka et al. 2014. 32
Figure 2- 15: Schematic illustration of RTD technique, the substrate is soaked in the precursor (a), heated in the oven (b), and the membrane (c). (Shah et al., 2013b). Reproduced with permission from Shah et al. 2013. 33
Figure 2- 16: SEM images of ZIF-8 membranes synthesised by RTD top view (a, b), and a cross-sectional view (c, d). (Shah et al., 2013b). Reproduced with permission from Shah et al. 2013. 34
Figure 2- 17: XRD patterns of ZIF-8 membranes as a function of synthesis time (Kwon and Jeong, 2013). Reproduced with permission from Kwon and Jeong 2013. 36
Figure 2- 18: Surface and cross-section SEM images of ZIF-8 membrane growth at 2 mins (a, b), 30 mins (c, d), 2 hours (e, f), and 4 hours (g, h). (Kwon and Jeong, 2013). Reproduced with permission from Kwon and Jeong 2013. 36
Figure 2- 19: Cross-section SEM image (a) and SEM-EDX line analysis of aluminium and zinc with a more magnified view of the outer cross-sectional image (b) at a reaction time of 72 h (Hara et al., 2014). Reproduced with permission from Hara et al. 2014. .. 37
Figure 2- 20: SEM images of the surface and cross-sectional images of ZIF-8 membranes prepared from zinc nitrate (a, b), zinc chloride (c, d), and zinc acetate (e, f). (Tran et al., 2020b). Reproduced with permission from Tran et al. 2020. 39
Figure 2- 21: Diffusion cell for the formation of ZIF-8 membrane (a), and the schematic formation of the ZIF-8 films on both sides of the nylon substrate via counter diffusion of the Zn^{2+} and $Hmim^{-}$ (Yao et al., 2011). Reproduced with permission from Yao et al. 2011. 40
Figure 2- 22: Stability measurement over time of ZIF-8 membrane prepared on tubular substrates. Permeances of CO_2 and CH_4, and separation factor of equimolar CO_2/CH_4. Feed stream conditions of 2 bar and 100 °C. (Zhu et al., 2016). Reproduced with permission from Zhu et al. 2016. 43
Figure 2- 23: CO_2 (a) and CH_4 (b) permeances, and CO_2/CH_4 ideal selectivity (c) for ZIF-8 membrane at pressure differences between 100 to 700 kPa and temperature between 303 to 343 K. (Lai et al., 2016a). Reproduced with permission from Lai et al. 2016. 44
Figure 2- 24: Single gas permeance of CO_2 and CH_4 across temperature range between 303 to 343 K at a pressure difference of 100 (a) and 700 (b) kPa. CO_2/CH_4 ideal selectivity CH_4 across temperature range between 303 to 343 K at a pressure difference of 100 (c) and 700 (d) kPa. (Lai et al., 2016a). Reproduced with permission from Lai et al. 2016. 45
Figure 2- 25: The effect of CO_2 feed composition on permeance of CO_2 and CH_4 (a) and CO_2/CH_4 separation factor of ZIF-8 membrane at 100 kPa pressure and 303 K temperature. (Lai et al., 2016a). Reproduced with permission from Lai et al. 2016. 46
Figure 2- 26: Shows the heating profiles of microwave (a) and conventional (b) heating. 47
Figure 2- 27: Cross-sectional images of (a) unmodified (Bux et al, 2009) and (b) modified (Bux et al, 2011) membranes synthesis on flat alumina disk substrates. Reproduced with permission from Bux et al. 2009 and Bux et al. 2011. 52
Figure 2- 28: Surface images of ZIF-8 membranes synthesised on APTES modified tubular substrates under (a) microwave and (b) conventional heating (Zhu et al., 2016). Reproduced with permission from Zhu et al 2016. 53

Figure 2- 29: Schematic of the three nozzles alternating between the metal and linker precursor. The substrate was sprayed with ethanol between each step to act as the rinsing step (Arslan et al., 2011). Modified with permission from Arslan et al. 2011. ... 54
Figure 2- 30: EDX analysis of cross-sectional membranes prepared with 100 (a) and 150 (b) cycles (Hurrle et al., 2017). Reproduced with permission from Hurrle et al. 2017. ... 55
Figure 2- 31: Plot of temperature vs velocity across the different air pressures. Taken from Kim et al. (Kim et al., 2016a). Reproduced with permission from Kim et al. 2016. ... 56
Figure 2- 32: XRD patterns of spray coated ZIF-8 films deposited onto copper substrates with airstream at 250 °C (a) with and (b) without DMF. The insert shown in (a) is the XRD pattern of the ZIF-8 powder (Kim et al., 2016a). Reproduced with permission from Kim et al. 2016. ... 57

Figure 3-1: Typical structure of a porous ceramic substrate. (Mestre et al., 2019). Reproduced with permission from Mestre et al. 2019. ... 58
Figure 3- 2: Schematic of steps involved in seeding the substrate (a), and schematic of the main steps involved in synthesising the membrane (b). Each schematic moves left to right. ... 61
Figure 3-3: Spray work set up when coating flat substrates using MOF slurry. ... 63
Figure 3-4: Schematic of the atomiser set up. ... 64
Figure 3- 5: Schematic showing the incident and reflected X-rays making an angle of θ symmetrical to the crystal planes' normal (He, 2009). Reproduced with permission from He et al. 2009. ... 65
Figure 3- 6: Illustrated schematic of crystal morphology of ZIF-8 evolving, initially starting as a cube (a), a cube with truncated edges (b), rhombic with truncated corners (c) and then rhombic dodecahedron (d). (Schejn et al., 2014). Reproduced with permission from Schejn et al. 2014. ... 66
Figure 3- 7: XRD pattern of ZIF-8, peaks labelled with corresponding crystallographic planes represented by corresponding peaks. ... 67
Figure 3- 8: Schematic showing the scanning electron microscopy's main components (Goodhew et al., 2000). Modified with permission from Goodhew et al. 2000. ... 68
Figure 3- 9: Schematic of the electrons' interaction zone from the probe and sample atoms beneath the specimen surface (Leng, 2013). Reproduced with permission from Leng et al. 2013. ... 69
Figure 3- 10: Surface and cross-section images of typical cubic and rhombic crystals of ZIF-8 membrane on the alumina substrate. ... 70
Figure 3- 11: Schematic of 3D shapes, sphere (a), cube (b) and rhombic (c). The red arrows reflect the points from which distance the sizes were measured. ... 70
Figure 3- 12: The alumina substrate's surface image with ZIF-8 crystal growth of typical cubic and rhombic. ... 71
Figure 3- 13: Surface images of substrates with varied ZIF-8 crystal growth, sparse (a) and dense growth (b). ... 71
Figure 3- 14: EDS spectrum recorded by SEM of ZIF-8 crystal growth on an alumina substrate. The sample composed of Zn, Al and O. ... 72
Figure 3- 15: Transitions of the K, L, M and N shells of an atom which lead to the X-ray lines indicated. (Goodhew et al., 2000). Reproduced with permission. ... 73
Figure 3- 16: Gas separation system with labelled components. ... 74

Figure 4- 1: Scanning electron microscopy images of ZIF-8 seed crystals collected via centrifuge, synthesised with the linker/metal ratio 8 and metal concentration of 36 mM. 78
Figure 4- 2: X-ray diffraction patterns of ZIF-8 seeds and of seeds collected from bulk solution after membrane synthesis..... 79
Figure 4- 3: Cross sectional and surface SEM images of uncoated bare alumina substrate, unseeded and seeded membranes synthesised at 150 °C for 5 hours with a linker/metal ratio of 8 and metal concentration of 36 mM. 81
Figure 4- 4: XRD patterns of seeded and unseeded membranes synthesised at 150 °C for 5 hours at linker/metal ratio of 8 and metal concentration of 36 mM. The dashed lines refer to the positions of the most prominent characteristic peaks of ZIF-8..... 82
Figure 4- 5: Surface SEM images of membranes synthesised at linker/metal ratio 8, metal concentrations of 36 mM, 72 mM, 144 mM, and 288 mM. Synthesised at 150 °C for 5 hours. 84
Figure 4- 6: XRD patterns of seeded membranes synthesised with mixed MOF solution at 150 °C for 5 hours, using a linker/metal ratio of 8 and metal concentrations of 36 mM, 72 mM, 144 mM and 288 mM. Dashed lines refer to the positions of the most prominent characteristic peaks of ZIF-8. 85
Figure 4- 7: Surface and cross section SEM images of seeded membranes synthesised at 150 °C for 5 hours using linker/metal ratio of 2 and metal concentrations of 72 mM and 288 mM. The white line marks the internal surface of the substrate where ZIF-8 growth has begun on the substrate surface with the arrow indicating membrane thickness..... 88
Figure 4- 8: XRD patterns of seeded membranes synthesised at 150 °C for 5 hours using a linker/metal ratio of 2 at metal concentrations of 72 mM and 288 mM. Dashed lines refer to the positions of the most prominent characteristic peaks of ZIF-8..... 89
Figure 4- 9: SEM surface images of membranes synthesised at 150 °C for 5 and 10 h, using linker/metal ratio of 8 and metal concentrations of 36 mM and 144 mM..... 90
Figure 4- 10: Schematic of two systems with high and low metal concentrations, depicting growth on the substrate surface. The high concentration surface shows that with increasing time the gaps between the crystals get filled due to more nuclei on the substrate surface beforehand. The low concentration system depicts that the gaps are filled with increasing time whilst some remain due to the fewer nuclei on the surface at the beginning of the synthesis..... 90
Figure 4- 11: SEM cross sectional images of membranes synthesised at 150 °C for 5 and 10 h with linker/metal ratio of 8 and metal concentrations of 36 and 144 mM. The dashed red lines and arrows indicate the inside of the substrate surface where the growth of ZIF-8 occurred..... 91
Figure 4- 12: XRD patterns of membranes synthesised at 150 °C at linker/metal ratio of 8 and metal concentrations of 36 mM and 144 mM for 5 and 10 h. Dashed line refers to the positions of the most prominent characteristic peaks of ZIF-8. 92
Figure 4- 13: Surface and cross section images of two layer seeded membranes synthesised using zinc nitrate hexahydrate, and zinc acetate dihydrate. Membranes were synthesised at 150 °C for 5 hours using a linker/metal ratio of 8 and metal concentration of 36 mM. 93
Figure 4- 14: XRD patterns seeded membrane synthesised using zinc nitrate hexahydrate and zinc acetate dihydrate at 150 °C for 5 hours at linker/metal ratio of 8 and metal concentration of 36 mM with two cycles. The dashed lines refer to the positions of the most prominent characteristic peaks of ZIF-8..... 95
Figure 4- 15: Surface SEM images of membranes synthesised using mixed salts (50:50) with seeds synthesised using zinc nitrate and zinc acetate. Metal concentration

of 36 and 144 mM with linker/metal ratio of 8. Synthesis conditions of 150 °C for 5 hours for one cycle. 96
Figure 4- 16: Cross sectional images of membranes synthesised using mixed salts (zinc nitrate hexahydrate and zinc acetate dihydrate = 50:50 molar ratio), metal concentrations of 36 mM and 144 mM, and linker/metal ratio of 8 at 150 °C for 5 hours. 97
Figure 4- 17: XRD patterns of membranes synthesised using mixed salts (zinc nitrate hexahydrate and zinc acetate dehydrate = 50:50 molar ratio), linker/metal ratio of 8 and metal concentrations of 36 mM and 144 mM. Synthesis conditions: 150 °C for 5 hours, one cycle. The dashed lines refer to the positions of the most prominent characteristic peaks of ZIF-8..... 98

Figure 5- 1:Schematic of sealed substrate in a reaction vessel filled with linker solution, and two Teflon plugged alumina substrates filled with metal solution. 111
Figure 5- 2: Surface images of the unseeded membranes synthesised (metal solution out) at room temperature for 24 hours with linker/metal ratio of 8 and metal concentrations of 72 mM and 288 mM. 114
Figure 5- 3: Surface and cross sectional SEM images of membranes synthesised on unseeded substrates with isolated pre-cursors (metal outside) at 150 °C for 5 hours (Linker/metal ratio= 8, metal concentration= 72 and 288 mM)..... 115
Figure 5- 4: XRD patterns of membranes synthesis on unseeded substrates with isolated pre-cursors (metal outside) using conventional heating at 150 °C for 5 hours with a linker/metal ratio of 8 at metal concentration of 72 mM and 288 mM. The dashed lines refer to the position of the most prominent characteristic peak of ZIF-8. 116
Figure 5- 5: Surface images and cross sectional SEM images of the membranes synthesised on seeded substrates with isolated pre-cursors (metal outside) at 150 °C for 5 hours (Linker/metal ratio= 8, metal concentration= 36 mM, 72 mM, and 288 mM). 117
Figure 5- 6: XRD patterns of membranes synthesised on seeded substrates at 150 °C for 5 hours (linker/metal ratio= 8, metal concentration= 36 mM, 72 mM and 288 mM, metal solution was outside). The dashed lines refer to the position of the most prominent characteristic peak ZIF-8. 119
Figure 5- 7: Surface SEM images and EDX elemental analysis of membranes, synthesised with isolated pre-cursors (metal outside) at 150 °C for 5 hours with linker/metal ratio of 8 and metal concentrations of 72 mM and 288 mM. Green represents Zinc. 120
Figure 5- 8: Cross section SEM images of membranes synthesised on unseeded substrates with isolated pre-cursors (metal inside) at 150 °C for 5 hours with a linker/metal ratio of 8 and metal concentrations of 72 mM and 288 mM. Red lines (and arrows) show where the cross section of the substrate begins..... 121
Figure 5- 9: XRD patterns of membranes synthesised without seeds with isolated pre-cursors (metal inside) at 150 °C for 5 hours using a linker/metal ratio of 8 and metal concentrations of 72 mM and 288 mM. The dashed lines refer to the position of the most prominent characteristic peaks of ZIF-8..... 123
Figure 5- 10: Cross section SEM images and XRD patterns of membrane synthesised on seeded substrates with isolated pre-cursors (metal inside) at 150 °C for 5 hours at a linker/metal ratio of 8 and metal concentrations of 36 mM, 72 mM, and 288 mM. 124

Figure 5- 11: Surface images and zinc analysis of seeded membranes synthesised at 72 mM and 288 mM at 150 °C for 5 hours. Isolated pre-cursors (metal inside) and linker/metal ratio of 8. 125
Figure 5- 12: Surface images of membranes synthesised on seeded substrates with isolated pre-cursors (metal outside) using conventional heating at 150 °C for 5 hours with a linker/metal ratio of 2 and metal concentrations of 72 mM and 288 mM. 127
Figure 5- 13: XRD patterns of membranes synthesised on seeded substrates with isolated pre-cursors (metal outside) at 150 °C for 5 hours using linker/metal ratio of 2 and metal concentration of 72 mM and 288 mM. The dashed lines refer to the position of the most prominent characteristic peak of ZIF-8. 128
Figure 5- 14: Surface image and EDX analysis of a membrane, showing Zn ions (in green), synthesised on seeded substrates with isolated pre-cursors (metal outside) at 150 °C for 5 hours, linker/metal ratio of 2 and metal concentration of 72 mM. 129
Figure 5- 15: Surface images of membranes synthesised on seeded substrates with isolated precursors (metal inside) at 150 °C for 5 hours, at linker/metal ratio of 2 and metal concentration of 72 mM and 288 mM. 129
Figure 5- 16: XRD patterns of membranes synthesised on seeded substrates with isolated pre-cursors (metal inside) at 150 °C for 5 hours using linker/metal ratio of 2 and metal concentration of 72 mM and 288 mM. The dashed lines refer to the position of the most prominent characteristic peaks of ZIF-8. 130
Figure 5- 17: XRD pattern and surface image of a membrane synthesised on seeded substrates with isolated pre-cursors (metal inside) at 150 °C for 5 hours, two cycles, using linker/metal ratio of 8 and metal concentration of 288 mM. 131
Figure 5- 18: XRD pattern and surface image of a membrane synthesized on seeded substrates with isolated pre-cursors (metal inside) at 150 °C for 5 hours at a linker/metal ratio of 32 and metal concentration of 288 mM. Red arrow highlights region of bare substrate. 132
Figure 5- 19: XRD pattern and surface image of a membrane synthesised on seeded substrates using zinc nitrate hexahydrate with isolated pre-cursors (metal inside) at 150 °C for 5 hours, at a linker/metal ratio of 8 and metal concentration of 288 mM. 133
Figure 5- 20: Schematic view of the edge of a tubular substrate with deposited seeds (filled red circles) on the outer and inner sides of the substrate surface, r_1 and r_2 representing inner and outer radius of the tubular substrate. 134

Figure 6- 1: Schematic of unplugged tubular substrate in CEM glass vial (8 ml capacity) with lid and filled with MOF solution (4 ml solvent volume). 143
Figure 6- 2: Photos of substrates in CEM glass vial with solvent volume of 4 ml and 2 cm alumina substrate in a 8 ml capacity vial (approximate diameter of 20 mm) (a), total solvent volume of 4 ml (2 ml inside plugged substrate) with 6 cm alumina substrate with Teflon plugs in a 8 ml capacity vial (b), solvent volume of 16 ml and 2 cm alumina substrate in a 32 ml capacity vial (approximate diameter of 30 mm) (c), CEM cavity with the selected attenuator (red arrow indicating where vial is inserted) for the 8 ml pressure vial (d) - the “IntelliVent” lid is withdrawn as the microwaves are not engaged. 144
Figure 6- 3: Surface images of seeded membranes synthesised with mixed MOF solutions with metal concentrations of 72 mM at linker/metal ratio of 8 (a) and linker/metal ratio of 2 (b). Surface images of seeded membranes synthesised with mixed MOF solutions with metal concentrations of 288 mM at linker/metal ratio of 8 (c)

and linker/metal ratio of 2 (d). Membranes synthesised with microwave heating at 100 °C for 1 hour. 147
Figure 6- 4: Cross sectional image of membrane synthesised with mixed ZIF-8 solution with metal concentration of 288 mM and linker/metal ratio of 8. Synthesised at 100 °C for 1 hour using microwave heating. Red arrows highlighting the inside of the substrate lining where crystal growth is expected. 148
Figure 6- 5: Particle size histograms of crystals on the substrate surface synthesised at linker/metal ratio of 8 and metal concentrations 288 mM synthesised with mixed MOF solution. 149
Figure 6- 6: XRD patterns of seeded membranes synthesised with mixed MOF solutions with metal concentration of 72 mM at linker/metal ratio of 8 (a) and linker/metal ratio of 2 (b). Surface images of seeded membranes synthesised with mixed MOF solutions with metal concentrations of 288 mM at linker/metal ratio of 8 (c) and linker/metal ratio of 2 (d). Membranes synthesised with microwave heating at 100 °C for 1 hour. The dashed lines refer to the position of the most prominent characteristic peaks ZIF-8. 150
Figure 6- 7: Surface images of seeded membranes synthesised with mixed MOF solutions at linker/metal ratio of 8 and metal concentrations of 72 mM with microwave heating for 3 hours at 100 °C (a) and conventional heating for 5 hours at 100 °C (b). Surface images of seeded membranes synthesised with mixed MOF solutions at linker/metal ratio of 8 and metal concentrations of 288 mM with microwave heating for 3 hours at 100 °C (c) and conventional heating for 5 hours at 100 °C (d). 151
Figure 6- 8: XRD patterns of seeded membranes synthesised with mixed MOF solutions at linker/metal ratio of 8 and metal concentrations of 72 mM using conventional heating (a) and microwave heating (b), and metal concentration of 288 mM using conventional heating (c) and microwave heating (d). Membranes were synthesised at 100 °C for 3 and 5 h using microwave and conventional heating, respectively. The dashed lines refer to the position of the most prominent characteristic peaks ZIF-8. 152
Figure 6- 9: Surface images of seeded membranes synthesised with mixed MOF solutions at linker/metal ratio of 2 and metal concentration of 72 mM via microwave (a) and conventional (b) heating. Surface images of seeded membranes synthesised with mixed MOF solutions with linker/metal ratio of 2 and metal concentration 288 mM via microwave (c) and conventional (d) heating. Membranes synthesised at 100 °C for 3 and 5 hours under microwave and conventional heating, respectively. 154
Figure 6- 10: Particle size histograms of crystals on the substrate surface synthesised at linker/metal ratio 2 and metal concentrations 72 mM using conventional (a) and microwave (b) heating. Membranes were synthesised at 100 °C for 3 and 5 h using microwave and conventional heating, respectively. 155
Figure 6- 11: Schematics of metal ions and respective solvation spheres. Diluted (a) and concentrated (b) systems each with different number of ions, and a diluted system with the same number of ions as b now in larger solvent volume (c). The dashed lines represent microwaves. 157
Figure 6- 12: XRD patterns of the seeded membranes synthesised with mixed MOF solutions at linker/metal ratio of 2 with metal concentrations of 72 mM using conventional (a) and microwave (b) heating, and metal concentration of 288 mM using conventional (c) and microwave (d) heating. Membranes were synthesised at 100 °C for 3 and 5 h using microwave and conventional heating, respectively. The dashed lines refer to the position of the most prominent characteristic peaks ZIF-8. 158
Figure 6- 13: Surface (a) and cross sectional (b) images of seeded membrane synthesised with mixed MOF solution (solvent volume of 16 ml) with linker/metal ratio

of 8 and metal concentration of 288 mM using microwave heating at 100 °C for 3 hours. 161
Figure 6- 14: SEM surface image (a) and EDX images of the surface showing Zn in green (b) and Al in red (c) of seeded membrane synthesised with mixed ZIF-8 solution (total solvent volume of 16 ml) with linker/metal ratio of 8 and metal concentration of 288 mM using microwave heating at 100 °C for 3 hours. 162
Figure 6- 15: XRD pattern of seeded membrane (a) and of ZIF-8 crystals collected from synthesis solution (b). MOF chemistry of linker/metal ratio of 8 and metal concentration of 288 mM, synthesised using microwave heating at 100 °C for 3 hours. The dashed lines refer to the position of the most prominent characteristic peaks of ZIF-8. 163
Figure 6- 16: Cross sectional (a) surface (b) images of seeded membrane synthesised with mixed MOF solutions at linker/metal ratio of 8 and metal concentration of 36 mM via microwave (at 100 °C for 3 h). Blue arrows pointing to the inside of the substrate surface and green arrows pointing towards the outside of the substrate. 164
Figure 6- 17: XRD patterns of the seeded membranes synthesised with mixed MOF solutions at linker/metal ratio of 8 with metal concentrations of 36 mM using microwave heating synthesised at 100 ^{o}C for 3 hours. The dashed lines refer to the position of the most prominent characteristic peaks ZIF-8. 165
Figure 6- 18: Surface (a) and cross sectional (b) images of seeded membrane synthesised with mixed MOF solution using zinc nitrate hexahydrate at linker/metal ratio of 8 and metal concentration of 288 mM via microwave heating. Synthesised at 100 °C for 3 hours. Red arrows highlighting potentially failed nucleated seeds. 166
Figure 6- 19: XRD patterns of the seeded membrane synthesised with mixed MOF solutions using zinc nitrate hexahydrate at linker/metal ratio of 8 with metal concentrations of 288 mM using microwave heating synthesised at 100 °C for 3 hours. The dashed lines refer to the position of the most prominent characteristic peaks ZIF-8. 166
Figure 6- 20: Surface images of seeded membranes synthesised with isolated precursors (metal inside) with metal concentration of 72 mM and linker/metal ratio of 8 (a) and linker/metal ratio of 2 (b). Surface images of seeded membranes synthesised with isolated precursors (metal inside) with metal concentration of 288 mM and linker/metal ratio of 8 (c) and linker/metal ratio of 2 (d). Membranes synthesised at 100 °C for 1 hour using microwave heating. 170
Figure 6- 21: XRD patterns of seeded membranes synthesised with isolated precursors (metal inside) with metal concentration of 72 mM and linker/metal ratio of 8 (a), and linker/metal ratio of 2 (b). Surface images of seeded membranes synthesised with isolated precursors (metal inside) with metal concentration of 288 mM and linker/metal ratio of 8 (c) and linker/metal ratio of 2 (d). Membranes synthesised at 100 °C for 1 hour using microwave heating. The dashed lines refer to the position of the most prominent characteristic peaks ZIF-8. 171
Figure 6- 22: Surface images of seeded membranes synthesised with isolated precursors (metal inside) at linker/metal ratio of 8 and metal concentration of 72 mM at 100 °C using conventional heating for 5 hours (a, b), and microwave heating for 3 hours (c). Surface images of seeded membranes synthesised with isolated precursors (metal inside) with linker/metal ratio of 8 and metal concentration of 288 mM at 100 °C using microwave heating for 3 hours (d) and conventional heating for 5 hours (e, f). 172
Figure 6- 23: Particle size histogram of crystals on the substrate surface synthesised at linker/metal ratio 8 and metal concentrations 72 mM using microwave heating. Membranes synthesised for 3 hours at 100 °C. 173
Figure 6- 24: XRD pattern of seeded membranes synthesised with isolated precursors (metal inside) with linker/metal ratio of 8 at metal concentration of 72 mM using

conventional heating for 5 hours (a, b) and microwave heating for 3 hours at 100 °C (c), and metal concentration of 288 mM hours using conventional heating for 5 hours (d, e) and microwave heating for 3 hours at 100 °C (f). The dashed lines refer to the position of the most prominent characteristic peaks ZIF-8. 174
Figure 6- 25: Surface images of seeded membranes synthesised with isolated precursors (metal inside) with linker/metal ratio of 2 at 100 °C and metal concentration of 72 mM using conventional heating for 5 hours (a, b), and microwave heating for 3 hours at 100 °C (c). Surface images of seeded membrane synthesised with isolated precursors (metal inside) with linker/metal ratio of 2 at 100 °C and metal concentration 288 mM using microwave heating for 3 hours (d), and conventional heating for 5 hours (e, f). Red arrows highlighting ZIF-8 crystals. 175
Figure 6- 26: Particle size histogram of crystals on the substrate surface synthesised with isolated precursors (metal inside) at linker/metal ratio 2 and metal concentrations 72 mM microwave heating for 3 hours at 100 °C. 176
Figure 6- 27: XRD pattern of seeded membranes synthesised with isolated precursors (metal inside) with linker/metal ratio of 2 with metal concentration of 72 mM using conventional heating at 100 °C for 5 hours (a, b) and microwave heating for 3 hours (c). XRD pattern of seeded membranes synthesised with isolated precursors (metal inside) with metal concentration of 288 mM using conventional heating at 100 °C for 5 hours (d, e) and microwave heating for 3 hours (e). The dashed lines refer to the position of the most prominent characteristic peaks of ZIF-8. 177
Figure 6- 28: Surface image of seeded membrane synthesised with isolated precursors (metal inside) with metal concentration of 288 mM and linker/metal ratio of 8. Membranes synthesised at 100 °C for 3 hours using microwave heating with total solvent volume of 16 ml. 178
Figure 6- 29: Particle size histogram of crystals on the substrate surface synthesised with isolated precursors (metal inside) at linker/metal ratio 8 and metal concentrations 288 mM using microwave heating with total solvent volume of 16 ml. Membranes synthesised for 3 hours at 100 °C. 179
Figure 6- 30: XRD pattern of seeded membranes synthesised with isolated precursors (metal inside) with linker/metal ratio of 8 at metal concentration of 288 mM. Membranes synthesised at 100 °C for 3 hours using microwave heating with total solvent volume of 16 ml. The dashed lines refer to the position of the most prominent characteristic peaks of ZIF-8. 180
Figure 6- 31: XRD pattern of ZIF-8 seeds synthesised from zinc nitrate hexahydrate and 2-methylimidazole using methanol at 150 °C for 5 hours (a), and the metal precursor zinc acetate dihydrate (b) and the linker precursor 2-methylimidazole (c) used for ZIF-8 membrane synthesis. The dashed lines refer to the position of the most prominent characteristic peaks of ZIF-8. 181

Figure 7- 1: Schematic of MOF suspension injected into high-pressure gas stream. 185
Figure 7- 2: Photo of Dymet gun, extendable arm, suspension feed line feeding into spray nozzle. 187
Figure 7- 3: Schematic of the atomiser set up. 188
Figure 7- 4: SEM surface images of uncoated flat alumina substrate (a) and uncoated flat alumina photo (b). 189
Figure 7- 5: SEM images of substrates synthesised with the suspension released from the side of the airstream at pressures of 2, 4 and 6 bar. Photo of coated substrates of 2 bar (a), 4 bar (b), and 6 bar (c). 190

Figure 7- 6: SEM surface images and photos of coated substrate sprayed at 2, 4 and 6 bars pressure. Other synthesis parameters, suspension flow rate of 0.25 ml/s, gun speed of 20 mm/s, SOD of 100 mm, single-pass, angle of injection of 90 °, HKUST suspension with an 7 wt.%, and distance between nozzle and suspension release point 20 mm and height above nozzle 10 mm..... 191
Figure 7- 7: XRD patterns of coated substrate sprayed at 2 (a), 4 (b) and 6 (c) bars pressure. Other synthesis parameters, suspension flow rate of 0.25 ml/s, gun speed of 20 mm/s, SOD of 100 mm, single-pass, angle of injection of 90 °, HKUST suspension with a 7 wt.%, and distance between nozzle and suspension release point 20 mm and height above nozzle 10 mm. The dashed lines refer to the position of the most prominent characteristic peaks of HKUST-1. 192
Figure 7- 8: SEM images and photos of coated substrates prepared at SOD of 300 mm, 600 mm, and 900 mm. Prepared with a suspension flow rate of 0.25 ml/s, gun speed 20 mm/s, 2 bar pressure, single-pass, angle of injection of 90 °, HKUST suspension with a 7 wt.% and distance between nozzle and suspension release point 20 mm and height above nozzle 10 mm..... 194
Figure 7- 9: XRD patterns of coated substrate sprayed at SOD of 300 (a), 600 (b) and 900 (c) mm. Other synthesis parameters, suspension flow rate of 0.25 ml/s, gun speed of 20 mm/s, 2 bar pressure, single-pass, angle of injection of 90 °, HKUST suspension with a 7 wt.%, and distance between nozzle and suspension release point 20 mm and height above nozzle 10 mm. The dashed lines refer to the position of the most prominent characteristic peaks of HKUST-1. 195
Figure 7- 10: SEM images and photos of coated substrates prepared with 2, 4 and 6 passes. Other synthesis parameters, suspension flow rate of 0.25 ml/s, gun speed 20 mm/s, SOD of 300 mm, angle of injection of 90 °, HKUST suspension with an 7 wt.% and distance between nozzle and suspension release point 20 mm and height above nozzle 10 mm. 196
Figure 7- 11: XRD patterns of coated substrate sprayed at 2 (a), 4 (b) and 6 (c) passes. Other synthesis parameters, suspension flow rate of 0.25 ml/s, gun speed of 20 mm/s, 2 bar pressure, 300 mm SOD, angle of injection of 90 °, HKUST suspension with a 7 wt.%, and distance between nozzle and suspension release point 20 mm and height above nozzle 10 mm. The dashed lines refer to the position of the most prominent characteristic peaks of HKUST-1. 198
Figure 7- 12: SEM images and photos of coated substrates of samples prepared with an angle of injection of 30 °, 50 °, and 70 °. Other synthesis parameters, suspension flow rate of 0.25 ml/s, gun speed 20 mm/s, SOD of 300 mm, 2 passes, HKUST suspension with a 7 wt.% and distance between nozzle and suspension release point 20 mm and height above nozzle 10 mm..... 200
Figure 7- 13: SEM images of samples synthesised with an angle of injection of 30 °, 50 ° and 70 °. Other synthesis parameters, suspension flow rate of 0.25 ml/s, gun speed 20 mm/s, SOD of 300 mm, 2 passes, HKUST suspension with a 7 wt.% and distance between nozzle and suspension release point 20 mm and height above nozzle 10 mm. 200
Figure 7- 14: XRD patterns of coated substrate sprayed with an angle of injection of (a) 30, (b) 50 and (c) 70 °. Other synthesis parameters, suspension flow rate of 0.25 ml/s, gun speed of 20 mm/s, 2 bar pressure, 300 mm SOD, 2 passes, HKUST suspension with a 7 wt.%, and distance between nozzle and suspension release point 20 mm and height above nozzle 10 mm. The dashed lines refer to the position of the most prominent characteristic peaks of HKUST-1. 201
Figure 7- 15: High speed camera images at the flow rates of 30 ml/min (a), 50 ml/min (b), 75 ml/min (c) and 100 ml/min (d). Figures (i), (ii), (iii) and (iv) represent 5, 10, 20

and 30 mm distance between air nozzle and suspension exit, respectively. The angle of injection across all flow rates is 90 °. 204
Figure 7- 16: Subtracted images of HKUST-1 suspension at 7 wt.% (a) and water (b). A flow rate of 75 ml/min with 10 mm distance between the air nozzle and suspension release point. The angle of injection of 90 °. 205

Figure 8- 1: Photo of the gas separation system near to completion. 208
Figure 8- 2: Flow diagram of the gas separation system (Campbell and Tokay, 2017). Reproduced with permission from Campbell and Tokay 2017. 209
Figure 8- 3: Cross sectional images of membranes synthesised at 150 °C for 5 hours at linker/metal ratio 8 for one cycle at metal concentration of 36 mM on unseeded substrate (a) and seeded substrate (b), and metal concentration 144 mM on seeded substrate (c). Cross sectional image of seeded membranes synthesised at linker/metal ratio 8 at 150 °C for 10 hours at metal concentration of 36 mM (d) and 144 mM (e). Cross sectional image of seeded membrane synthesised at 150 °C for 5 hours at linker/metal ratio 8 and metal concentration of 36 mM for two cycle synthesis. Red arrows and dashed lines highlighting the inside of the substrate lining where crystal growth is expected. 216

List of tables

Table 2- 1: Surface modification techniques that have used for ZIF-8 membrane synthesis..... 24
Table 2- 2: ZIF-8 membrane growth methodologies..... 29
Table 2- 3: Selected single gas permeances and selectivities of ZIF-8 membranes for CO_2 and CH_4..... 42
Table 2- 4: Single gas permeances of CO_2 and CH_4 of ZIF-8 membranes published in the literature, synthesised using microwave heating as functions of synthesis time, synthesis temperature, and precursor concentration and ratios. 51

Table 3- 1: Chemical and suppliers used in this study..... 59

Table 4- 1: Metal salts, concentrations, linker/metal ratio, seeding and synthesis time used for batch synthesis. 76
Table 4- 2: Summarising surface coverage and thicknesses of membranes synthesised using mixed precursors..... 99

Table 5- 1: Metal salts, concentrations, linker/metal ratio, seeding and synthesis time used for batch synthesis. 111
Table 5- 2: Summarising fluxes and crystal sizes of the isolated system at linker/metal ratio 8 at their respective precursor location and metal concentration. 126
Table 5- 3: Membrane thickness and surface coverage of membrane synthesised using isolated precursors at their respective precursors' concentrations and ratios. 135

Table 6- 1: Metal concentration and linker/metal ratio of the isolated membranes synthesis (metal in) and mixed precursor solutions via conventional (5 h) and microwave (3 h) heating at 100 ^{o}C. 145
Table 6- 2: Solvent volumes, moles of precursors used in the synthesis of ZIF-8 membranes using microwave heating from literature and this study. 160
Table 6- 3: Summary of surface coverage of membrane synthesised using microwave heating with their respective precursors concentration and ratios. 182

Table 8- 1: Permeance and ideal selectivities of seeded membranes synthesised using mixed ZIF-8 solution under conventional heating. Membranes synthesised at linker/metal ratio 8 for 5 hours at 150 °C, washed, dried at 100 °C for 2 hours in the conventional heated oven unless indicated differently in footnotes. Permeance and ideal selectivity of ZIF-8 membranes from literature for the CO_2/CH_4 mixtures are also tabulated..... 210

1. Introduction

1.1 General background

Although there has been a rapid expansion in renewable energies, the global energy demand for fossil-derived fuels has not decreased and remains around 80 % of the total primary energy demand (Kenarsari et al., 2013, Mondal et al., 2012, Johnsson et al., 2019). Johnsson et al. reported that despite the combined investments across nations in renewable energy sources being an approximate 230 US billion dollars between 2004 and 2015, which is when the expansion in renewables had been the strongest, the demand for fossil derived energy has not decreased, rather increasing from 80.5% in 2004 to 81.4% in 2015, yet the demand for non-hydro renewable energy demand grew by only 0.2%, from 11.0 to 11.2% between 2004 and 2015, respectively. (Johnsson et al., 2019).

Natural gas is one of the cleanest fossil-derived fuels. Globally it only accounted for 20 % of CO_2 emissions in 2016, whereas CO_2 emissions from coal, oil and other sources accounted for 44%, 35% and 1%, respectively (International Energy Agency, 2018). The demand for natural gas has been increasing with production, rising every year since 2009 and seeing a global increase of 3.6% in 2017 from the year before. Production of natural gas reached a record of 3768 billion cubic metres in that same year (International Energy Agency, 2018). Nationally, in the UK, natural gas makes nearly 40% of the total primary energy supply (TPES), where fossil fuels dominate at 80% of the TPES (Bioenergy, 2018). With the consumption of natural gas in the UK set to rise to 74% in 2050 (Richards and Al Zaili, 2020). It is clear, the demand for natural gas will rise, both nationally and internationally.

To help reduce the dependence on fossil fuels, the ‘renewable natural gas’, biomethane, is also being used as a fuel. It is derived from biogas that is a mixture of CH_4/CO_2 (with trace amounts of other gases), which is produced by anaerobic digestion - the biological breakdown of organic matter without oxygen (Ileleji et al., 2015). The organics can be manures, municipal wastes, food wastes, green wastes, and plant residues. The biomethane can either be used directly or inserted into the gas network. Although biomethane represents 0.1% of today’s global methane demand (International Energy Agency, 2020), it supports waste management, is carbon neutral, and helps a nation move towards energy security (Chen et al., 2015). Within the EU, Germany is the largest producer of biogas followed by the UK and Italy with 46.7, 16.2

and 11.3 % shares of the total produced biogas in the EU, respectively, with the UK having 92 biogas to biomethane upgrading plants (Lombardi and Francini, 2020). There is a great deal of potential for biomethane in the UK.

The challenge with natural gas and the renewable biogas is that they are contaminated with CO_2 with concentrations up to 70 and 45%, respectively (First et al., 2014). The CH_4/CO_2 mixture cannot be consumed without removing the CO_2 contaminant since it lowers the calorific value of the CH_4, affecting its selling price. Another challenge in the transporting pipeline network is water content. The CO_2 causes the water to become acidic, leading to the corrosion of the pipes, increasing operational costs. The CO_2 also causes issues when cooling the natural gas to liquified natural gas (LNG) for transportation, the CO_2 can freeze leading to blockages in the transporting pipeline system, inflating operations costs further (First et al., 2014, Mohshim et al., 2012, Shimekit and Mukhtar, 2012).

Currently, amine absorption is the more dominant process for the removal of carbon dioxide from the CH_4/CO_2 mixture. Although it is a promising technology for CO_2 separation, alternative technologies are being sought since amine absorption is an energy intensive process due to the heating and cooling required for the regeneration of amine solvent. There is also regular maintenance and close monitoring of the equipment is needed because of the corrosive nature of the amine solvent, thus increasing operational costs further. There are also the environmental and safety concerns due to amine emissions degrading into volatile components, nitrosamines, and nitramines (Kohl, 1997, Hägg et al., 2017, Leung et al., 2014).

Another option for the separation of the gas mixtures of CH_4/CO_2 are using membrane-based separation technologies. Membranes are semi-permeable barrier materials. The technology requires no phase change and are therefore up to 50% more energy efficient than the absorption process. The advantage with membrane separations is that they are less energy intensive, and there is also the ease of retrofitting to existing unit operations since membrane separation equipment is very simple, compact, and easy to operate and control. Because the systems are modular, they can be easily scaled up, and partially operated depending on demand (Stern, 1994). Commercially, for the separation of CO_2/CH_4, the membranes used in industry are polymeric membranes due to ease of manufacture and low cost. Polymeric membranes that are being used for natural gas purification from as early as the 1980s, are cellulose acetate, polysulfone and polyimide (Baker and Lokhandwala, 2008). However, because of the high pressures and temperatures of the natural gas streams and impurities, such

as the hydrocarbons and condensable gases (H_2S, N_2, and CO_2) the polymeric structure swells and plasticizes (Wang et al., 2017b). This impedes selectivity leading to methane losses, reducing the overall longevity of the membrane. Because of these reasons, amine absorption continues to dominate the market today (Baker and Lokhandwala, 2008, Wang et al., 2017b, Xie et al., 2019, Usman et al., 2019).

An alternative to polymers is the relatively new hybrid structure of metal organic frameworks (MOFs), which are consisted of metal centres, linked together by organic units (Qiu and Zhu, 2009). An attractive feature of MOFs is the high internal surface area of up to 10000 m^2/g (Furukawa et al., 2013), porosity, and tailorability of the structure. The publication of MOF structures can be found from early as 2001, focusing on gas storage (Eddaoudi et al., 2002). Since MOFs have pore sizes up to 5 Å giving them molecular sieving properties when separating gas molecules (Zhu et al., 2020), and CO_2 adsorption capacities of up to 8 mmol/g (Ban et al., 2020). The chemistry of MOFs is described as 'click chemistry' since they can be formed by simply changing either or both the metal centre and inorganic linker, thereby allowing for infinite combination of structures to be constructed (Li et al., 2019). This allows the MOF structure to be tailored for its purpose.

Although thousands of MOF structures have been fabricated, only a fraction have been fabricated as membranes, order of magnitude fewer (Shah et al., 2011, Adatoz et al., 2015) with the earliest reports of MOF membranes being published in 2009 (Aceituno Melgar et al., 2015). This reflects the difficulty in achieving defect free, dense, and continuous films on the substrates. It comes as no surprise that additional preparatory steps are needed for most MOF membranes to achieve a more robust growth of the structures onto the substrates. In most synthesis methodologies, surfaces of the substrates are modified to provide sites of nucleation or 'anchors' to promote continuous and dense growth of the MOF structures onto the substrates. Hence the membrane synthesis methodology adopted does impact the microstructure and hence final separation performance of the MOF films (Aceituno Melgar et al., 2015).

Zeolitic imidazole framework-8 (ZIF-8) belongs to the ZIFs family, that are a subclass of MOFs. ZIF-8 is made up of the metal centre, zinc, and the organic linker, imidazole. ZIFs have similar properties to the inorganic structure of zeolites, such as their chemical and thermal stabilities. However, one difference between the two structures is that zeolites have a more rigid structure resulting in a more robust molecular sieving property when separating gas mixtures when compared to the flexible ZIF structures (Shah et al., 2011). However, the hydrophobic ZIF-8 structure is ideal for the

separation of the CO_2/CH_4 mixture. The structure can withstand impurities such as aromatic hydrocarbons and water in natural gas streams. Another advantage of the structure is the preferential adsorption of polar molecules such as CO_2 to its structure via electrostatic interaction (Lai et al., 2014b). In addition, the large pores of 11.6 Å can accommodate more gas species in its ZIF-8 cage. The pore aperture of 0.34 nm makes ZIF-8 ideal for separation of the CH_4/CO_2 mixture, since the kinetic diameters of CH_4 and CO_2 are 0.38 and 0.33, respectively (Venna and Carreon, 2009).

Over 70 % of the published papers on ZIFs membrane belong to ZIF-8 (Zhang and Koros, 2015). In addition to, the reported challenges with repeatability and reproducibility further limit commercialisation of ZIF-8 membranes (Zhang et al., 2013).

There are difficulties in upscaling the separation surface areas of ZIF-8 membranes from the average working area of 10 cm^2 in the lab to several hundred metre squared at the pilot scale. There are also concerns whether the separation properties can be maintained when upscaling. These criteria's limit commercialisation opportunities. The associated costs of the substrate modules that ZIF-8 is grown onto is another challenge, though this may change in the future (Zhang and Koros, 2015).

To commercialise the membrane technology from the bench scale, longer and multiple tube synthesis is needed to maximise surface area, and a continuous synthesis methodology is needed for ease of scalability. In addition, to maximise the efficiency of growth of MOFs onto the substrate a robust surface modification is needed.

1.2 Aims, objectives and novelty.

Therefore, the aim of this thesis is understanding heterogenous growth (growth of the membrane on a substrate surface) of ZIF-8 onto substrates, and present novel methods to circumvent difficulties with the heterogenous growth of ZIF-8 onto tubular substrates. Also, develop novel synthesis methodologies that have identified limitations of membrane fabrication techniques from literature and establish a theory of the respective methodologies when coating MOFs onto substrates.

The objectives of this thesis are:

- Determine the effects of metal and linker precursor concentration and linker/metal ratios have on microstructure of ZIF-8 in heterogenous growth onto substrates.
- Evaluate the heterogenous growth on the surface of substrates by isolating precursors.
- Determine the effects of conventional and microwave heating on the growth of ZIF-8 onto substrates.
- Develop a mechanical set-up for the continuous spray coating of MOFs by designing the atomiser.
- Characterise membranes using X-ray Diffraction, Scanning Electron Microscopy and Energy Dispersive X-ray analysis to determine the synthesis conditions effect on structure relation.

The thesis presents novelty in three key areas:

1. The single step metal-linker isolation work is the study of reaction and diffusion effects of ZIF-8 precursors across the substrate surface. For the first time, the work is presented with the flux calculations across various concentrations and ratios (with and without seeding) with the precursors' location being alternated. This has not been done before in literature for ZIF-8 using tubular substrates.
2. Microwave chapter presents novel metal-linker isolation work and for the first time the role of microwave chemistry on the growth of ZIF-8 onto tubular substrates (in both mixed and isolated batch systems). This will allow optimising the microwave reaction chemistry for membrane growth. This has not been done for MOF or zeolite membranes.
3. The dynamic cold spraying chapter delivers a novel study where the mechanical design of the atomiser for the coatings of MOFs onto substrates was conducted using unheated air streams. This has not been reported in literature before even though papers highlight its importance when coating substrates. The work was involved studying the momentum transfer between air and liquid streams, and deposition efficiency onto target substrates by varying mechanical parameters. The novel atomiser design created a starting point to progress the work to the pilot scale using tubular substrates.

1.3 Chapter outlines

Chapter 1 provides the motivation behind the research, the challenges associated with the established natural gas purification technologies, the need for more research in membranes and gas separation area, and existing research done on the ZIF, ZIF-8.

Chapter 2 provides a literature review, covering membrane theory in general, MOF chemistry, and past and present synthesis methods of MOF membranes in batch systems with a in depth review of microwave chemistry. This also shows studies published so far on cold spray coating of MOFs or their precursors.

Chapter 3 provides the details of the experimental work done in the PhD.

Chapter 4 discusses the synthesis of membranes using conventional heating. The aim of the chapter was to study how the changes in the precursor concentration and ratios affect membrane microstructure.

Chapter 5 introduces the novel metal-linker isolation system. The aim of the chapter was to study how the ZIF-8 forms at the substrate surface via changing precursor locations, and its impact on membrane microstructure. This was evaluated at the different precursor concentrations and ratios.

Chapter 6 evaluates the effects of the microwave heating mechanism on the heterogenous growth of MOFs, the role of microwave chemistry in the heterogenous nucleation to better design future experiments.

Chapter 7 introduces the novel study of the design of the atomiser for the continuous coating of MOFs using cold spray. This is a preliminary study in this area of work and provides a platform for future experiment.

Chapter 8 presents the testing of ZIF-8 membranes synthesised using mixed precursors in the batch system under conventional heating.

Chapter 9 summarises and concludes the thesis and provides suggestions for future direction of the work.

1.4 Planned publications

1. The novel metal-linker isolation work under conventional heating across a range of metal concentrations and linker/metal ratios, and alternating precursor location.
2. The role of microwave chemistry on the heterogenous growth of MOFs in both mixed and isolated systems.
3. The design of the atomiser and continuous coating of tubular substrates with MOFs.

1.5 Research work presented at conferences

Attended the ChemEngDayUK2017 conference organised by the IChemE at the University of Birmingham in February 2017. Was invited to present both a Power Point and poster presentations on the mixed batch system. Received 1st prize award for the presented poster under the theme “Energy Generation, Storage and Utilisation”.

Euromembrane 2018 conference organised by the European Membrane Society in Valencia, Spain. Presented poster on the novel metal-linker isolation work.

2. Literature review

2.1 Membranes

A membrane is a discrete interface that selectively moderates the movement of molecules across a semi-permeable barrier. The molecular restrictions can be based on size, solubility, diffusivity, and molecules' charge. A membrane separation process is described as a rate process (Terry, 2004), for separation to occur one of the species must move through the barrier faster than the other (Kao et al., 2012). The measure by which degree the gaseous component is permitted across the membrane barrier is referred to as permeance (Li et al., 2008a), and retentate is the second concentrated stream retained by the membrane (Adatoz et al., 2015). Driving forces for separation can be pressure difference, temperature difference, electric potential, concentration difference, or chemical potential. For gas separations the most common driving forces is pressure (Baker, 2012, Terry, 2004)

Figure 2-1 shows a gas pair schematic across a semi-permeable barrier under a pressure difference.

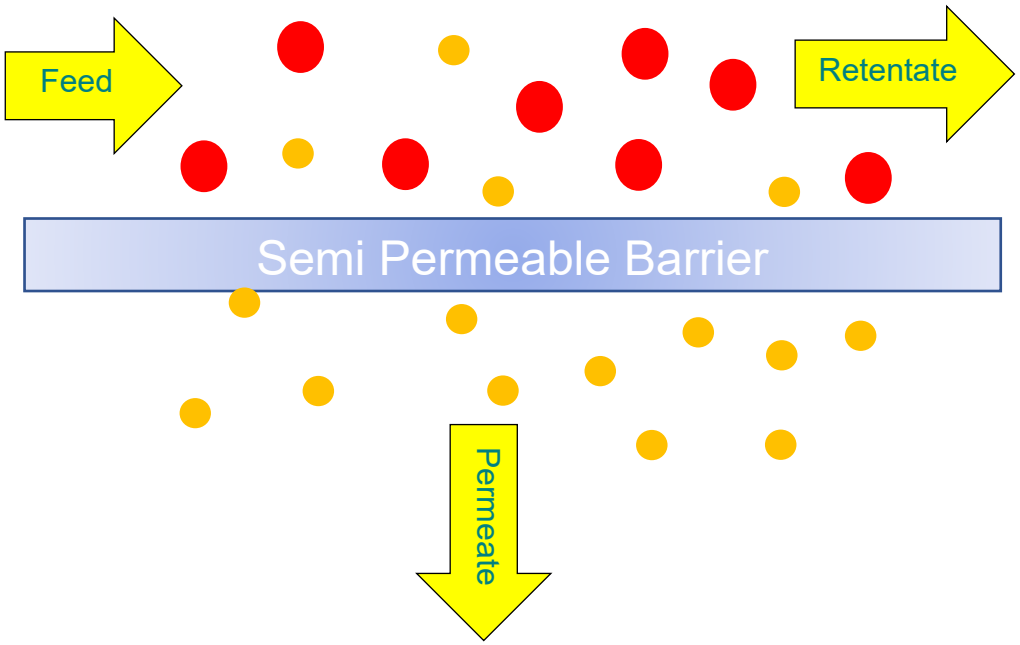


Figure 2- 1: Schematic of the separation of gas mixture moving across a porous membrane with pressure as the driving force for separation.

The membrane materials may also influence separation, as gas species may interact with chemical moieties present in the membrane. For example, one of the gas species may preferentially adsorb onto its structure (Prasetya et al., 2020). Membranes are

categorised as organic, polymers, and inorganic, such as ceramic and metals (Terry, 2004).

Figure 2-2 provides a generic schematic of membrane structures; dense, symmetrical, asymmetrical, and composite.

Polymer membranes can be categorized as symmetric (Figure 2-2a, b), asymmetric (Figure 2-2c), and composite (Figure 2-2d) (Terry, 2004). Symmetric can be a dense non-porous structure in which the permeants are transported by diffusion under a driving force such as concentration, pressure, or electrical potential gradient. Hence, since the separation is driven by their solubilities similar size permeants can be separated (Baker, 2012). Dense membranes are used for gas separation, pervaporation, and reverse osmosis (Baker, 2012). Symmetrical porous structures filter particles based on the pore size distribution of the membrane. Hence molecules with considerably different sizes can be separated effectively by these membranes. These symmetrical porous membranes are ideal in ultrafiltration and microfiltration applications (Baker, 2012, Uragami, 2017). An asymmetrical membrane has a denser outer layer that becomes less dense as it moves away from the outer surface (Figure 2-2c). The asymmetry creates less resistance as the molecules pass through the structure. Composite membranes (Figure 2-2d) are made up of different polymers; the top and support layer are optimised independently for the designated purpose. The top layer purpose is separation, usually a thin selective layer, while the bottom is to provide mechanical support and minimal resistance to mass transfer (Terry, 2004).

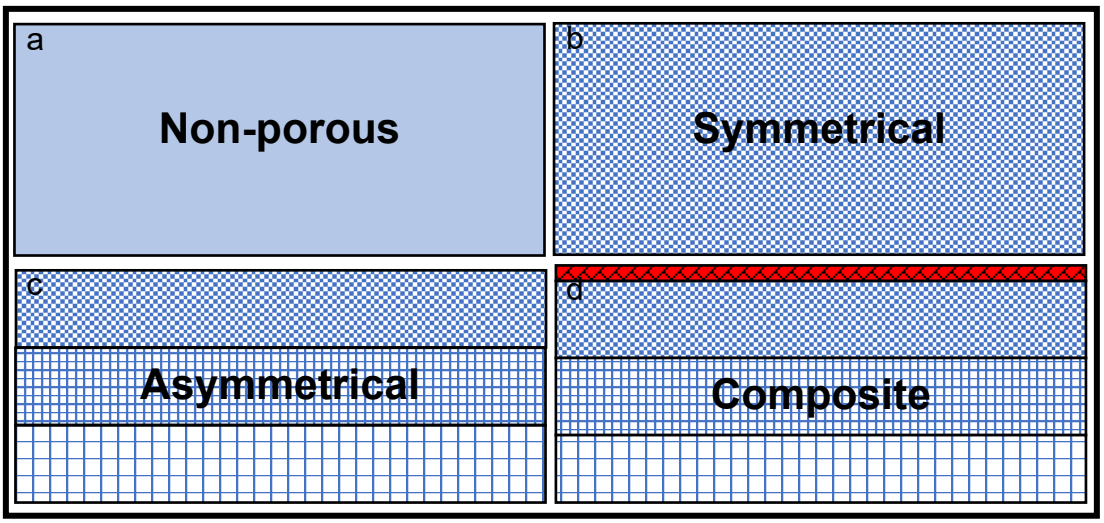


Figure 2- 2: Schematics representing the cross section of membranes. Non-porous membrane (a), symmetrical porous structure (b), asymmetrical porous structure (c) and composite structure (d). Schematics adapted from Terry et al. (Terry, 2004). Reproduced with permission from Terry et al. 2004.

Inorganic membranes are heat-, chemical-, and organic-solvent-resistant membranes synthesised from materials such as ceramics, metal, and zeolites. Composite membranes can also be prepared using inorganic membranes (Uragami, 2017). An advantage of ceramic membranes is that they are stable at high temperatures and chemically inert (Baker, 2012). Inorganic structure role in gas separations will be discussed later in the literature review.

For membranes to be used commercially, surface areas of 100's to 1000's m^2 of the membrane are required. Hence packing the membranes efficiently in the most economical manner must be considered (Baker, 2012), which can be achieved via modules. Membrane modules can be flat (plate-frame), spiral wound, tubular, and hollow fibre (Terry, 2004). Figure 2-3 shows the schematics of the different membrane's modules. The plate-frame modules are one of the earliest modules and have been developed for small applications. However, they are expensive when compared to the alternatives and suffer from leakages. They are used mainly electrodialysis, pervaporation, and in some cases, reverse osmosis and ultrafiltration. The separation is straightforward, the feed is pushed against the plates, and the permeate and retentate exit in separate channels (Mazzotti et al., 2016). Spiral wound modules are formed by a flat membrane wrapped into a 'swiss roll' structure separated by mesh separators (Harker et al., 2002). The feed comes into the module axially, where some of the feed permeates into the membrane envelope and then travels towards the central channel of the module to exit (Baker, 2012). Spiral wound modules are used for reverse osmosis, ultra-filtration, and gas separation (Mazzotti et al., 2016). Another form of geometry for membrane modules are tubular modules, housing membranes synthesised on the inside of the porous tubular substrates (Harker et al., 2002); substrates usually made from ceramic or stainless steel (Uragami, 2017). Each module houses a cluster of tubular substrates with substrate lengths of between 1-6 meter (Harker et al., 2002), with diameters over 3-5 mm (Uragami, 2017). Substrates with smaller diameters than this are classed as capillary or hollow-fibre membranes, and these are made up of a bundle of fine fibres sealed in a tube (Uragami, 2017). Hollow-fibre membranes are the most efficient mode of packing efficiency and are one of the few membranes geometry that has been successfully commercialized for gas

separations (Zhang and Koros, 2015). There are two geometries for feed streams, shell-side (outside) and bore-side (inside) favoured for high and low pressures feeds, respectively, with the shell side layout used for gas separations (Mazzotti et al., 2016). Although the module has the advantage of housing large membrane areas, up to 4924 m^2/m^3, the production costs are expensive due to the sophistication of the production process and capital investment required for the hollow fiber production. (Obotey Ezugbe and Rathilal, 2020)

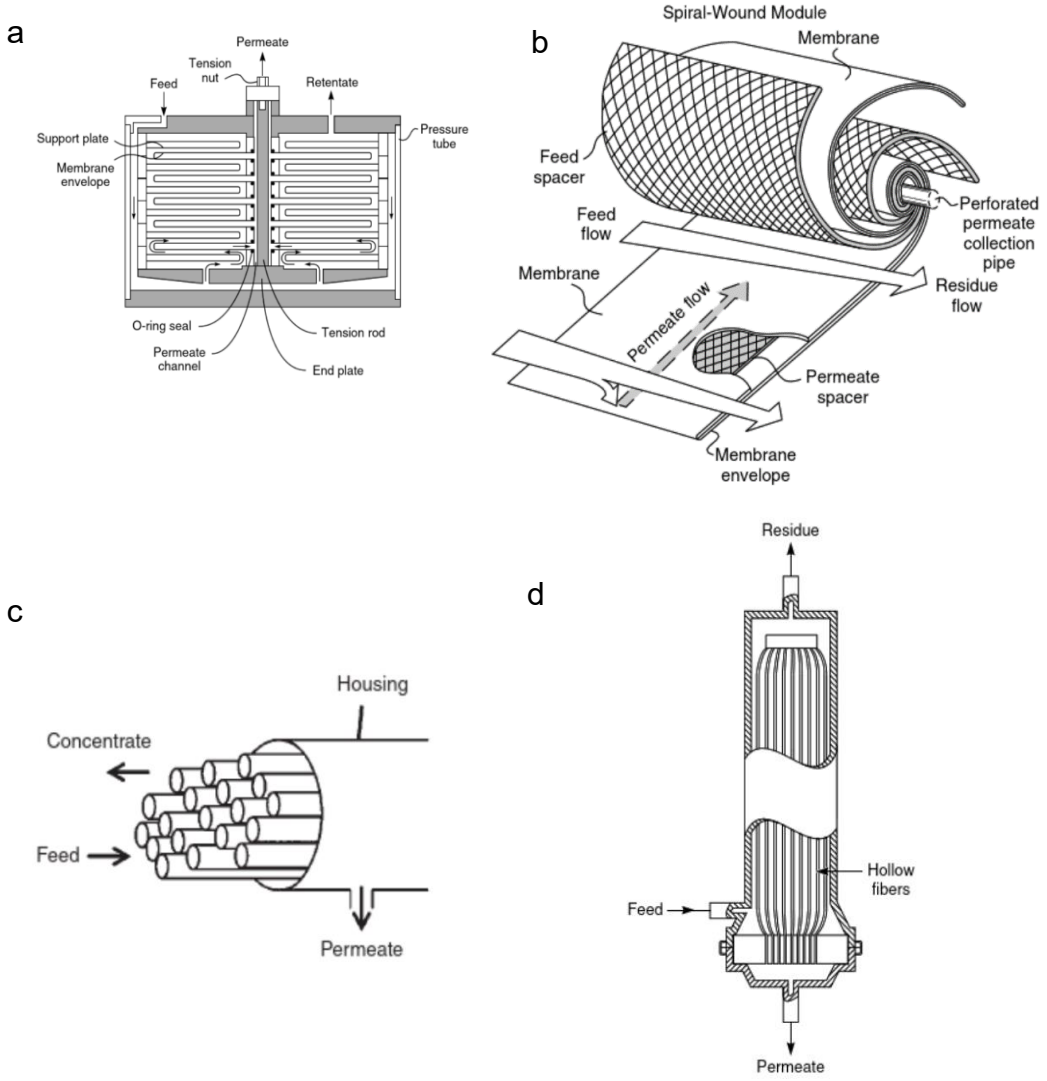


Figure 2- 3: Schematic of membrane modules: (a) plate and frame membrane module, where two endplates enclose membranes, feed and product spacers (Baker, 2012). (b) exploded view of a spiral module, where the membranes and spacers wrapped around the central permeate collection channel (Baker, 2012). (c) tubular modules, a cluster of tubes housed in a single, larger tube acting as the pressure vessel (Uragami, 2017). (d) Hollow fibre module, schematic of shell side, feed passes through the shell side, and

permeate passes through the fibre walls exiting the module via the fibre ends (Baker, 2012). Reproduced with permission from Baker et al. 2012 and Uragami et al. 2017.

2.2 Gas separation with membranes

A membrane's performance is measured by permeance that is the flux of the gas species per unit area and pressure (Yao and Wang, 2014), , or measured by permeability that is the permeance divided by the membranes thickness (Spigarelli and Kawatra, 2013). The separation of gas pairs is measured by selectivity which is expressed as a ratio of the gas species permeances (Spigarelli and Kawatra, 2013).

The diffusion mechanisms by which membranes separate depends on how the gas species interact with the membrane. It can often be a combination of mechanisms. Figure 2-4 shows schematics of the general mechanisms by which molecules can selectively be separated across a semi-permeable barrier. For the gas species to separate in porous membranes, they must interact with the pore walls more than each other, i.e., not a viscous flow instead an independent flow regime, Knudsen diffusion. Gas species can also be transported via surface diffusion. Surface diffusion can also improve selectivity by reducing the effective pore diameter for gases with low affinity for the membrane surface. Another factor that aids selective separation is molecular sieving, excluding gas species based on their kinetic diameters. (Terry, 2004, Adatoz et al., 2015).

In the dense structures, random polymers, the separation mechanism is the solution-diffusion model (Figure 2-4d). The permeability is affected by the solubility (solution component) of the molecule in the membrane material and its size (diffusion component). The diffusion is affected by the transient gaps between the polymer matrix voids. The intermolecular spacing creates these voids in the polymer, referred to as free volume (Terry, 2004, Prasetya et al., 2020).

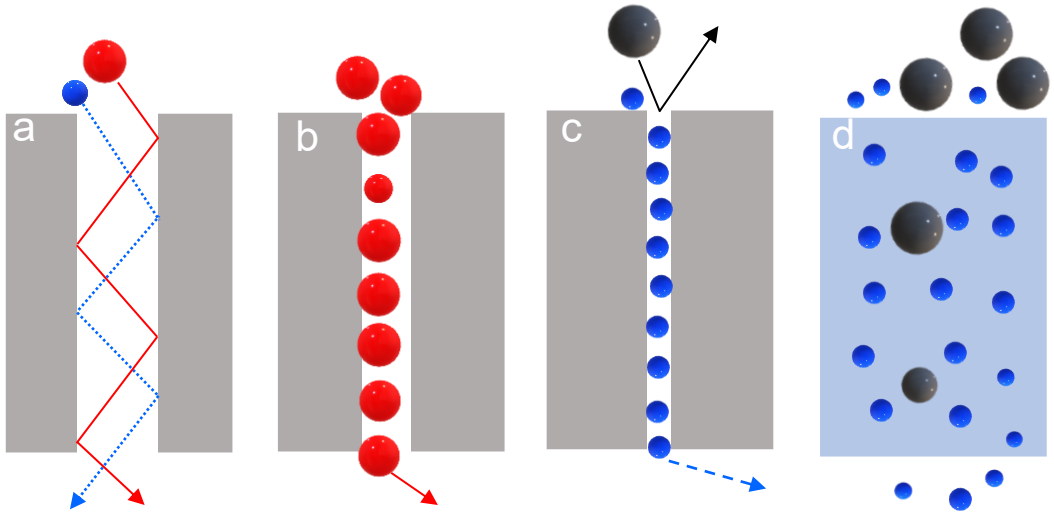


Figure 2- 4: Schematics of diffusion mechanisms, Knudsen (a), surface diffusion (b) molecular sieving (c) and solution diffusion (d). Some membranes may have a combination of the three separations mechanism (a-c) depending on material structure. Adapted from Terry et al. 2004 and Prasetya et al. 2020 (Terry, 2004) and (Prasetya et al., 2020). Reproduced with permission from Terry et al. 2004 and Prasetya et al. 2020.

The difference in how the gas molecules interact with the different materials results in different separation performances. The membranes' performance can be graphically presented with single gas permeance of the preferentially permeating gas component against the gas pair's selectivity. The Robeson plot is the graphical representation of the separation performance of hundreds of polymeric membranes. The plot has observed an upper bound applicable to the polymeric membranes, Robeson upper bound (Robeson, 2008). It represents a limitation to the separation performance of the polymers. It implies a 'tradeoff', an inverse relationship between permeability and selectivity. The solution-diffusion separation mechanism with polymer structure governs the inverse relationship, where the sorbed gas molecules slip through the transient gaps (free volume) between polymeric chains. Hence the diffusion of the gas species and the free volume governs their respective molecular size in the polymer – less volume means slower permeability (Koros and Fleming, 1993). Where the solubility governs the sorption of the gas molecule into the polymer, this relationship can be mathematically expressed, as shown in equation 2-1 (Kim and Lee, 2013), where permeability for a dense polymeric membrane is the product of diffusivity (D) and solubility (S) (Kim and Lee, 2013). Hence, the thickness impacts the permeability of the gas species diffusing along the polymer chain since the transient polymer chains slow down diffusing molecules due to their narrow passages (Kim and Lee, 2013), which

would not be the case with larger pore sizes. Hence, the upper bound relationship is a diffusion dominated relationship since the diffusivity selectivity of components i and j, D_i/D_j, decreases with permeability. Whereas the solubility selectivity of the components i and j, S_i/S_j remains constant (Robeson, 2008).

$$\boldsymbol{P} = \boldsymbol{D}.\boldsymbol{S} \quad \text{(Equation 2- 1)}$$

Figure 2-5 shows a Robeson plot schematic where polymeric membranes' performance cannot surpass the upper bound, representing the tradeoff between permeance and selectivity in the polymer.

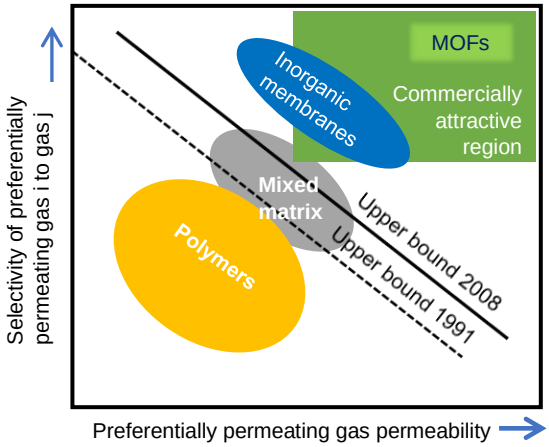


Figure 2- 5: The Robeson plot shows two upper bounds from the years 1991 and 2008. The plot shows the different regions the different materials' performance can reach depending on materials derived from.

The Robeson plot is also an ideal platform for the performance measurement of new and existing materials synthesised into membranes, besides mapping out polymeric membranes' performance. The hybrid structures, metal organic frameworks (MOFs), and zeolitic imidazole frameworks (ZIFs) can reach the membranes' commercially attractive region by achieving high permeability and selectivity. This is achieved by the MOF/ZIF structures having high porosity (Lai, 2018), control over interaction between gas species via functional sites, and molecular sieving effect (Guo and Peng, 2019, Li et al., 2017). Also, structures like ZIFs/MOFs are ideal for membranes since they have large surface to volume ratios (Adatoz et al., 2015). However, there are challenges associated with the commercialization of ZIF/MOF membranes (Zhang and Koros, 2015, Duan et al., 2018).

2.3 Membrane materials for CO_2/CH_4 separation

Although researchers have explored hundreds of polymeric structures as membranes, less than ten have reached the commercial market (Baker and Low, 2014, Qian et al., 2020, Wang et al., 2017b). Membranes represent only 10% of the natural gas purification market, with the polymer cellulose acetate dominating the market (Baker and Low, 2014). The amine absorption dominates the remainder of the market because the polymers have a relatively low permeability and selectivity (Qian et al., 2020), allowing better performing materials to enter the market.

The relatively low performing polymers are due to the materials' testing at high pressures of 20-60 bar, reflective of those encountered in industry, which leads to losing much of their achieved selectivity at the laboratory scale. The difficulties are created by the contaminants, CO_2, light hydrocarbons, water, and aromatics. The standard operating pressures (20-60 bars) of natural gas streams leads to the contaminants reaching their dew points and then dissolving into the polymer, causing plasticization and reducing separation performance (Baker and Low, 2014). The major contributory component to plasticization is CO_2, adsorbing between 30 to 50 cm^3 of CO_2 per cm^3 polymer, equating to 5-10 wt.% of CO_2 in the polymer (Baker and Lokhandwala, 2008). This mechanical structure breakdown reduces the membrane's overall life span and results in low selectivities (Shah et al., 2011). Although the cellulose acetate membrane dominates the natural gas processing market (Mazyan et al., 2016) it only delivers a CO_2/CH_4 selectivity between 12-15 under normal operating conditions, which is significantly less than pure gas measurements (Baker, 2002).

Inorganic materials are more stable than polymers since the structures are resistant to deformation under the high pressures of the CO_2 stream. The materials can also withstand harsh environments, are shape-selective, and are chemically and thermally stable. The plasticization and physical ageing stability issues are not a limitation for inorganic structures (Qian et al., 2020). Zeolites are inorganic materials with the advantages mentioned earlier, with the added advantage of molecular sieving properties meaning they can selectively separate gas molecules based on size (Lai et al., 2014a, Caro et al., 2000).

Zeolite membranes have been investigated from as early as the 1990s with the consideration of gas permeation. Xiaochun et al. commented on the molecular sieving capabilities of the silicalite-1 when studying the permeances of light alkanes, including

CH_4 (Xu et al., 1998). Zeolites have been reported to separate CO_2/CH_4 gas mixtures as early as 1998 (Poshusta et al., 1998).

A zeolite structure studied for CO_2/CH_4 mixture is SAPO-34. The structure shows CO_2 preferentially adsorbs and diffuses faster than CH_4 (Li et al., 2004). Although the structure shows excellent separation qualities - selectivity as high as 270 for CO_2/CH_4 mixture (50/50) at 253 K and 0.14 MPa pressure drop (Li et al., 2005), it has limitations. SAPO-34 is hydrophilic, making it susceptible to mechanical breakdown in moisture, leading to its selectivity to reduce by up to 99 % (Rehman et al., 2020).

Although zeolite membranes demonstrate good thermal and chemical stabilities and good separation performance due to their molecular sieving properties, their lack of chemical tailorability (Shah et al., 2011) and reproducibility are critical challenges with these membranes (Kosinov et al., 2016).

Another way to surpass the Robeson upper bound with the polymers, enhance the resistance towards the plasticization and reduce physical ageing is to incorporate inorganic materials as fillers in the form of nano- or microparticles and disperse them into the polymer-based matrix, forming mixed matrix membranes (MMMs) (Qian et al., 2020, Tanh Jeazet et al., 2016). This then allows the selectivity of the inorganic structures and permeability of the polymer to be combined (Shah et al., 2011), thereby gaining the advantages of processability and economics of polymers (Bastani et al., 2013). In addition to the fillers improving material integrity and stability, they can also facilitate CO_2 transport through the matrix. However, this depends on the interaction properties of the selected inorganic materials and gas molecules (Wang et al., 2017a, Tanh Jeazet et al., 2016).

A factor to consider with MMMs is the amount of inorganic filler dispersed into the polymer. Although the particle loadings are increased to enhance the polymer structure's performance, too high a loading may reduce the two materials' interactions. The weak interactions lead to defects and reduced mechanical stability of the membrane; hence, there is an optimum filler limit threshold (Qian et al., 2020). In addition to filler loading limitations, another factor to consider is the weak interactions leads to interstitial gaps through which gas molecules diffuse through, thereby reducing the separation efficiency (Bastani et al., 2013, Basu et al., 2011). This can be overcome by considering the selected inorganic material (Wang et al., 2017a) and using surface modifiers to act as an adhesive between filler and polymer (Rezakazemi

et al., 2014). Another consideration is the nature of the inorganic material being incorporated into the matrix. For example, Jeazet et al. used the hybrid ZIF structures as fillers since the ligands interact with the bulk polymer structure and help eliminate the interstitial gaps. The separation performance showed that the selectivity did increase (Tanh Jeazet et al., 2016).

Figure 2-6 shows a schematic of a polymer matrix with dispersed inorganic species, including interfacial voids between the matrix and dispersed inorganic particle (Figure 2-6b). The voids act as an extra channel for the transportation of non-selective transport of gas species, affecting selectivity (Lin et al., 2018).

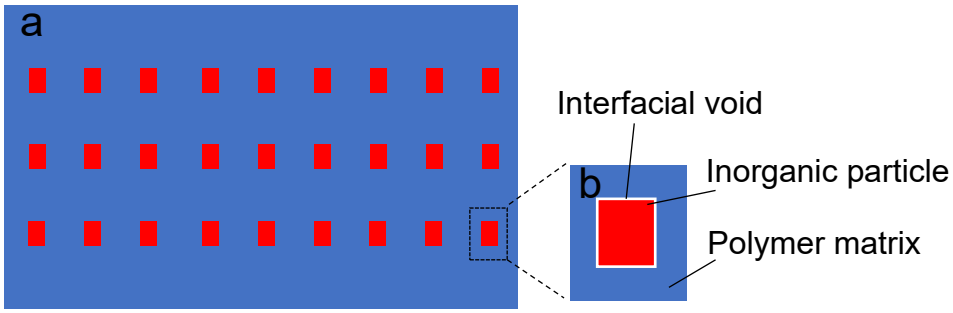


Figure 2- 6: Schematic of dispersed inorganic species in an ideal mixed matrix membrane (a), and an interfacial void between inorganic particle and polymer matrix (b).

Metal organic frameworks (MOFs) are hybrid structures consisting of metal centres linked by organic linkers. They have ultra-micro and mesoscale pore sizes, making them an ideal candidate for the separation of gas molecules. Figure 2-7 shows a schematic of a generic MOF cage structure and several ZIF frameworks (Zhang et al., 2020). The different ZIF structures can be formed by interchanging the metal centres between Zn or Co and the organic linkers, imidazole, or imidazole derivatives (Zhang et al., 2020).

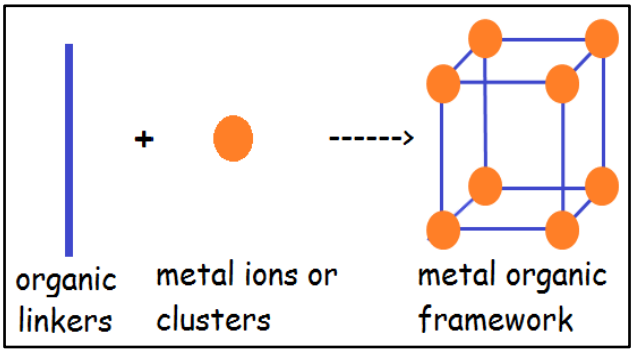


Figure 2- 7: Schematic of metal organic frameworks self-assembly from metal ion and organic linker.

Another advantage of MOFs that an infinite number of structures can be obtained by changing the combination of the organic and inorganic units – over 90,000 have been reported up to 2020 by the Cambridge Structural Database (Qian et al., 2020). The structures can be tailored for their intended purpose, e.g., the pore size and chemistry can be optimised for target gas molecules and processing conditions. The MOF structures are highly porous, as high as 50% of crystal volume with low density (0.2-1 g/cm^3) and very high surface areas up to 10,000 m^2/g (Furukawa et al., 2013), and some with high chemical and thermal stabilities (Hiroyasu Furukawa, 2013, Keskin and Kızılel, 2011, Li et al., 2009). With industrials processes requiring large membrane areas, 1000-500,000 m^2, they are ideal structures. If they can be formed into thin membranes, this area can be reduced further (Baker and Lokhandwala, 2008), making them ideal for separating gas mixtures (Adatoz et al., 2015).

Zeolitic imidazolate frameworks (ZIFs) are a subclass of MOFs, Zn-N bond series (Shah et al., 2011, Venna and Carreon, 2009). Although they have a similar topology to zeolites, their porosity and surface areas are more comparable to MOFs because of the exposed faces and edges of the organic unit, Imidazole (Kyo Sung Park, 2006, Chae et al., 2004). ZIFs are also attracting interest for gas separation because of their nanopores on the scale of small gas molecules (Yoo et al., 2009, Liu et al., 2009, Yao and Wang, 2014). Although ZIFs have the same coordination bonds to MOFs, they are more stable than MOF structures. This is due to acids and bases prefer to form 'like for like' bonds. In ZIF-8, the Zn^{2+} is an intermediate acid, and when bonding to intermediate base, imidazolate ion, $HmIm^-$, it forms a strong bond. Hence, ZIFs show similar chemical and thermal stabilities to zeolites. They are stable under harsh conditions such as organic solvents, water and alkaline solutions (Kyo Sung Park,

2006). Mainly ZIF-8 shows it can remain stable in boiling solvents such as benzene and water, which are typical impurities in natural gas (Shah et al., 2011)—making ZIF-8 an ideal candidate for the separation of CO_2 in the natural gas stream. Figure 2-8 shows the typical ZIF-8 cage (Morris et al., 2012) and an SEM image of a typical rhombic ZIF-8 crystal (Linder-Patton et al., 2018).

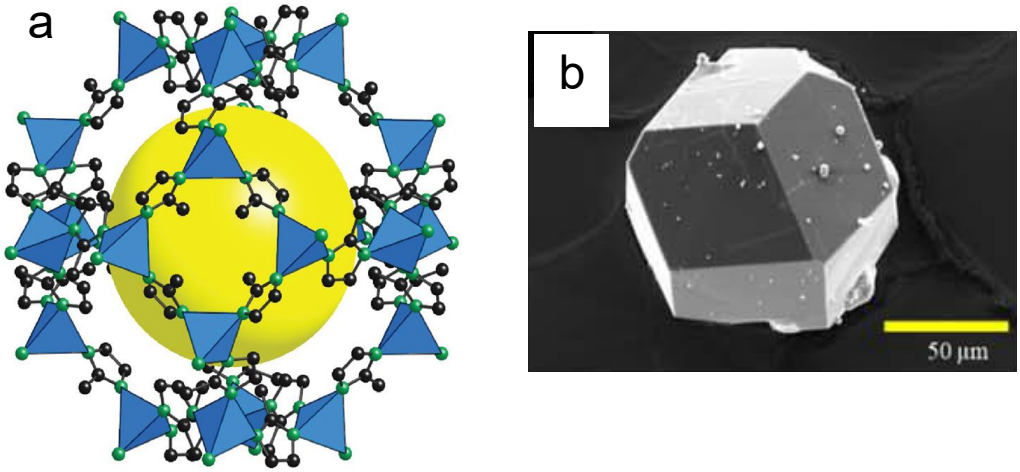


Figure 2- 8: Typical ZIF-8 cage with the yellow sphere representing free volume within the framework (Morris et al., 2012) (a) and rhombic shape representing the equilibrium shape of ZIF-8 (Linder-Patton et al., 2018) (b). Reproduced with permission from Morris et al. 2012 and Linder-Patton et al. 2018.

The ZIF-8 structure also shows molecular sieving properties. The ZIF-8 structure is ideal for natural gas processing since it has a pore aperture of 0.34 nm (Li et al., 2015), comparable to CO_2 and CH_4 with kinetic diameters of 0.33 and 0.38 nm, respectively. Also, there is a greater adsorption rate of CO_2 due to the electrostatic interaction between CO_2 molecules and ZIF-8 structure because of the CO_2 molecule's quadrupolar moment (Lai et al., 2014a). That will lead to the selective adsorption of CO_2 onto the ZIF-8 membrane and then diffusion through the matrix and then desorption onto the permeate side (Chmelik et al., 2012, Lai et al., 2014a). However, the molecular sieving effect is not as sharp as zeolites since ZIFs (and MOFs) have a 'breathing effect' (Figure 2-9a), triggered by an external factor such as pressure or temperature (Qian et al., 2020). The breathing effect can also be accompanied by the gate opening/closing effect (Figure 2-9b), which is the rotation of linkers in the ZIF-8 structure, which obstructs the guest molecules' diffusion (Qian et al., 2020). The linker

rotation results in the 0.34 nm pore aperture delivering an effective 0.40-0.42 nm pore aperture (Lai et al., 2014a, Daglar and Keskin, 2020).

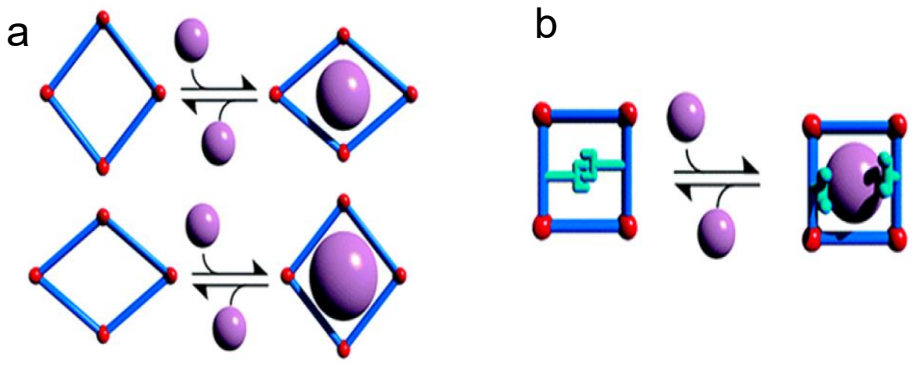


Figure 2- 9: Breathing (a) and linker rotation (b) are two types of structural behaviours of flexible MOF structures. (Qian et al., 2020). Reproduced with permission from Qian et al. 2020.

2.4 Growth of ZIF-8 crystals

Park et al. developed the ZIF structure based on zeolite nets in 2009. From the developed ZIFs, the focus of the study was ZIF-8 and -11. The work's significance was the porosity of the ZIFs surpassing that of zeolites, with a reported surface area of 1947 m^2/g for the ZIF-8 structure. Unlike other metal-organic structures, ZIFs demonstrated to be more chemically and thermally stable. The powder x-ray diffraction in an N_2 atmosphere confirmed the ZIF-8 stability at 500 °C. The chemical stability of the ZIF-8 structure rivalled mesoporous silica performance when the structure remained stable in boiling water for seven days. (Park et al., 2006)

When designing the experiments to synthesise ZIF-8 membranes on substrates (heterogeneous nucleation), the chemistry of precursors, nucleation, and crystal evolution of the powder synthesis (homogeneous nucleation) should be considered. Once this is achieved, robust novel synthesis methodologies can be delivered to address the challenges associated with heterogeneous growth, such as synthesizing a continuous and dense membrane on the substrate surface with a measure of repeatability (Zhang et al., 2013).

Venna et al. categorized the evolution of ZIF-8 crystals into three stages, incubation - nucleation, growth, and stationary phase. The stages were measured as a function of time and pH. The nucleation stage was identified as $t < 10$ min, the period in which ZIF-

8 nuclei form. The second stage was the growth stage, 10 < t < 60 min. Finally, the stationary phase, t > 60 min, where the crystallization remains constant and the ZIF-8 particles evolve into larger and more evolved entities (Venna et al., 2010, Schejn et al., 2014).

The changes in pH also reflect the different ZIF-8 evolution stages. Which is possible since imidazole releases protons. Venna et al. reported pH values of 7.5, 7.4, 7.3 and 7.2 at 10, 20, 40, and 50 minutes, respectively, from an initial solution value of 7.8. Jian et al. also reported on the evolution of ZIF-8 structures accompanied by changes in pH (Jian et al., 2015, Kida et al., 2013b), supporting the three stages of ZIF-8 formation.

Figure 2-10 shows TEM images of ZIF-8 evolving. As time increased from 10 min to 24 h, the crystal size increased from 50 nm to 500 nm. The increase in crystal size is due to the Ostwald ripening effect. Ostwald ripening is a particle system mechanism to reduce the system's energy by reducing the interfacial surface area. Therefore, with increased time, crystals disappear at the expense of the other crystals growing, rather than the number of the crystals remaining the same. This disappearance is achieved by the dissolution of the smaller and less stable crystals into the solution, and at supersaturation, they then condense on the larger and more stable crystals (Voorhees, 2002, Venna et al., 2010).

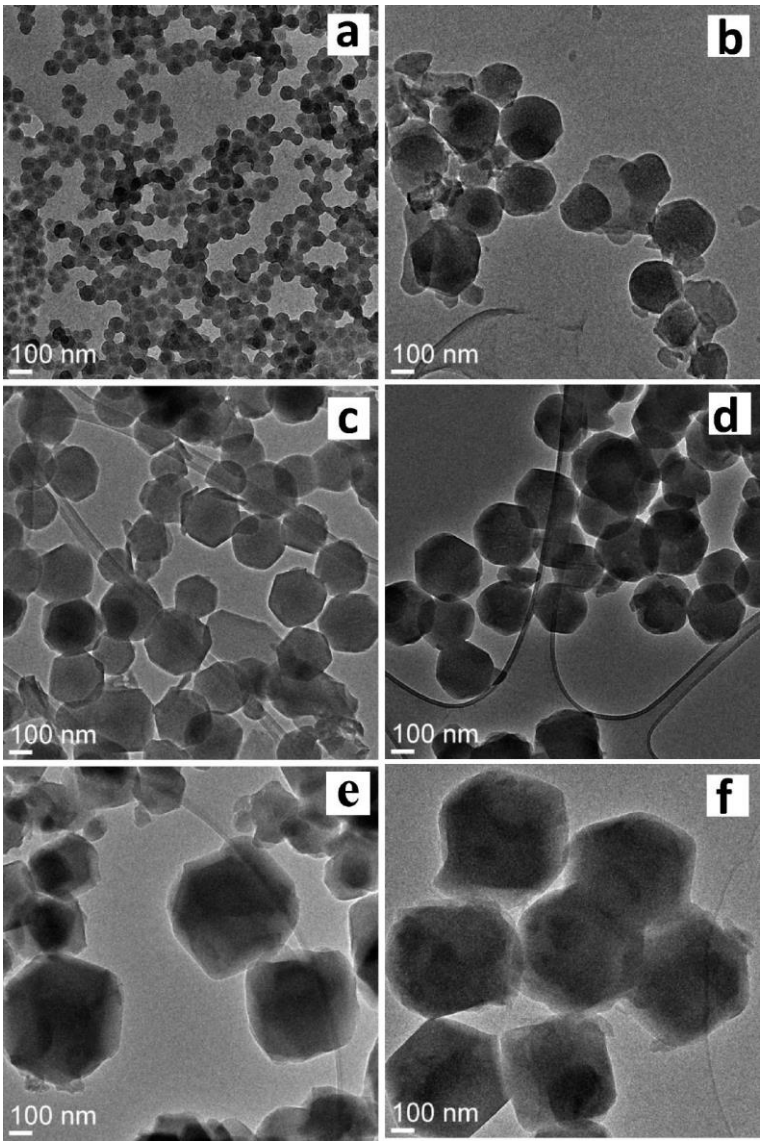


Figure 2- 10: Transmission electron microscopy images of ZIF-8 as a function of synthesis time 10 mins (a), 30 mins (b), 40 mins (c), 60 mins (d), 12 h (e) and 24 h(f). (Venna et al., 2010). Reproduced with permission from Venna et al. 2010.

The crystal structures' evolution was taken further, that the conjugate bases associated with the Zn^{2+} were studied with crystal morphology (Schejn et al., 2014). Schejn et al. reported that the conjugate base affected the ZIF-8 nucleation rate and the crystal shape and size. With hard bases such as NO_3^-, there is a large amount of Zn^{2+} made available for the coordination with the $Hmim^-$ ions creating many nuclei with small crystal sizes of 192 nm. With the less reactive, soft base such as Br^-, there is a less amount of Zn^{2+} and a crystal size of 1160 nm. Understanding the dissociation rate can give an idea of the type of growth rate, size, and morphology to be expected when synthesising membranes. Torad et al. investigated the carbonization of ZIF-8 and its

effects on the rate of dissociation of Zn^{2+}, associated with the bases NO_3^- and CH_3COO^-, the former having a quicker rate of dissociation producing smaller sized crystals than the CH_3COO^- conjugate base (Schejn et al., 2014, Torad et al., 2013).

In conclusion, when heterogeneously growing the ZIF-8 structure, the conjugate bases associated with the zinc will control the membrane microstructure and thickness since the conjugate bases associated with the zinc salt shown to affect the crystal morphology and size. Schejn et al. and Torad et al. may indicate that ZIF-8 derived from metal salts with hard bases will generate thinner membranes since the nuclei are smaller.

2.5 Synthesis of ZIF-8 membranes and films

Many synthesis methodologies of ZIF-8 membranes have been adapted from those used for zeolites. The main reason behind ZIF-8 membranes difficulties in comparison to zeolites is the coordination bond between the metal and linker units in the structure (Elsevier, 1996). When growing ZIF-8 onto substrates, the growth process is a competitive process over precursors being spent in the bulk of the solution and growth on the substrate being coated. Often, the substrates are modified with species to help promote nucleation on its surface.

2.5.1 Substrate modification

Table 2-1 summarizes the different surface modification reported in literature for the synthesis of ZIF-8 membranes. The respective surface modifications listed in the table will be discussed in more detail in this section of the thesis.

Table 2- 1: Surface modification techniques that have used for ZIF-8 membrane synthesis.

Surface modification technique	Authors
Seeding - manual deposition	(Venna and Carreon, 2009, Yao et al., 2013, Tao et al., 2013b)
Seeding - seed suspension	(Pan et al., 2012, James et al., 2020, Tran et al., 2020a, Tran et al., 2020b, Venna et al., 2014, Li et al., 2020, Wu et al., 2020, Tao et al., 2013a, Bux et al., 2011)
Reactive seeding - ZnO	(Kong et al., 2015, Yang et al., 2014, Lee et al., 2019, Wang et al., 2016, Wang et al., 2016, Yu et al., 2016, Drobek et al., 2015)
Chemical modification - silane coupling agents	(Tanaka et al., 2014b, Tanaka et al., 2017, Zhu et al., 2016, Xie et al., 2012)
2-methylimidazole	(Michael C. McCarthy, 2010)
Sodium formate	(Shah et al., 2013a)

The deposition of ZIF-8 crystals on a substrate surface is referred to as seeding. These seeds act as sites for nucleation during membrane growth on the substrate. Seeding can be done by rubbing or dip coating. During rubbing, a pipe cleaner or sandpaper is used to deposit ZIF-8 crystals on the substrate surface (Venna and Carreon, 2009, Yao et al., 2013, Tao et al., 2013b). During dip coating, the substrate is immersed in a solution containing crystals for a duration of time.

ZIF-8 membranes synthesis by Venna et al. and Yao et al. successfully synthesised membranes on tubular substrates via manually depositing seeds before membrane growth (Yao et al., 2013, Venna and Carreon, 2009). However, Venna et al. continuous membrane growth was reported after the second synthesis cycle that may suggest that the first cycle membrane was very thin since zinc nitrate was used for membrane growth. Venna et al. used methanol, linker/metal ratio 8, metal concentration 36 mM and synthesised in an autoclave at 150 °C for 5 hours. Yao et al. also synthesised membranes in an autoclave derived from zinc nitrate in water, however, membranes were derived from a single synthesis cycle. Yao et al. studied growth as a function of

concentration (Zn^{2+}: Hmim:H_2O, 1:70:1238-9904), temperature (25-100 °C), and time (6-72 hours). Yao et al. reported how the effect of dilution controlled the rate of heterogeneous nucleation, and the system concentration of 1:70:4952 was found to be optimum, the more concentrated system led to a weak level of heterogenous nucleation, and the more diluted system yielded crystals of non-typical ZIF-8 morphology – no identifiable shape. Yao et al. reported dense and continuous membranes at 50 and 70 °C with a synthesis time of 24 hours. In conclusion, although both Venna et al. and Yao et al. manually deposited seeds onto the substrates and used the same metal salt, zinc nitrate, the synthesis conditions and precursor concentrations and ratios impact the level of heterogenous nucleation onto the substrates.

Tao et al. took a different approach to the initial methodology of depositing seeds on the substrate surface. The seed layer was formed from the first membrane growth obtained on an unmodified substrate as opposed to physical depositing ZIF-8 nuclei. The first growth cycle on the unmodified tubular substrate yielded membrane growth with intercrystalline gaps and some substrate areas remaining uncovered. A high-quality membrane was synthesised after a second growth cycle, however, only after rubbing the loose growth obtained from cycle one with fine sandpaper ($1500^{\#}$) yielding a uniform nano seed layer. For the second growth cycle, the nano seed layer (Tao et al. reported size of 60 nm) acted as heterogeneous sites of nucleation, yielding a dense and continuous membrane with a 5 µm thickness (Tao et al., 2013b). In conclusion, nucleation sites are needed on substrates to achieve a dense and continuous membrane.

Studies reported dip coating procedures using up to 5 wt.% crystal containing seed suspensions dispersed in methanol (Pan et al., 2012, James et al., 2020, Tran et al., 2020a, Tran et al., 2020b, Venna et al., 2014, Li et al., 2020, Wu et al., 2020), and water (Tao et al., 2013a, Bux et al., 2011), with immersion times up to 5 min. All substrates were at room temperature before the dip coating treatment except for Tao et al. hot dip coating procedure where the substrate was heated to 150 °C (Tao et al., 2013a). In some cases, the dip coating step was applied twice with 10 min gap between immersions (James et al., 2020, Venna et al., 2014). The seeded substrates were dried e.g., at room temperature (Pan et al., 2012, Tran et al., 2019, Tran et al., 2020a), 60 °C for 30 min (Wu et al., 2020), 80 °C for 4 hours (Bux et al., 2011), and 95 °C for 3 hours (James et al., 2020). The review indicates that the nature of dip coating conditions is system specific. For example, Tao et al. investigated dip coating using an

unheated substrate that produced a membrane with defects. Whereas the other researchers reported successful heterogeneous growth with unheated substrates when using dip coating.

Some studies incorporated polymers such as polyethyleneimine (PEI) into the seed suspension since the PEI helps ensure hydrogen bonds formed between the ZIF-8 seeds and the free hydroxyls on the substrate (Bux et al., 2011). Figure 2-11 shows substrates immersed in PEI solution with (Figure 2-11a) and without (Figure 2-11b) seeds. The substrate dip coated in the PEI suspension without seeds yielded gaps between the ZIF-8 crystals on the substrate, indicating that the PEI suspension without seeds is not enough to achieve a dense and continuous growth (Bux et al., 2011).

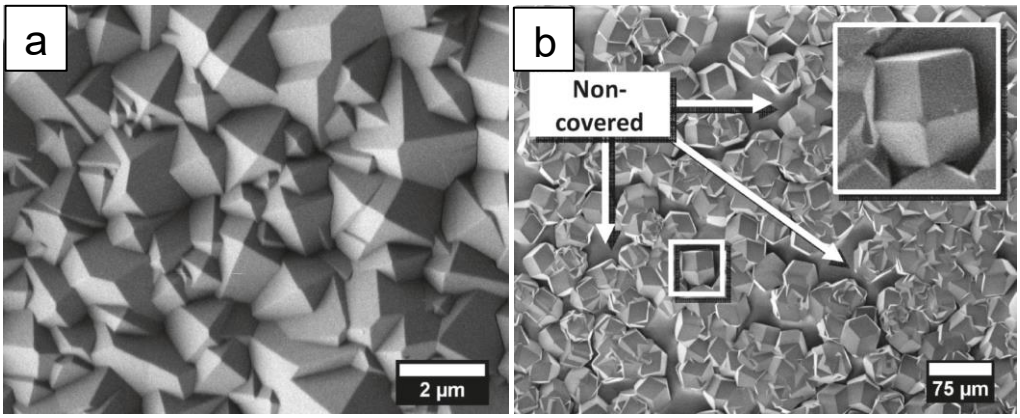


Figure 2- 11: ZIF-8 growth on flat alumina substrates using suspension with PEI with (a) and without (b) seed (Bux et al., 2011). Reproduced with permission from Bux et al. 2011.

Reactive seeding is another method that was used in literature (Kong et al., 2015) (Yang et al., 2014) (Lee et al., 2019, Wang et al., 2016) (Wang et al., 2016) (Yu et al., 2016) (Drobek et al., 2015). To achieve this, ZnO was deposited on the surface, supplying the Zn^{2+} when partially dissolved in linker solution. This then forms ZIF-8 crystals on the surface that can then act as anchors' sites during membrane synthesis. Kong et al. conducted tests to study the binding strength of the attached seeds on the substrate surface, formed from the Zn^{2+} derived from ZnO's deposition via rubbing and deposited ZIF-8 seeds from the seed solution. The 15 minute sonication results showed that the ZIF-8 membrane using ZnO as seeds was more stable than that of the seed suspension's growth due to weaker capillary forces and hydrogen bonds (Kong et al., 2015). Yang et al. also commented on how ZnO acted as a nucleation site for the ZIF-8 growth since the cross-sectional image showed an intermediate layer between the ZIF-8 film and the NaA filler particles used to fill the substrate pores. The EDS

mapping showed no gap between the membrane layer and substrate (Yang et al., 2014). Zhang et al. also used ZnO to provide Zn^{2+} followed by linker activation for $Hmim^-$ where both acted as SBU on the substrate surface rather than forming ZIF-8 nucleation sites for the membrane synthesis step (Wang et al., 2016).

Studies have also shown that silane containing coupling agents used for substrate modification form a bridge, bonding between the substrate's surface hydroxyls and ZIF-8 structure, Figure 2-12 (Tanaka et al., 2014b).

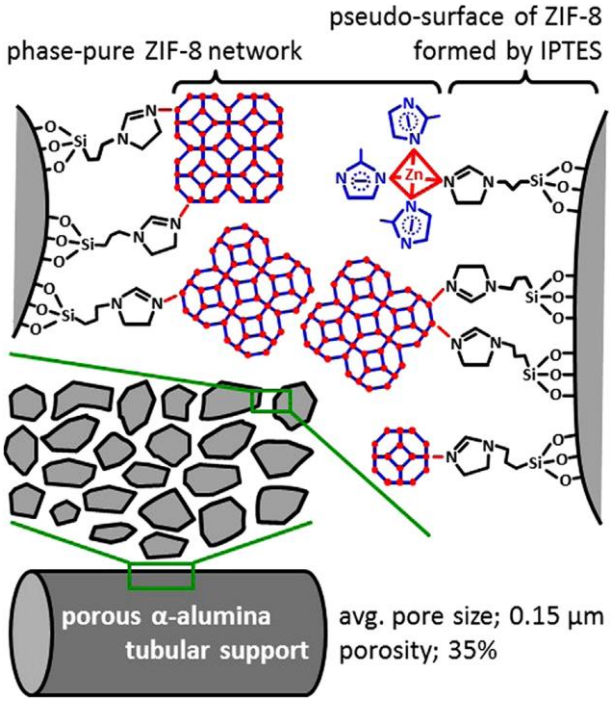


Figure 2- 12: Schematic of the growth between the hydroxyl group on the alumina substrate and the imidazoline group of the ZIF-8 structure (Tanaka et al., 2014b). Reproduced with permission from Tanaka et al. 2014.

Typical examples of those agents that used for ZIF-8 synthesis are 3-(2-imidazoline-1-yl)propyltriethoxysilane, IPTES (Tanaka et al., 2014b, Tanaka et al., 2017), and 3-aminopropyltriethoxysilane, APTES (Zhu et al., 2016, Xie et al., 2012). Zhu et al. reported that APTES promoted densely packed crystal growth on the tubular substrates (Figure 2-13). However, this was after a two-cycle synthesis, including the APTES surface modification stage.

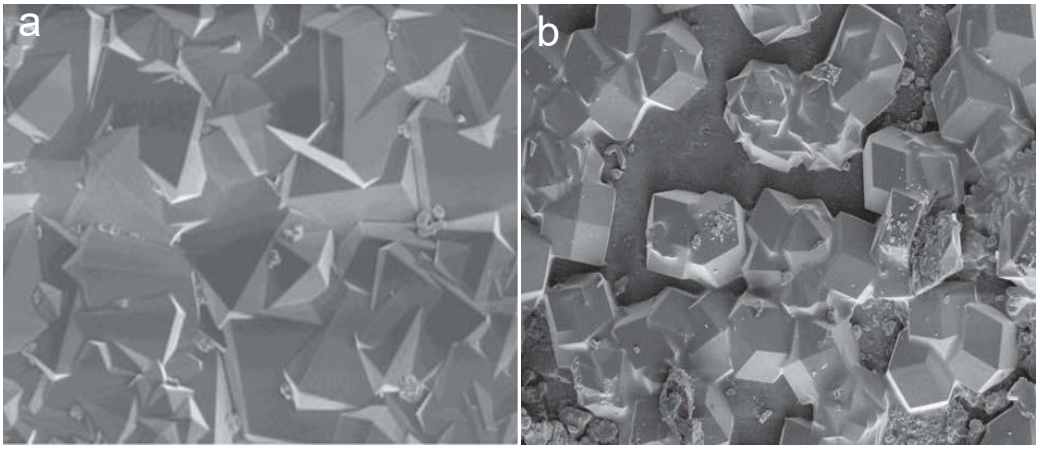


Figure 2- 13: The surface image of two cycle synthesis of ZIF-8 including the APTES treatment stage (a), and surface image of two cycle synthesis on unmodified substrate with no APTES treatment. Synthesis conditions were microwave heating at 105 °C for 3 hours per cycle growth using zinc chloride (Zhu et al., 2016). Reproduced with permission from Zhu et al. 2016.

Alternatively, substrate modifications were reported using linkers (Michael C. McCarthy, 2010) and zinc chloride and sodium formate (Shah et al., 2013a) for ZIF-8 membrane synthesis. Shah et al. concluded that sodium formate promoted a more basic solution, promoting the linkers' deprotonation. The ZnO on the substrate surface acted as a secondary metal source since the XRD peak of ZnO decreased as the ZIF-8 peaks increased, i.e., it is consumed as ZIF-8 is formed, acting as a nucleation site for heterogeneous growth. McCarthy et al. reported the modification the substrate surface with linker, which was significantly different to dip coating since only a linker solution is used for the surface modification and is not a secondary growth technique; the nucleation and growth onto the substrate surface occur in-situ. The substrate was modified by heating it to 200 °C, and the linker solution was dropped onto the substrate (approximately 0.5-1 ml per 2.2 cm^2 alumina disk), after which the disk was returned to the oven for 20 minutes. After 20 minutes, the disk was sonicated and returned to the oven. This process was repeated until a colour change, dark brown, usually six repetitions. McCarthy et al. reported this was not achievable at room temperature, suggesting a covalent bond between linker and alumina, confirmed by XPS of the surface-modified disk yielding the peak characteristic Al-N bond. McCarthy et al. also highlighted the importance of sodium formate in their system too, where no membrane was obtained in the system without it (Michael C. McCarthy, 2010). In conclusion, the integration of sodium formate acts as a catalyst and promotes a more robust heterogeneous nucleation than synthesizing without the base.

In conclusion, the literature indicates that seeding is needed to promote ZIF-8 crystal growth onto the substrate irrespective of seeding methodology. Although researchers are growing the same structure, ZIF-8, each researcher adopts different seeding conditions implying the surface modification steps are system unique, i.e., depends on metal salt, substrate geometry, and synthesis conditions.

2.5.2 Synthesis methodologies

The synthesis of ZIF-8 membranes can be categorized into three key methodologies: seeding and secondary growth (two stages involved), in-situ (nucleation and growth in a single step), and continuous circulation of precursors. Table 2-2 summarizes the different the synthesis methodologies for ZIF-8 membranes that will be discussed in this section of the literature review.

Table 2- 2: ZIF-8 membrane growth methodologies.

Membrane growth mechanism	Author
Secondary growth (including seeded growth)	(Venna and Carreon, 2009, Yao et al., 2013, Tao et al., 2013b, Pan et al., 2012, James et al., 2020, Tran et al., 2020a, Tran et al., 2020b, Venna et al., 2014, Li et al., 2020, Wu et al., 2020, Tao et al., 2013a, Bux et al., 2011, Kong et al., 2015, Yang et al., 2014, Lee et al., 2019, Wang et al., 2016, Wang et al., 2016, Yu et al., 2016, Drobek et al., 2015)
In-situ	(Tanaka et al., 2014b, Tanaka et al., 2017, Zhu et al., 2016, Xie et al., 2012)

Contra (single step) – isolated precursors	(Yao et al., 2011, Xie et al., 2012)
Counter (two step) – isolated precursors	(Kwon and Jeong, 2013, Hara et al., 2014, Hara et al., 2015, Tran et al., 2020b)
Circulation	(Marti et al., 2017, Kong et al., 2014, Brown et al., 2014b)
Rapid thermal deposition (RTD)	(Shah et al., 2013b)

The first group to synthesize ZIF-8 membranes was Venna et al. in 2009, focusing on gas separations. The group adopted the secondary growth seeding via manually depositing the seeds to act as sites of nucleation. Both seeds and membranes were derived from zinc nitrate synthesised in methanol. The membranes and seeds were synthesised at a linker/metal ratio of 8 and metal concentration of 36 mM, with each synthesis cycle (one cycle equal one layer) at 5-hours and 150 °C under conventional heating. The membranes presented were 2 and 8 layers with thicknesses of 5 and 9 µm, synthesised on tubular alumina substrates. Venna et al. reported the small thickness difference due to partial dissolution of the first layers. The membranes yielded separation performance with CO_2 permeances as high as 2.4 x10^{-5} mol/m^2.s.Pa (2 layer membrane), and separation selectivity of 5 and 7 for 2 and 8 layered membranes, respectively. Venna et al. reported that the high permeances were not only associated with the thinner membranes because of the small crystal sizes with the narrow size distribution of 110 ± 15 nm, but also the textural properties of the porous alumina structure. This may suggest it helps reduce resistance to the permeating gas species. (Venna and Carreon, 2009)

The circulation of precursors through the tubular substrate has been adopted from zeolite synthesis (Pina et al., 2004, Pera-Titus et al., 2007, Aguado et al., 2009, Brown et al., 2014b). Although Arti et al., Kong et al., and Brown et al. synthesised ZIF-8 membranes via pumping of precursors through the tubular substrates' lumen, the

experimental conditions were very different. Kong et al. had the substrate in an autoclave with the precursors entering the substrate's lumen and mixing. In contrast, Arti et al. and Brown et al. had the precursor's streams flowing separately, forming a reaction zone in the substrate pores, with Brown et al. using immiscible solvents. The conclusions drawn from the three research groups publication are the advantages of overcoming the mass transfer limitation in the substrate's lumen and the weak level of heterogenous growth on tubular substrates in a static synthesis (Kong et al., 2014). The pumping of isolated precursors showed that the Zn^{2+} precursor determined the substrate's side where the membrane would form (Marti et al., 2017, Brown et al., 2014b). An advantage of synthesizing ZIF-8 membrane with such a methodology is scalability, bringing the reaction zone to the vicinity of the substrate, and being able to circumvent the difficulties with low mass transfer efficiency inside the tubular substrate space (Marti et al., 2017, Kong et al., 2014, Brown et al., 2014b).

The role of linker/metal ratios and metal concentrations has also been investigated on the influence on heterogeneous growth of ZIF-8 using water (Tanaka et al., 2014a, Kida et al., 2013a) and methanol (Lu et al., 2012). Kida et al. and Tanaka et al. investigated heterogeneous growth of ZIF-8 with linker/metal ratios at 60 and 100 (Kida et al., 2013a) and between 30 to 60 (Tanaka et al., 2014a). In comparison, Lu et al. linker/metal ratios were between 1 to 5 (Lu et al., 2012). The differences in linker/metal ratios between the aqueous and solvent systems are due to the aqueous systems requiring a significant excess of linker ions because the Zn^{2+} ions can be easily complexed with the OH^- forming byproducts (Tanaka et al., 2012, Tanaka et al., 2014a, Kida et al., 2013b), such as zinc hydroxide nitrate (Tanaka et al., 2014a). Hence, by increasing the population of the linker ions, the formation of byproducts can be reduced. Tanaka et al. adjusted the linker/metal ratio of 30, 40 and 60 by altering the linker concentration while the metal concentration was kept constant at 25 mM. Although the surface and cross-sectional images confirmed a continuous membrane at linker/metal ratio of 60 (Figure 2-14), Tanaka et al. reported no characteristic XRD peaks of ZIF-8 suggesting no definite sodalite (crystalline) structure. While the membranes synthesised with linker/metal ratios of 30 and 40 showed all characteristic peaks of ZIF-8, confirming phase pure crystalline ZIF-8 structure. Figure 2-14 shows that there is a difference in surface microstructures across the three linker/metal ratios. Tanaka et al. commented that it was difficult to determine the membrane thickness across the three ratios because the interface between the substrate and ZIF-8 film were indistinguishable. However, the ideal selectivities of H_2 from CO_2 and CH_4 increased with decreasing ratio. Suggesting enhanced microstructures with decreased

linker/metal ratios. In conclusion, the linker/metal ratios do impact the microstructure of the membrane formed leading to differing separation performances.

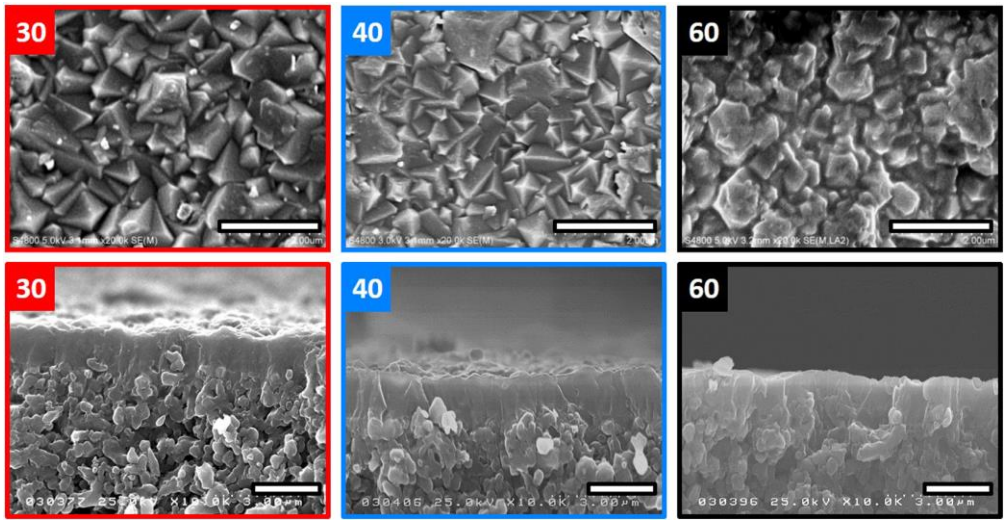


Figure 2- 14: Surface and cross-sectional SEM images of ZIF-8 membranes synthesized from zinc acetate dihydrate at room temperature and synthesis time of 24 hours. Synthesised at linker/metal ratios of 30, 40, and 60 (Tanaka et al., 2014a). Scale bar 2 µm. Reproduced with permission from Tanaka et al. 2014.

Although Kida et al. and Lu et al. synthesized films and not membranes, the respective works are relevant to understand the role of precursors concentrations and ratios have on heterogeneous nucleation. Kida et al. reported on how the primary grain size of the films decreased with increasing linker/metal ratios (Kida et al., 2013a), and Lu et al. reported how both metal concentration and linker/metal ratios could be selected to optimize surface growth (Lu et al., 2012). In conclusion, the precursor concentration and ratios can be optimised to obtain the most effective microstructure for the membrane.

Shah et al. developed a rapid thermal deposition (RTD) method for ZIF-8 membrane growth, an evaporation-induced crystallization process using zinc acetate dihydrate (Figure 2-15). The kinetic process was categorized into four stages: 1. The evaporation of the solvents, 2. The flow of precursors from inside to the outside of the substrates, 3. The heterogeneous and homogeneous crystallization, and 4. Drying of the structure – partial activation of crystals. The evaporation (t_e) and crystallization (t_c) stages were studied since too short t_e compared to t_c would mean the formation of no crystals inside the substrate. However, too long a t_e compared to t_c would yield inhomogeneous

formation of crystals on the substrate and not well-intergrown microstructure (Shah et al., 2013b).

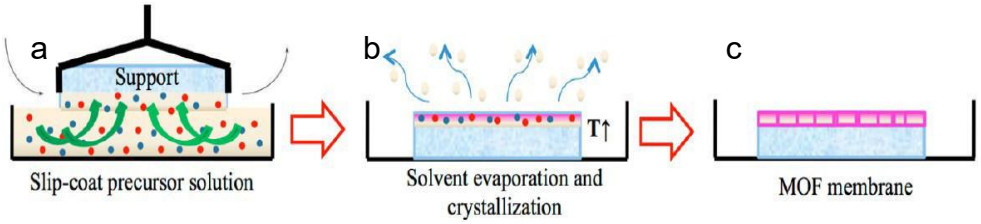


Figure 2- 15: Schematic illustration of RTD technique, the substrate is soaked in the precursor (a), heated in the oven (b), and the membrane (c). (Shah et al., 2013b). Reproduced with permission from Shah et al. 2013.

Shah et al. optimized these parameters by studying catalysts such as deprotonators to increase the reaction rate, temperature, molar composition, precursor solutions, solvents, and vapour pressure. They determined the following membranes synthesis conditions: N,N-dimethyl acetamide (DMA): deionized water with a 2:1 ratio, RTD temperature and time of 200 °C and 15 minutes, respectively. After synthesis, the membranes were slowly cooled down to room temperature. The membranes were then rinsed with DMA, then ethanol and then placed in ethanol for 3 days for a solvent exchange, after which the membrane was dried at 85 °C for 12 h (Shah et al., 2013b). Figure 2-16 shows the surface and cross-sectional images of the ZIF-8 membranes synthesised under these conditions (Shah et al., 2013b). The associated advantages with such a process are the minimal use of chemicals that can deliver tens of membranes for what other synthesis methodologies use in one synthesis, making this a promising contender for pilot scale (Shah et al., 2013b). However, the activation is prolonged, and the flat disk is not as easy to scale up as tubular substrates (Kong et al., 2017).

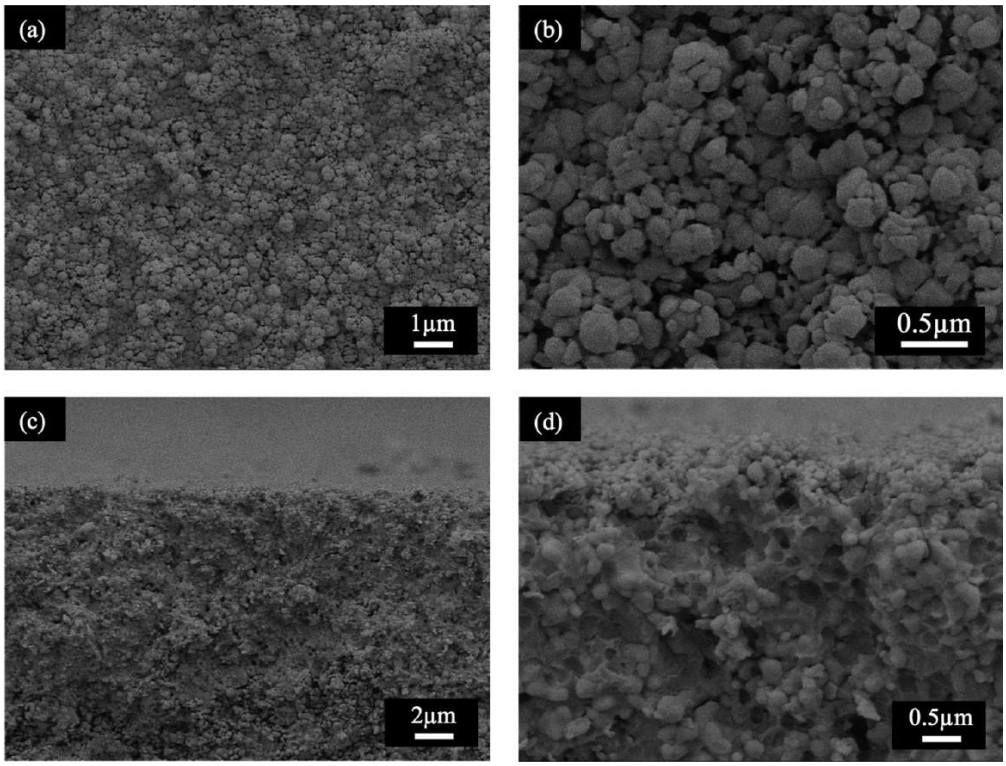


Figure 2- 16: SEM images of ZIF-8 membranes synthesised by RTD top view (a, b), and a cross-sectional view (c, d). (Shah et al., 2013b). Reproduced with permission from Shah et al. 2013.

Considering the literature studies, it is essential to understand the interaction between substrate surface, metal, and linker precursors during the membrane synthesis i.e., the growth taking place within the substrate's vicinity (Xie et al., 2012, Yao et al., 2011). Literature has reported on single-step contra diffusion and a two-step counter diffusion method methodology for ZIF-8 (Kwon and Jeong, 2013, Hara et al., 2014, Hara et al., 2015, Tran et al., 2020b). In the counter diffusion method, the substrate is treated with either metal or linker precursor, after which it is then subjected to the other precursor in a batch system for ZIF-8 membrane synthesis. This methodology creates a concentration gradient, a driving force, and a reaction zone within the vicinity of the substrate surface. The contra diffusion method is where substrates are exposed to both precursors at the same time in an isolated system. The interaction zone begins from within the substrate pores, where the precursors first interact, suggesting growth initiation from within substrate pores, thereby acting as anchors for the film growth on the substrate surface (Yao et al., 2011, Xie et al., 2012).

Kwon et al. 2013 synthesized ZIF-8 on the flat disk substrates, which were soaked for an hour into a metal solution prepared from zinc chloride and methanol, and then transferred to the reaction vessel with the linker solution and sodium formate in methanol at 120 °C for 4 h. Which created a concentration gradient, a reaction zone in the support's vicinity, driven by diffusion, promoting heterogeneous nucleation and ZIF-8 growth onto the substrate. The synthesis process relies on the reaction and diffusion processes being optimum. Too slow a reaction rate will result in the ions diffusing away from the substrate surface into the linker solution's bulk, resulting in homogenous nucleation. Ideally, a fast reaction faster than diffusion is ideal, which will allow heterogeneous nucleation before the metal ions are depleted from the substrate. A diluted concentration is ideal for reducing homogenous nucleation whilst larger crystals are formed, leading to thicker membranes reducing permeances. However, Kwon et al. was able to maintain a high metal concentration of 180 mM and linker/metal ratio of 9 by using the catalyst, sodium formate, to maintain a high reaction rate leading to a large number of nuclei being formed within the vicinity of the substrate surface, leading to a thinner membrane. The XRD patterns in Figure 2-17 shows typical characteristic peaks of ZIF-8 even at 2 minutes, reflecting the reaction zone due to the high precursor concentrations and catalyst (Kwon and Jeong, 2013). In conclusion, for a diffusion-controlled heterogeneous growth process, the precursor concentration plays a pivotal role in the heterogeneous growth's nature, and a catalyst can be used to optimize the process.

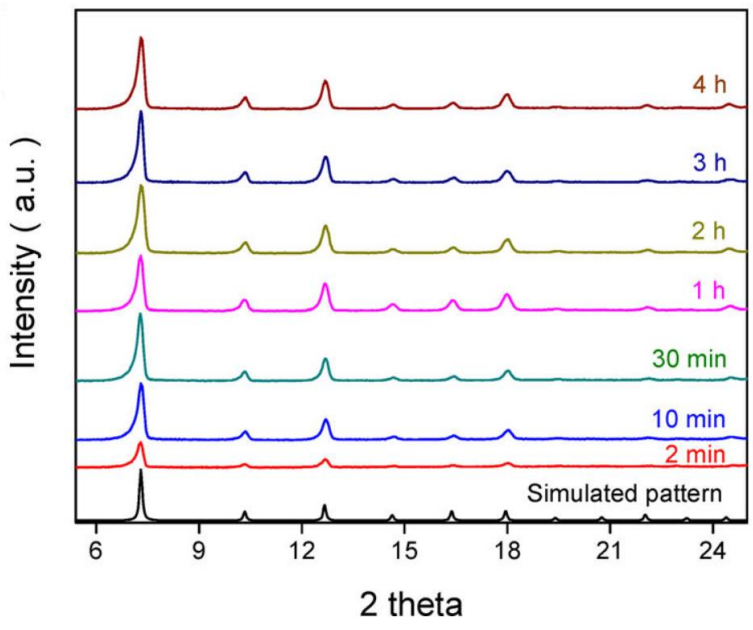


Figure 2- 17: XRD patterns of ZIF-8 membranes as a function of synthesis time (Kwon and Jeong, 2013). Reproduced with permission from Kwon and Jeong 2013.

After 30 minutes, the SEM images' growth shows a membrane thickness of 1.5 µm that did not change with further increase in time (Figure 2-18). This is due to the relatively fast reaction, leading to a lot of nuclei formation and smaller nuclei. Since the nuclei are in the substrate's vicinity, thinner membranes are observed (Kwon and Jeong, 2013).

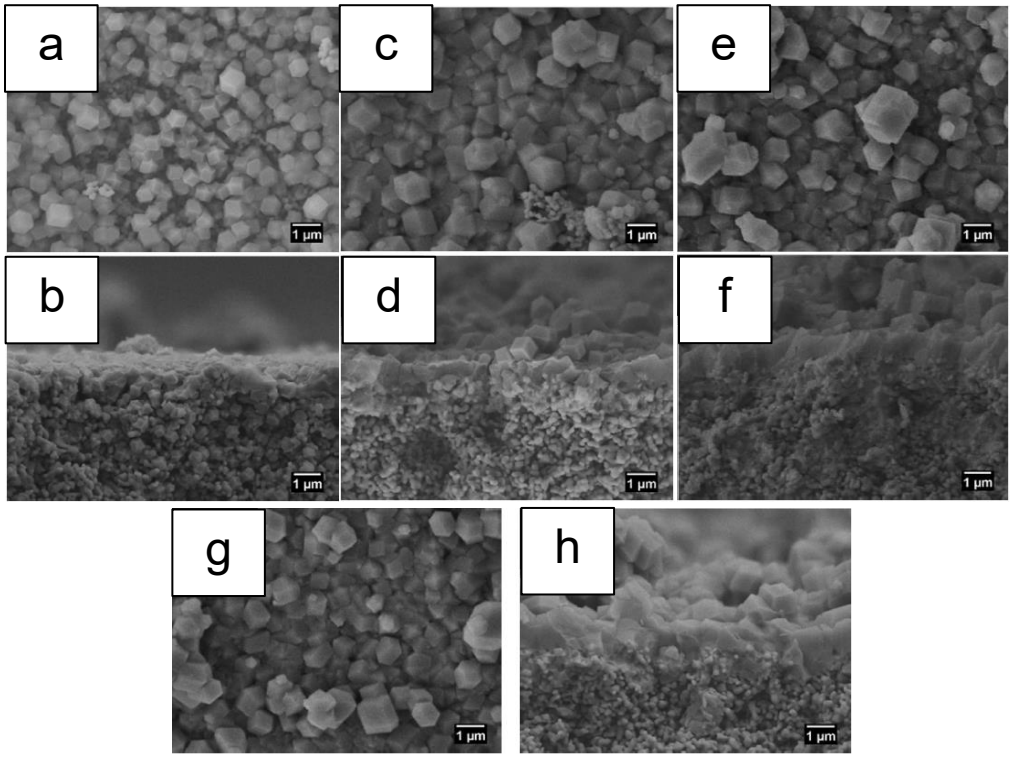


Figure 2- 18: Surface and cross-section SEM images of ZIF-8 membrane growth at 2 mins (a, b), 30 mins (c, d), 2 hours (e, f), and 4 hours (g, h). (Kwon and Jeong, 2013). Reproduced with permission from Kwon and Jeong 2013.

In further control experiments, Kwon et al. concluded that the diffusion of the precursors was from metal to linker side, since the substrate that soaked in the linker (with sodium formate) solution and synthesised in metal solution resulted in no substantial heterogeneous growth (growth on the substrate) with the visible microstructure of the substrate. Growth without the catalyst, sodium formate, resulted in sparse crystal growth even with the metal inside the substrate pores (Kwon and Jeong, 2013). Kwon et al. 2015 also studied the effect of sodium formate, metal, and linker concentrations on growth. The results supported that the sodium formate acts as a catalyst. With an increasing ratio between sodium formate and linker, the

membrane's intergrowth and continuity improved, reporting an optimum ratio of 0.12 for the sodium formate to linker ratio (Kwon and Jeong, 2015).

A counter diffusion study was conducted by Hara et al., where tubular substrates were used. The substrate was first submerged in a zinc nitrate solution prepared using methanol and placed in a vacuum oven for 20-40 seconds to remove bubbles from substrate pores. A plastic tube was inserted into the lumen of the substrate to separate inner and out sections of the substrate and then transferred to the linker solution (synthesized using methanol) in a glass vial. The membrane was synthesised at 50 °C for 12-96 hours. After synthesis, the membrane was washed with methanol at 50 °C for 24 hours and dried at 90 °C for 24 h in a vacuum oven. The results (at 72 hours) showed that the growth of ZIF-8 was on the metal side (Figure 2-19), indicating there was a layered structure of the zinc complexes across the cross-section of the substrate. The EDX results also indicated that the thickness of the ZIF-8 layer is 80 µm made up of a cover layer of 1 micron on the substrate surface. Hence, the substrate pores' growth was dominant for permeation since with increased synthesis time, the permeance of H_2 increased from 1 x 10^{-8} to 9.1 x 10^{-8} mol/m^2.s.Pa from 12 to 72 hours of synthesis times, respectively. In conclusion, the substrate pores' growth had more of an impact on gas separation performance (Hara et al., 2014).

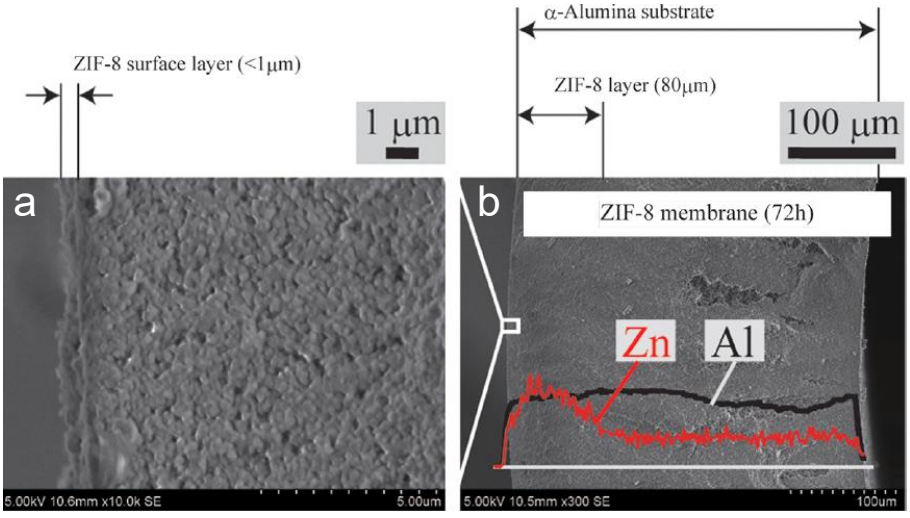


Figure 2- 19: Cross-section SEM image (a) and SEM-EDX line analysis of aluminium and zinc with a more magnified view of the outer cross-sectional image (b) at a reaction time of 72 h (Hara et al., 2014). Reproduced with permission from Hara et al. 2014.

In a more recent publication, the counter diffusion study was expanded using immiscible and miscible solvent pairs (Hara et al., 2015). The synthesis methodology was the same as the Hara et al. 2014. The zinc nitrate solution was prepared in water,

supplied from the inner part of the substrate. The linker solution was prepared in immiscible 1-octanol and miscible methanol, supplied from the outer part. One membrane was synthesised for 1 hour with linker solution in 1-octanol, three membranes were synthesized for 72 hours; synthesised with linker solution in 1-octanol for 72 hours, 1-octanol for 1 hour and then in methanol for 72 hours, and fourthly methanol for 72 hours. Hara et al. concluded that using immiscible pairs led to the formation of defective layers, influencing the membrane's microstructure. However, defects were decreased with the successive reaction in the miscible pairs of water and methanol due to reactivity and miscibility, suggesting the miscible pair healed the defected flaws in the membrane. Their best performing membrane achieved permeance of 1.2×10^{-8} mol/m^2.s.Pa for propylene and propylene/propane selectivity of 20 (Hara et al., 2015).

Similarly, Tran et al. performed a counter diffusion experiment, using zinc acetate dihydrate, zinc nitrate hexahydrate and zinc chloride to synthesize ZIF-8 membranes. The tubular substrates were first treated in the respective metal solutions for one hour and then were synthesised in linker solution using autoclave at 120 °C for 4 hours. When growing on the tubular substrate's outer area, the lumen was isolated by placing Teflon caps at both ends, and when growing inside the substrate, the outer area was covered using Teflon tape. Tran et al. reported difficulty achieving dense and continuous crystal growth when attempting to grow inside the substrate, resulting in failing to separate propylene from propane. The lack of growth could be due to restricted mass transfer from the bulk of the solution due to the narrow spacing of tubular substrate - internal diameter of 8 mm. Growth conducted on the substrate's external area reported differences in microstructure between the three metal salts. The membrane microstructure derived from zinc nitrate was smoother with more uniform micro-sized crystals, whereas zinc chloride produced a thicker and coarser surface, and zinc acetate produced crystals with more irregularities – size variety and lacking uniformity. Figure 2-20 shows the surface and cross-sectional SEM images of the membranes derived from the various metal salts (Tran et al., 2020b). The work reiterates the microstructures' difference when using different metal salts and difficulty in heterogeneously growing ZIF-8 onto tubular substrates, particularly when on a negative curvature.

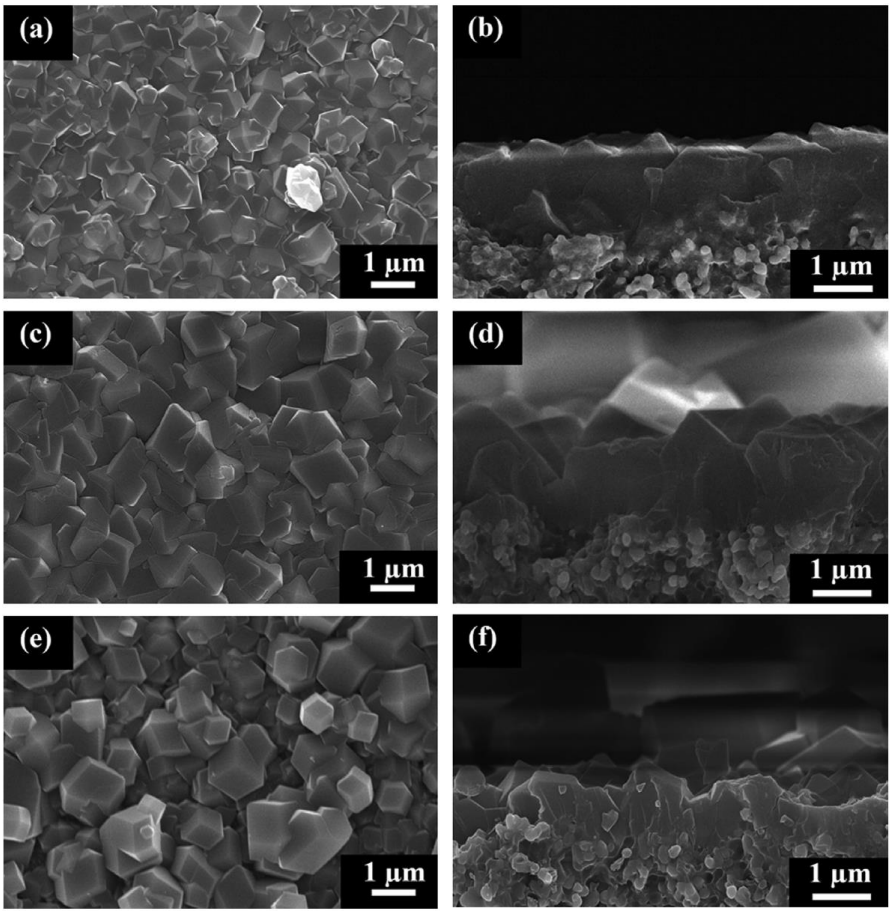


Figure 2- 20: SEM images of the surface and cross-sectional images of ZIF-8 membranes prepared from zinc nitrate (a, b), zinc chloride (c, d), and zinc acetate (e, f). (Tran et al., 2020b). Reproduced with permission from Tran et al. 2020.

Yao et al. synthesised ZIF-8 membranes on a flat disk nylon substrate via contra diffusion method at room temperature for 16-72 hours. Nylon was ideal since the ligand of the ZIF-8 structure has favourable interactions between the polymer, thereby promoting a more robust heterogeneous nucleation. Zinc nitrate hexahydrate in methanol was used for the synthesis of the membrane. Figure 2-21 shows diffusion cell and schematic formation of ZIF-8 films on the nylon substrate (Yao et al., 2011). Although they fixed the linker/metal ratio at 8, the linker side's crystals were larger than the metal side, with a size range between 100-400 nm, implying the linker diffused slowly. The surface microstructure also suggested that the local molar ratios was created due to a difference in precursor flux across the substrate boundary (Yao et al., 2011). Therefore, the study indicated that the membrane microstructure was controlled by precursor location due to local molar ratios. In conclusion, this indicates the

membranes' microstructure can be controlled by changing precursor locations at the same precursor concentration and ratios.

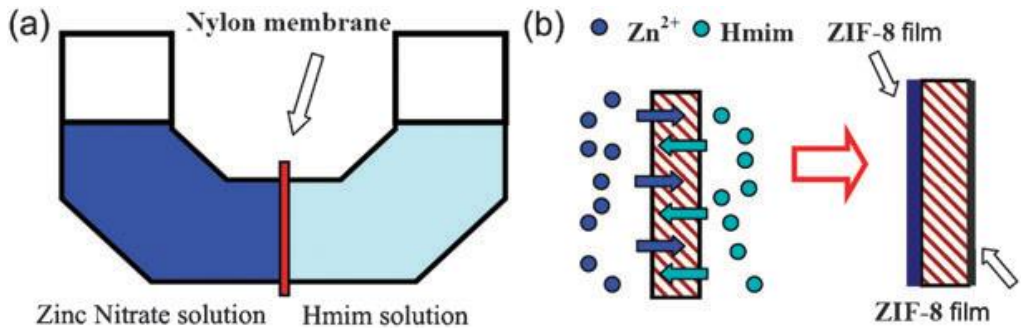


Figure 2- 21: Diffusion cell for the formation of ZIF-8 membrane (a), and the schematic formation of the ZIF-8 films on both sides of the nylon substrate via counter diffusion of the Zn^{2+} and $Hmim^{-}$ (Yao et al., 2011). Reproduced with permission from Yao et al. 2011.

Similarly, Xie et al. synthesised ZIF-8 membranes on the outer side of the tubular substrates with a pore size of 3 microns via contra diffusion, using zinc nitrate hexahydrate at 150 °C for 5 hours. Before the in-situ experiments, the substrate surface was modified via the hot dip coating method (at 150 °C for 20 s), using 500 nm alumina particles, treated with APTES. The treated alumina particles acted as both fillers for the large pore substrate and as anchors for the ZIF-8 structure. The metal solution was supplied from the substrate's lumen and linker solution from the Teflon reaction vessel. The cross-sectional SEM images indicated the growth of a dense and defect-free membrane of approximately 2 µm thickness with the XRD confirming the presence of ZIF-8 growth showing all the characteristic peaks of the structure. This suggests the Zn^{2+} ions diffused to the substrate's outer volume due to the concentration gradient, bind to the APTES modified alumina particles and form a continuous membrane (Xie et al., 2012).

Tanaka et al., Kida et al. and Ramu et al. studied the effects of the metal salt's reactivity on the growth of ZIF-8 onto substrates. Kida et al. 2013 showed the effects of reactivity of the metal salt on heterogeneous nucleation. Kida et al. suggested that the film growth in their systems derived from the $Zn(OAc)_2$ had thicker growth on the substrate and no defects, whereas the membrane derived from $Zn(NO_3)_2$ had grain

boundary cracks. Similarly, Tanaka et al. reported membranes derived from $Zn(OAc)_2$ have a much better microstructure than $Zn(NO_3)_2$. The dissociation rate of $Zn(NO_3)_2$ is faster than $Zn(OAc)_2$, in which an intermediary structure of $Zn\text{-}CH_3COO$ forms before the Zn^{2+} ions become available to form ZIF-8. Tanaka et al. also carried out similar experiments to study the membrane microstructure and commented on the advantages of a slower dissociation rate of $Zn(OAc)_2$ compared to $Zn(NO_3)_2$ and better heterogeneous nucleation. They also commented on the intermediate structure in the case of $Zn(OAc)_2$. In both cases, the silane coupling agent IPTES was used (Tanaka et al., 2014b, Kida et al., 2013a).

Ramu et al. studied zinc nitrate, zinc chloride and zinc acetate on membrane microstructure and gas permeation. The works showed that the best performing membrane was where both seeds and membrane growth was derived from zinc nitrate. The permeances for all membranes were of the same order of magnitude of 10^{-10} ($mol/m^2.s.Pa$), whilst the selectivity of the membrane synthesised from zinc nitrate was an order magnitude greater with a propylene/propane selectivity of 105. Ramu et al. suggested the lower selectivities of the other membranes synthesised from zinc acetate and zinc chloride may be because of poorer grain boundary structure (Ramu et al., 2018).

Kwon et al. 2015 investigated the roles of the conjugate bases associated with the zinc ion. ZIF-8 membrane derived from zinc nitrate was just above the substrate surface, while the membrane derived from zinc acetate and zinc chloride originated from within the substrate pores. The difference between the microstructure derived from the bases acetate and chloride was the lack of intergrowth from acetate. However, the propylene/propane separation factors for these membranes were comparable, but no separation from the membrane derived from nitrate. The microstructure was also investigated by synthesizing the membranes using a mixture of zinc salts. They concluded that the membrane microstructure was a combination of the membrane microstructures derived from individual zinc salts. (Kwon and Jeong, 2015)

In conclusion, Kwon et al. 2015 study indicates the conjugate bases associated with the zinc control the microstructure and membrane intergrowth. The work also demonstrated growth within the substrate's pores more of an impact on the separation performance of the membranes than the film above the surface. (Kwon and Jeong, 2015)

2.5.3 Gas separation Performance of ZIF-8 Membranes

Understanding the synthesis methodologies of ZIF-8 is essential to review the gas separation data for the ZIF-8 membranes tested for the gas mixture CO_2/CH_4. Table 2-1 summarizes the ZIF-8 membranes tested for CO_2 and CH_4 permeances and ideal CO_2/CH_4 selectivity.

Table 2- 3: Selected single gas permeances and selectivities of ZIF-8 membranes for CO_2 and CH_4.

Author	Substrate	Temperature (°C)	Feed Pressure (bar)	Permeance (mol/s.m^2.Pa)		Ideal selectivity
				CO_2	CH_4	
(Venna and Carreon, 2009)	Tubular	25	1.4	$2.1x10^{-5}$	$5.17x10^{-5}$	4.1
(Zhu et al., 2016)	Tubular	100	2	$0.97x10^{-8}$	$1.43x10^{-9}$	6.8
Lai et al. 2016	Disk	30	1	$1.31x10^{-8}$	$0.59x10^{-8}$	2.2

Venna et al. synthesised a 2- and 8-layer ZIF-8 membrane with 5 and 9 µm thickness, respectively. Although the 8-layer membrane yielded a selectivity of 7, the permeances decreased to $1.69\ x10^{-5}$ and $2.42\ x10^{-5}$ for CO_2 and CH_4, respectively. Most likely, due to the increase in membrane thickness. The selectivities were not very high, 5.1 and 7.0 for the 2- and 8-layer membranes, respectively. However, the separation indexes were comparable to that of zeolites, between 6.5-10 (Venna and Carreon, 2009). A more recent publication by Zhu et al. on tubular ceramic substrates reported selectivity of 6.8. However, the permeances of both CO_2 and CH_4 were lower than Venna et al. by

several magnitudes (Table 2-1), most likely due to Zhu et al. membrane thickness of ~25 µm. Zhu et al. also assessed the thermal stability of the ZIF-8 membranes over 48 hours at 100 °C. Figure 2-22 shows that the single gas permeances and ideal CO_2/CH_4 selectivity remained the same, suggesting that the ZIF-8 structure is stable and a good candidate for the separation of CO_2.

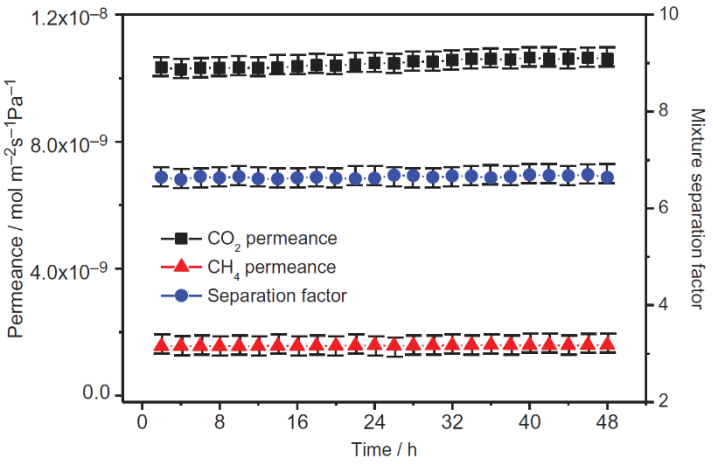


Figure 2- 22: Stability measurement over time of ZIF-8 membrane prepared on tubular substrates. Permeances of CO_2 and CH_4, and separation factor of equimolar CO_2/CH_4. Feed stream conditions of 2 bar and 100 °C. (Zhu et al., 2016). Reproduced with permission from Zhu et al. 2016.

Lai et al. studied the effects of temperature (303, 323, 343 K), pressure (100 and 700 KPa), and feed composition (15, 50, and 90 % of CO_2) of the gas stream using ZIF-8 membranes. Figure 2-23 presents permeances and the ideal selectivities as a function of pressure. No change was observed for CO_2 permeance, while there was a slight increase in the permeance of CH_4 from 0.58 to 0.73 $x10^{-8}$ at 303 K (Fig 2-23b). This is due to the viscous flow and Knudsen diffusion that dominates the permeation of CH_4 over the ZIF-8 membrane, which increases with increasing pressure. However, at 323 and 343 K, the permeation of CH_4 remains almost constant with increasing pressure (Figure 2-23b). This may indicate the expansion of the pores at the higher temperatures resulting in the change in permeance of CH_4 at 323 K and 343 K. Figure 2-23 also shows that the permeance of CO_2 slightly increased at 323 and 343 K with increasing pressures, this is due to the higher temperature and the pressure increasing permeation of the CO_2 molecule (Lai et al., 2016a).

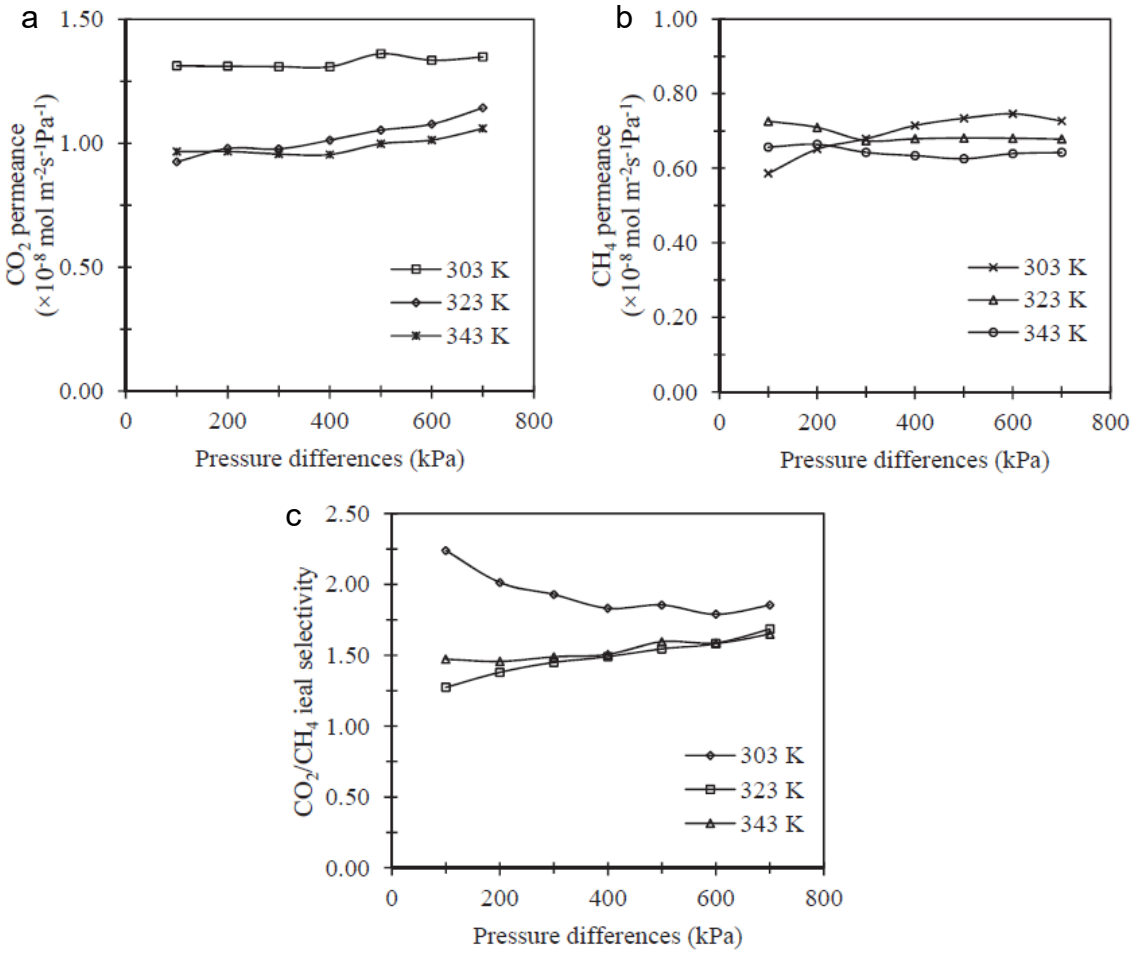


Figure 2- 23: CO_2 (a) and CH_4 (b) permeances, and CO_2/CH_4 ideal selectivity (c) for ZIF-8 membrane at pressure differences between 100 to 700 kPa and temperature between 303 to 343 K. (Lai et al., 2016a). Reproduced with permission from Lai et al. 2016.

Figure 2-24 shows that with increasing temperature (300 to 350 K) the permeance of CO_2 decreased since the permeance is adsorption controlled rather than diffusion controlled. Hence, with increasing temperature, the level of coverage of CO_2 on the ZIF-8 surface decreased. Another role of temperature can be to expand the breathable ZIF-8 structure at higher temperature, increasing the CH_4 permeance since it is diffusion controlled, though this was only observed at 100 kPa. Whereas at 700 kPa the permeance of CH_4 slightly decreased rather than increase. This is most likely due to the decrease in the viscous flow because of increased gas viscosity with increasing temperature. Hence, the CH_4 permeance remained unchanged with increasing pressure (Figure 2-23).

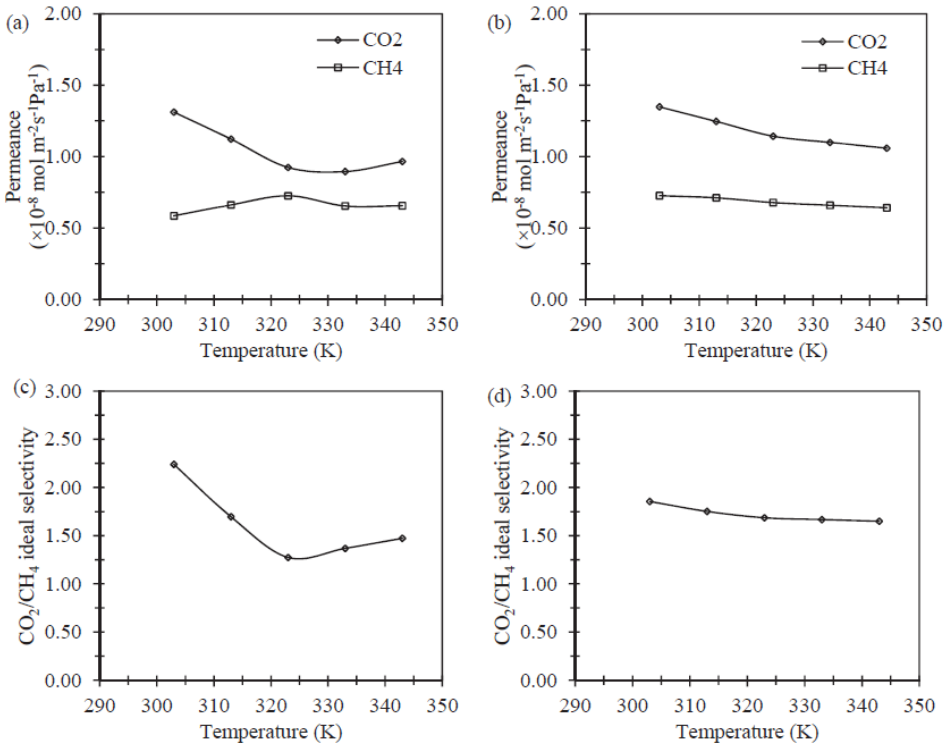


Figure 2- 24: Single gas permeance of CO_2 and CH_4 across temperature range between 303 to 343 K at a pressure difference of 100 (a) and 700 (b) kPa. CO_2/CH_4 ideal selectivity CH_4 across temperature range between 303 to 343 K at a pressure difference of 100 (c) and 700 (d) kPa. (Lai et al., 2016a). Reproduced with permission from Lai et al. 2016.

The feed compositions influenced the separation performance of the membranes for the binary gas mixtures. A maximum separation factor of 5.07 was obtained at the low feed composition of 15% CO_2 at 100 kPa and 303 K. The data showed that with increasing CO_2 feed composition the permeance of CO_2 reduced since more CO_2 molecules were covering the membrane surface (Figure 2-25). This also results in a reduction of the permanence of the CH_4 due to the competitive adsorption between preferentially adsorbed CO_2. In conclusion, when measuring a synthesised membrane's performance, it is important to understand the role of the testing conditions on the collected data.

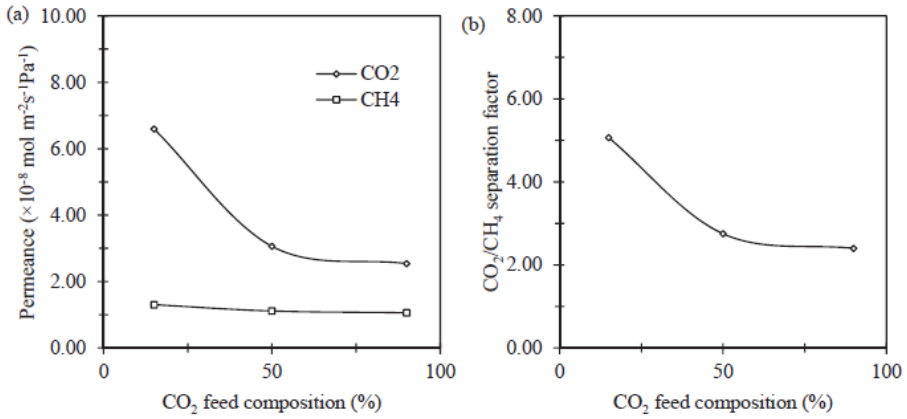


Figure 2- 25: The effect of CO_2 feed composition on permeance of CO_2 and CH_4 (a) and CO_2/CH_4 separation factor of ZIF-8 membrane at 100 kPa pressure and 303 K temperature. (Lai et al., 2016a)**.** Reproduced with permission from Lai et al. 2016.

2.6 ZIF-8 Membrane Synthesis using Microwave Heating

With the vast range of techniques used to synthesise MOF membranes being developed from that of zeolite membranes, microwave (dielectric) heating was no exception. Microwaves are a form of electromagnetic energy that is made up of a magnetic and electric field. The electric field transfers the energy to heat in a substance (Hayes, 2002). In conventional heating, the heat is transferred via conduction, convection, or radiation. In microwave (dielectric) heating, the heat is formed from transforming the electromagnetic energy into heat rather than being transferred (Li and Yang, 2008).

Reported advantages associated with microwave heating are higher heating rates, remote introduction into the reaction medium, rapid volumetric heating without wall or heat diffusion effects associated with conventional heating, selective heating dependent on material dielectric properties, and the superheating effect – heating of the solvent above its boiling point (Caro, 2011).

Microwave heating has been used to synthesise zeolites from as early as the 1990s (Xu et al., 2000). Xu et al. reported thinner NaA membranes with a narrow crystal size distribution and shorter synthesis time of 15 and 180 minutes for microwave and conventional heating, respectively (Xu et al., 2000). Recently, Wang et al. shorten the DDR zeolite membrane's synthesis time from several days to an hour by accelerating the crystallization kinetics by using microwave heating. Other publications indicated

similar findings on the synthesis of zeolite membranes via microwave heating (Wang et al., 2019, Chen et al., 2005, Bao et al., 2016, Li et al., 2006, Chew et al., 2011, Cheng and Qin, 2014, Madhusoodana et al., 2006, Zhang et al., 2016, Ng et al., 2019, Bai et al., 2016, Baig et al., 2015, Caro and Noack, 2008).

To understand microwave heating and MOF growth it is necessary to understand the theory of microwave heating mechanisms. Figure 2-26 shows the microwave and conventional heating to have linear and asymptotic heating profiles, respectively. With conventional heating the temperature is constrained to the temperature inside the oven. Whereas with microwave heating the average temperature continues to rise so long as there is an input of power. A secondary factor affecting the heating effects of microwave heating is the heat transfer because of surface heating and cooling, though this depends on the microwave reaction chamber condition, temperature and humidity (Meredith, 1998).

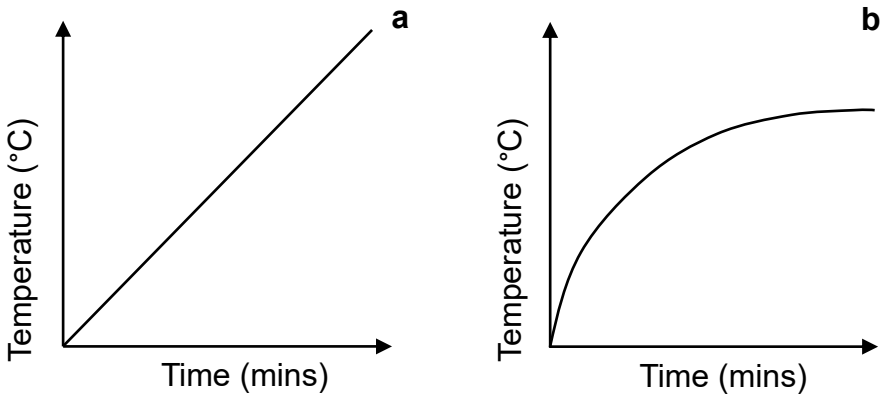


Figure 2- 26: Shows the heating profiles of microwave (a) and conventional (b) heating.

Microwave heating has two mechanisms, thermal and non-thermal. The thermal is from the friction generated because of the ions rotational movement following the oscillating electromagnetic waves, and the non-thermal is the direct interaction of the molecules and the electromagnetic waves (Li and Yang, 2008, Herrero et al., 2008, Chen et al., 2014).

The dielectric properties of the material indicate how well that material will interact with the microwaves. The dielectric constant, ε' is a measure of a materials ability to store electromagnetic energy (via being polarized). The dielectric loss factor, ε'', is a measure of the efficiency of how well the material can convert the stored energy into heat. Therefore a low ε'' shows material heats weakly in the electromagnetic field, and

high heats strongly. Electromagnetic energy loss occurs because of two factors; conduction, energy being dissipated when the charge travels through the material. Hence the material state (solid, liquid or gas) will impact the rate of electromagnetic energy loss since conduction varies between physical states. Secondly, a dielectric loss means a loss of energy when the charges' switch to keep up with the alternating electromagnetic field – the dielectric constant drops when it cannot keep up with the switching electric field. It is important to note that both parameters, dielectric constant and dielectric loss factor, do vary with frequency (DoITPoms, 2019, Gabriel et al., 1998).

The loss tangent, expressed as the ratio of the dielectric loss factor and dielectric constant is, $\tan \delta = \varepsilon''/\varepsilon'$, gives a measure of how well a material can convert the stored energy into heat, i.e. how well a material heats with microwave heating hence the selective heating with microwaves. Materials can then be categorized into groups based on their dielectric properties, (1) materials reflecting microwaves, typically bulk metals and alloys, (2) materials transparent to microwaves, typically ceramics (low tan δ), and (3) materials absorbing microwaves typically aqueous solutions, polar solvents (high tan δ). Generally, a material with a higher dielectric loss factor, ε'', heat well. (Li and Yang, 2008, Caro, 2011, Mingos and Baghurst, 1991)

With ionic solutions, the anions and cations are displaced by the electric field that leads to an overall polarization. The ions mobility and concentration through the oscillating electric wave must be considered. Dipolar mechanisms are from molecules that have permanent dipoles, such as water. The molecules reorient themselves by a torque they experience because of the electric field. As the electric field alternates, the molecules reorient because of their dipoles, and this rotational movement creates friction from neighbouring molecules. From this friction, heat is generated, achieving moderate losses (ε''). (Dudley et al., 2015, Laybourn et al., 2016)

A third parameter in microwave chemistry is the bulk dielectric permittivity, ε*. Laybourn et al. discussed how dielectric constant (ε') and dielectric loss factor (ε'') can be used to express the bulk dielectric permittivity, ε*, which is a measure of how well a material can be polarized - how well the structure can be charged. For molecules in solution, ε* reflects the polarization that is dependent on frequency, this is the polarization that occurs by the interaction of the ions with the oscillating electromagnetic field via ionic and dipolar polarization mechanism. Equation 2-2 shows ε* mathematical expressed as

ε'and ε", and j, the imaginary number where $j^2 = -1$. (Gabriel et al., 1998, Laybourn et al., 2016)

$$\varepsilon = e' - je''$$ (**Equation 2- 2)**

Another important parameter in microwave chemistry is the penetration factor. This is measure by how much the power falls when penetrating the medium being heated. Tompsett et al. studied microwave chemistry and zeolites. They discussed that the ability of the solution to be charged depends on the pH of the solution. Sun et al summarized materials with high loss values (good at converting the microwave energy to heat) have low penetration depths, and materials with high loss values (transparent to microwave energy) have large penetration depths since have very little energy loss when passing through the material (Tompsett et al., 2006, Sun et al., 2016).

The concentration of the solvent is another parameter to consider with microwave heating. With increasing concentration, the ε' and ε" decrease and increase, respectively. This is because of the ions and their hydration (or solvation) spheres no longer being independent. With increasing number of ions the movement becomes retarded by the surrounding solvation spheres leading to the dielectric decrement. However, the losses increase since selective heating is more dominant at the higher concentrations because there being more hot spots (ions) in the solution (Dudley et al., 2015, Laybourn et al., 2016).

Another critical parameter in microwave chemistry is the power and volume, the amount supplied and the rate at which the power is delivered. ZIF-8 membrane papers do not discuss the effects of the power deliverance, whilst understanding its role is important to understand the interpretation of results better, especially when precursors concentrations and volumes are being altered.

Experimental and simulation results by Robinson et al. suggested that the increased solvent volumes provided a higher heating rate, when increasing solvent volume from 1 to 3 ml increased power per unit volume to dissipate three-fold. With 0.39 W and 1.19 W of power dissipated for the 1 and 3 ml of solvent used, respectively, for an applied power of 30 W at 30 °C. It should be noted that the power dissipated is dependent on the dielectric constant of the solvent. Robinson et al. used the solvent MeCN that had a dielectric constant of 36.5 (methanol 33.6). (Gregory and Clarke, 2005, Robinson et al., 2010).

Laybourn et al. conducted a study on the interaction of electromagnetic energy with MIL-53(Al) interaction while maintaining the total delivered energy constant. Which was achieved by changing the power (250 - 4000 W) supplied to the reaction mixture while keeping the total energy fixed at 21 kJ (or 56 kJ/mol based on water). The results suggested that yields between 16 and 30 % for 269 and 3819 W, respectively. This suggests that heating is higher than the loss of heat at the higher powers due to the higher yields. Therefore, the reaction mixture remains hotter for longer while the MOF is being formed, increasing its overall reaction rate. The higher power of 1739 delivered well defined cubic shaped MIL-53(Al) crystals with a ratio of 10:90 of irregular to well defined cubes. Laybourn et al. also commented that with increased power, the particle size observed by SEM becomes much narrower, suggesting rapid nucleation within a short time (4.3 seconds at respective power of 3819 W) (Laybourn et al., 2017). In conclusion, the rate at which the power is delivered can be optimised to control membrane microstructure.

An advantage of microwave heating is the vessel contents' volumetric heating, whilst this is not always the case because of the penetration depth of the microwaves. Materials with a high loss factor results in most of the microwaves being absorbed in the surface of the volume forming a ‘skin’ of heating, and the remainder of the contents being heated via convection. Sun et al. discussed how this challenge with microwave heating could be overcome by mixing good absorbers of microwaves and transparent to microwaves such as activated carbon and high-purity quartz sands, respectively. This reaction technique is analogous to synthesizing ZIF-8 with precursors with a low concentration to reduce the dielectric losses. Bux et al. reflected this by reducing the precursor's concentrations and the synthesis time from 4 to 2 h whilst a seeded substrate was used for the 2-hour synthesis. Yoo et al. also used microwave heating for the seeding of MOF-5 crystals onto a flat substrate and showed that the dilute solutions reduced homogenous nucleation of the MOF in the bulk of the heating solution. This may suggest that volumetric heating is maximised in dilute systems. (Sun et al., 2016, Tompsett et al., 2006, Yoo et al., 2009)

The gas separation performance of ZIF-8 membranes synthesised using Microwave heating is summarized in Table 2-2.

Table 2- 4: Single gas permeances of CO_2 and CH_4 of ZIF-8 membranes published in the literature, synthesised using microwave heating as functions of synthesis time, synthesis temperature, and precursor concentration and ratios.

Time (h)	Temperature (°C)	Metal concentration (mM)	Linker/ metal ratio	Solvent volume (l)	Permeance 10^{-8} (mol/m^2.s.Pa)		Reference
					CO_2	CH_4	
5	140	98	1.5	0.16	1.31	0.59	(Lai et al., 2016c)
4	100	74	1.5	0.8	1.33	0.48	(Bux et al., 2009)
3	105	79	2.5	0.22	0.97	0.143	(Zhu et al., 2016)
2	100	49	1.5	0.8	1.9	-	(Bux et al., 2011)

Bux et al. 2009 synthesized a relatively thick ZIF-8 membrane with a thickness between 29-36 µm using microwave heating on an unmodified flat titania disk (Figure 2-27a) (Bux et al., 2009). They achieved thinner membranes with a thickness of 12 µm on a seeded alumina disk and precursor concentrations at approximately half of the previous study (Figure 2-27b) (Bux et al., 2011). This may suggest that seeding provided more nucleation sites on the substrate, thereby creating more sites for membrane growth to initiate from. Hence, smaller crystals are generated, leading to a thinner membrane. The shorter synthesis times have proven successful for membrane growth from the microwave chemistry perspective because of the diluted precursor solution. That may be due to the diluted system maximising volumetric heating mechanism achieved by the microwaves (Bux et al., 2009, Bux et al., 2011). In

conclusion, this indicates the reaction chemistry can be optimised to accommodate the microwave heating mechanism and reinforce to reduce synthesis time and membrane thickness.

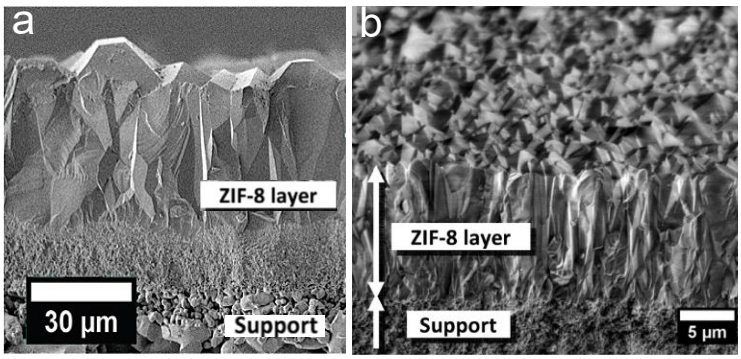


Figure 2- 27: Cross-sectional images of (a) unmodified (Bux et al, 2009) and (b) modified (Bux et al, 2011) membranes synthesis on flat alumina disk substrates. Reproduced with permission from Bux et al. 2009 and Bux et al. 2011.

Lai et al. also reported using microwave heating to synthesise ZIF-8 membranes onto a flat substrate seeded via solvent evaporation seeding. The substrate was seeded for 2.5 hours using conventional heating at 65-70 °C, and membrane synthesised for 5 hours at 140 °C. Although microwave heating was used to synthesise the membrane, the membrane was very thick (50 µm). With the membrane delivering single gas permeances of 1.31 $x10^{-8}$ and 0.59 $x10^{-8}$ mol/m^2.s.Pa for CO_2 and CH_4, respectively (Lai et al., 2016c). This may imply that the selected surface modification and synthesis time continue to play a role in the membrane microstructure while using microwave heating.

Zhu et al. synthesized a dense ZIF-8 membrane onto tubular substrates with a thickness of 25 µm with a two-step synthesis process, including the APTES surface modification stage on tubular supports. The membrane was synthesized for 3 hours at 105 °C under microwave heating. They studied the effects of conventional and microwave heating on the heterogeneous nucleation of ZIF-8. Figure 2-28 shows SEM surface images of APTES surface modified membranes synthesised under conventional and microwave heating. The results showed a sparse growth on APTES-modified substrate with conventional heating (Figure 2-28b). While the results of the membrane synthesised under microwave heating showed dense and continuous growth (Figure 2-28a). They suggest that the superheating effect from the selective heating of the Zn^{2+} in the precursor solution provides high temperature regions, thus

accelerating the kinetics of the reaction under microwave heating. However, the APTES is still needed to provide sites of ‘anchors’ for the ZIF-8 structure to attach to the tubular support for a more robust heterogeneous nucleation. (Zhu et al., 2016)

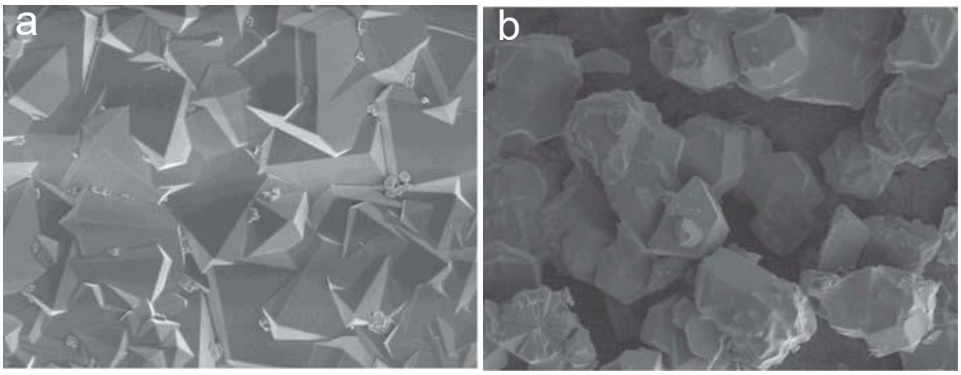


Figure 2- 28: Surface images of ZIF-8 membranes synthesised on APTES modified tubular substrates under (a) microwave and (b) conventional heating (Zhu et al., 2016). Reproduced with permission from Zhu et al 2016.

Microwave literature reiterates the difficulty with the growth of ZIF-8 membranes. Since evolved ZIF-8 crystals can be synthesised in the solution's bulk within minutes (Butova et al., 2016, Xing et al., 2014, Lai et al., 2016b). This suggests that the reaction kinetics for the heterogeneous growth of ZIF-8 is more challenging even with the volumetric heating mechanism of microwaves (Butova et al., 2016, Xing et al., 2014, Lai et al., 2016b).

2.7 Dynamic cold spray coating of MOFs

Dynamic cold spray coating is the coating of substrates by impacting particles at high velocities in a supersonic jet of compressed gas created by a convergent-divergent De Laval nozzle. The strong bonding between impacting particles and substrate is achieved by the high kinetic impact energy created by the particles' velocity. The work by Kim et al. and Smith et al. showed that minimum kinetic energy (particle velocity) is needed to deposition the particle on the substrate's surface (Smith, 1998, Kim et al., 2016b). One of the advantages of spray coating is the scale-up possibilities since large surfaces can be uniformly coated during the continuous process.

Arslan et al. and Hurrle et al. synthesized HKUST-1, using spray coating analogous to the layer-by-layer (LBL) methodology whilst with shorter synthesis times. For example, 100 layers of MOF on a substrate using LBL requires 400 immersion cycles with a 3 day time period (Arslan et al., 2011). However, spray coating can be reduced to 30 minutes than 48 hours when using a conventional LBL process (Arslan et al., 2011).

The critical mechanical parameters selected by Arslan et al. were 1.5 bar air pressure, a slurry flow rate of 0.25 ml/s and 0.1 m distance from nozzle and substrate – stand of distance (SOD). The solvents were released from a stationary point, using three dosing valves perpendicular to the substrate (Figure 2-29). Arslan et al. concluded that the micron range MOF coatings could be obtainable with the reduced deposition time (30 min) for 20 complete cycles, compared to 48 h using the conventional LBL process. After drying and solvent removal, there were no structural defects on both the micro and macro scale.

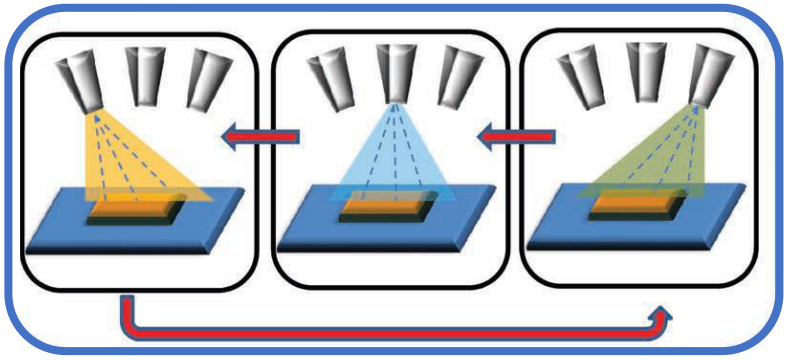


Figure 2- 29: Schematic of the three nozzles alternating between the metal and linker precursor. The substrate was sprayed with ethanol between each step to act as the rinsing step (Arslan et al., 2011). Modified with permission from Arslan et al. 2011.

Hurrle et al. used an automated step-by-step moving spray nozzle laterally. A gold substrate with an area of 78 cm^2 with a 50-cycle process was used to measure the process's scalability. The EDX analyses from over 200 different locations concluded a variation of less than 10%, indicating the lateral spray movement (along x, y, and z axis) of the nozzles promoted a more homogenous coverage of MOF growth. An alumina substrate (with a diameter of 18 mm) coated between 50-150 cycles, achieving a thickness of up to 500 nm for the gas performance tests (Figure 2-30). Films fabricated with 75 or fewer cycles did not successfully cover the alumina substrate, evidenced by their non-selectivity. The minimum was 100 cycles yielding selective permeances of 3 $x10^{-7}$ and 6 $x10^{-8}$ for H_2 and CO_2, respectively, indicating homogenous coating. The gas separations measurements were done by feeding an equimolar mixture of H_2/CO_2 fluxes, with the permeate side at 1 bar pressure. They concluded that spray coating of precursors, prepared analogous to the LBL method, can control film thickness, gas separation performance and has the potential to prepare MOF membranes with industrially relevant areas; the only limitations being the traverse paths of the robot arms (Hurrle et al., 2017).

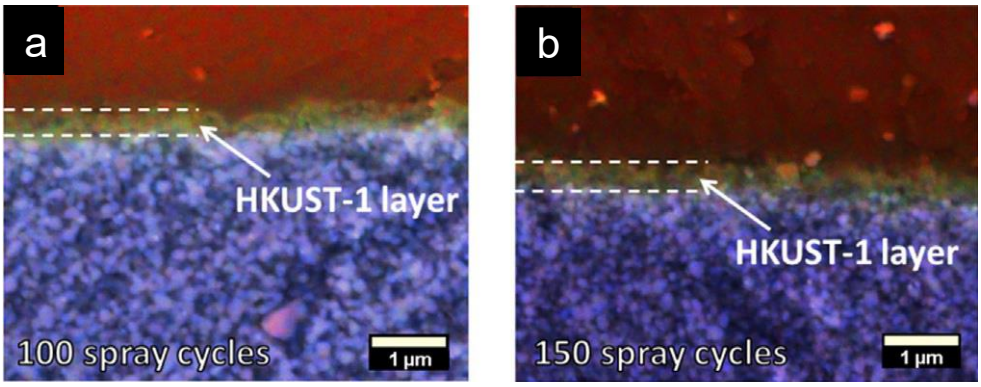


Figure 2- 30: EDX analysis of cross-sectional membranes prepared with 100 (a) and 150 (b) cycles (Hurrle et al., 2017). Reproduced with permission from Hurrle et al. 2017.

Kim et al. studied the effects of pressure (2-7 bar) and temperature (150-350 °C) of the airstream on the microstructure and coverage of ZIF-8 onto copper and glass substrates. The slurry was made up of 1 g of 150 nm ZIF-8 particles suspended in isopropyl alcohol (50 ml) and DMF (10 ml), with 6 wt.% nylon to promote adhesion to the target substrate. Four deposition cycles were performed per sample to generate uniform coating. Figure 2-31 shows a linear profile between velocity and temperature across all pressures. With increasing velocities impacting pressures of the particles

increases providing better adhesion onto the target substrate. However, this can lead to the amorphization of the ZIF-8 structure (Kim et al., 2016a).

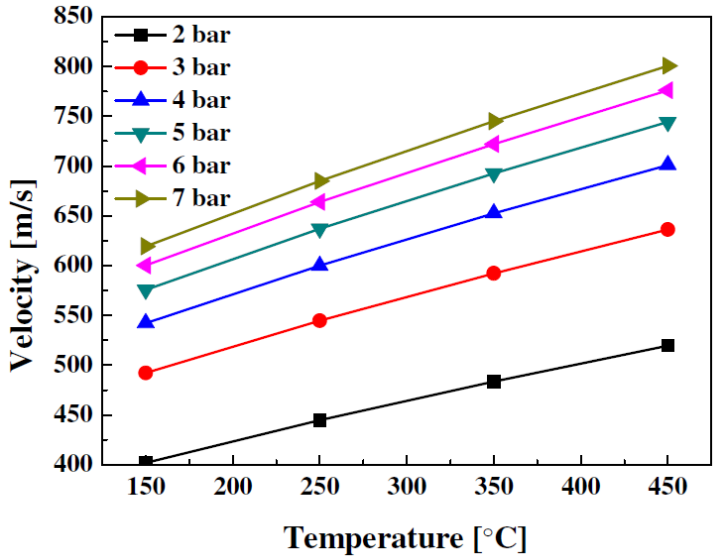


Figure 2- 31: Plot of temperature vs velocity across the different air pressures. Taken from Kim et al. (Kim et al., 2016a). Reproduced with permission from Kim et al. 2016.

Kim et al. also investigated the ability to achieve oriented and non-oriented growth from spray coating technique by using the solvent DMF. They concluded that DMF molecules in the ZIF-8 structure stabilize the structure on impact. This is due to the high boiling point of DMF (150 °C). Figure 2-32 shows XRD patterns of the films formed across 2, 4 and 6 bars in heated air streams (250 °C), with (Figure 2-32a) and without (Figure 2-32b) DMF. The inset in Figure 2-32a showing the typical peaks corresponding to the respective crystallographic planes of ZIF-8 powder, highlighting oriented growth achieved with DMF with the single peak reflecting 112 crystallographic planes. It is important to note, with or without DMF, at 7 bar, the structure amorphized due to the high impacting velocity, which increased with increasing pressure (Figure 2-31) (Kim et al., 2016b). In conclusion, to maintain crystalline structures' structural integrity, either a low air stream temperature or low pressures need to be used.

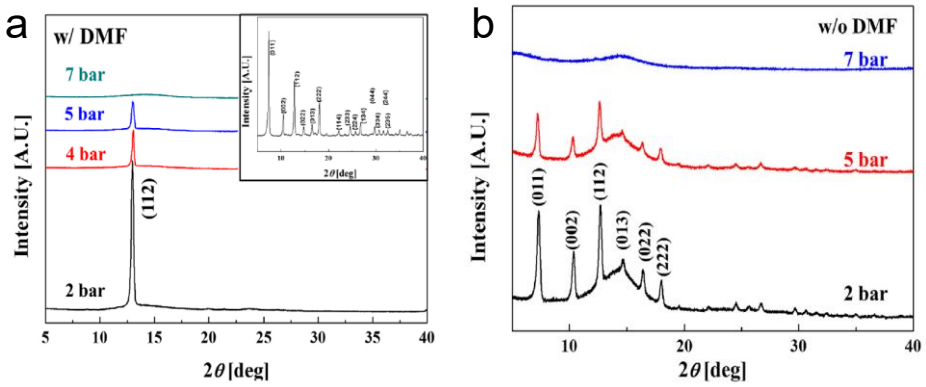


Figure 2- 32: XRD patterns of spray coated ZIF-8 films deposited onto copper substrates with airstream at 250 °C (a) with and (b) without DMF. The insert shown in (a) is the XRD pattern of the ZIF-8 powder (Kim et al., 2016a). Reproduced with permission from Kim et al. 2016.

In conclusion, literature has reported on MOF precursors' cold spray layering analogous to the LBL technique and slurry deposition. However, no study has been performed on the interaction between slurry and air stream and the atomization stage. This is an exciting field of research that can help make this scalable process more efficient with the potential to coating tubular substrates.

3. Experimental Methods

3.1 Materials

Inopor GmbH supplied the porous tubular alumina (α-Al2O3) substrates that were used during batch studies. The substrate has a 200 nm membrane layer at the inside surface of the substrate onto which the MOF film was grown. This was supported by a gradient of more porous layers, becoming more porous as moving away from the centre, with maximum pores of 3 µm on the substrate's outer side. Figure 3-1 shows a generic schematic of porous layers of a ceramic membrane. The tubular substrate has outer and internal diameters of 11 and 7 mm, respectively. The 1 m length tubes supplied by Inopor GmbH were cut to 2 and 6 cm pieces for the isolated and mixed precursor batch reactions.

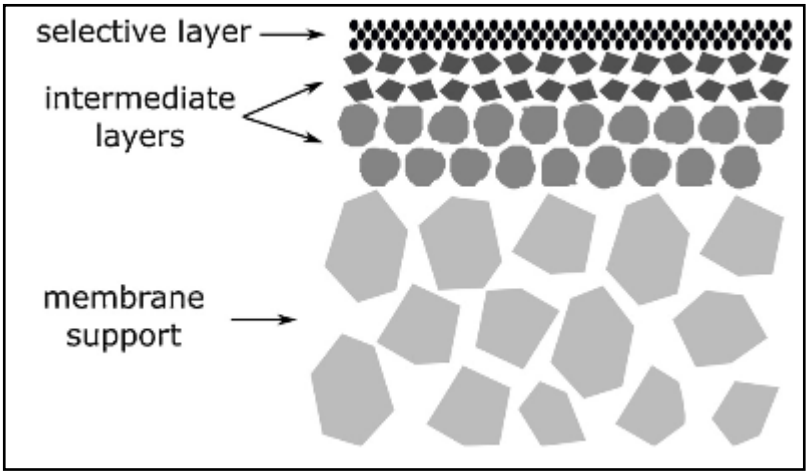


Figure 3-1: Typical structure of a porous ceramic substrate. (Mestre et al., 2019). Reproduced with permission from Mestre et al. 2019.

Before use, the substrates were boiled in deionised water at 100 °C for 2 hours and dried in a conventional electric oven for 2 hours at 100 °C.

The ends of selected 6 cm substrates were glazed with DUNCAN ENVISION™ GLAZE to create airtight seals with the silicon O-rings when mounting into the membrane module being tested in the gas separation system. The glazing was done using a furnace at 900 °C for 60 minutes, with heating and cooling rates of 1 °C/min. After removal, the substrates were rinsed with deionised water and dried at 100 °C for 2 hours.

The Teflon® plugs were used to isolate precursors in the alumina substrate for the metal-linker isolation work. These were supplied by the L4 technicians in the Chemical

and Environmental Engineering Department. The Teflon® plugs were thoroughly washed with deionised water and dried at room temperature before use.

Table 3-1 summarises the chemicals used in this study. All the dried chemicals were used as supplied. The Basolite® C 300 slurry was diluted to a 7 wt.% using methanol.

Table 3- 1: Chemical and suppliers used in this study.

Chemical	Chemical Formula	Supplier	Purity
Methanol	CH_3OH	Fisher Scientific	≥ 99.9 %
Deionised Water	H_2O	Chemical and Environmental Engineering Department	
Zinc acetate dihydrate	$Zn(CH_3COO)_2 2.H_2O$	Fisher Scientific	98 %
Zinc nitrate hexahydrate	$Zn(NO_3)_2 6.H_2O$	Fisher Scientific	99 %
2-Methylimidazole	$C_4H_6N_2$	Fisher Scientific	99 %
Basolite® C 300	HKUST-1	Promethean	Supplied as slurry suspended in methanol at 12 wt.% grade

3.3 Batch synthesis system

The batch synthesis system for the heterogeneous growth of ZIF-8 is investigated using conventional (electric) and microwave heating. The preparation of precursor solutions and surface modification of the tubular substrates is the same for both systems. This is a novel study giving the research community an opportunity to better understand the difference between heterogeneous growth achieved between the two heating mechanisms. First strategy was to find the ideal reaction chemistry for the batch system under conventional heating. The second strategy was for better understanding the microwave reaction chemistry of ZIF-8 membranes and compare to

the conventional heated system at the same temperature (100 °C). Once this is understood the work can be taken further via the pilot scale synthesis. In conclusion, the batch systems work towards finding an optimised synthesis conditions with a focus on upscaling.

The membranes were characterised using scanning electron microscopy (SEM) and X-ray Diffraction (XRD) to assess the microstructure and identify crystalline growth on the substrate surface, respectively.

A seeded growth method was used for the synthesis of ZIF-8 membranes. The ZIF-8 seeds were synthesised using zinc nitrate hexahydrate at 150 °C for 5 hours. The reaction mixture was heated under pressure in a PARR digestion reaction vessel lined with a Teflon® liner of 32 ml capacity. After removal, the ZIF-8 slurry was centrifuged twice, between the centrifugation the seeds were washed with methanol. The obtained seeds had an approximate size of 150 nm.

The ZIF-8 seeds were manually deposited inside of the substrate via physically rubbing seeds using pipe cleaners. The deposition of seeds (approx. 0.12 g per 6 cm substrate) was done systematically, e.g., the seeds were rubbed along the length of the tube rotating the substrate around the axis. Seeds were rubbed for 10 minutes, for a total of four rotations, two and a half minutes per rotation. More seeds were attached to the pipe cleaner per rotation before continuing with the seeding. The seeds were attached to the pipe cleaner by rotating the pipe cleaner in the petri dish with approximately 5 g of seeds. Figure 3-2a provides a schematic of the seeding procedure.

The metal precursor used to synthesise ZIF-8 membranes was either zinc acetate dihydrate or zinc nitrate hexahydrate. 2-methylimidazole was an organic linker. The mixed precursor solutions were prepared by measuring the respective quantities of zinc salt and 2-methylimidazole and then dissolving into the solvent methanol. The solutions were mixed until the solute dissolved. The ZIF-8 mixed precursor solution was prepared by adding the linker solution to the metal solution as fast drops. The mixture was stirred for 5 minutes, including the time taken to add the linker solution to the metal solution. After five minutes, the mixed precursor solution was transferred to the PARR digestion reaction vessel lined with the Teflon® liner with the seeded substrate already in place. Figure 3-2b shows a schematic of the main steps involved with the synthesis of the membrane.

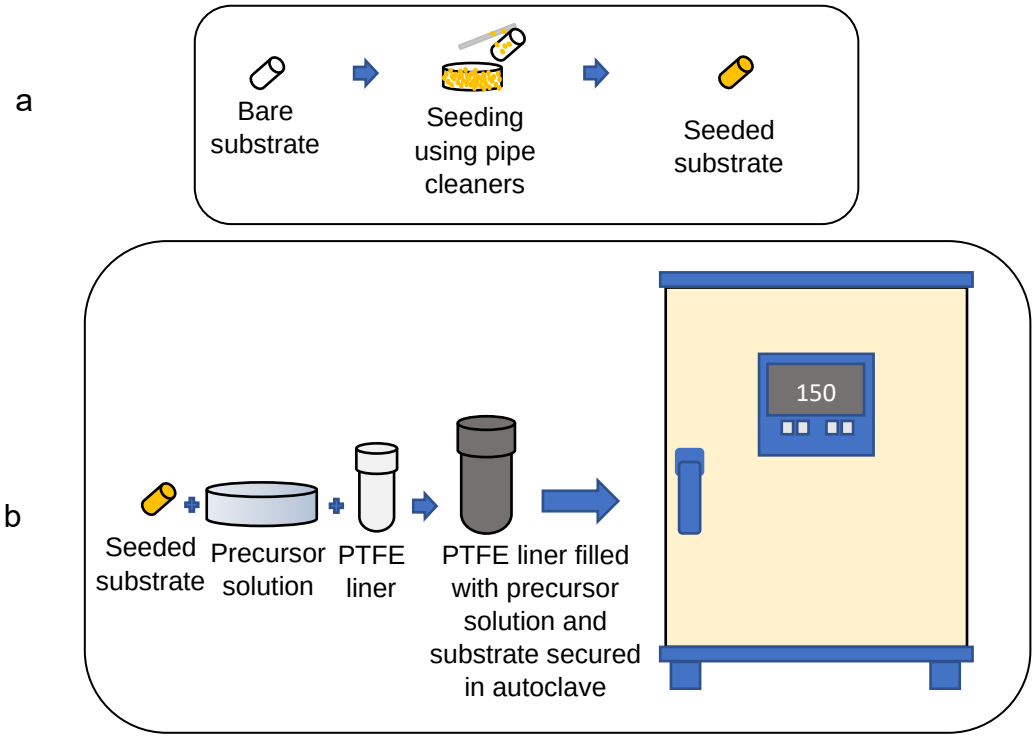


Figure 3- 2: Schematic of steps involved in seeding the substrate (a), and schematic of the main steps involved in synthesising the membrane (b). Each schematic moves left to right.

For the novel metal-linker isolation system, the substrate was filled with a fixed volume of 2 ml of either linker or metal solution using a pipette. Both ends of the substrate were plugged using Teflon® plugs secured in place using PTFE tape, wrapped tightly around the point, where plug and substrate meet. The linker or metal solution was transferred to the PARR digestion reaction vessel lined with the Teflon® liner. The novel metal-linker isolation study of isolated precursors gives the opportunity to study the reaction chemistry in a single step membrane synthesis at the surface of tubular substrate via changing precursor locations and mathematically calculating the respective fluxes across the substrate boundary (not been published by literature before). That reduces the concentration gradient difficulties in the lumen of tubular substrates as reported by literature (Marti et al., 2017, Kong et al., 2014, Brown et al., 2014b).

Two heating mechanisms were used in the batch system in this thesis, conventional and microwave heating. Temperatures were between 100-150 °C and 100 °C for the conventionally and the microwave heated systems, respectively. The synthesis times for batch syntheses were between 1-3 and 5-10 hours for the microwave and conventional heated systems, respectively.

The conventionally heated oven was heated to the desired temperature before preparing the reaction mixtures. The microwave setup and control parameters of the CEM microwave were saved as a dynamic programme before preparing the respective reaction mixtures.

After the reaction time, the Parr® reaction vessel (autoclave) was removed from the Heratherm™ (Thermoscientific) oven using heat resistant gloves and placed in a steel bucket. The bucket with reaction vessel was then transferred to the sink and quenched under running cold water for approximately 5 minutes and then left in the cold water for another 5 minutes. The reaction vessel was removed, placed on the bench, and dried with paper towels. The vessel was then transferred to the holding fixture secured in a vice, the screw cap to the vessel was unscrewed using the hook spanner. The Teflon® liner was removed and transferred to the fume cupboard. The synthesis solution was transferred to the centrifuge bottle and labelled with the respective experimental code.

For the microwave system, the CEM glass vial was removed from the CEM reaction vessel using heat resistant gloves and transferred to the fume cupboard where the membrane was placed in a petri-dish. The synthesis solution was transferred to a glass vial and labelled with the respective experimental code.

For the metal-linker isolation study, the substrate's solutions were also collected and transferred to a vial and labelled with the respective experimental code.

For both conventional and microwave heated systems, the membrane was rinsed under the tap for approximately 2 minutes and then rinsed with approximately 300 ml deionised water.

3.4 Continuous Spray Coating

The continuous system used for coating substrates was the cold spray coating of MOF slurry onto flat alumina substrates. The spray coating work involved the transfer of momentum between the high-speed air stream to the injected slurry. This advantage of the continuous coating mechanism is temperature sensitive MOFs can be coated onto substrates for separation purposes and large surface areas can be covered within minutes (Arslan et al., 2011), circumventing mass transfer limitations difficulties. There are no work on spray coating of tubular substrates even though tubular is favoured for commercialisation (section 2.5.2). However, preliminary work is needed on cold spray coating before the work can move onto coating of tubular substrates, which is the aim of this thesis.

The continuous coating of a non-porous flat alumina substrate with MOF suspensions involved the atomiser's novel design to maximise the deposition of MOFs onto the target substrate. The unheated air streams at room temperature help the MOF structures maintain stability when being sprayed.

Figure 3-3 shows a photo of the mechanical spray coating sessions. The syringe pump was used to release the HKUST-1 slurry at a predefined flow rate. The high-speed air streams were generated by the converging and diverging nozzle in the Dymet gun. The Dymet gun was attached to the vertical moving arm, that traversed at a speed of 20 mm/s. The Dymet 423 panel was positioned away from the coating area. The extraction fan system was turned on for all coating sessions. Two operators carried out the spray coating sessions.

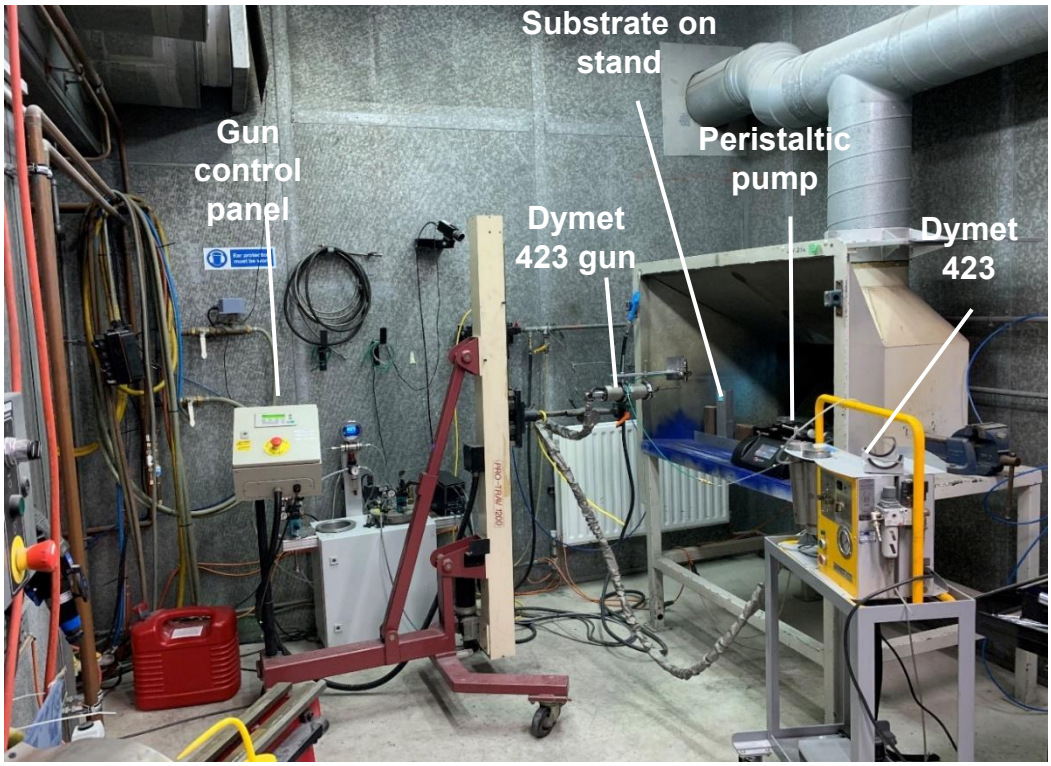


Figure 3-3: Spray work set up when coating flat substrates using MOF slurry.

Mechanical parameters were selected that impact the particles' velocity in the air stream, and deposition of particles onto the target substrate. The airstream pressure was varied between 2-6 bars, the distance between air nozzle and target substrate – stand of distance (SOD), 30-90 cm, number of passes, 2-12 passes, and angle of injection, 30-90 °. A high-speed camera was used to study the air and liquid streams' interaction, which allowed the investigation of the momentum transfer between the two streams. Figure 3-4 shows a schematic of the injection setup. By maximising momentum transfer from the air to liquid streams, overspray is minimised, reducing

slurry waste and maximising deposition onto the target substrate. The distance (d) of slurry release point from the Dymet gun nozzle and its height (h) above the airstream was related to the penetration level with liquid stream, which was assessed at various liquid flow rates.

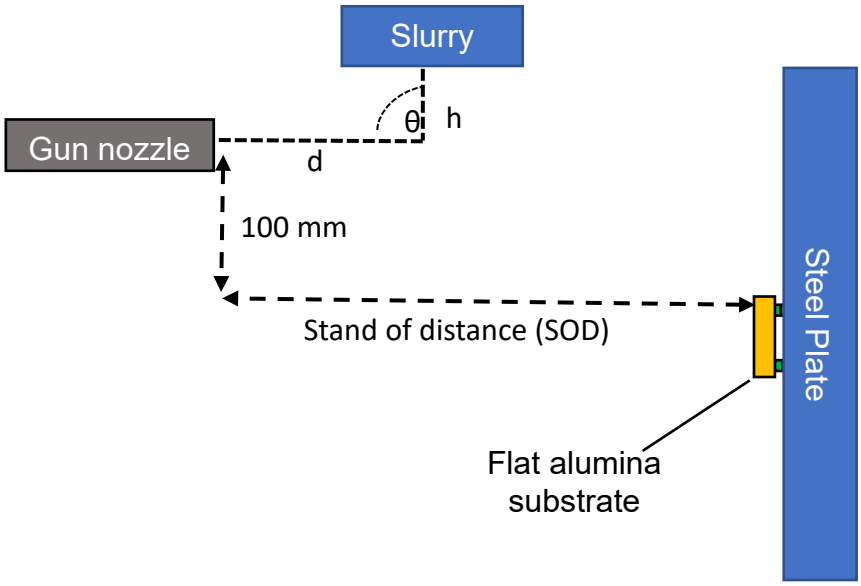


Figure 3-4: Schematic of the atomiser set up.

3.5 Characterisation of MOF seeds and membranes

3.5.1 X-ray Diffraction

X-ray Diffraction (XRD) method uses X-rays to identify a crystalline structure from its unique 'fingerprint' instead of its chemical composition. Metal organic frameworks are crystalline structures, making XRD an ideal characterisation tool to identify MOF structures. Hence, the XRD tool was used to analyse the crystals grown on the substrate surface and the bulk solution of membrane batches.

XRD data were collected by using the Bruker D8 Advance. A Cu K(α) beam of 1.54056 Å wavelength with a diffracted beam slit size of 0.12 mm. Both membranes and powders scanned in a 2θ range between 3 - 20 ° with a step size of 0.04 ° and a step time of 16 seconds.

The X-rays are emitted from the X-ray tube under vacuum that is directed out in a controlled manner via windows directing the X-rays out towards the sample holder. The

X-rays are generated in the tube made up of two electrodes across which a high voltage is maintained. The high voltage draws high-speed electrons from the cathode to the anode. The electrons with sufficient energy from the cathode that impact the anode causes an electron from the inner shell to vacate and that now-vacated seat are filled from an electron from the outer shell. The change in the outer electron's seating moving to the inner shell is accompanied with a release of energy, and this is released in the form of an X-ray. This emitted X-ray is then directed out towards the sample (Clark, 2020, Leng, 2013, Corporation, 2020).

The interaction of the X-rays is between the electrons of the atoms that make up the crystal structure. The crystallographic planes are created by atoms being neatly arranged in a regular manner at well-defined distances. The X-rays then measure this unique distance between the regularly arranged atoms. When X-rays penetrate the crystalline structure, scattering occurs, and on the satisfaction of Braggs law (equation 3.1) constructive interference and diffraction occurs. In short, the Braggs law states the scattered waves incidence and scattered sides; combined must travel whole wavelengths through the material to achieve constructive interference. The detector then processes the X-ray signal and converts it to a count rate (s^{-1}) that is then recorded onto a computer (Clark, 2020, Leng, 2013, Corporation, 2020, He, 2009).

$$n\lambda = 2d\,sin\theta \quad \textbf{(Equation 3- 1)}$$

Figure 3-5 shows a schematic of how the X-rays are diffracted through the crystallographic planes at specified angles upon satisfaction of the Braggs law.

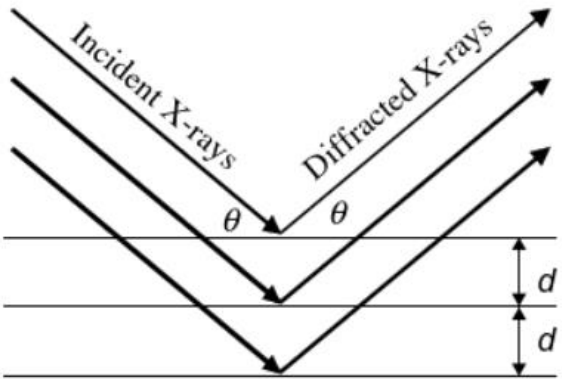


Figure 3- 5: Schematic showing the incident and reflected X-rays making an angle of θ symmetrical to the crystal planes' normal (He, 2009). Reproduced with permission from He et al. 2009.

An example of identifying crystalline materials can be the crystalline structure zeolitic imidazole framework-8 (ZIF-8). Initially beginning with a cubic morphology and then evolving into its equilibrium rhombic shape. This evolution of shape from a cube is achieved by the different growth rates of the respective crystal faces. Figures 3-6 shows a schematic of the cubic crystal evolving into the equilibrium rhombic shape. (Schejn et al., 2014, Bux et al., 2011).

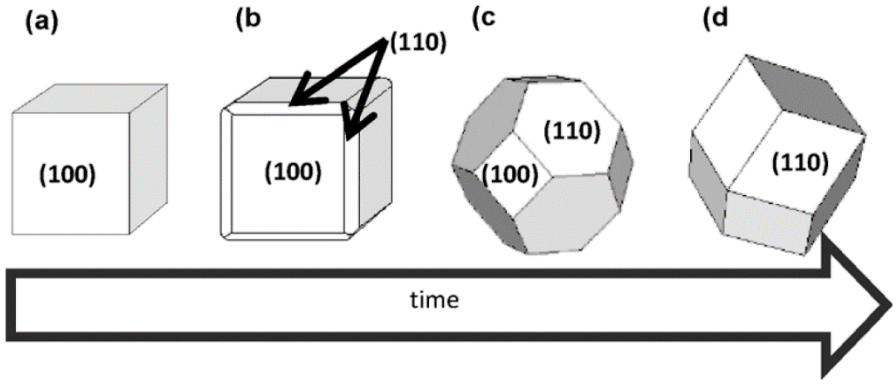


Figure 3- 6: Illustrated schematic of crystal morphology of ZIF-8 evolving, initially starting as a cube (a), a cube with truncated edges (b), rhombic with truncated corners (c) and then rhombic dodecahedron (d). (Schejn et al., 2014). Reproduced with permission from Schejn et al. 2014.

Figure 3-7 shows the XRD pattern of bulk ZIF-8 powder from this thesis derived from zinc nitrate hexahydrate. Each peak reflects a crystallographic plane of the ZIF-8 crystal (Kida et al., 2013b).

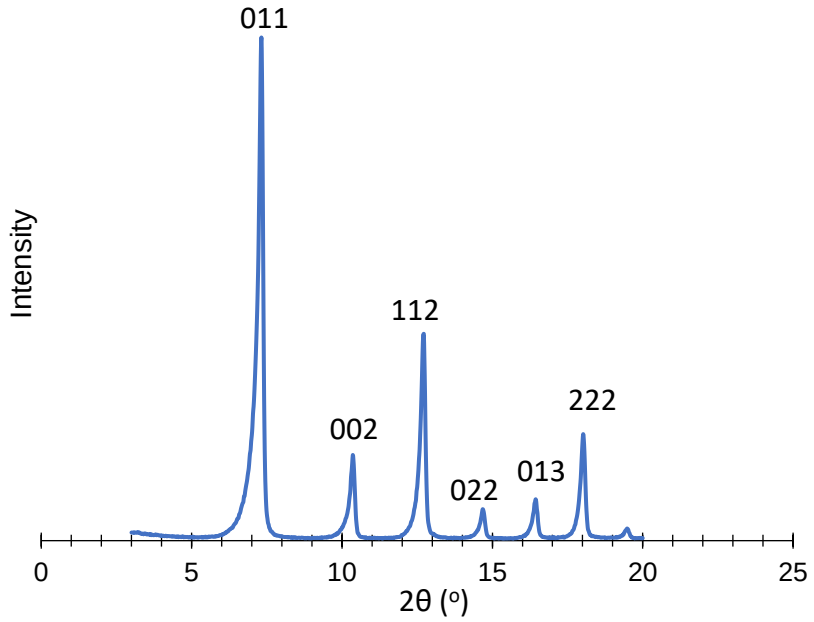


Figure 3- 7: XRD pattern of ZIF-8, peaks labelled with corresponding crystallographic planes represented by corresponding peaks.

3.5.2 Scanning Electron Microscopy

Scanning electron microscopy is used by many researchers working with membranes to allow for a more robust judgement of the level of success of the growth achieved on the substrate surface. In literature reports show SEM images of the surface and cross section to identify microstructure defects and determine membrane thicknesses, respectively. Hence, in this thesis, both the surface and cross sectional images were studied, with each respective image taken from different samples, obtained from different locations of the membrane that was characterised for a more critical analysis of the membrane growth. In some instances, SEM measurements were repeated to clarify the nature of the growth and the second samples were taken randomly. When repeated images were taken from the same membrane but a different area this was clearly stated in the discussion of the results for the respective membrane.

The microstructure and the continuity of MOF growth on the substrates inform the following stages of the experimental variables to be changed. In this thesis, the Philipps XL30 FEG ESEM and JEOL 6490 LV electron microscope were used for both surface and cross-sectional analysis of coated substrates with a 10 – 20 keV beam voltage. Before analyses, samples were coated with a platinum layer using the Sputter Coater SC7640 (Quorum Technology) at 2.2 voltage and 0.8 mA. The coating was needed to make the sample conductive, preventing charging when the electrons scan the sample surface.

To operate characterisation equipment more efficiently and to better prepare samples, it is essential to understand the theories behind them. The fundamental operation of SEM is based on the interaction of electrons with the sample. Emitted electrons generate the beam of electrons from the gun passing through a series of lenses. The two condenser lenses reduce the electron beam's cross over diameter, and the objective lens focuses the beam as a probe (Fig. 3-8). The beam then scans the surface systematically in a rectangular raster. The rectangular raster is created by the pivotal movement achieved when the two pairs of electromagnetic coils deflect the beam. The detector then collects and amplifies the emitted electrons from the specimen being scanned, from which a topographical image is created (Australia, 2020, Leng, 2013). Figure 3-8 below provides a schematic of the description of the scanning electron microscopy.

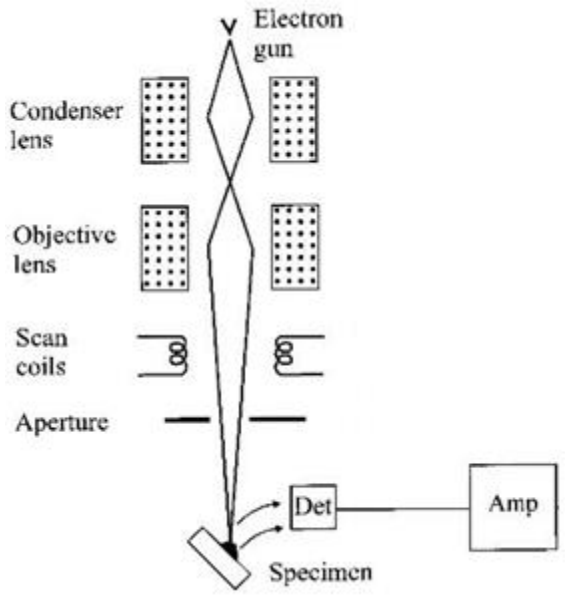


Figure 3- 8: Schematic showing the scanning electron microscopy's main components (Goodhew et al., 2000). Modified with permission from Goodhew et al. 2000.

The nature of emitted electrons from the sample depends on how they interact with the atoms that make up the sample. Electrons can be deflected by atoms of the sample, elastic scattering, and are called backscattered electrons (BSEs). The other interaction is where the electrons are ejected from the specimen atoms and are referred to as secondary electrons (SEs), inelastic scattering. With the BSEs and SEs providing topographic and elemental composition contrast, respectively. The SEs can provide

elemental analysis since the emitted X-ray energy and the SEs are unique to the elemental atoms from which they are emitted (Ul-Hamid, 2018, Leng, 2013).

Figure 3-9 shows a schematic of the BSEs, SEs, and X-rays' escape zone from the specimen volume at different depths. The SEs can only escape from the volume near the surface, whereas the BSEs can escape from a greater depth since their energy is un-par the incident electron (Leng, 2013).

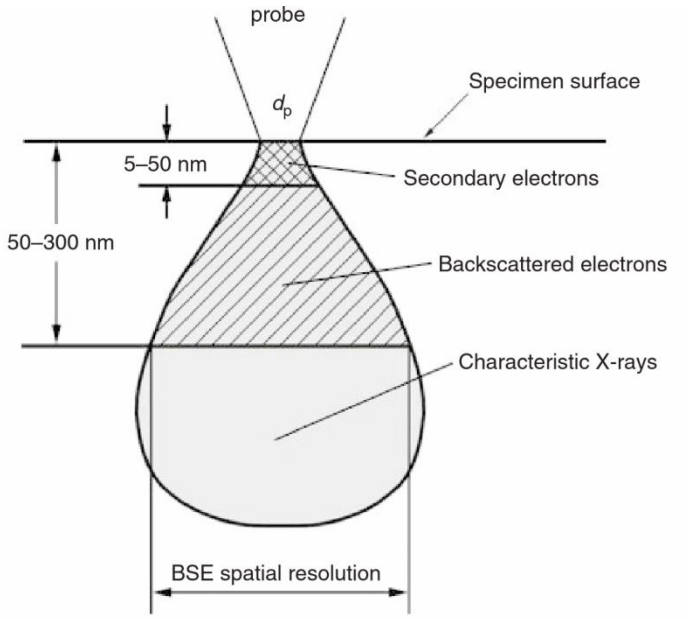


Figure 3- 9: Schematic of the electrons' interaction zone from the probe and sample atoms beneath the specimen surface (Leng, 2013). Reproduced with permission from Leng et al. 2013.

Figure 3-10 shows surface and cross-section SEM images of the ZIF-8 membrane on a tubular alumina substrate.

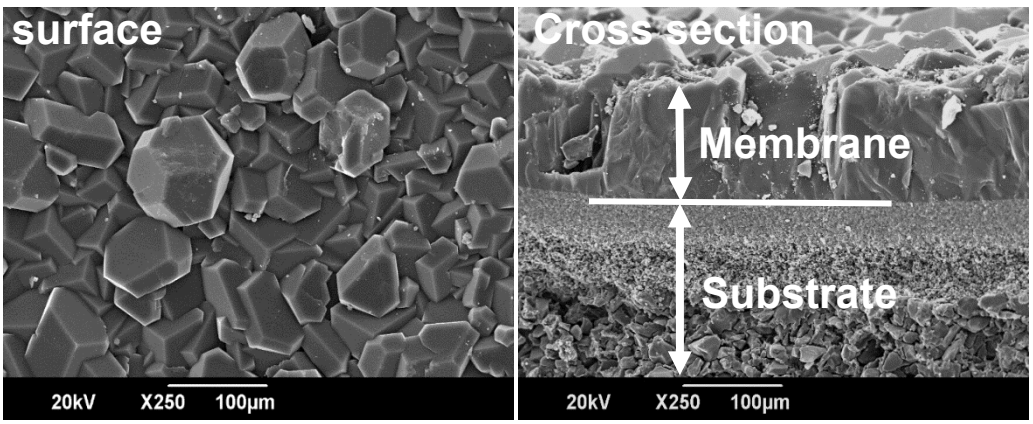


Figure 3- 10: Surface and cross-section images of typical cubic and rhombic crystals of ZIF-8 membrane on the alumina substrate.

The software ImageJ® was used to measure crystal sizes, membrane thickness, and surface coverage. With the evolution of MOF structures, there are various growth stages from nucleation, crystal formation, and structure evolution. For example, for ZIF-8, there are three stages of growth reflected with crystals taking the forms of a sphere at nucleation, a cube at the initial stage of crystallisation and a final rhombic shape at equilibrium (Venna et al., 2010). Figure 3-11 shows a schematic of the three shapes and the red arrows indicating the start and endpoints from where the 3D shapes were measured when using ImageJ®. One side length was taken for a cube, the sphere's diameter, and the most extended length of the rhombic crystal.

An approximate 100 measurements were taken per membrane, though this may not always be possible because of the intergrowth. The surface image in Fig. 3-12 can be taken as an example; the intergrowth can make it challenging to decipher individual crystal entities, hence achieving the target measurement of 100 may not always be possible even when using multiple SEM images from different regions of the membrane sample.

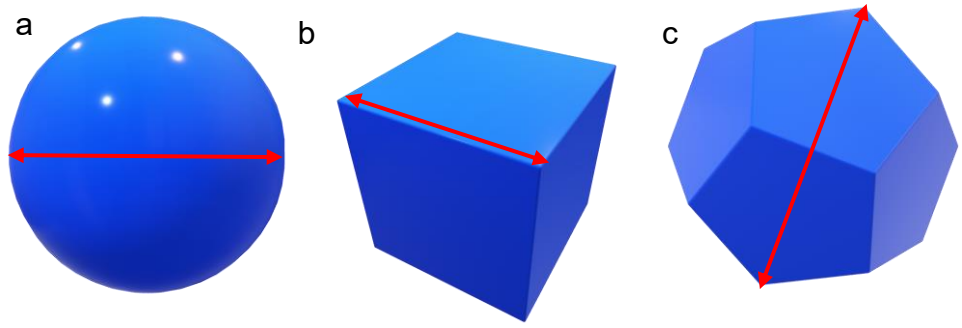


Figure 3- 11: Schematic of 3D shapes, sphere (a), cube (b) and rhombic (c). The red arrows reflect the points from which distance the sizes were measured.

Figure 3-12 shows a typical surface image of the alumina substrate with ZIF-8 crystals with typical cubic and rhombic morphology. Red arrows reflect the technique depicted in Fig. 3-10 when measuring crystal size.

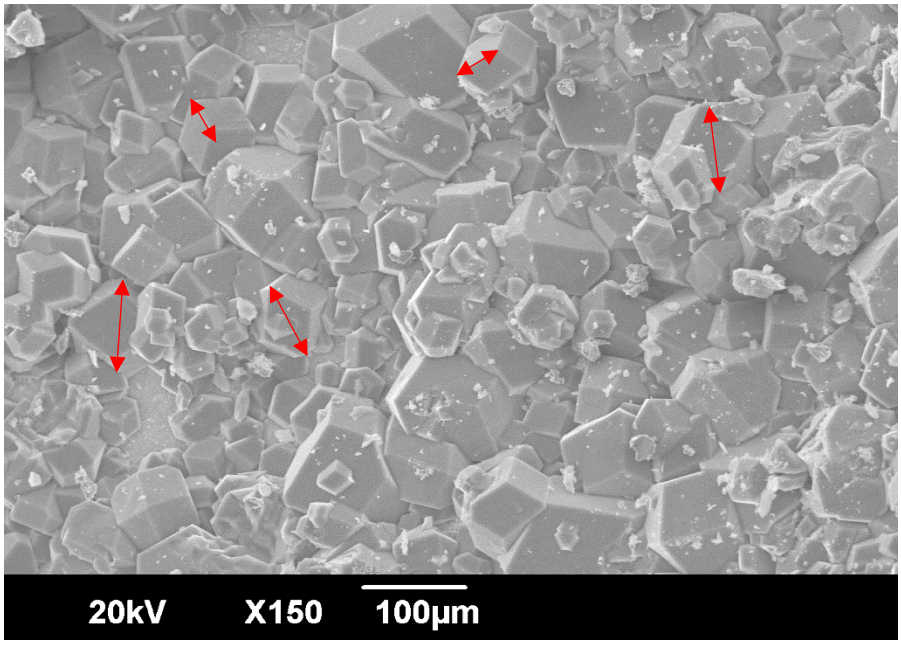


Figure 3- 12: The alumina substrate's surface image with ZIF-8 crystal growth of typical cubic and rhombic.

Figure 3-13 shows typical SEM surface images with ZIF-8 crystal surface growth. Figure 3-13a has little surface growth and the crystals 'painted' over, the respective area the crystals covered were then measured using ImageJ®, and the percentile of surface growth calculated by dividing by the total surface area (Equation 3-2). Figure 3-13b has dense growth, so the regions where there is no growth was 'painted' over and measured, then respective growth area and respective percentile calculated. In this thesis the surface growth was measured for two different sites per membrane – where possible, and a range given of the percentile growth.

$$\frac{Surface\ area\ with\ crystal\ growth}{Total\ substrate\ area} \times 100\ \%\ \textbf{(Equation 3- 2)}$$

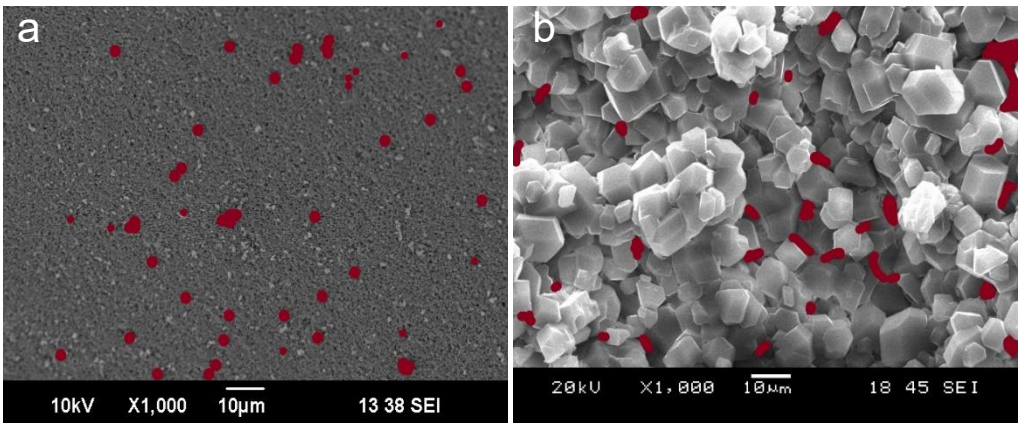


Figure 3- 13: Surface images of substrates with varied ZIF-8 crystal growth, sparse (a) and dense growth (b).

3.5.3 Energy Dispersive Spectroscopy (EDS)

Energy dispersive spectroscopy identifies elements that make up the material being scanned by the beam of electrons. The emittance makes the identification of X-ray energy that is unique to the element that has produced it. The EDS microanalysis collects the emitted X-rays, sorts, and plots them by energy (Leng, 2013) (PhotoMetrics, 2020). Hence, ZIF-8 growth can be verified via elements Zn etc., especially for thinner films where XRD cannot detect the ZIF-8 characteristic peaks. Figure 3-14 shows a typical EDS plot of the alumina substrate's elemental analysis coated with ZIF-8, data collected from the results produced from this thesis. Each peak corresponds to the X-ray's characteristic energy of the respective element detected in the sample (Dibenedetto and Aresta, 2013).

The X-ray is emitted by the incoming electron knocking out one of the atoms electrons from its original position. The atom's now-vacated position results in the atom becoming ionised (an excited state), the atom returns to its normal state by filling the vacated position with an electron from the outer shell. The energy difference between the outer-shell and inner-shell electrons generates the X-ray with a unique energy characteristic to the atom from which it is emitted (Fig. 3-14). For example, K and L shell electrons' energy difference has an energy difference of Kα (Leng, 2013).

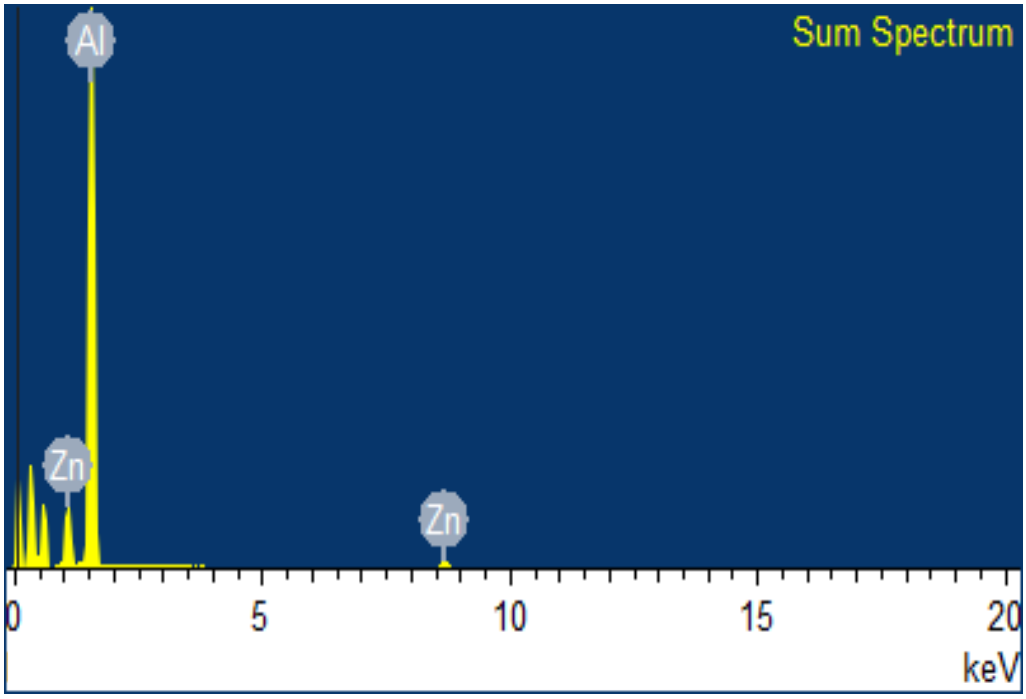


Figure 3- 14: EDS spectrum recorded by SEM of ZIF-8 crystal growth on an alumina substrate. The sample composed of Zn, Al and O.

When using X-rays for EDS analysis, it is helpful to understand which X-ray line is the strongest for analysing the individual element (Figure 3-14). The K_α series lines are the most intense, seven to eight times more intense than K_β. However, as the atomic number of the element increases, electrons' displacement becomes more difficult, requiring more energy to displace the K-shell electron. For example, elements with a 50 or greater molecular mass need incoming electrons of more than 25 keV to excite the K lines and need 75 keV to produce K X-rays. Hence, where electron energies of 30 keV are only available at the user's disposal, other characteristic energies are needed. L series is far stronger than the M lines and suitable for heavier atoms (Goodhew et al., 2000). In conclusion, when analysing samples with EDS, it is important to understand that X-ray lines for some samples may not be suitable for the other samples, which must be considered when operating the instrument.

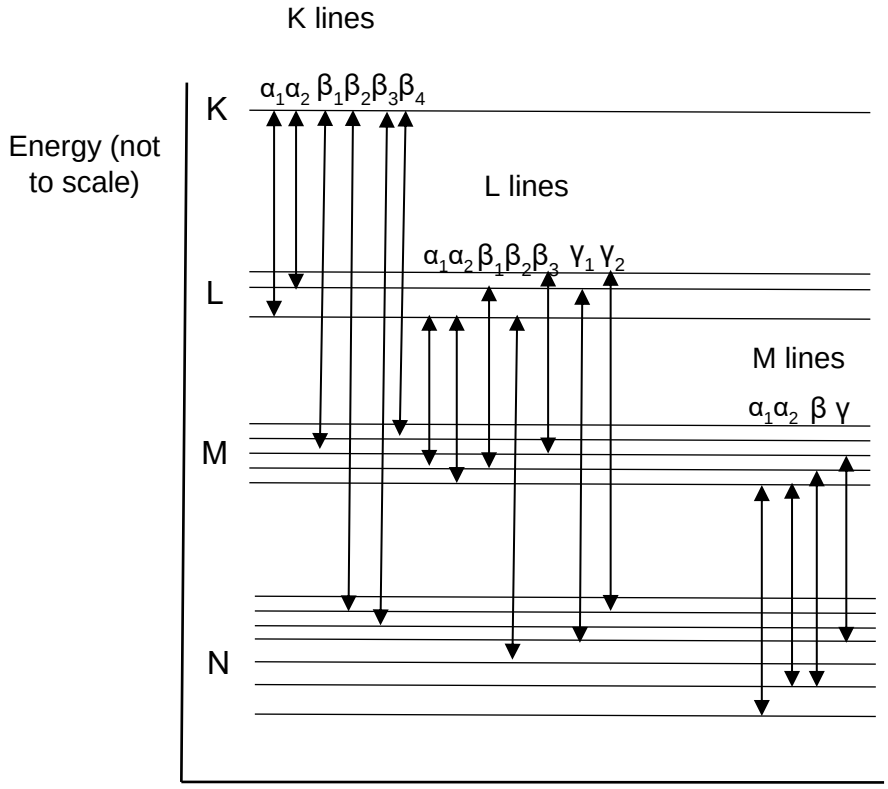


Figure 3- 15: Transitions of the K, L, M and N shells of an atom which lead to the X-ray lines indicated. (Goodhew et al., 2000). Reproduced with permission.

3.5.4 Gas separation system

Single gas CO_2 and CH_4 permeances were measured at room temperature in a gas separation system built by the University of Nottingham L4 workshop technicians. Figure 3-16shows a photo of the gas separation system. Digital equipment (and software) was supplied from Bronkhurst and piping and relief valves from Swagelok.

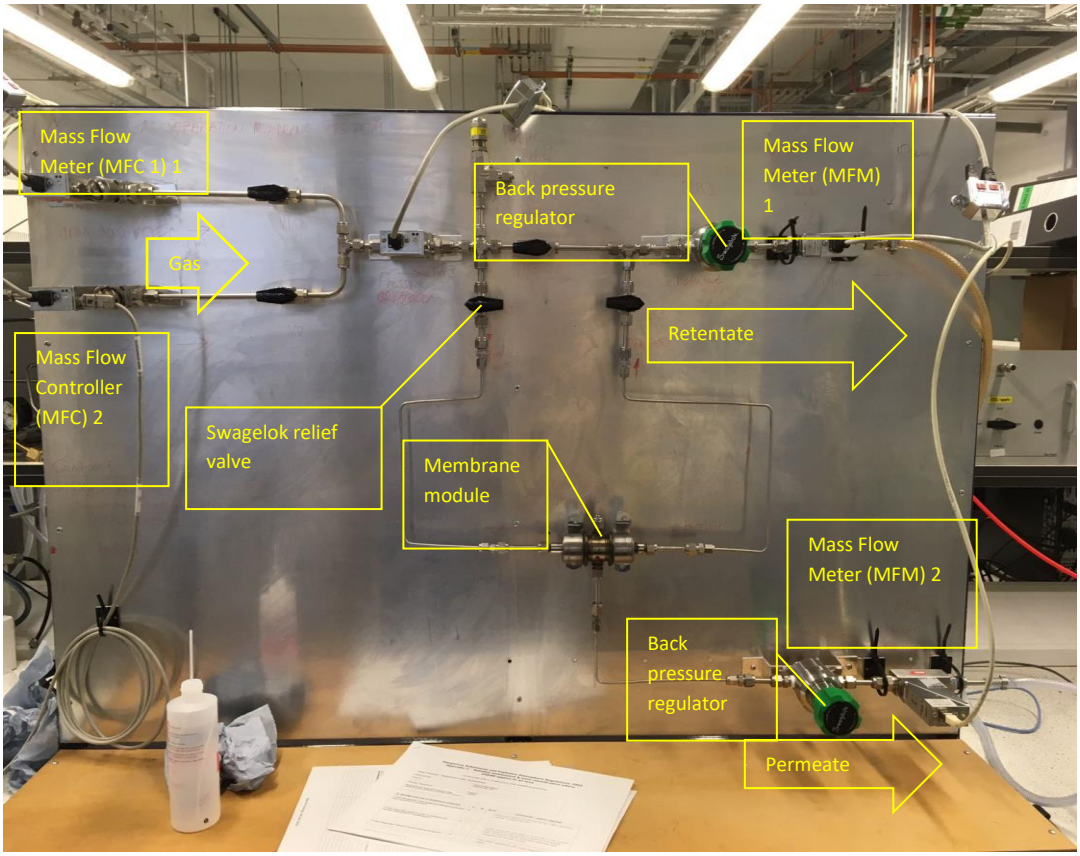


Figure 3- 16: Gas separation system with labelled components.

Single gas permeance performance of ZIF-8 membranes was measured using CH_4 and CO_2 using a pressure difference of 1 bar, while the feed and permeate pressures was controlled with back pressure regulators. The feed flow rates were between 0-150 mL/min for CO_2 and 0-550 mL/min for CH_4 controlled by mass flow controllers, and the permeates fluxes were measured with mass flow meters. Airtight seals were created around the membranes using silicone O-rings when secured into the stainless-steel membrane module.

4. Batch synthesis of ZIF-8 membranes using mixed precursors under conventional heating

4.1 Introduction

A variety of ZIFs have been studied for the heterogenous growth onto substrates for the application of gas separations. Recently, ZIF-8 structure has been the most studied of all the ZIFs with a focus on gas separations because of its ideal pore structure and naturally affinity to the natural gas contaminant, CO_2. However, there are continued challenges with the heterogenous growth of ZIF-8 because of its weak interactions with substrate surfaces. This has led to considerable interest from the research community. Studies in literature comment on the challenges with repeatability and reproducibility with the heterogenous growth of ZIF-8 crystals on substrates, especially with tubular substrates.

This chapter aims to investigate the heterogeneous growth in the batch system using conventional heating. The parameters controlling the microstructure of ZIF-8 such as conjugate bases, metal concentration, linker/metal ratio, and synthesis time, were studied to determine the effects that they caused on the heterogeneous growth of ZIF-8 onto the tubular substrates.

4.2 Experimental procedure

4.2.1 Substrate preparation

Tubular alumina substrates (11 mm OD, 7 mm ID Inopor GMbH) with 200 nm pores were cut into 2 and 6 cm pieces. Before membrane synthesis the tubes were cleaned in boiling deionised water at 100 °C for 2 hours and then dried at 100 °C for 2 hours.

To study the effect of seeding on membrane growth, both seeded and unseeded substrates were used to synthesise membranes. The substrates were seeded by rubbing ZIF-8 crystals with average size of 131 nm (derived from zinc nitrate hexahydrate) for ~ 10 min using pipe cleaners to provide nucleation sites for the growth of membrane onto the substrate surface.

4.2.2 Seed synthesis

The tubular supports were first seeded using ZIF-8 crystals to provide nucleation sites for the growth of membrane onto the support. Seeds were produced by seed synthesis with linker/metal ratio of 8.

Seeds were synthesized using the methodology reported in literature (Venna and Carreon, 2009). Typically, 0.3 g of zinc nitrate hexahydrate was added to 14 ml methanol, which was then placed on a stirrer until all dissolved. Then 0.66 g of 2-methylimidazole was added to 14 ml methanol, which was then placed on a stirrer until all dissolved. 2-methylimidazole solution was then added to the metal solution using a pipette whilst stirring the solution vigorously for 5 minutes. The final MOF solution was transferred to a Parr® stainless steel vessel with Teflon® liner and placed in a Heratherm™ (Thermoscientific) oven at 150 °C for 5 hours. After quenching the reaction vessel in cold water, the seeds were centrifuged at 4,000 rpm for 20 minutes twice. Between each step, the seeds were washed with methanol and then then dried at 100°C overnight.

4.2.3 Membrane synthesis using mixed precursors.

The ZIF-8 membranes studied in this chapter are predominantly synthesised using zinc acetate dihydrate and for one cycle, if stated otherwise. The precursor solutions were prepared by dissolving either zinc acetate dihydrate or zinc nitrate hexahydrate and 2-methylimidazole in 16 ml methanol, separately, on a magnetic stirrer for ~ 10 minutes or until solute was dissolved. For the 50:50 metal salt dissociation studies each respective metal salt was prepared separately in 8 ml solvent and once the solute was dissolved then the metal solutions were combined into one beaker. The linker solution was added to the metal solution drop-wise while stirring. After 5 minutes mixing, the synthesis solution was transferred to a 45 ml Parr® reaction vessel with a Teflon® liner. The sealed vessel was then placed in a Heratherm™ (Thermoscientific) oven at 150 °C for 5 hours. On removal, the reaction vessel was quenched under running water for 5 minutes and then left in the cooling water for another 5 minutes. Each membrane was rinsed under the tap water for ~ 2 minutes and then rinsed with ~ 300 ml deionised water. The membranes were then dried into the oven at 100 °C for 2 hours. Table 4-1 summarises metal salts, precursors ratios, concentrations and synthesis times investigated.

Table 4- 1: Metal salts, concentrations, linker/metal ratio, seeding and synthesis time used for batch synthesis.

Metal salt	Linker/metal ratio	Metal concentration (mM)	Synthesis time	Seeded (Yes/No)
Zinc nitrate hexahydrate	8	36[1]	5	Yes
Zinc acetate dihydrate and Zinc nitrate hexahydrate (50:50 molar ratio)	8	36 144	5	Yes
Zinc acetate dihydrate	8	36[2]	5	Yes/No
		72 144 288		Yes
	8	36 144	10	Yes
	2	72 288	5	Yes

[1] Synthesised one and two cycle membrane.
[2] Synthesised one and two cycle membrane.

4.2.5 Particle size and surface area measurement

Crystal sizes and surface area were estimated using ImageJ® software. Approximately 100 crystals boundaries were identified and measured from up to three SEM images taken per membrane synthesised where possible. The results were then presented in histograms for interpretation (Appendix). The surface area was measured from two different locations per membrane where possible and the surface area covered with crystal growth presented as a percentile range between the locations. The surface area results are tabulated for (Conclusion).

4.3 Results

4.3.1 Seed Synthesis

Figure 4-2 shows SEM images of rhombic seed crystals synthesised. Seeds were a combination of crystals produced by seed synthesis and collected from the bottom of the reaction vessel after membrane synthesis (36 mM bulk solutions). Average seed size was estimated as 131 nm (Fig 4-1) collected via centrifuge. The crystal sizes were 3 times larger than the reported 60 nm by Venna et al. at the linker/metal ratio of 8. The larger crystal size indicated by the SEM images maybe due to agglomeration.

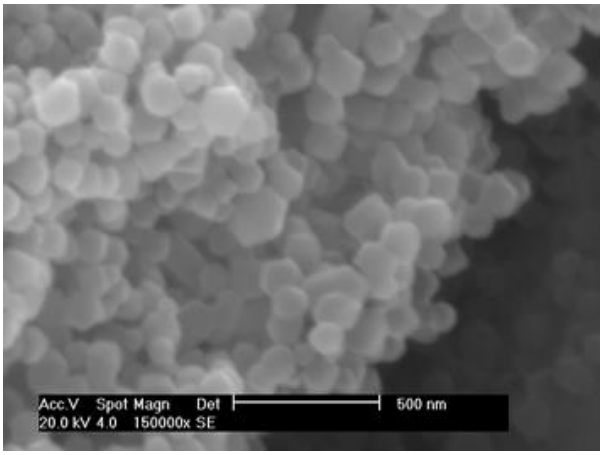


Figure 4- 1: Scanning electron microscopy images of ZIF-8 seed crystals collected via centrifuge, synthesised with the linker/metal ratio 8 and metal concentration of 36 mM.

X-ray diffraction patterns of crystals collected from seed and after membrane synthesis confirm the formation of ZIF-8 structure as the characteristic peaks at 7.36, 10.41, 12.76 and 18.09 (°) were observed (Fig. 4-2).

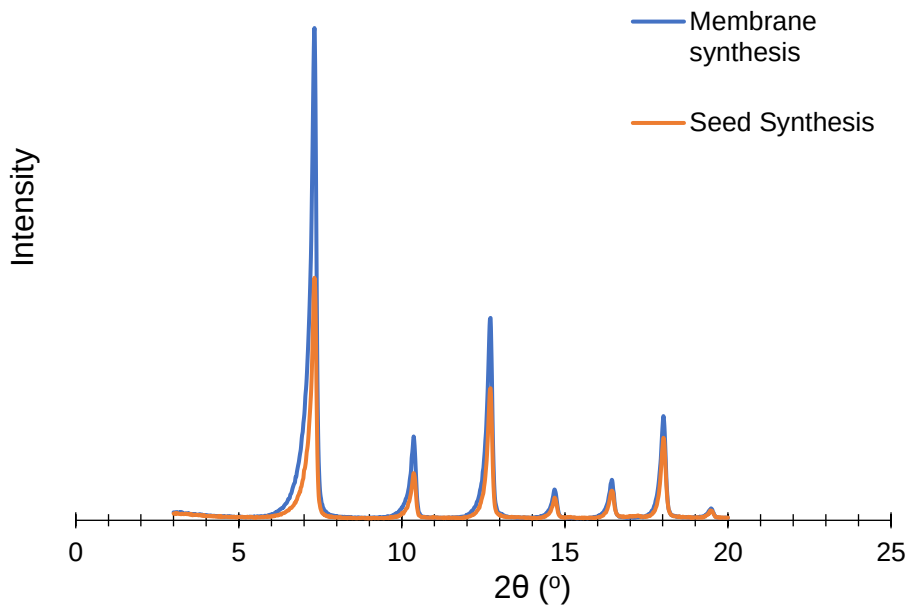


Figure 4- 2: X-ray diffraction patterns of ZIF-8 seeds and of seeds collected from bulk solution after membrane synthesis.

4.3.2 Membrane synthesis using mixed precursors.

Numerous studies reported surface modification techniques in order to induce agents to promote the attachment of the MOF crystals. Reports have also highlighted that the surface modification step is system unique i.e. depends on metal salt, substrate geometry, and synthesis conditions. Therefore, the role of seeding and its effects on heterogenous nucleation for this system were explored. Figure 4-3 shows the surface and cross sectional images (not of same scale) of the bare substrate, and membranes synthesised with and without seeds with linker/metal ratio of 8 and metal concentration of 36 mM at 150 °C for 5 hours. The surface image of the unseeded substrates shows that only several crystals were grown with non-typical ZIF-8 morphology. The cross sectional image of another sample of the unseeded substrate taken elsewhere from the same substrate indicates a layer of deposition similar to unreacted metal oxide rather than crystals with defined morphology. In contrast, both surface and cross sectional SEM images of the seeded substrates exhibit spherical and cubic crystals, suggesting the spherical and cubic shapes in the metastable and initial stage of evolution phases, respectively. The larger non-typical ZIF-8 particles structures suggest unreacted precursors. This may indicate seeded growth helps promote nucleation on the substrate, supporting a more robust heterogeneous growth. However, the growth is not

dense and continuous that will lead to the gas molecules passing through the gaps in the microstructure, making this a poor candidate for gas separation. This result was not expected for a seeded membrane. This may indicate the seeds may have not been uniformly deposited to accommodate dense and continuous growth, and those that were deposited may later have detached. This may indicate that a more robust methodology of seed deposition is needed, however, several previous studies reported successful membrane synthesis success using physical deposition of seeds (Venna and Carreon, 2009, Ge et al., 2012, Tao et al., 2013b), hence all substrates were seeded systematically using pipe cleaners. In addition, there are other factors to consider when synthesizing membranes such as two competing nucleating mechanisms, homogenous and heterogenous nucleation where nucleation occurs in the bulk solution and on the substrate surface, respectively (Tuninetti et al., 2015). Therefore, it is viable to investigate the role of increased precursor concentrations to help compensate for the ions spent in the homogenous nucleation and thus impact on the final membrane microstructure.

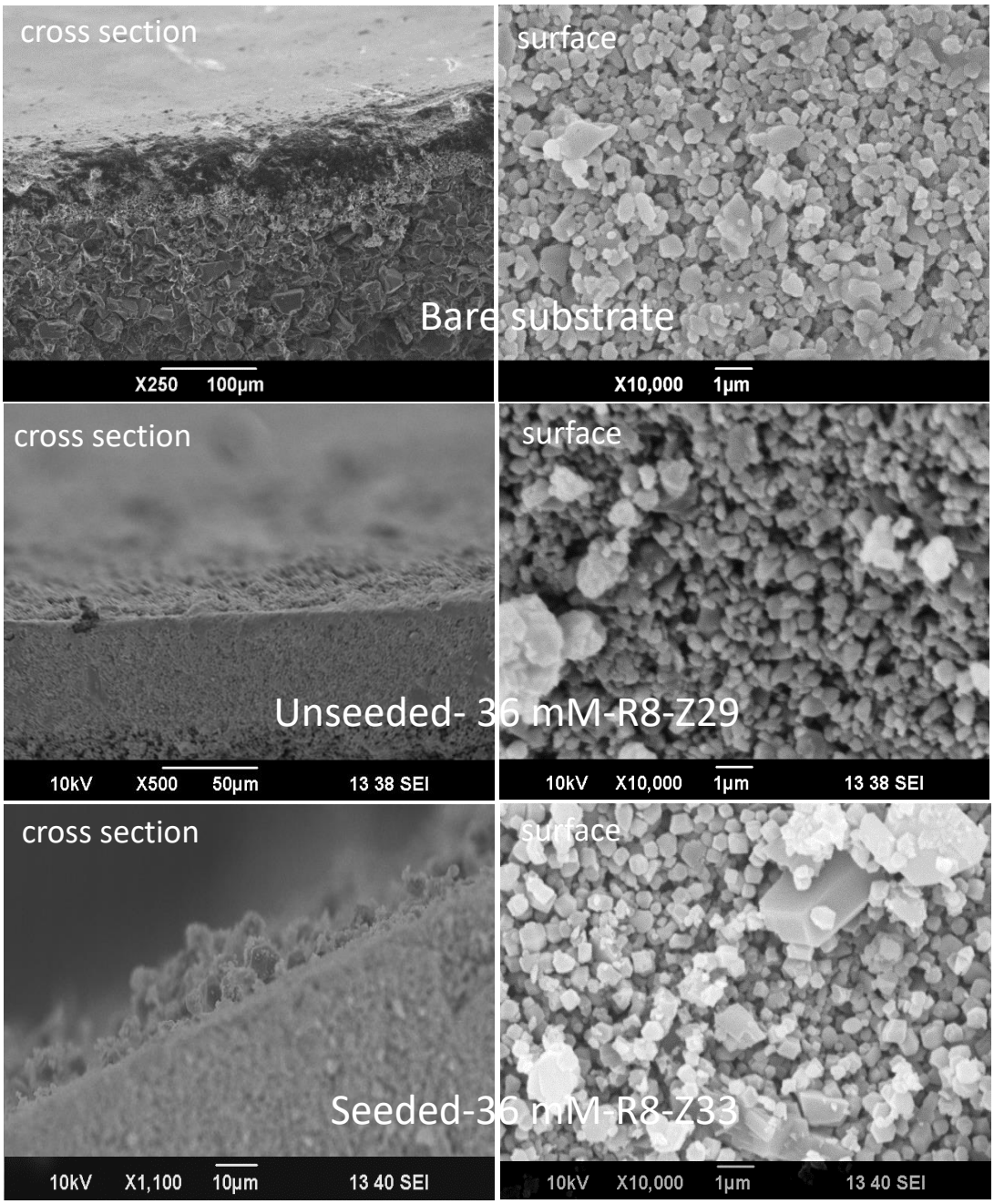


Figure 4- 3: Cross sectional and surface SEM images of uncoated bare alumina substrate, unseeded and seeded membranes synthesised at 150 °C for 5 hours with a linker/metal ratio of 8 and metal concentration of 36 mM.

Figure 4-4 shows the XRD patterns of the seeded and unseeded membranes synthesised with linker/metal ratio of 8 and metal concentration of 36 mM at 150 °C for 5 hours. Surprisingly, the unseeded piece shows the characteristic peaks of ZIF-8, confirming the presence of ZIF-8 crystals. However, this does not match with the growth seen in the surface and cross sectional SEM images of the unseeded membrane (Fig. 4-3). This may suggest that the crystal growth is not achieved throughout the substrate surface. Therefore, randomly selected substrate pieces for

analyses show conflicting results, reinforcing the importance of analysing both SEM and XRD results of coated substrates together. In addition, the unseeded substate used for XRD measurement may have a couple of big crystals, that are sufficient to obtain characteristic peaks. The XRD of the seeded substrate shows all the characteristic peaks of ZIF-8, indicating that the sample characterised for XRD to have similar growth, shown in SEM images (Figure 4-3) for another piece of substrate. In contrast to unseeded substrate, this may suggest that seeds deposited act as sites of nucleation and help to promote a similar level of heterogenous growth throughout the substrate surface. In conclusion, the XRD and SEM results indicate that when the surface of the substrate has favourable moieties on its surface it can reduce the time for heterogenous nucleation to initiate thereby helping to promote a more continuous growth, rather than growth initiating from precursors directly interacting with the surface of the substrate without any deposited moieties. Where the delayed heterogenous growth (Tuninetti et al., 2015) leads to less dense growth compared to using a modified substrate surface, as the experimental results (Figures 4-3 and 4-4) imply. Therefore, in this study, membranes were synthesised using seeded substrates.

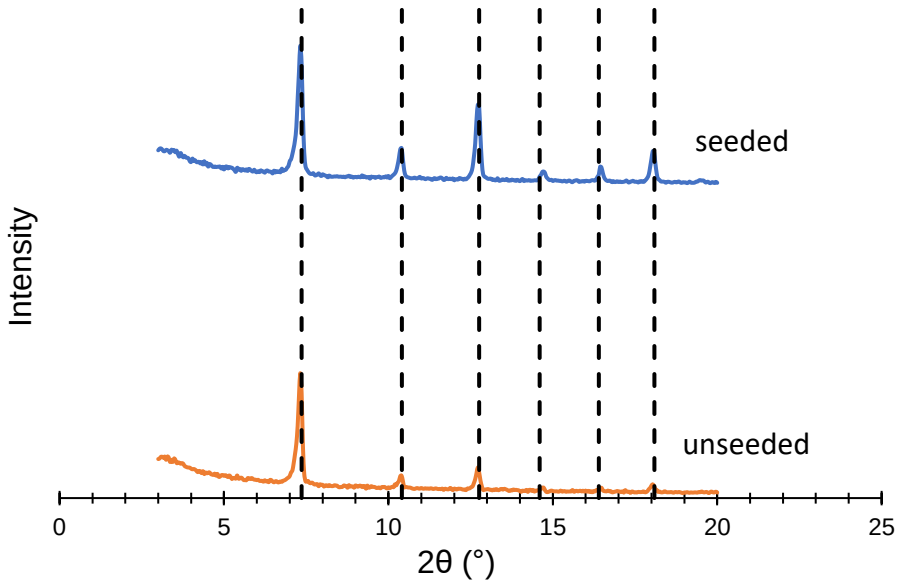


Figure 4- 4: XRD patterns of seeded and unseeded membranes synthesised at 150 °C for 5 hours at linker/metal ratio of 8 and metal concentration of 36 mM. The dashed lines refer to the positions of the most prominent characteristic peaks of ZIF-8.

As well as a requirement for a thin and well intergrown ZIF-8 membrane for high permeances and selectivities, crystal size and shape are also of importance since control grain size and control permeation of flux (Tanaka et al., 2014a, Isaeva et al.,

2015). Tanaka et al. reported on the role of precursors concentration and ratio on membrane microstructure (Tanaka et al., 2014a), however, they used water. Figure 4-5 shows the surface images of the membranes synthesised using linker/metal ratio of 8 and metal concentrations of 36-288 mM. The surface images exhibit crystal sizes in the range of 0.29 – 16.3 µm for the concentrations studied. Crystals synthesised were in various shapes and some degree of agglomeration was identified for crystals synthesised at all concentrations. At the metal concentration of 36 mM, spherical crystals were observed. This may indicate that the metastable phase formed, prior to the initial crystallisation phase of ZIF-8, as reported by Venna et al. and Schejn et al. (Schejn et al., 2014, Venna et al., 2010). When metal concentration was increased to 288 mM, the crystals were evolved to rhombic shapes with sharp edges - ZIF-8's equilibrium state. This is highly likely since higher metal concentrations can generate more nuclei for longer during the nucleation. Therefore, there may be more thermodynamically unstable nuclei in the system once the nucleation is completed. To reduce the energy of the system, the interfacial surface area must be reduced. Hence, smaller crystals disappear at the expense of growing into larger crystals on the substrate surface. Similar findings were reported on heterogeneous systems (membrane synthesis), where the intercrystalline gaps between the evolving crystals diminished by the smaller crystals *via* Ostwald ripening (Kwon et al., 2016b). Therefore, the crystals are bigger, and the crystal size range (4.5-16.3 µm) is wider for 288 mM metal concentration. It is evident, the metal concentration controls the microstructure of the obtained membrane indicating the metal concentration will impact the membrane performance. Although Tanaka et al. did not investigate the role of metal concentration role on membrane microstructure, they investigated impact of the linker/metal ratio and metal salts on membrane microstructure. Tanaka et al. reported that membranes derived from zinc acetate and at smaller linker/metal ratios (ratio of 30) enhanced the membrane microstructures since the ideal selectivities increased for several gas pairs: H_2/N_2, H_2/CH_4, H_2/C_3H_6, and H_2/C_3H_8. Therefore, when synthesising membranes it is viable to work in a range of precursors concentration and ratio – the range must be investigated since is dependent on system conditions. For example the minimum linker/metal ratio is 1.5 with a catalyst (Lai et al., 2016c, Bux et al., 2011, Bux et al., 2009) whilst is 2 without catalyst in organic solutions (Lu et al., 2012, Kida et al., 2013b), and 20 when using water (Kida et al., 2013b). In conclusion, a range between 36-288 mM and 2-8 is used for metal concentration and linker/metal ratio, respectively, for the batch system in this chapter. The crystal sizes were quantified by using histograms (Figure A-3). The ranges observed for 36-72 mM were 0.29-0.86 and 0.9-

2.6 micron, respectively. For 144 mM, since the crystals were fused, the estimated crystal size range (0.9-2.6 micron) may not be very accurate.

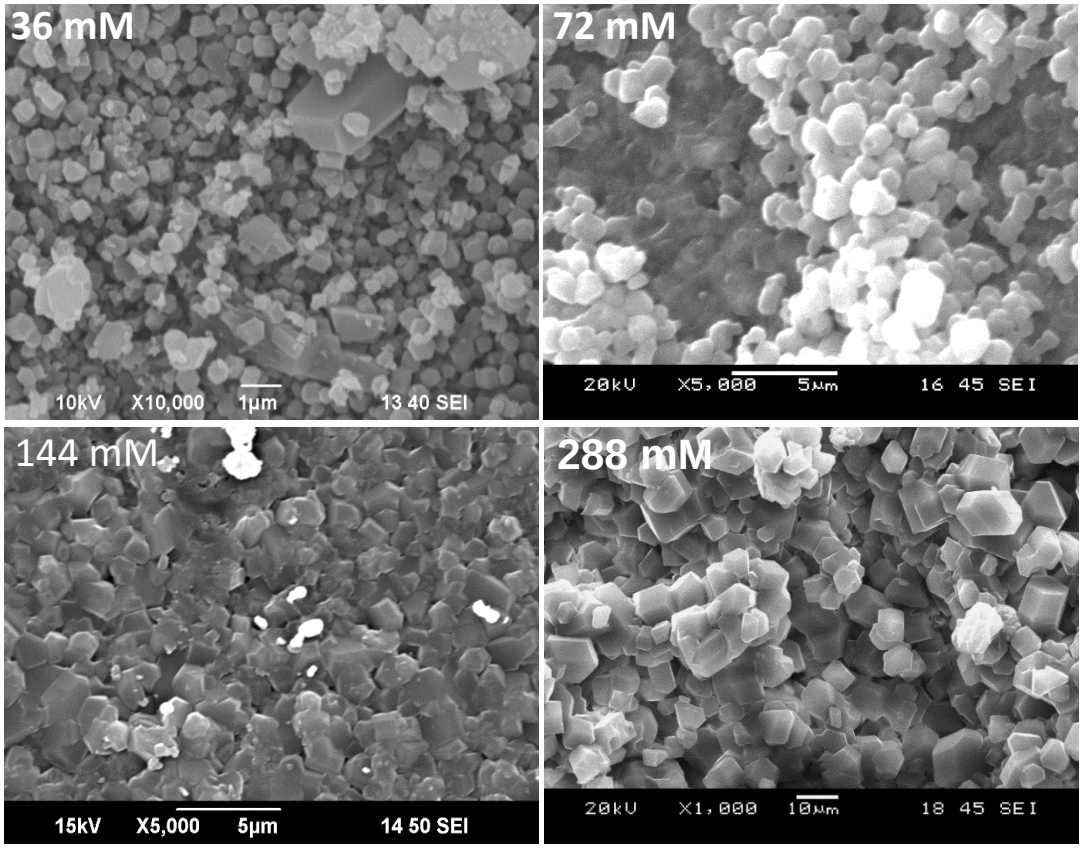


Figure 4- 5: Surface SEM images of membranes synthesised at linker/metal ratio 8, metal concentrations of 36 mM, 72 mM, 144 mM, and 288 mM. Synthesised at 150 °C for 5 hours.

Figure 4-6 shows the XRD patterns of the membranes synthesised using the linker/metal ratio of 8 and metal concentrations of 36-288 mM. The XRD patterns for all concentrations, except for 144 mM, show all the characteristic peaks of ZIF-8 with various intensities, confirming the presence of ZIF-8. The XRD pattern of 288 mM shows higher intensities at 16° and 18.09° (double), which are characteristic peaks for metal salt and the linker, respectively (Fig. A-2). This implies that metal salt and linker residue are present on the substrate surface. Moreover, intensities of the characteristic peaks for 288 mM concentration are lower than the peaks observed for other concentrations whilst large and evolved crystals cover the substrate surface. However, the characteristic peak intensity is not only related to the thickness of the film but also on crystal orientation and packing density. Kida et al. 2013 commented that the membranes synthesised from zinc acetate at the linker/metal ratio of 60 and metal

concentration of 25 mM, with a film thickness of 3.5 µm. The film growth suggested oriented growth with the preferred orientation of the crystallographic planes of 200 (10.41°), 211 (12.76°) and 222 (18.09°), in relation to the 110 (7.36°) plane. In addition, Bux et al. reported that the shorter synthesis times (0.5 - 2 hours) yielded more randomly oriented crystals. As the packing density of crystals was increased with increased reaction time, the crystals became more oriented since their lateral neighbours restricting their growth. This is due to the competitive growth of the different faces with the perpendicular to the substrate, forming the upper surface of the growth layer. Su et al. also showed that the XRD only detects the crystallographic plane, facing the detector. This may imply that the crystals on the membrane synthesised with 288 mM metal concentration are more oriented (Bux et al., 2011, Su et al., 2019, Kida et al., 2013a).

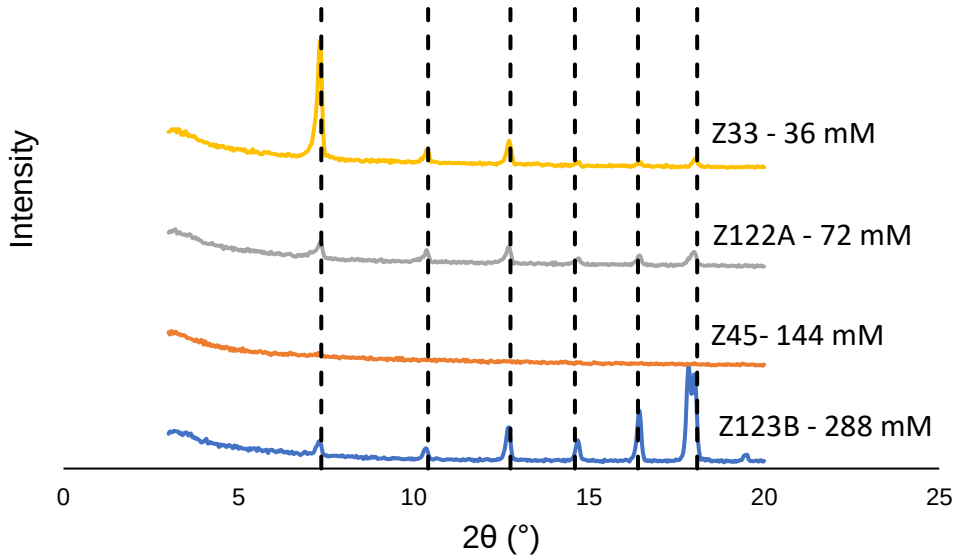


Figure 4- 6: XRD patterns of seeded membranes synthesised with mixed MOF solution at 150 °C for 5 hours, using a linker/metal ratio of 8 and metal concentrations of 36 mM, 72 mM, 144 mM and 288 mM. Dashed lines refer to the positions of the most prominent characteristic peaks of ZIF-8.

Lack of characteristics peaks in the XRD pattern for 144 mM suggest that either ZIF-8 layer on the substrate, which was randomly chosen for the measurements, is too thin or the substrate surface is not homogeneously covered with crystals. The sample used for the SEM picture is not the same with the one used for the XRD measurement. Different pieces were chosen to critically analyse the level of homogeneity for the ZIF-8 growth on the tubular substrate. The SEM picture clearly shows fused crystals (Figure

4-5). In addition, the crystal layer is visible from the cross-section image, taken from another region of the same sample (Figure A-1). This may show that the growth on the substrate at 144 mM concentration may not be uniformly distributed on the substrate.

The cross-sectional images in Figure A-1 exhibit growth on the substrate at the concentrations of 36, 144, and 288 mM. However, the membrane sample taken for the cross-sectional analysis at 72 mM, which is different than the one for the surface SEM image, shows no growth from that region of the substrate (Fig A1, b). This indicates continuous crystal growth was not achieved at 72 mM concentration since a similar level of surface growth is desired to be obtained on each sample characterised. The crystals clustered at 36 and 144 mM concentrations, forming individual entities or agglomerates on the surface rather than continuous film (Fig. A-1a, c). The film growth observed at 288 mM concentration may not be securely attached to the substrate. The detachment of the ZIF-8 layer may be due to breaking the tubular substrate while preparing the sample for characterisation. Although material peeling from the substrate surface was not observed, this cannot be ruled out because of the growth in the nano and micro level. Studies have not reported the binding strength of membranes synthesised from physical deposited seeds. For future work it would be very interesting to study the binding strength of membranes synthesised from physically deposited seeds via ultrasonication method (Kong et al., 2015) since the strength tests performed by Kong et al. produced conclusive results. Kong et al. reported the seed layer peeled off within one minute from seeded substrates indicating weak binding between seeds and substrate whereas the seed layer remained secure on the substrate modified with ZnO for five minutes. Initially, the test would have to be conducted on flat disks substrates since these substrates do not have to be destroyed for characterisation, and then synthesised for a second time on tubular substrates. This test could be extended for membranes derived from other adopted surface modifications and a conclusion can be drawn on the most secure surface modification technique for ZIF-8 membranes.

The effect of decreasing the linker/metal ratio (from 8 to 2) on the growth and the microstructure of membranes were investigated while selecting metal concentrations 72 and 288 mM. The linker/metal ratio was reduced to 2, which is limiting ratio to synthesise ZIF-8 in organic solvents, as reported by Kida et al (Kida et al., 2013b). Although, studies reported synthesis of ZIF-8 membranes using linker/metal ratio of 1.5 (Lai et al., 2016c, Bux et al., 2011, Bux et al., 2009) and 2.5 (Zhu et al., 2016), these experiments were conducted in a microwave oven and in the presence of sodium formate as a catalyst to help promote the deprotonation of the linkers.

Figure 4-7 shows the surface and cross-sectional images (not of same scale) of the membranes synthesised, using metal concentrations of 72 mM and 288 mM at linker/metal of 2. The surface images show rhombic shaped crystals synthesised for both metal concentrations. Histograms (Figure A-4) indicate that the crystal size ranges are between 17-36 and 41-129 micron for the membranes synthesised using 72 and 288 mM metal concentrations, respectively. Decreasing the linker/metal ratio to 2 increases the crystal size that agrees with reports in literature (Kida et al., 2013a, Tanaka et al., 2014a, Öztürk et al., 2017). Obtaining bigger crystals with lower linker/metal ratio is due to the fewer nuclei formed in the system. Studies reported that the reduced linker/metal ratio slows down the nucleation rate because of the lower deprotonation rate. This may suggest that the growth can be sustained longer due to the Ostwald ripening effect, by unstable nuclei dissolved in the system. In relation to the ZIF-8 system, the larger and more evolved crystals have more neighbouring atoms, making them more energetically favourable. The smaller and less stable nuclei dissolve into the solution, which then form on the larger more stable crystals, and thus increase their crystal size further (Voorhees, 2002, Venna et al., 2010). Except for Tanaka et al. publication have not discussed the separation performance, relating to membrane microstructures for varied different linker/metal ratio. In conclusion, it is clear from the results of Tanaka et al., and this thesis that smaller linker/metal ratios will lead to thicker membranes, yielding reduced permeances (Duan et al., 2018, Kang et al., 2017). The cross-sectional images may also suggest that at the linker/metal ratio of 2, thicker film growth can be achieved with an estimated membrane thicknesses of 38 and 104 µm for metal concentrations of 72 and 288 mM, respectively (Fig 4-7). This suggests that the smaller number of nuclei formed into larger sized crystals and created denser films on the substrate surfaces. This was not the case at the linker/metal ratio 8 (Figure A-1). Tanaka al. reported similar thickness (approx. 2 µm) values for their membranes across all linker/metal ratios (30, 40, and 60) at the metal concentration of 25 mM, due to the challenges in identifying the interface between the substrate and ZIF-8 film. (Tanaka et al., 2014a).

Although the results indicated that the growth of dense and continuous films of ZIF-8 on the substrates are possible, the membranes are too thick. Literature reported CO_2 permeances for ZIF membranes at room temperature and 1 bar pressure in the magnitude of 10^{-8} and 10^{-5} mol/s.m^2.Pa with a thickness of ~30 µm (Yichang Pan, 2012) and 5-9 µm (Yao et al., 2013), respectively, (Aceituno Melgar et al., 2015). This implies that these membranes, synthesised with linker/metal ratio of 2, regardless from the metal concentration, may only achieve permeances below 10^{-8} mol/s.m^2.Pa.

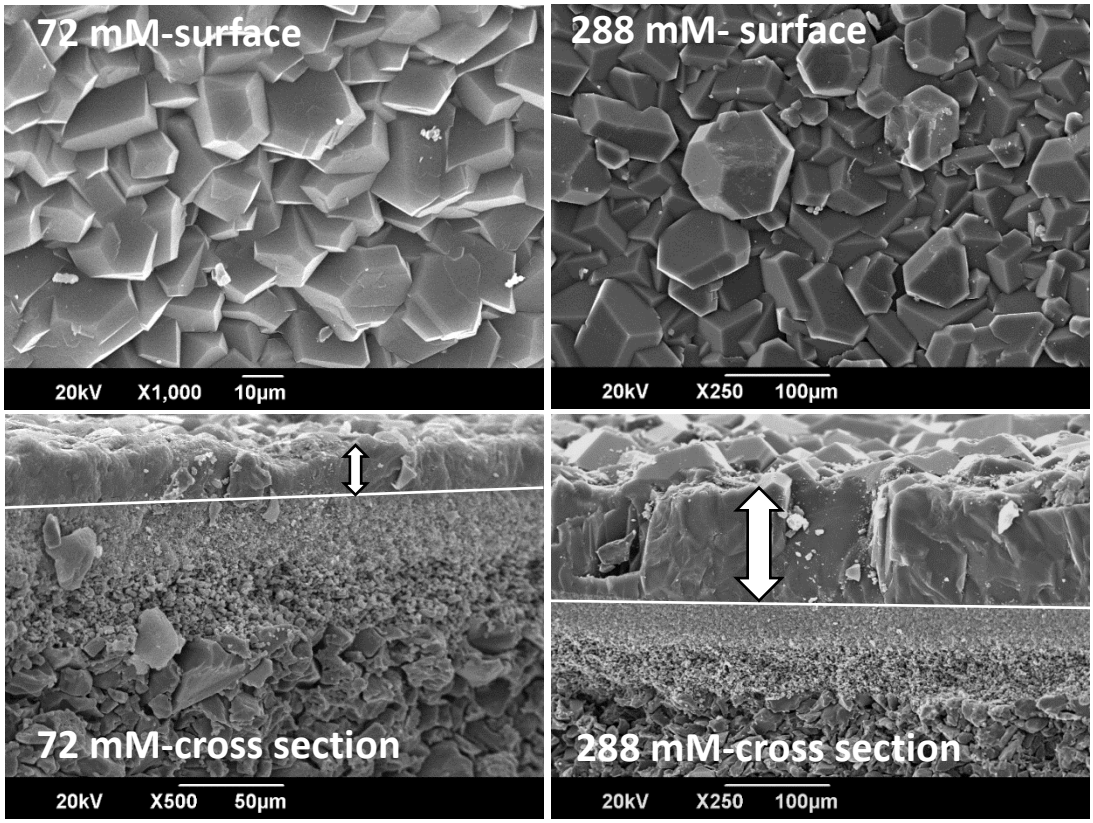


Figure 4- 7: Surface and cross section SEM images of seeded membranes synthesised at 150 °C for 5 hours using linker/metal ratio of 2 and metal concentrations of 72 mM and 288 mM. The white line marks the internal surface of the substrate where ZIF-8 growth has begun on the substrate surface with the arrow indicating membrane thickness.

Figure 4-8 shows the XRD patterns of membranes synthesised at linker/metal ratio of 2 and metal concentrations of 72 and 288 mM. The XRD patterns show all the characteristic peaks of ZIF-8 for the membrane synthesised at 72 mM. However, at 288 mM, the 10.41^{o} peak is not present that may indicate the faces of the outer layer of crystals that are parallel to the substrate do not reflect the crystallographic plane 002, and hence is not detected by the detector.

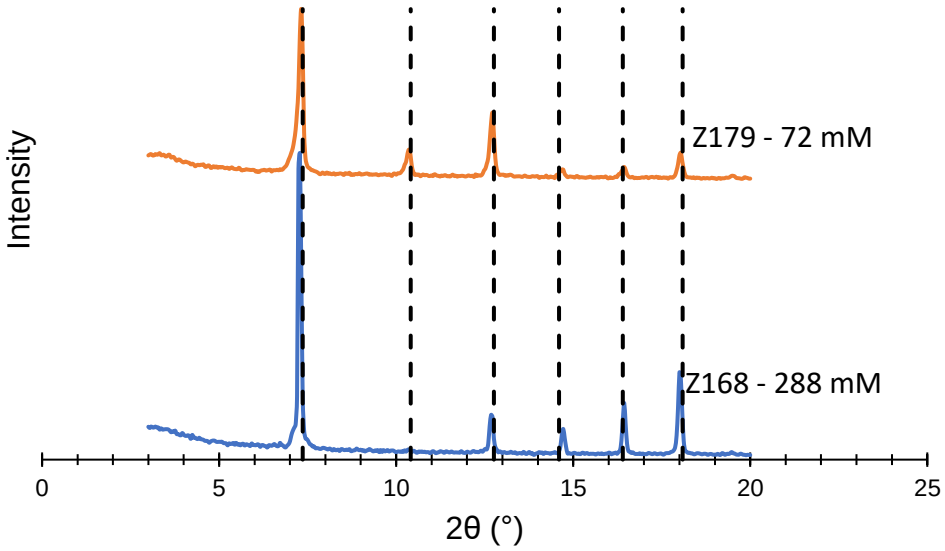


Figure 4- 8: XRD patterns of seeded membranes synthesised at 150 °C for 5 hours using a linker/metal ratio of 2 at metal concentrations of 72 mM and 288 mM. Dashed lines refer to the positions of the most prominent characteristic peaks of ZIF-8.

The effect of synthesis time on heterogenous growth was studied for 5 and 10 hours using linker/metal ratio of 8 and metal concentrations of 36 mM and 144 mM (Fig. 4-9). The surface images show that the crystals become larger and more evolved, when the synthesis time was increased from 5 to 10 h (Fig 4-9). The size ranges shifted from 0.29-0.86 to 0.3-5 µm and 0.9-2.6 to 2-11 µm for 36 mM and 144 mM metal concentrations, respectively (Fig. A-7 histogram). However, the particles are not fused with each other for 36 mM metal concentration even after 10 h synthesis and gaps are still visible between the crystals. The particles are more fused for 144 mM metal concentration, compared to 36 mM, for both 5 and 10 h. This indicates that the level of intergrowth is controlled by the concentration rather than the synthesis time. This is not surprising since the concentration effects the number of nuclei formed at the beginning of the synthesis. This nucleation time is limited to approx. the first 60 minutes, as reported in literature (Venna et al., 2010, Öztürk et al., 2017, Schejn et al., 2014). Therefore, extended synthesis times without changing the concentration only changes the crystal stability rather than the intergrowth. With increasing metal concentration, the concentration of the nuclei on the surface is increased. Therefore, they can be more tightly packed, achieving better intergrowth. Another consideration would be to explore an alternative synthesis methodology that can potentially overcome the 60 minute nucleation limitation of ZIF-8, so new nuclei can continue to form past 60 minutes. This is discussed in the next chapter where the novel system, metal-linker isolation system

is introduced. Figure 4-10 shows a schematic depiction of the difference in growth on substrate over time.

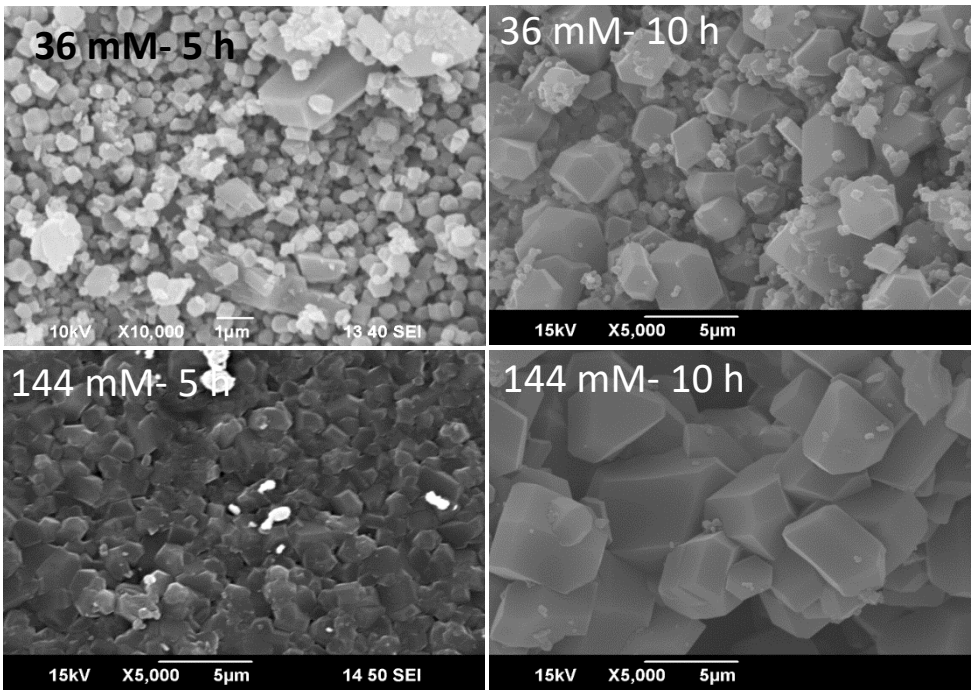


Figure 4- 9: SEM surface images of membranes synthesised at 150 °C for 5 and 10 h, using linker/metal ratio of 8 and metal concentrations of 36 mM and 144 mM.

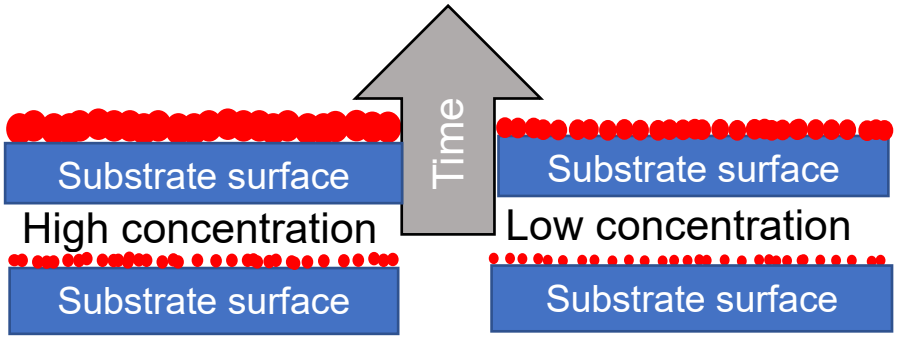


Figure 4- 10: Schematic of two systems with high and low metal concentrations, depicting growth on the substrate surface. The high concentration surface shows that with increasing time the gaps between the crystals get filled due to more nuclei on the substrate surface beforehand. The low concentration system depicts that the gaps are filled with increasing time whilst some remain due to the fewer nuclei on the surface at the beginning of the synthesis.

Figure 4-11 shows the cross-section images of the membranes synthesised for 5 and 10 hours using linker/metal ratio of 8 and metal concentrations of 36 and 144 mM. The dashed red line and arrow highlight the inside of the substrate. The samples from the same substrate suggest a few crystals on the surface at the 36 mM concentration, at

both 5 and 10 hours. ZIF-8 film growth was observed over the cross section using 144 mM concentration for 10 hours. Similarly, cross sectional images show similar growth from the surface images whereas no ZIF-8 layer was visible for 36 mM concentration for 10 h. This implies that there is no significant effect of increasing the synthesis time since initial metal concentration and consequently nucleation is more critical. This implies that setting the initial ratios and concentrations for sufficient nuclei deposition is one of the keys for membrane growth. Therefore, the synthesis time was maintained at 5 hours for the batch synthesis.

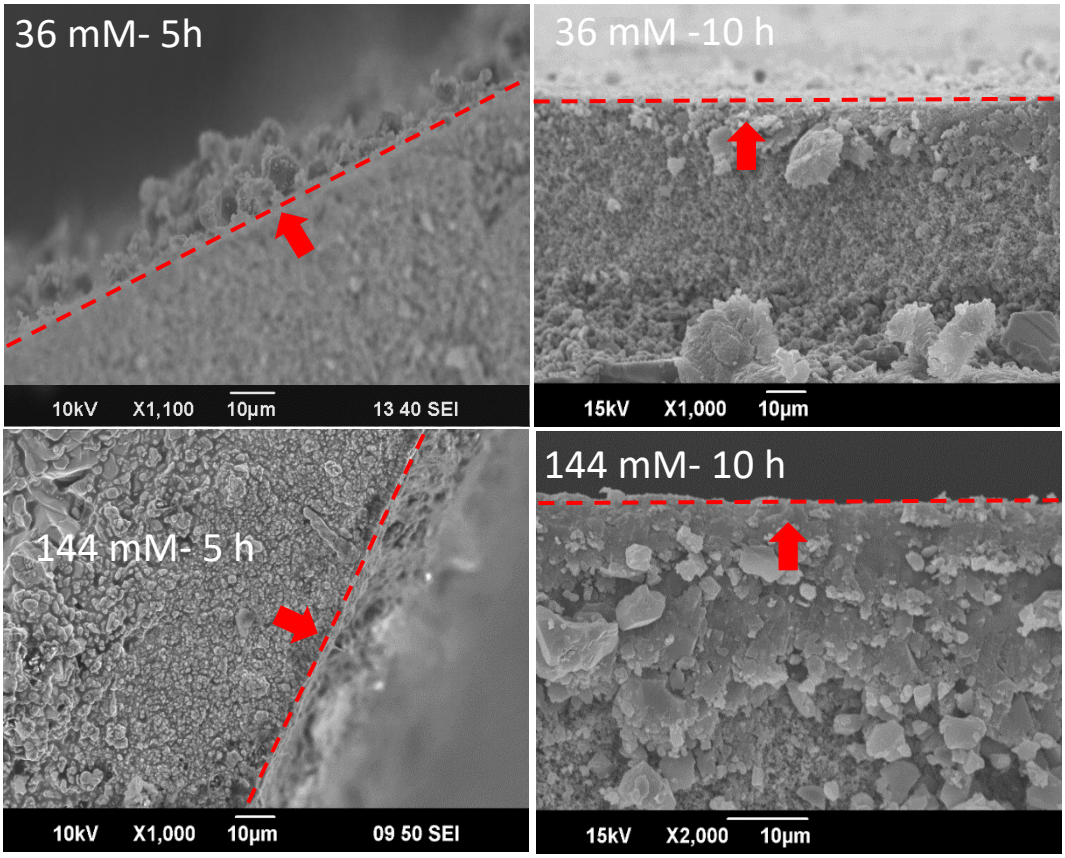


Figure 4- 11: SEM cross sectional images of membranes synthesised at 150 °C for 5 and 10 h with linker/metal ratio of 8 and metal concentrations of 36 and 144 mM. The dashed red lines and arrows indicate the inside of the substrate surface where the growth of ZIF-8 occurred.

Figure 4-12 shows the XRD patterns of the membranes synthesised for 5 and 10 hours at linker/metal ratio of 8 and metal concentrations of 36 mM and 144 mM. The XRD pattern of the membrane synthesised at 36 mM for 5 hours show all characteristic peaks of ZIF-8 whilst the membrane synthesised for 10 hours there are no peaks. This may imply that there is a sparse or very thin layer of ZIF-8 on the selected substrate piece for XRD analysis. The membranes synthesised with the metal concentration of 144 mM for 5 and 10 hours show all characteristic peaks of ZIF-8. This suggests that

the level of growth observed at the concentration of 144 mM in the surface images are continuous throughout the substrate.

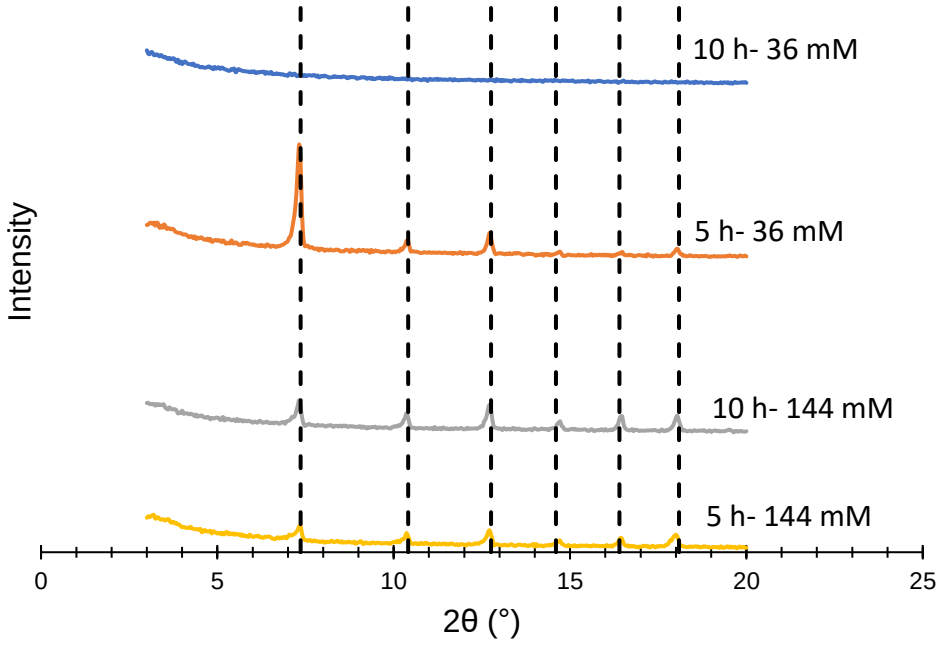


Figure 4- 12: XRD patterns of membranes synthesised at 150 °C at linker/metal ratio of 8 and metal concentrations of 36 mM and 144 mM for 5 and 10 h. Dashed line refers to the positions of the most prominent characteristic peaks of ZIF-8.

The effect of metal salt dissociation was studied for the batch system (literature review sections 2.4 and 2.5.2 pages 21 and 30, respectively). Figure 4-13 shows the surface and cross section images (not of same scale) of membranes synthesised with zinc acetate dihydrate (zinc acetate) and zinc nitrate hexahydrate (zinc nitrate) metal salts. Membranes were synthesised using a linker/metal ratio of 8 and metal concentration of 36 mM at 150 °C for 5 hours with two cycles. The growth of zinc nitrate was performed as one cycle synthesis whilst there was no considerable growth on the surface even with a seeded substrate. Only after two cycles, crystal growth was observed, as seen in Figure A-5. This may indicate that the first synthesis acts as reactive seeding step. Therefore, experiments were conducted with 2 cycles to compare the salt effect. Surface image and cross section images show that the membrane synthesised with zinc acetate are densely packed with a thickness of 15-17 µm. Crystals are the more thermodynamically stable rhombic shape, and the size range was relatively between 1.2-13.5 µm (Fig. A-6a). In contrast, zinc nitrate crystals (131-526 nm-Fig. A-6b)

observed on the surface are less evolved, spherical, and cubic, suggesting that the crystals are in the metastable and initial stages of ZIF-8 evolution, respectively.

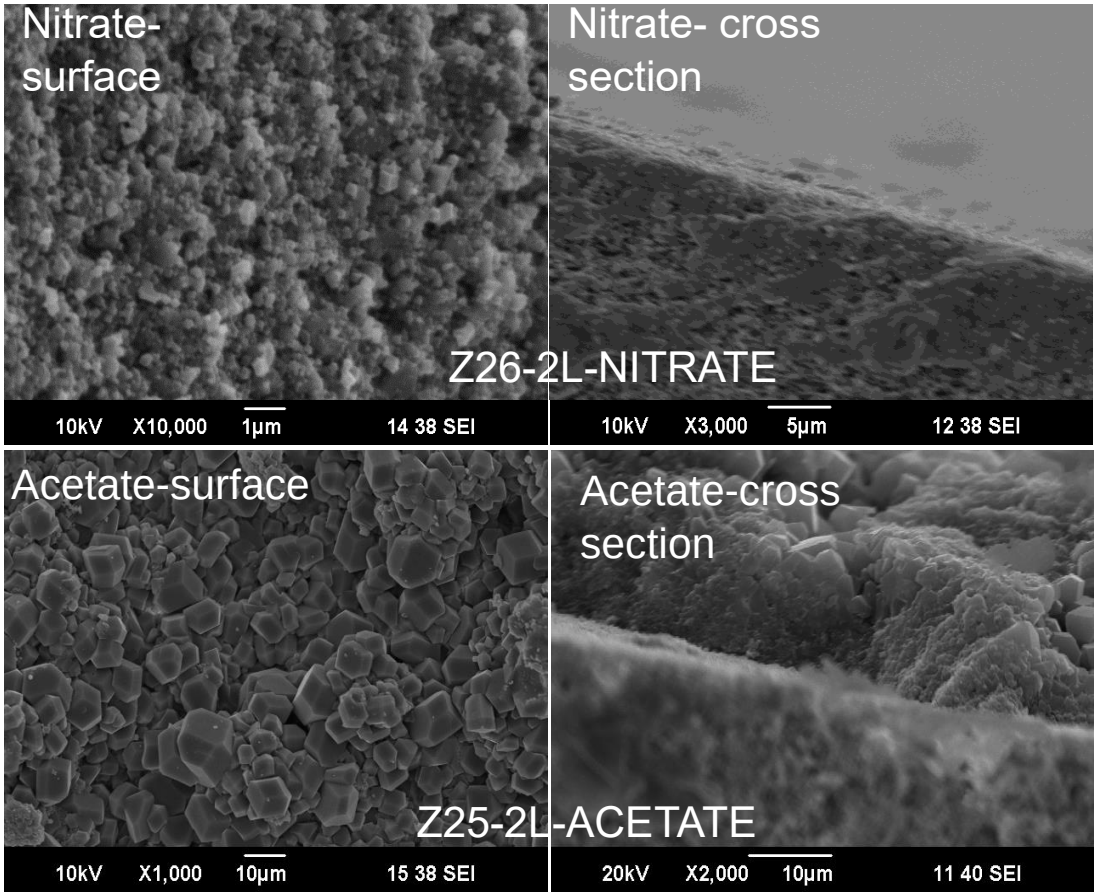


Figure 4- 13: Surface and cross section images of two layer seeded membranes synthesised using zinc nitrate hexahydrate, and zinc acetate dihydrate. Membranes were synthesised at 150 °C for 5 hours using a linker/metal ratio of 8 and metal concentration of 36 mM.

The difference in the distribution of the crystal sizes reflects the effects of the conjugate bases associated with the Zn^{2+}. The smaller crystal size is the reflection of faster nucleation, where the soft metal (zinc) association with the hard base (NO^{3-}), releases a vast amount of Zn^{2+}. In contrast, the Zn^{2+} derived from zinc acetate is slowly released due to the intermediate stage created by CH_3COO^-, associated with Zn^{2+}, the final release to bind to the imidazole ions (Tanaka et al., 2014a). Kida et al. reported how the slow releasing zinc acetate delivered dense films (Kida et al., 2013a), and Tanaka et al. (using tubular substrates) reported membranes with better crystallinity leading to better performing membranes with H_2 permeance twice as high than those membranes prepared from zinc nitrate (Tanaka et al., 2014a). However, Ramu et al. (using flat disks) reported that zinc nitrate delivering separation factor (propylene/propane) an

order magnitude higher than the membrane derived from zinc acetate, delivering a separation factor of around 10. Ramu et al. also indicated that the zinc nitrate delivered membranes with better grain boundaries.

In conclusion, the nature of the conjugate base must complement the system - substrate geometry and surface modification adopted. Since if the surface has less sites of nucleation and zinc nitrate is used for membrane growth, the nature of heterogenous growth can yield gaps in between the membrane growth because zinc nitrate delivers smaller nuclei. Additional synthesis cycles provide growth via oligomerisation – linker coordinated metals from synthesis solution (Öztürk et al., 2017) and additional deposition of nuclei in the additional growth cycles, thereby filling the intercrystalline gaps on the substrate surface. Hence, the two-cycle membrane growth in this thesis.

The cross-sectional images may imply more robust heterogeneous growth on the substrate is achieved from growth derived from zinc acetate, suggesting densely packed crystals on the surface with thickness of 15-17 µm. Surface growth derived from zinc nitrate indicates a very thin layer of growth. This thin layer of growth depicts how the intermediate ion, CH_3COO^-, allows a more 'paced' release of Zn^{2+} thereby promoting growth onto the substrate, reducing nucleation in the bulk of the solution. These results are consistent with the reports (Tanaka et al., 2014a, Kida et al., 2013a) that discussed the intermediate ion, CH_3COO^-, delays the nucleation of ZIF-8, achieving more robust growth onto substrates, with fewer defects in comparison to when using zinc nitrate for membrane growth.

Figure 4-14 shows the XRD pattern of the membrane synthesised using zinc nitrate and zinc acetate. The membrane synthesised using zinc nitrate shows no characteristic peaks of ZIF-8 that may suggest no growth, or a very thin layer of ZIF-8 deposited on the substrate. In contrast, the membrane synthesised with zinc acetate shows the characteristic peaks of ZIF-8 supporting the growth observed in the cross sectional and surface images. This may imply that the growth of clustered crystals observed in the SEM images is continuous.

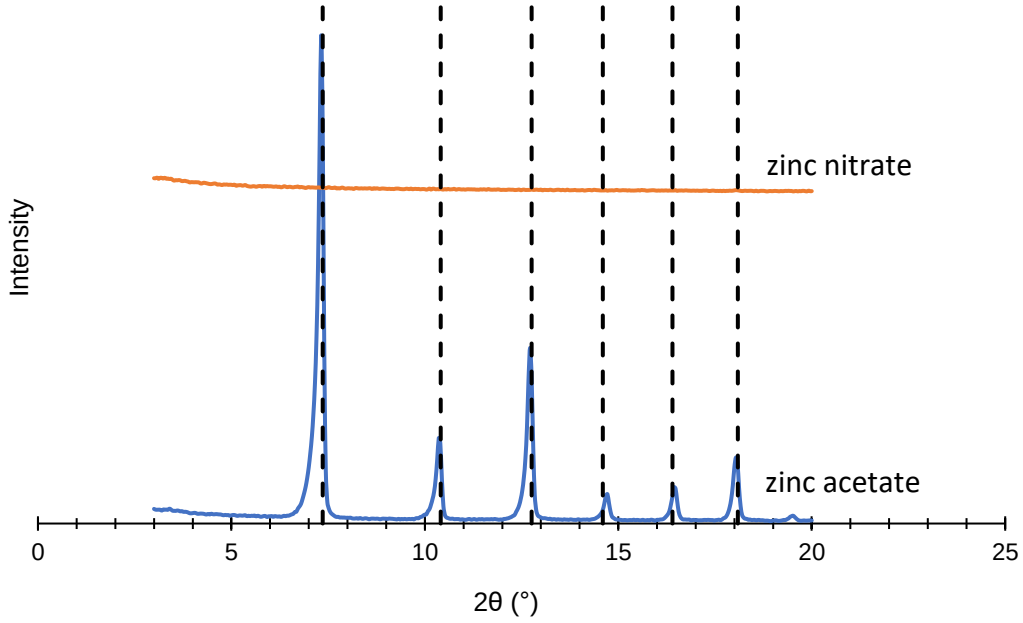


Figure 4- 14: XRD patterns seeded membrane synthesised using zinc nitrate hexahydrate and zinc acetate dihydrate at 150 °C for 5 hours at linker/metal ratio of 8 and metal concentration of 36 mM with two cycles. The dashed lines refer to the positions of the most prominent characteristic peaks of ZIF-8.

To further understand the effects of conjugate bases on heterogeneous growth of ZIF-8 onto tubular substrate, an equimolar (50:50) mixture of zinc acetate and zinc nitrate were used for the synthesis. Figure 4-15 shows the surface images of zinc nitrate (Fig. 4-15a, b) and zinc acetate (Fig. 4-15c, d) seeded membranes synthesised using metal concentrations of 36 mM and 144 mM with linker/metal ratio of 8. A one cycle synthesis was chosen to better study the role of the two conjugate bases in the same system without the layering system. The nitrate seeded substrates show very little to no growth on the surface. The surface image of the substrate synthesised at 144 mM suggests more deposited material, compared to 36 mM. However, the growth does not reflect the typical cubic and rhombic morphology of ZIF-8, implying these are failed nucleated seeds. The acetate seeded substrate synthesised at 36 mM indicates crystal growth with typical ZIF-8 cubic morphology while the acetate seeded substrate synthesised at 144 mM indicates surface growth without the typical ZIF-8 morphology, implying unreacted precursors.

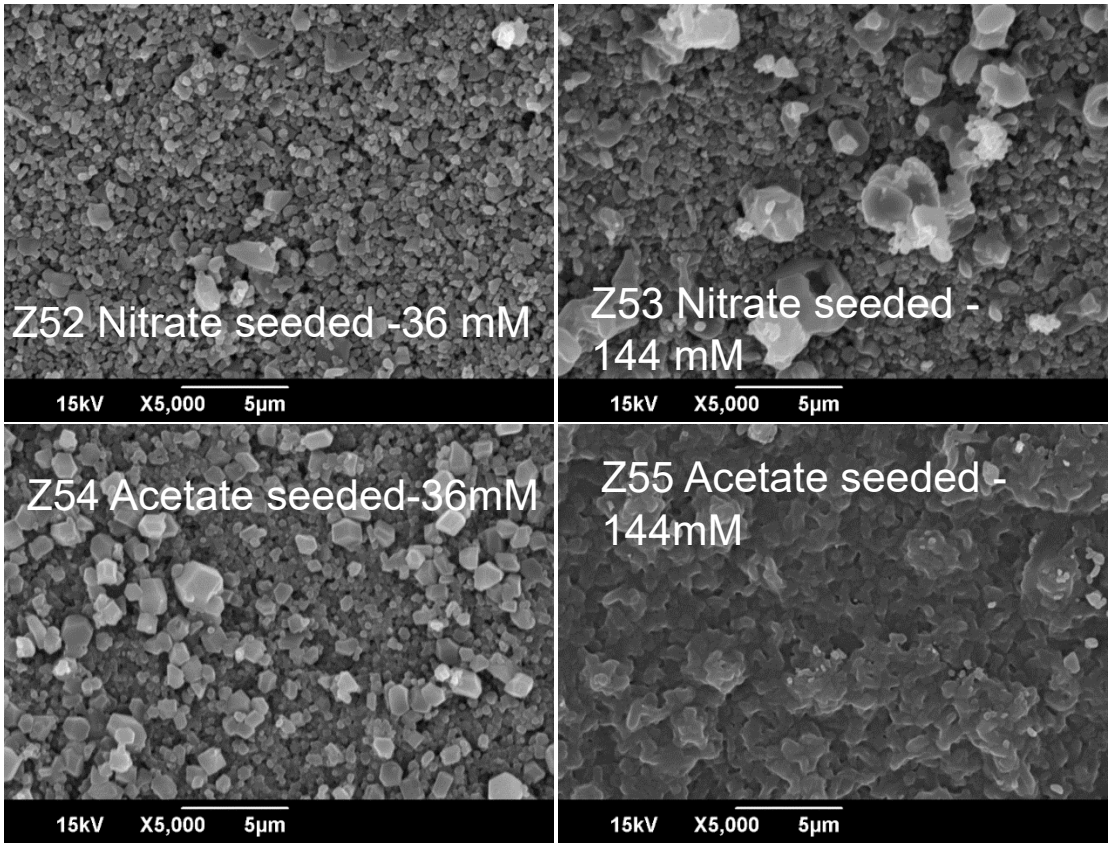


Figure 4- 15: Surface SEM images of membranes synthesised using mixed salts (50:50) with seeds synthesised using zinc nitrate and zinc acetate. Metal concentration of 36 and 144 mM with linker/metal ratio of 8. Synthesis conditions of 150 °C for 5 hours for one cycle.

Kwon et al and Ramu et al. synthesised membranes on flat disks using 50:50 metal salt in a one cycle synthesis on unseeded substrate via counter diffusion and seeding via microwave seeding, respectively. Kwon et al. and Ramu et al. used metal concentrations of 7.2 and 0.37 mM, respectively (Ramu et al., 2018, Kwon and Jeong, 2015). Ramu et al. reported that the addition zinc nitrate improved gas separation performance (achieving higher separation factor) as opposed to using zinc acetate alone since zinc nitrate delivers better grain boundaries because of the uniformity of the crystal derived from zinc nitrate. Kwon et al. obtained a membrane with a microstructure between zinc nitrate and zinc acetate, the membrane derived from the combination of the metal salts formed near to the surface a characteristic feature of the zinc nitrate membrane in Kwon et al. works. However, in this thesis, the 50:50 results suggest a weaker level of heterogenous growth when using zinc acetate and zinc nitrate together, irrespective of acetate or nitrate seeds used. For this reason, based on previous nitrate seeded membranes, and the 50:50 results, all future synthesis of ZIF-8

in this thesis was conducted using zinc acetate and zinc nitrate for the membrane and seed syntheses, respectively.

The cross section images (Fig. 4-16) of the nitrate seeded substrates support the growth observed in the surface images, suggesting very little to no growth on the surface, with non-typical ZIF-8 growth. The cross sectional image (Fig. 4-16) of the acetate seeded membrane synthesised at 36 mM suggests non typical ZIF-8 growth indicating the type of growth seen in the surface image is not isolated to the substrate sample characterised for the surface growth. While the acetate substrate at 144 mM indicates very little deposited material on the surface with non-typical ZIF-8 morphology.

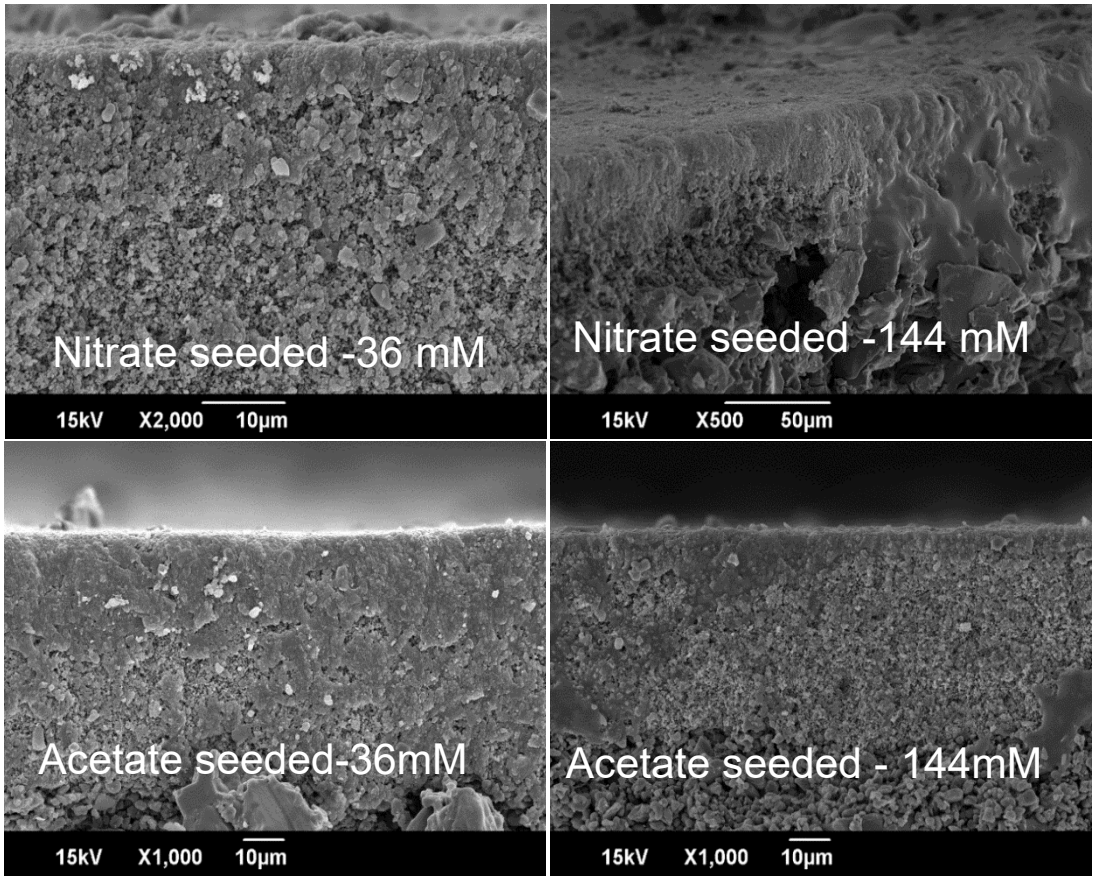


Figure 4- 16: Cross sectional images of membranes synthesised using mixed salts (zinc nitrate hexahydrate and zinc acetate dihydrate = 50:50 molar ratio), metal concentrations of 36 mM and 144 mM, and linker/metal ratio of 8 at 150 °C for 5 hours.

The XRD patterns (Figure 4-17) do not show any of the characteristic peaks of ZIF-8 for the zinc acetate and zinc nitrate seeded substrates, which may imply sparse or a very thin layer ZIF-8 growth on the substrate. The acetate seeded substrate synthesised at 144 mM shows peaks that are not reflective of ZIF-8. This may suggest

that two-layer synthesis is needed to grow crystals on the substrate or higher precursor concentrations are needed at one layer, regarding the results shown previously.

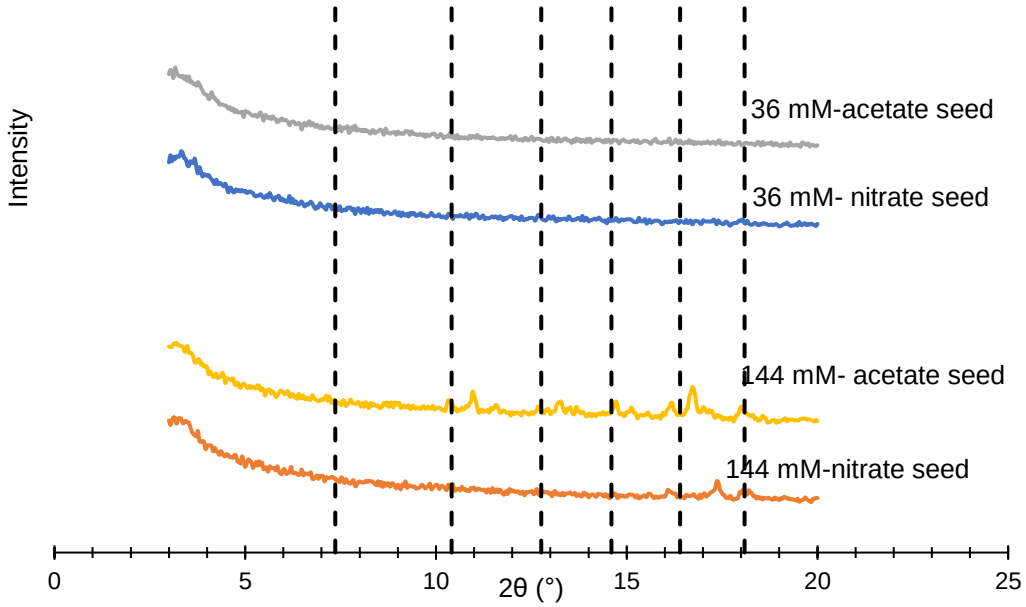


Figure 4- 17: XRD patterns of membranes synthesised using mixed salts (zinc nitrate hexahydrate and zinc acetate dehydrate = 50:50 molar ratio), linker/metal ratio of 8 and metal concentrations of 36 mM and 144 mM. Synthesis conditions: 150 °C for 5 hours, one cycle. The dashed lines refer to the positions of the most prominent characteristic peaks of ZIF-8.

4.4 Conclusion

In this chapter the heterogenous growth of ZIF-8 onto tubular substrates and the parameters that control the membrane microstructure were explored. The work was carried out systematically to better understand the optimum conditions for the synthesis of ZIF-8 membranes under conventional heating.

Results showed that sites of nucleation are needed to promote growth onto the substrate. The conjugate bases associated with the zinc controlled the membrane microstructure and level of heterogenous nucleation. For this system, zinc acetate delivered the more robust level of heterogeneous growth. While the synthesis time did not increase the heterogenous growth rather more crystal stability; the reaction chemistry and initial nucleation proved more critical. At linker/metal ratio of 2 and metal concentrations of 72 and 288 mM a 100 % surface coverage was achieved (Table 4-2). Membrane thicknesses were measured as 38 and 104 µm thickness achieved for 72 and 288 mM concentrations, respectively. Indicating, higher precursor concentrations provide better heterogenous growth, and smaller ratios generate thicker membranes.

The mixed batch system indicates that there is a competitive nucleation between homogenous and heterogenous nucleation in the batch system. The next stage is to investigate heterogenous nucleation where the reaction zone is brought to the surface via isolating precursors.

Table 4- 2: Summarising surface coverage and thicknesses of membranes synthesised using mixed precursors.

Metal salt	Concentration (mM)	Linker/metal ratio	Metal salt used for seeds	Synthesis time	Synthesis cycles	Surface coverage (%)	Thickness (µm)
Zinc acetate dihydrate	36	8	No seeds	5	1	2-28	-
Zinc acetate dihydrate	36	8	Zinc nitrate hexahydrate	5	1	34-73	-
Zinc acetate dihydrate	72	8	Zinc nitrate hexahydrate	5	1	96-97	-

Zinc acetate dihydrate	144	8	Zinc nitrate hexahydrate	5	1	96-98	-
Zinc acetate dihydrate	288	8	Zinc nitrate hexahydrate	5	1	97	-
Zinc acetate dihydrate	72	2	Zinc nitrate hexahydrate	5	1	100	38
Zinc acetate dihydrate	288	2	Zinc nitrate hexahydrate	5	1	100	104
Zinc acetate dihydrate	36	8	Zinc nitrate hexahydrate	10	1	97	-
Zinc acetate dihydrate	144	8	Zinc nitrate hexahydrate	10	1	96	-
Zinc acetate dihydrate	36	8	Zinc nitrate hexahydrate	10	2	97-99	15-17
Zinc nitrate hexahydrate	36	8	Zinc nitrate hexahydrate	5	2	98	-
Zinc nitrate hexahydrate and zinc acetate dihydrate (50:50)	36	8	Zinc nitrate hexahydrate	5	1	0-1	-
Zinc nitrate hexahydrate and zinc acetate	144	8	Zinc nitrate hexahydrate	5	1	0	-

dihydrate (50:50)							
Zinc nitrate hexahydrate and zinc acetate dihydrate (50:50)	36	8	Zinc acetate dihydrate	5	1	0	-
Zinc nitrate hexahydrate and zinc acetate dihydrate (50:50)	144	8	Zinc acetate dihydrate	5	1	0-10	-

4.5 Appendix

Figure A1 shows the cross-sectional images of the membranes synthesised with mixed MOF solutions with linker/metal ratio of 8 with metal concentrations of 36-288 mM. These substrate samples are taken from the centre that may show that central part of the substrate may have some empty bare substrate as is shown in b, the space between the layer and substrate at 288 mM may also suggest there may be poor interaction between substrate and MOF layer.

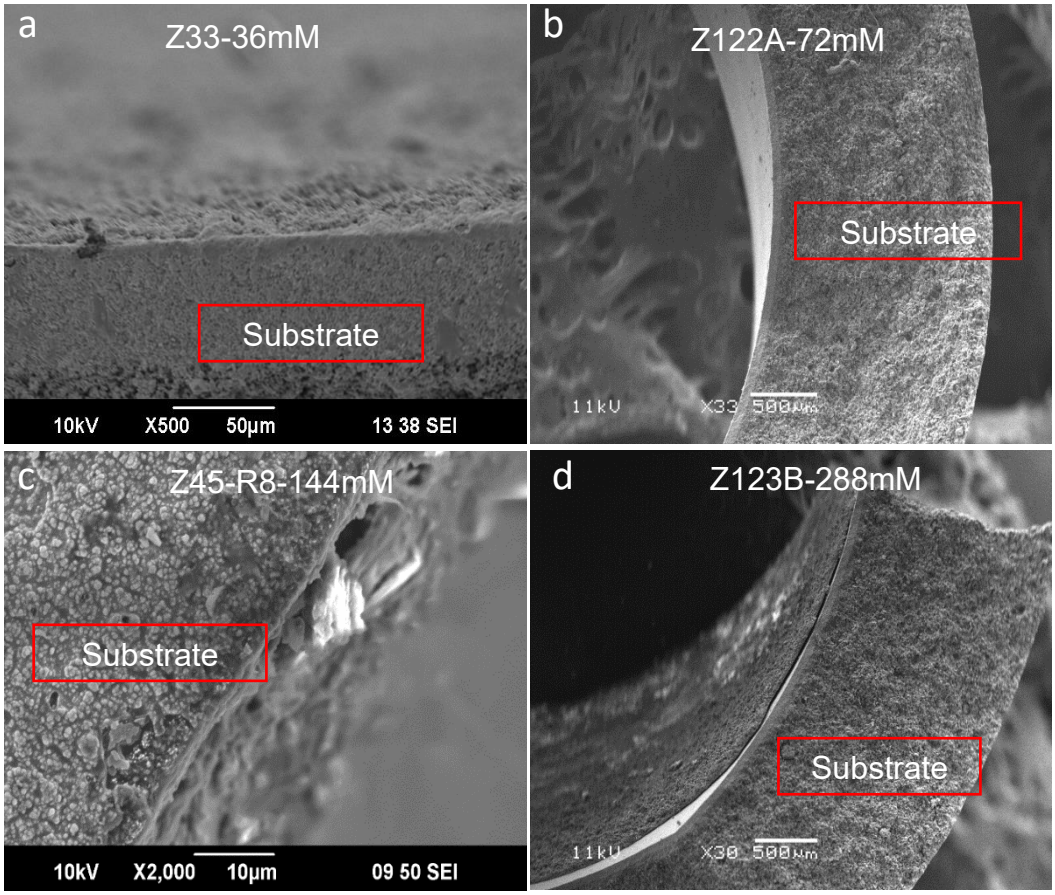


Figure A- 1: Cross sectional images of membranes synthesised at linker/metal ratio 8, metal concentrations of 36 (a), 72 (b), 144 (c), and 288 (d) mM. Membranes synthesised with mixed MOF solution at 150 °C for 5 hours.

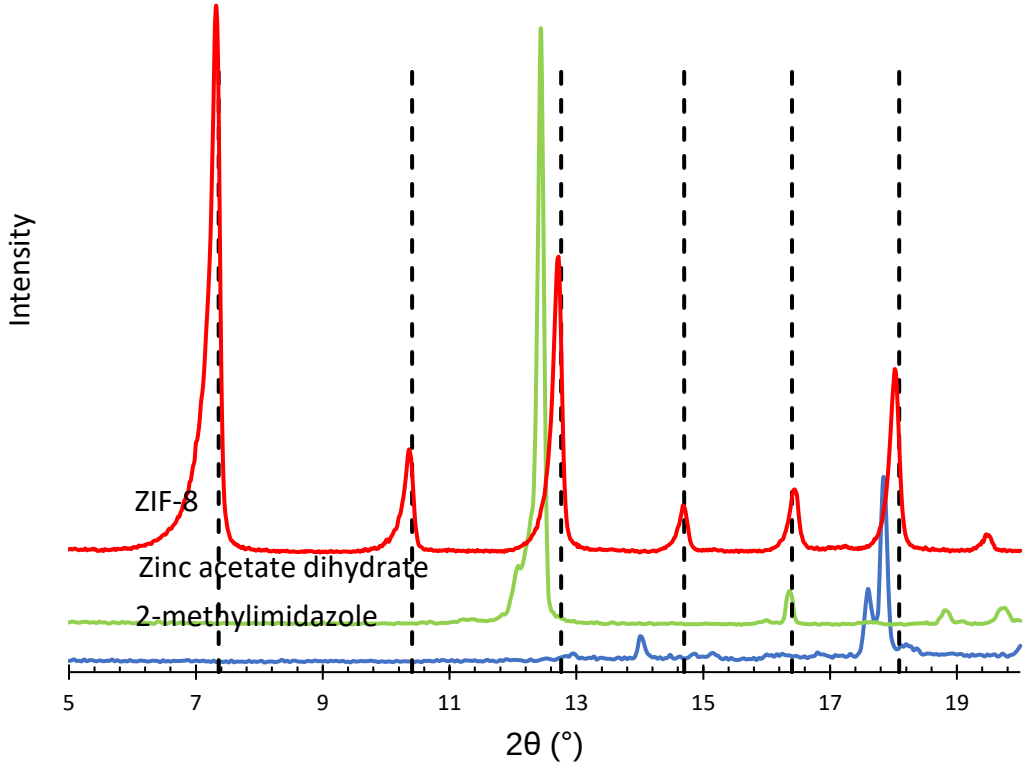
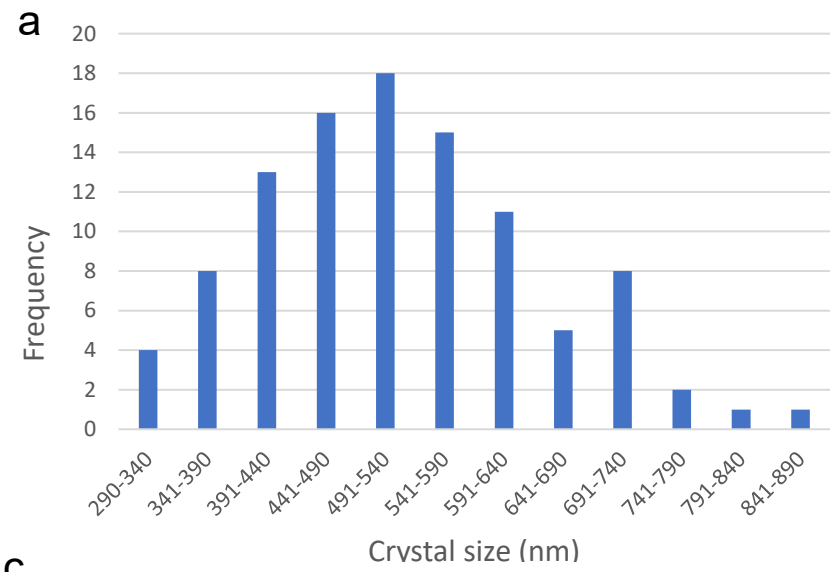
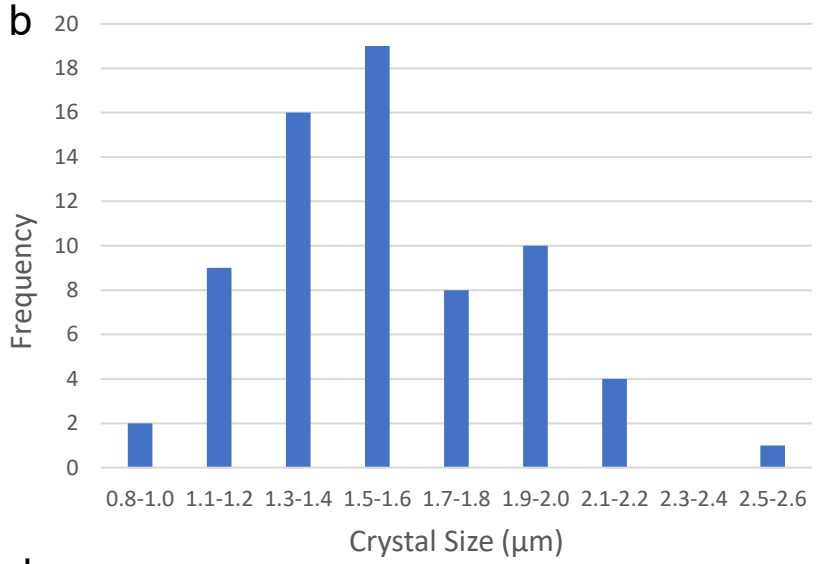
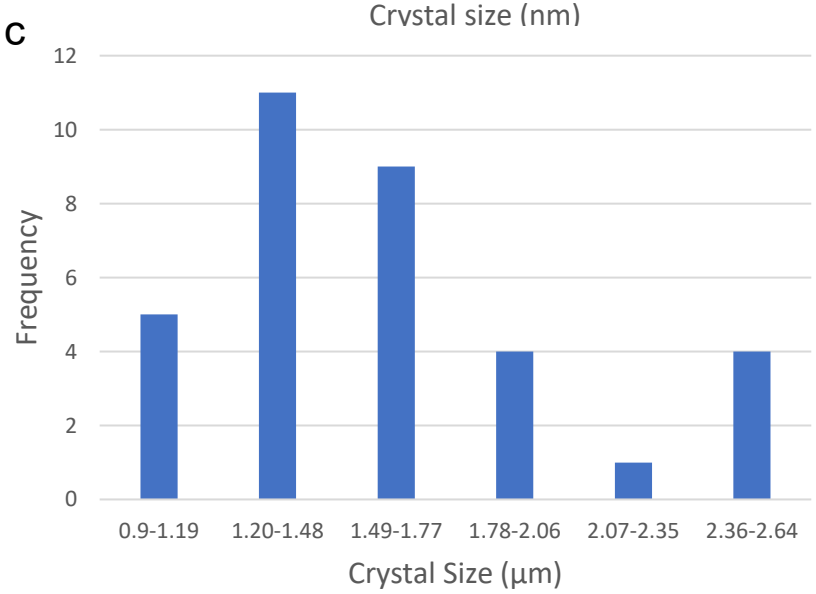


Figure A- 2: XRD pattern of ZIF-8 seeds synthesised from zinc nitrate hexahydrate and 2-methylimidazole using methanol at 150 °C for 5 hours, and the metal and linker precursors zinc acetate dihydrate and 2-methylimidazole used for ZIF-8 membrane synthesis, respectively.

Figure A-3 shows the histograms of the crystal sizes at the linker/metal ratio of 8 and metal concentrations 36-288 mM. The crystal size range were estimated from the SEM images up to 100 crystals where possible. Because of the fused nature of some of the crystals this was not possible for all concentrations. Particularly at 144 mM, where only 34 crystals could be measured which is why the 72 and 144 mM are very similar to each other. The crystal size range (min-max) at the respective concentrations were 0.29-0.86, 0.87-2.6, 0.9-2.6, 4.5-16.3 µm for 36, 72, 144 and 288-mM, respectively.


a
Frequency
Crystal size (nm)
290-340
341-390
391-440
441-490
491-540
541-590
591-640
641-690
691-740
741-790
791-840
841-890


b
Frequency
Crystal Size (µm)
0.8-1.0
1.1-1.2
1.3-1.4
1.5-1.6
1.7-1.8
1.9-2.0
2.1-2.2
2.3-2.4
2.5-2.6


c
Frequency
Crystal Size (µm)
0.9-1.19
1.20-1.48
1.49-1.77
1.78-2.06
2.07-2.35
2.36-2.64

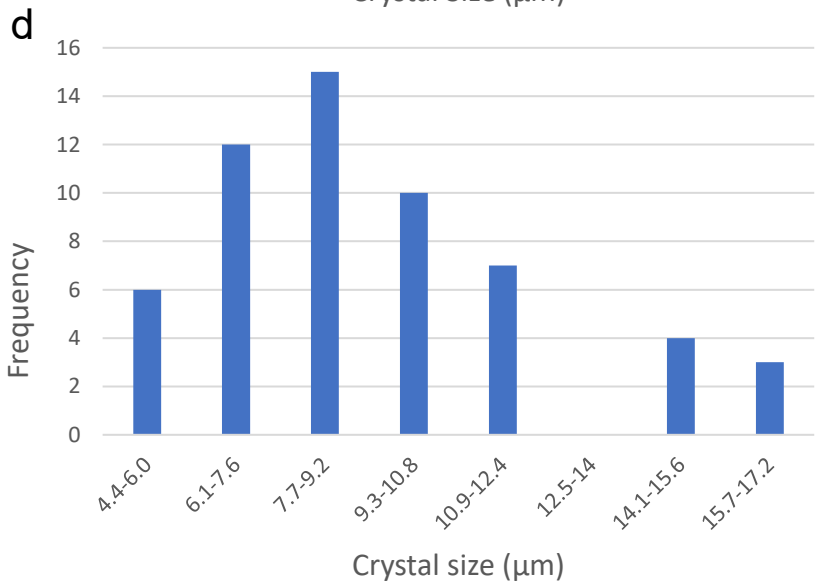

d
Frequency
Crystal size (µm)
4.4-6.0
6.1-7.6
7.7-9.2
9.3-10.8
10.9-12.4
12.5-14
14.1-15.6
15.7-17.2

Figure A- 3: Particle size histograms of crystals on the substrate surface synthesised at linker/metal ratio of 8 and metal concentrations 36 mM (a), 72 mM (b), 144 mM (c), 288 mM (d). Membranes synthesised for 5 hours at 150 °C.

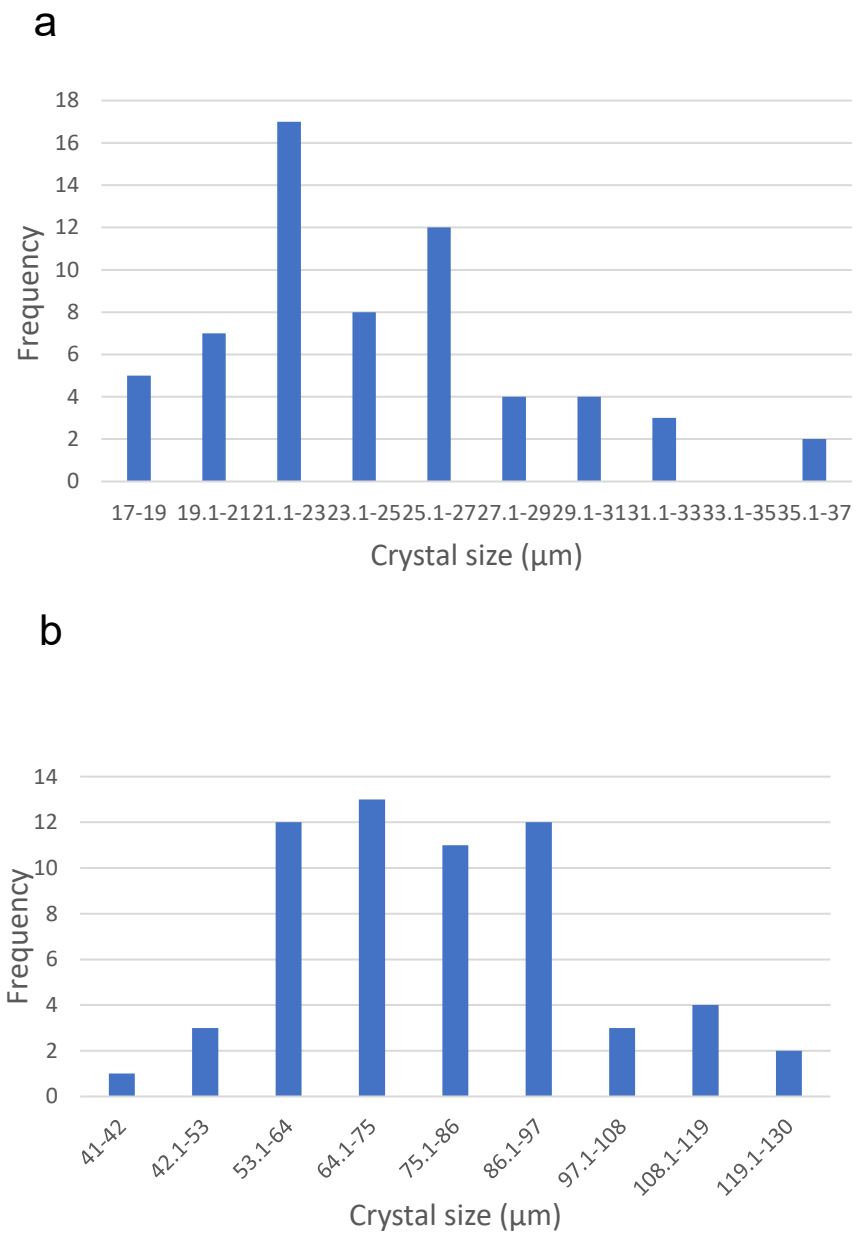


Figure A- 4: Particle size histograms of crystals on the substrate surface synthesised at linker/metal ratio of 2 and metal concentrations 72 mM (a) and 288 mM (b). Membranes synthesised for 5 hours at 150 °C.

Figure A-5 shows surface image of membrane synthesised using zinc nitrate hexahydrate for one cycle. Substrate surface is covered with patches of growth, this may suggest that the zinc nitrate produces a weaker level of growth on tubular substrates than zinc nitrate when coating with a single layer.

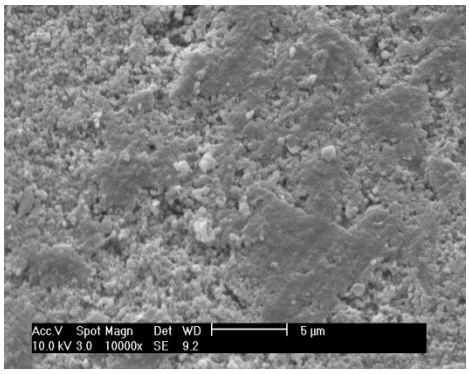


Figure A- 5: Surface image of membrane synthesised with zinc nitrate hexahydrate at linker/metal ratio 7 and metal concentration of 36 mM for one cycle. Synthesised at 150 °C for 5 hours using conventional heating.

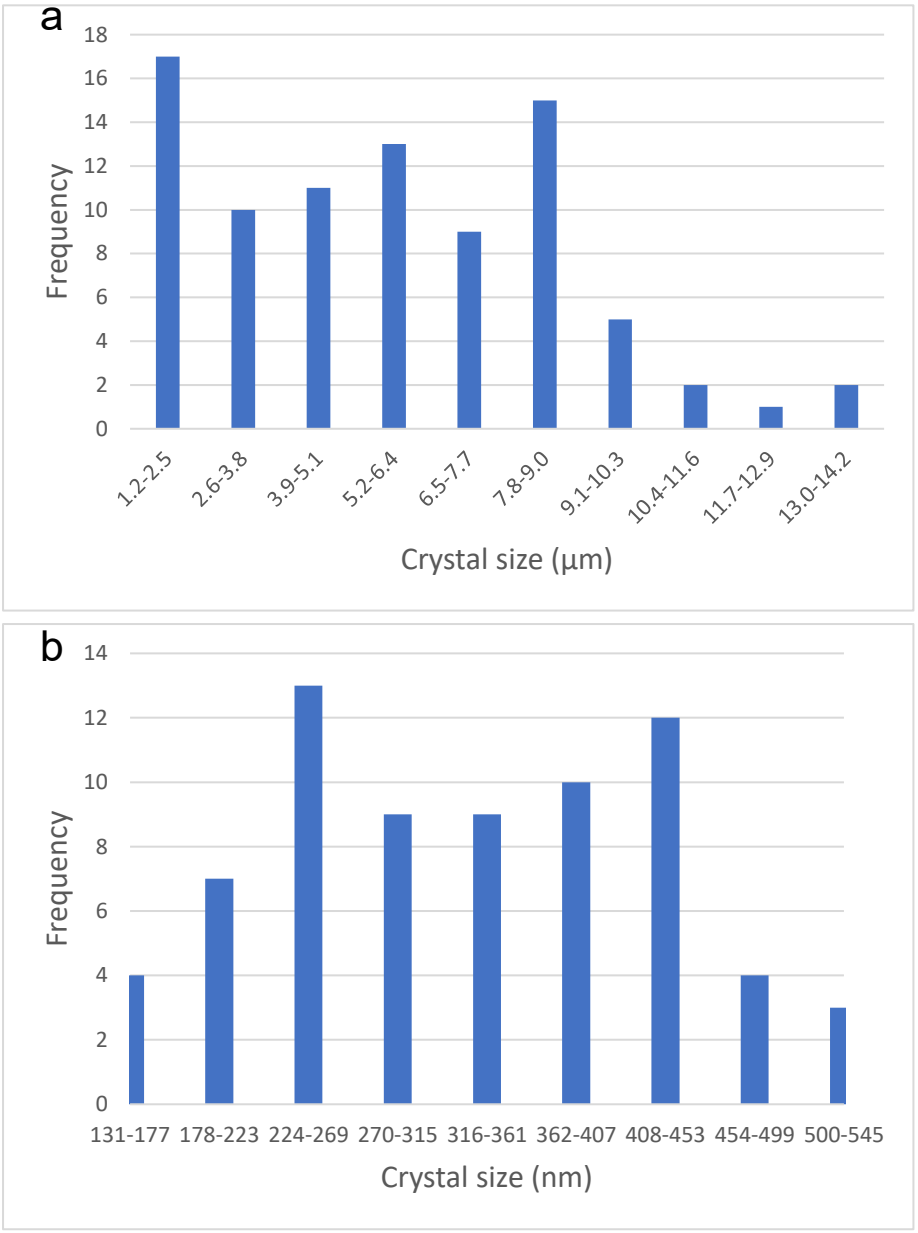


Figure A- 6: Particle size histograms of crystals on the substrate surface synthesised at linker/metal ratio 8 and metal concentrations 36 mM for two cycles using zinc acetate (a) and zinc nitrate (b). Membranes synthesised for 5 hours at 150 °C.

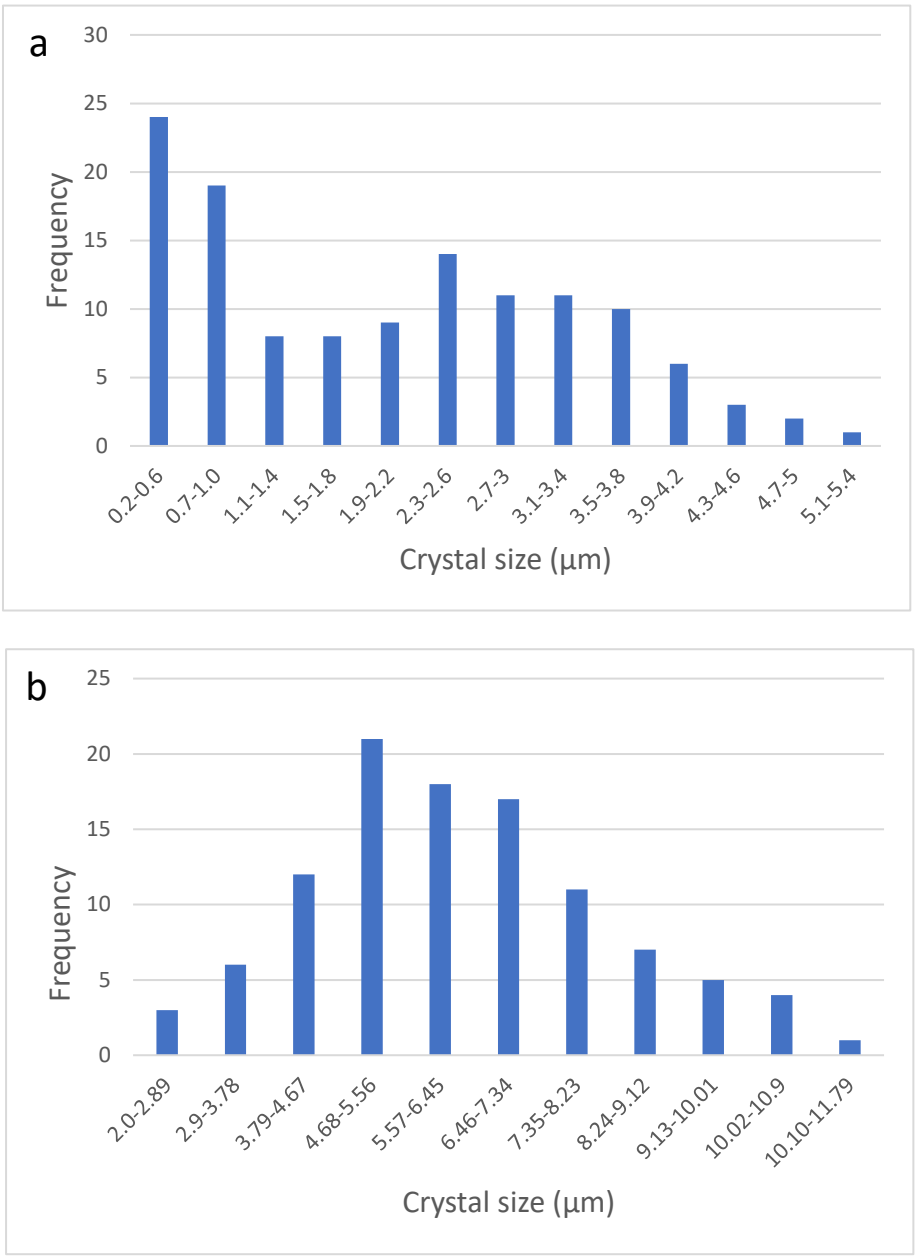


Figure A- 7: Particle size histograms of crystals on the substrate surface synthesised at linker/metal ratio 8 and metal concentrations 36 mM (a) and 144 mM (b). Membranes synthesised for 10 hours at 150 °C.

5. Batch synthesis of ZIF-8 membranes using isolated precursors under conventional heating

5.1 Introduction

The previous chapter investigated the heterogenous growth of ZIF-8 onto tubular substrates where mixed precursors were used, and the parameters that controlled the membrane microstructure. The work was carried out systematically to better understand the optimum conditions for the synthesis of ZIF-8 membranes under conventional heating.

The synthesis of ZIF-8 membranes using mixed precursors indicated that the formation of ZIF-8 is a predominantly homogeneous nucleating system. To further investigate the nature of heterogeneous growth of ZIF-8 in the batch system, a novel set-up while isolating metal and linker solutions is introduced to better understand the interaction of the precursors at the surface of the substrate. This chapter will continue with the same scientific approach of adopting a systematic study to better understand the optimum conditions for the synthesis of ZIF-8 membranes when the precursors are diffusing across the substrate pores. The reaction chemistry (concentrations, linker/metal ratio, conjugate base) will be investigated to understand its control on membrane microstructure with isolated precursors.

5.2 Experimental procedure

5.2.1 Membrane synthesis with precursor isolation

Membranes were prepared, where metal and linker solutions were isolated during the synthesis rather than mixing. Only linker/metal ratios of 2 and 8 and metal concentrations of 72 and 288 mM were used, respectively. The metal and linker solutions were prepared, as described in chapter 4.

Prior to the experiments, one end of the 6 cm long alumina substrate was sealed using a Teflon® plug. Teflon® tape was tightly wrapped around the joint between a plug and the substrate. Metal or linker solution was slowly added into the substrate until fully filled. The other end of the substrate was sealed with a plug and then Teflon® tape was

wrapped around the joint. Substrates were transferred to a 45 ml Parr® reaction vessel with a Teflon® liner along with 26 ml of metal or linker solution outside the substrate. The sealed vessel was then placed in a Heratherm™ (Thermoscientific) oven at 150 °C for 5 hours. Figure 5-1 shows a schematic of sealed substrates in a Parr reaction vessel.

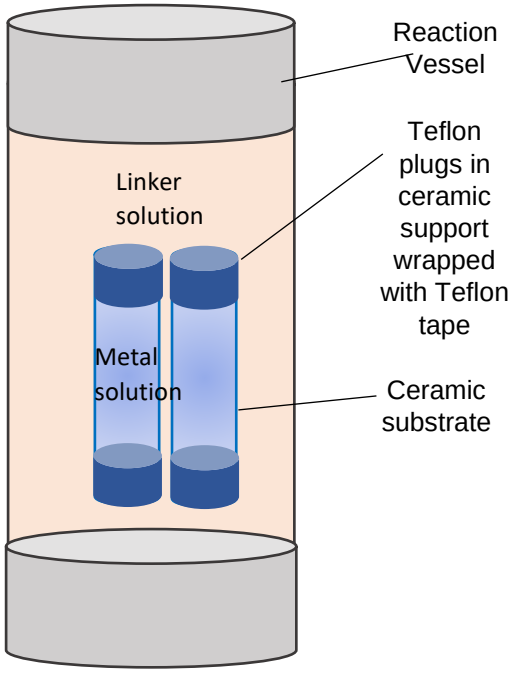


Figure 5- 1: Schematic of sealed substrate in a reaction vessel filled with linker solution, and two Teflon plugged alumina substrates filled with metal solution.

After quenching the reaction vessel, membranes were removed and rinsed under tap water for ~ 2 minutes and then rinsed with 300 ml deionised water. The membranes were then dried at 100 °C for 2 hours. The leftover linker and metal solutions were collected in glass vials and stored at room temperature. Table 5-1 shows the experimental conditions of the membranes synthesised with isolated precursors.

Table 5- 1: Metal salts, concentrations, linker/metal ratio, seeding and synthesis time used for batch synthesis.

Metal salt	Linker/ metal	Metal concentration (mM)	Synthesis time (h)	Temperature (°C)	Seed
Zinc acetate dihydrate	8	72	24	25	No
		288			
		36	5	150	Yes
	8, 2	72			Yes, No
		288			Yes, No
	32	288			Yes
Zinc nitrate hexahydrate	8	288			

For the calculation of molar flux of the precursors Equation 5-1 was used (Cengel, 2006):

$$\dot{N}_{diff,A,cyl} = 2\pi L D_{AB} \frac{C_{A,1} - C_{A,2}}{\ln(r_2/r_1)} \quad \textbf{(Equation 5- 1)}$$

Where, N is the molar flux, L is the length of the cylindrical tube, D_{AB} is the diffusivity coefficient, $C_{A,1}$ and $C_{A,2}$ is the concentration inside and outside of substrate, respectively, and r_1 and r_2 are the inner and outer radius of cylinder, respectively.

The diffusivity coefficient was calculated by using Equation 5-2 (Treybal, 1981):

$$D_{AB}^{0} = \frac{117.3\times10^{-18}(\varphi M_B)^{0.5}T}{\mu v_A^{0.6}} \qquad \textbf{(Equation 5- 2)}$$

Where, D^0_{AB} is diffusivity (m^2/s) of A in very dilute solution in solvent B, M_B (kg/kmol) is molecular weight of the solvent, T (K) is temperature, v_A is solute molar volume (m^3/mol), μ is solution viscosity (=0.001005 kg/m.s), and ϕ is the association factor (1.9 for methanol).

5.2.2 Particle size and surface area measurement

Crystal sizes and surface area were estimated using ImageJ® software. Approximately 100 crystals boundaries were identified and measured from up to three SEM images taken per membrane synthesised where possible. The results were then presented in histograms for interpretation (Appendix). The surface area was measured from two different locations per membrane where possible and the surface area covered with crystal growth presented as a percentile range between the locations. The surface area results have been tabulated.

5.3 Results

Figure 5-2 shows surface images of unseeded membranes synthesised with metal solution outside of the substrate at room temperature at a metal concentration of 72 mM and 288 mM with metal/linker ratio of 8. The surface images show neither the growth of dense crystals nor membrane films on the surface, which may be due to the room temperature synthesis. This may suggest that the energy needed for the precursors to diffuse through the substrate pores is not sufficient. In addition, the weak surface growth may be due to the absence of seeds on the surface as seeds promote nucleation and growth (Xie et al., 2012, Tanaka et al., 2014b, Zhu et al., 2016).

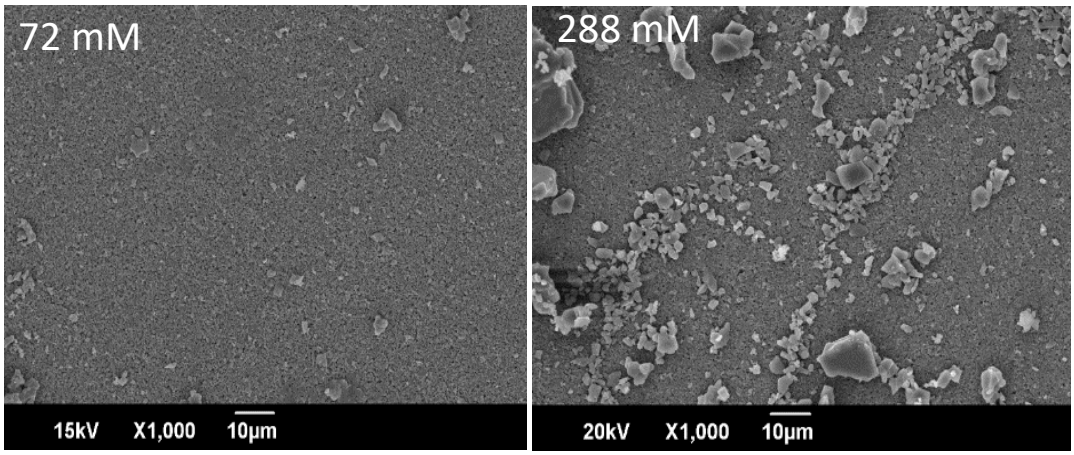


Figure 5- 2: Surface images of the unseeded membranes synthesised (metal solution out) at room temperature for 24 hours with linker/metal ratio of 8 and metal concentrations of 72 mM and 288 mM.

The isolated precursor system with metal solution outside of the substrate was repeated at 150 °C for 5 hours. Figure 5-3 shows the surface and cross-sectional SEM images of membranes synthesised at 72 and 288 mM concentrations, and linker/metal ratio of 8. From the SEM images, crystals were visible inside the substrate surface for both of 72 and 288 mM metal concentrations. This suggests that the metal ions diffused through the substrate pores and reacted with the linker inside the substrate. This approach probably slows the rate of ZIF-8 formation reaction because of slower metal ion diffusion flux (0.2×10^{-8} mol m^{-2} s^{-1}) when compared to linker (6×10^{-8} mol m^{-2} s^{-1}). This allows the crystal growth on the surface rather than in the solution. The SEM images reveals cubic and rhombic crystals on the substrate surface, suggesting ZIF-8 structure for both concentrations. At 288 mM concentration, the diffusion rates of metal and linker ions are estimated as 2×10^{-8} and 58×10^{-8} mol m^{-2} s^{-1}, respectively. At both concentrations, the linker ions are the faster diffusing component due to the excess linker concentration. In addition to this, the flux will be greater for the respective component located outside the substrate, since the solute molal volume (=c/v) is inversely proportional to the volume. Therefore it can be speculated that membrane microstructure can be controlled by the precursor location.

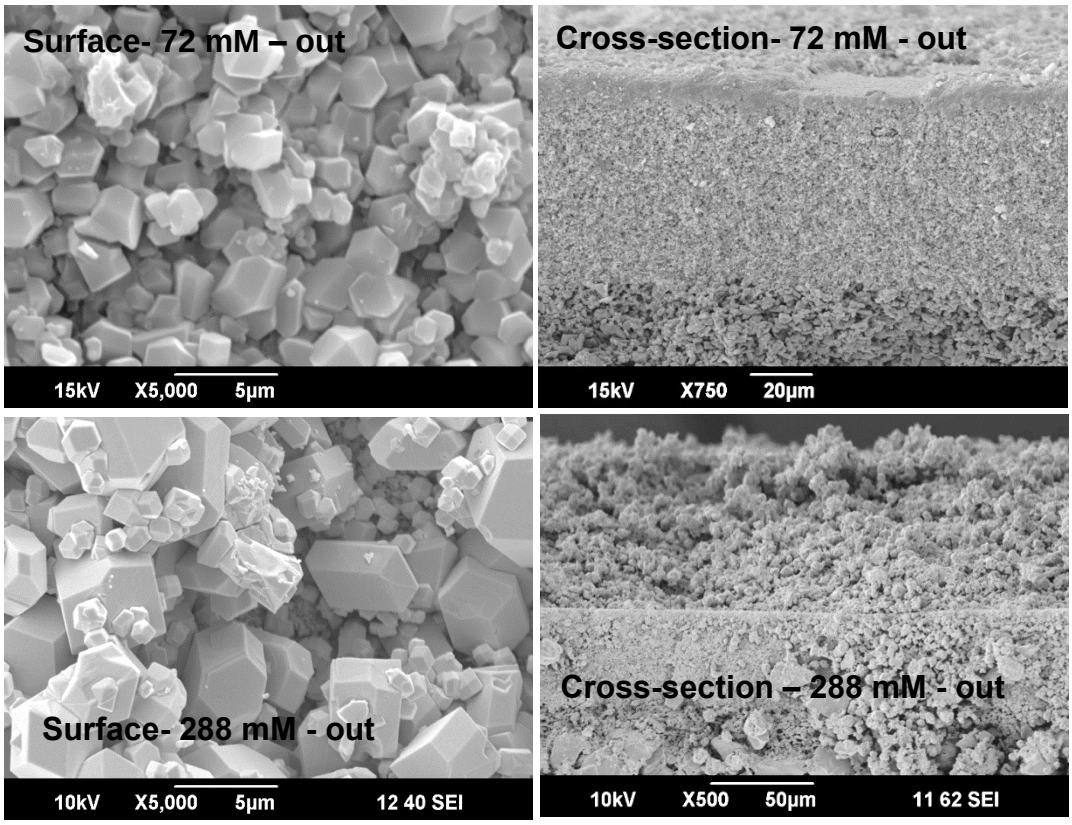


Figure 5- 3: Surface and cross sectional SEM images of membranes synthesised on unseeded substrates with isolated pre-cursors (metal outside) at 150 °C for 5 hours (Linker/metal ratio= 8, metal concentration= 72 and 288 mM).

The cross-section SEM images taken from another region of the same coated substrates, indicate a continuous film at both concentrations, particularly at 288 mM with approx. thickness of 60 µm. The film is thicker than the one synthesised (37 µm) with mixed solution using seeds at the same metal concentration. Obtaining thicker film may be due to the fewer nuclei formed in the system in the absence of seeds that slows down the nucleation rate. Xie et al. reported that a higher concentration of nucleation sites on the substrate surface leads to thinner membranes (Xie et al., 2012) since the higher concentrations of nuclei on the substrate surface reduces the amount of precursors available per nuclei is reduced. Subsequently, this limits the length of time for which the growth can be sustained for per nuclei and hence smaller crystals and thinner membranes are generated. The crystals for 72 mM concentration distributed along the substrate surface whilst the film is thinner. The nature of the growth suggests that there was a higher nucleation density on the surface of the selected 72 mM sample characterised thereby resulting in a thinner membrane. One

theory is to have high concentrations of precursors to help promote higher reaction rates rather than diffusion rates thereby encouraging ZIF-8 nuclei formation within the vicinity of the substrate surface. However, the weak interaction of ZIF-8 structure with the substrate surface limits the growth onto the substrate surface since favourable interactions between precursors and substrate surface promotes heterogenous nucleation (Tuninetti et al., 2015). This may reemphasise the importance of surface modification for ZIF-8 structure that may not be very critical for other ZIFs i.e.– Huang et al. achieved continuous ZIF-71 synthesis onto unseeded tubular alumina substrates in their isolated system (Huang et al., 2015). Figure 5-4 shows the XRD patterns of the unseeded membranes synthesised with the isolated pre-cursors (metal solution outside of the substrates). These membranes were synthesised at 150 °C for 5 hours using metal concentrations of 72 and 288 mM with linker/metal ratio of 8. The XRD pattern of the unseeded membrane at 72 mM shows all the peaks, indicating the nature of the growth seen in the SEM images to be continuous and sufficiently thick. The XRD pattern of the 288 mM indicates that the crystal growth is preferentially oriented since not all peaks of ZIF-8 are detected.

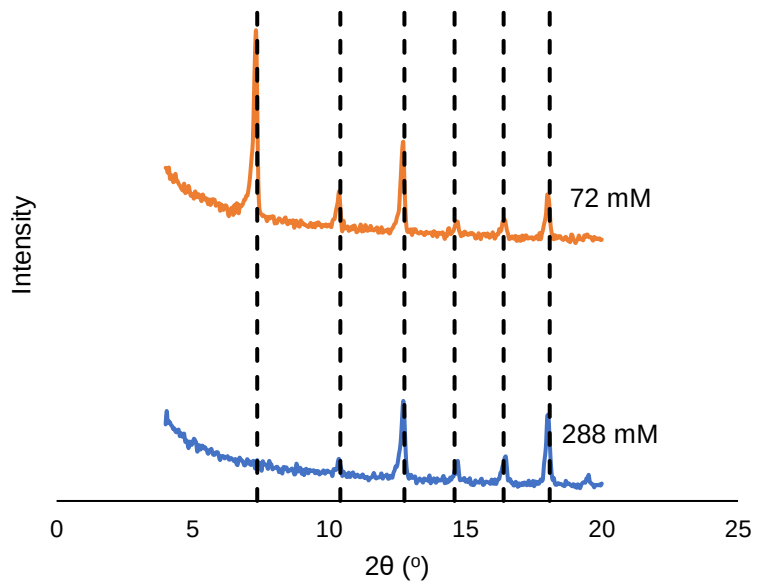


Figure 5- 4: XRD patterns of membranes synthesis on unseeded substrates with isolated pre-cursors (metal outside) using conventional heating at 150 °C for 5 hours with a linker/metal ratio of 8 at metal concentration of 72 mM and 288 mM. The dashed lines refer to the position of the most prominent characteristic peak of ZIF-8.

Figure 5-5 shows surface and cross-sectional images of the seeded membranes, synthesised (metal out) at 150 °C for 5 hours, using metal concentrations of 36, 72 and 288 mM and linker/metal ratios of 8. A third concentration of 36 mM was introduced into the seeded membrane synthesis to gain a better understanding of the effect of reduced flux on the microstructure of ZIF-8 growing onto the substrate.

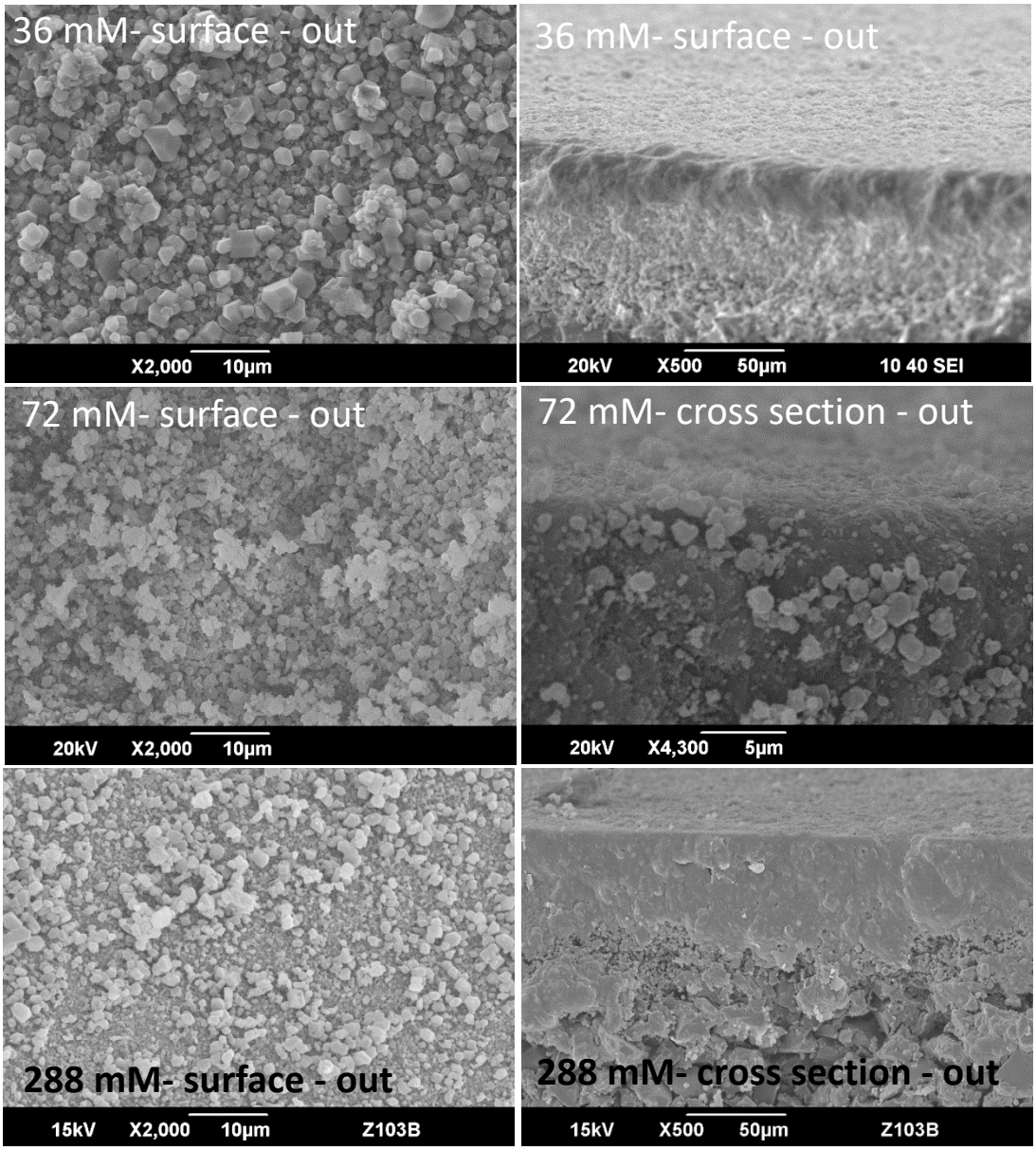


Figure 5- 5: Surface images and cross sectional SEM images of the membranes synthesised on seeded substrates with isolated pre-cursors (metal outside) at 150 °C for 5 hours (Linker/metal ratio= 8, metal concentration= 36 mM, 72 mM, and 288 mM).

Unlike the unseeded growth, the surface images suggest a similar level of surface growth across the three concentrations. The crystal size ranges were estimated in the

region of 0.42-2.78, 0.47-2.25, and 0.49-5.18 µm for 36, 72 and 288 mM, respectively. However, from the histograms (Figure A-1), a single modal crystal size was obtained for 36 mM whereas for 72 and 288 mM, this was bimodal. This indicates the crystals are growing with increasing precursor concentration. However, when relating the isolation (metal out) and mixed MOF seeded systems at their respective concentrations, there is a difference in crystal sizes. The crystal size range of the mixed MOF system at linker/metal ratio 8 were between 0.29-0.86, 0.87-2.51 and 4.56-16.30 µm at 36, 72 and 288 mM, respectively. In addition, the smaller crystal size in the isolated system suggests that there are more nuclei present at the surface at the respective concentrations. Potentially, this may imply that the reaction 'zone' at the substrate surface is ongoing for most of the 5 hours synthesis time and Ostwald ripening effect has been reduced since the smaller crystals remain on the substrate surface in the isolated system. To date studies on heterogenous nucleation of ZIF-8 in batch systems, where precursors are isolated are limited and provide no quantitative data on precursor fluxes. Except for Marti et al. continuous system that reported membrane thickness and morphology to be controlled by reagent flow rates. Marti et al. worked across three flow rate pairs of 0.1/0.1, 0.25/0.13, and 0.5/0.5 ml/min of Zn^{2+}/HmIm. Flow rates of 0.1/0.1 delivered no growth, 0.25/0.13 achieved a dense film on the outer surface with the growth originating from within the substrate microstructure, and a more brittle growth was obtained only on the outer surface of the substrate at 0.5/0.5. Although ZIF-8 membrane publications (Kwon et al., 2016a) and powders (Voorhees, 2002, Venna et al., 2010) commented on the Ostwald ripening process, the discussions were focused on the phenomena of the more evolved and larger crystals growing at the expense of the smaller and less stable nuclei disappearing (section 2.4).

Figure 5-6 shows the XRD patterns of the membranes when metal solution was outside of the substrates. Surprisingly, only some of the characteristic peaks (at 7.36, 12.76 and 18.09 reflecting planes 011, 112 and 222, respectively) of ZIF-8 were detected for the membranes synthesised at the 36 mM and 72 mM. This implies that the detected crystals on the surface have a preferred orientation. The preferred orientation may indicate that the growth maybe a film (as was suggested by the cross-sectional images), and the crystals from the film facing the detector are preferentially oriented. The XRD patterns of the coated substrates at 288 mM show all characteristic peaks of ZIF-8, whilst the intensity of the peaks reflecting the planes 022 and 113 at 14.6 and

16.4 °, respectively, are very low. This may suggest the oriented crystals are more densely packed than the growth detected at 36 and 72 mM concentrations.

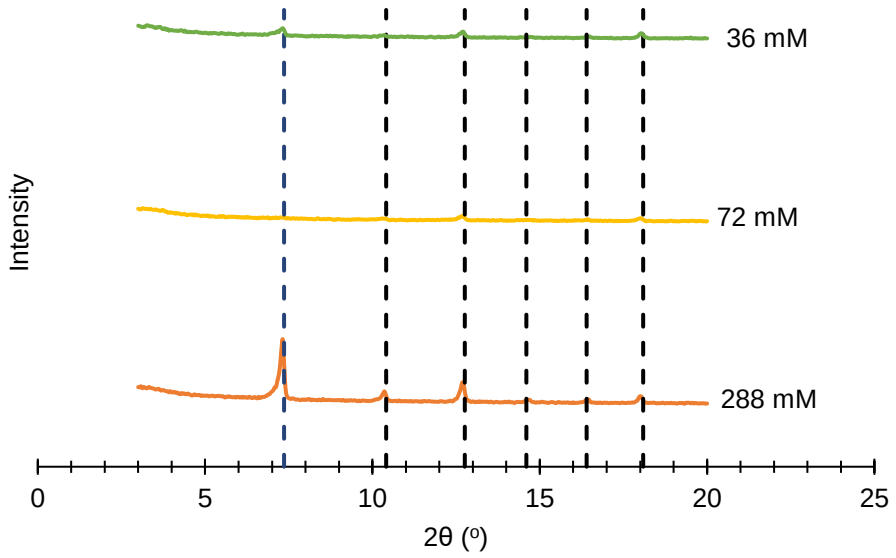


Figure 5- 6: XRD patterns of membranes synthesised on seeded substrates at 150 °C for 5 hours (linker/metal ratio= 8, metal concentration= 36 mM, 72 mM and 288 mM, metal solution was outside). The dashed lines refer to the position of the most prominent characteristic peak ZIF-8.

EDX measurements were conducted to further analyse the ZIF-8 growth on the substrates for 72 and 288 mM. Figure 5-7 shows surface SEM images and the respective mapping of Zn. At both concentrations, the elemental analyses prove that the surface of the substrates are covered with ZIF-8 crystals. Perhaps film thicknesses were either too thin to be detectable via XRD or the samples used for XRD were not covered.

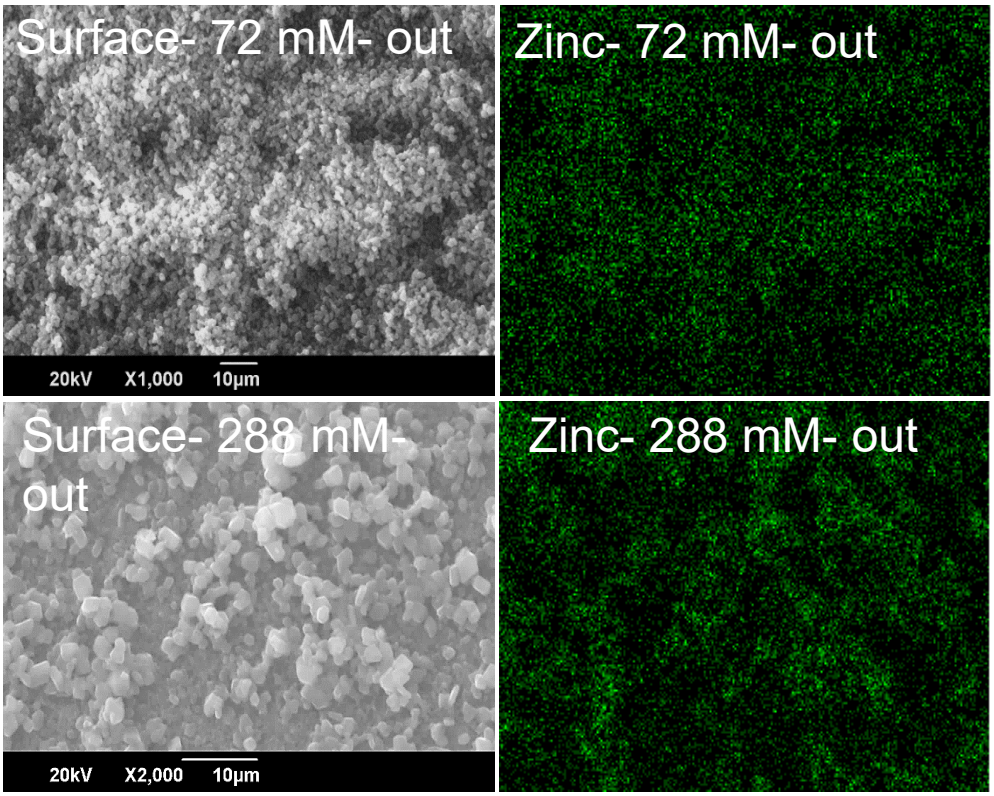


Figure 5- 7: Surface SEM images and EDX elemental analysis of membranes, synthesised with isolated pre-cursors (metal outside) at 150 °C for 5 hours with linker/metal ratio of 8 and metal concentrations of 72 mM and 288 mM. Green represents Zinc.

Figure 5-8 show the cross section SEM images (not of same scale) of unseeded membranes synthesised with isolated precursors (metal inside) using metal concentrations of 72 and 288 mM, and linker/metal ratio of 8. The images at both concentrations show crystals of rhombic nature of ZIF-8 and a denser growth at 288 mM when compared to the 72 mM.

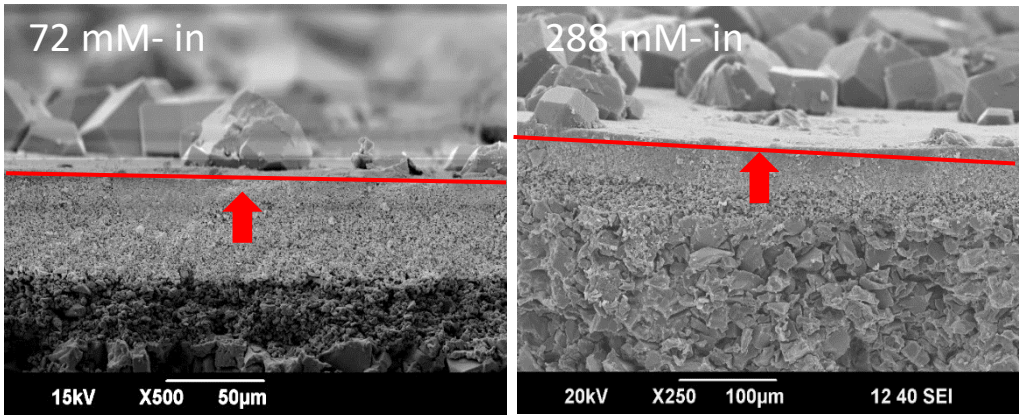


Figure 5- 8: Cross section SEM images of membranes synthesised on unseeded substrates with isolated pre-cursors (metal inside) at 150 °C for 5 hours with a linker/metal ratio of 8 and metal concentrations of 72 mM and 288 mM. Red lines (and arrows) show where the cross section of the substrate begins.

The cross-sectional images show loosely packed rhombic crystals on the substrate while there are cubic crystals on the surface too. This may be an indication of the less stable and evolved crystals continue to grow rather than dissolving and reappearing on the more evolved rhombic crystals. In conclusion, the unseeded metal-in system indicates that the reaction system is ongoing, past the first 60 minutes of the ZIF-8 nucleation stage.

Due to the changes in the precursors location and hence the change in the precursor fluxes, the dynamics of the reacting system changed with the metal out system. This is reflected in the surface growth when comparing the unseeded SEM images of metal out, at their respective concentrations. When the metal precursor is inside the substrate the flux of metal and linker ions at 72 mM concentration is $1x10^{-8}$ and $6x10^{-8}$ mol/m^2. s, respectively. At 288 mM concentration the flux of metal and linker ions is $10x10^{-8}$ and $58x10^{-8}$ mol/m^2. s, respectively. The cross-sectional images of metal out unseeded systems indicate growth of films from within the substrate pores. The metal in unseeded substrates suggest no film growth, which indicates the precursor diffusion rates are controlling the rate of reaction in the metal-linker isolation system as Kwon and Jeong et al. reported in their contra-diffusion system (Kwon and Jeong, 2013). To conclude, the metal-linker isolation system indicates that the precursor location can control the nature of the heterogeneous growth of ZIF-8. A similar study to the metal-linker isolation system was conducted by Yao et al. (Yao et al., 2011). They used

unmodified flat polymer disks because of the favourable interaction between the ZIF-8 linkers and polymer structure, and growth was achieved on both sides of the polymer substrate. However, Yao et al. reported there was a difference between the particle sizes of the membrane on the linker and metal precursor location sides. Although no mathematical data was presented, they reported this was due to local molar ratios, larger and smaller ZIF-8 particles were observed on the metal and linker sides of the substrate, respectively. Yao et al. reported the local molar ratios were close to zero and greater than their system design ratio of 8 on the metal and linker sides, respectively; reflecting 400 nm crystal size reported by Yao et al. for the metal side and the measured particle size of 200 nm on the linker side. Due to crystal fusion and irregular shapes (see Figure 3f) only a limited number of crystals could be measured for the linker side. In conclusion, the membrane microstructure can be controlled by the precursor location - difference in precursor fluxes, controls heterogenous growth of ZIF-8.

Figures 5-9 show the XRD pattern of the unseeded membranes synthesised when metal solution was inside the substrate with metal concentrations of 72 and 288 mM, and linker/metal ratio of 8. The XRD pattern of the unseeded membranes at 72 mM indicates that the growth on the surface with crystals of no preferred orientation. The absence of ZIF-8 peaks for 288 mM was not expected since the surface and cross sectional images - each taken from different locations of the same substrate for a more critical analysis, indicated growth of typical cubic/rhombic ZIF-8 crystals. The peaks that are detected could be peak shifting that can be due to sample height not being level. Because the peaks at 8.2, 11.4, 13.7, 15.7, 17.5 and 19.1 ° do not reflect precursor characteristic peaks.

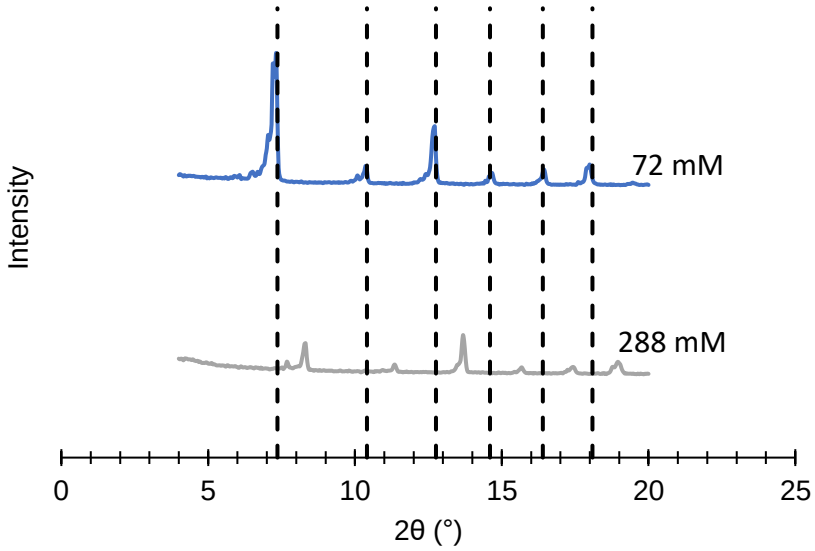


Figure 5- 9: XRD patterns of membranes synthesised without seeds with isolated precursors (metal inside) at 150 °C for 5 hours using a linker/metal ratio of 8 and metal concentrations of 72 mM and 288 mM. The dashed lines refer to the position of the most prominent characteristic peaks of ZIF-8.

Figure 5-10 shows the cross section and XRD patterns of seeded membranes synthesised with isolated precursors (metal inside) at metal concentrations of 36, 72 and 288 mM, and linker/metal ratio of 8. The SEM images suggest the ZIF-8 crystals are more evolved with morphology more representative of their equilibrium rhombic shape with crystal sizes between 4.57-14.01, 12.01-67.35, 33.92-171.89 μm at metal concentrations of 36, 72 and 288 mM, respectively (Figure A-2 for histograms), indicating that crystal sizes increase with increasing concentration. Because of the novelty of the metal-linker isolation work, there are limited ZIF-8 membrane papers similar to the metal-linker isolation system that relate reaction mechanisms, Zhu et al. and Xie et al. do not present quantitative data to relate the precursor fluxes to the crystal size distribution (Xie et al., 2012, Yao et al., 2011). However, a hypothesis can be formed, the nature of the distribution of crystal size does vary between the metal in and out systems at the respective concentrations, highlighting a difference between reacting systems based on precursor location and flux. At 36 and 72 mM a modal distribution is observed, and at 288 mM shows a multimodal distribution. Reflecting how the fluxes govern the reaction mechanisms across the systems. The multimodal distribution may imply an ongoing nucleation and evolution system past the reported 60

minutes of ZIF-8 growth cycle. This implies that the precursor fluxes across the system boundary changes the reaction rate, leading to a change in the rate of formation and evolution of the ZIF-8 nuclei in the metal-linker isolation system.

When the metal is outside, the largest crystals size was 16.30 µm at 288 mM. This indicates the precursor location/flux can control the microstructure of the ZIF-8 structures on the substrate even though the linker/metal ratio is the same. This suggests the creation of local molar ratios at the substrate surface, that are controlled by the precursor fluxes (Table A-1). However, even with the reaction zone being brought to the substrate surface and its pores, the SEM images suggest inhomogeneous growth on the substrate surface. This implies a more tailored surface modification is needed than the physical deposition of seeds – this is discussed in detail at the end of the chapter with Fig. 5-20.

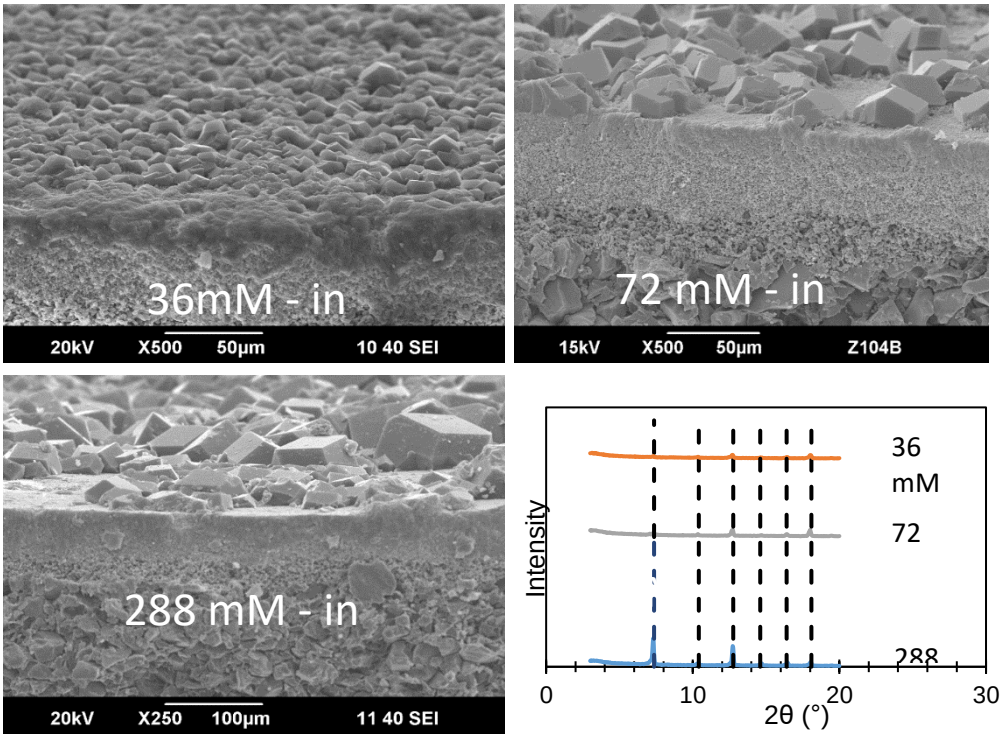


Figure 5- 10: Cross section SEM images and XRD patterns of membrane synthesised on seeded substrates with isolated pre-cursors (metal inside) at 150 °C for 5 hours at a linker/metal ratio of 8 and metal concentrations of 36 mM, 72 mM, and 288 mM.

The XRD patterns for the membranes at 36 and 72 mM may suggest that the growth is preferential since the characteristic peaks of ZIF-8 reflects 112 and 222 planes. The XRD pattern of the 288 mM sample indicates peaks reflective of the 011 and 112 crystallographic planes that are of higher intensity than other detected peaks, which

implies there is a higher concentration of crystals with the 011 and 112 faces parallel to the substrate, facing the detector.

Figures 5-11 shows EDX analyses for zinc ions from the respective SEM surface images, comparing crystal growth at metal concentrations of 72 and 288 mM. The analyses show that crystals are not densely packed since black areas are observed that indicates the substrate. The elemental analysis of metal inside suggests a more successful growth on the substrate than when the metal solution is outside of the substrate (Fig. 5-7) since there are areas with clear dense growth of Zn.

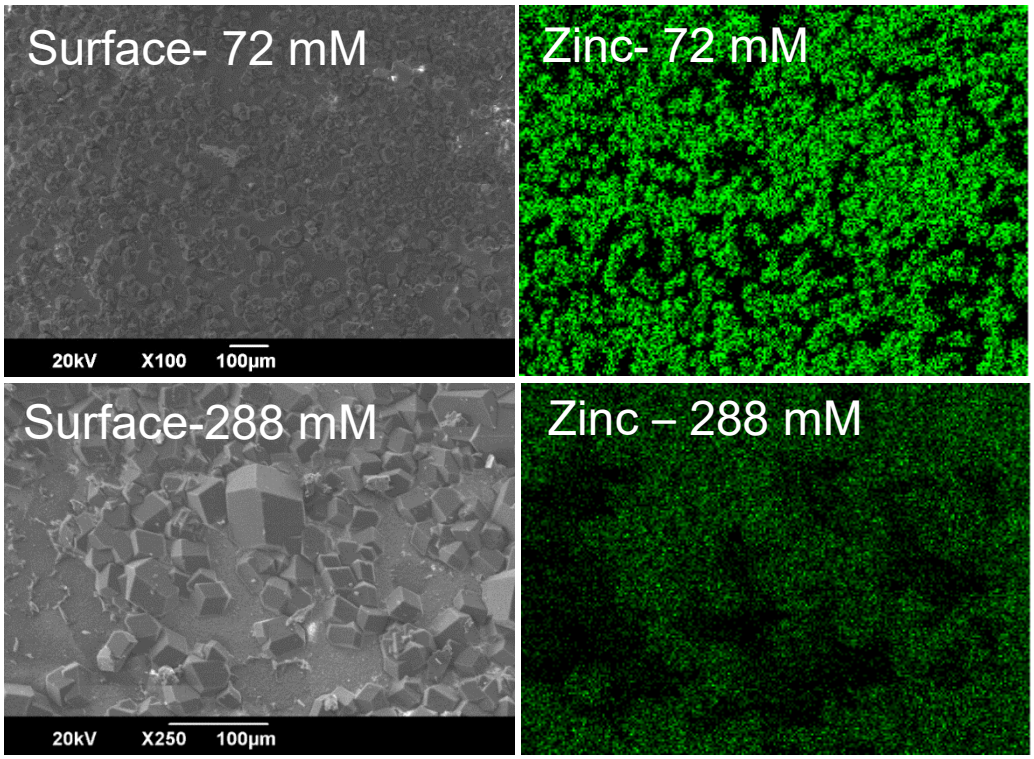


Figure 5- 11: Surface images and zinc analysis of seeded membranes synthesised at 72 mM and 288 mM at 150 °C for 5 hours. Isolated pre-cursors (metal inside) and linker/metal ratio of 8.

As well as investigating the growth of ZIF-8 onto the tubular substrates, the novel metal-linker isolation study allows the assessment of the interaction of linker and metal ions at the substrate surface. The novel study clearly shows how the change precursor location affects the microstructure of the deposited crystals at the substrate. Table 5-2 summarises the fluxes and respective crystal sizes of the isolated system at linker/metal ratio 8, tabulated by precursor location and concentration. The precursor location/flux controls the crystals size of ZIF-8 crystals even when at the same linker/metal ratio, allowing the membrane microstructure to be controlled. Suggesting

that the nature of heterogenous growth can also be controlled by the fluxes too. Although a counter diffusion system was used, Kwon and Jeong et al. similarly reported that the rate of diffusion is needed to be slower than nucleation rate to ensure the reaction takes place within the vicinity of the substrate surface and its pores (Kwon and Jeong, 2013). This was assessed, where the linker flux was reduced (linker/metal ratio adjusted to 2).

Table 5- 2: Summarising fluxes and crystal sizes of the isolated system at linker/metal ratio 8 at their respective precursor location and metal concentration.

Precursor measured and its location	Concentration of metal precursor (mM)	Crystal size range (µm)	Flux of precursors x 10^{-8} (mol/m^2.s)	
			Metal	Linker
Metal in/ linker out	36	4.6-14.0	0.35	58
	72	12.0-67.4	1	6
	288	33.9-171.9	10	2.1
Metal out/linker in	36	4.6-16.3	0.075	9.7
	72	0.87-2.5	0.2	29
	288	0.29-0.86	2	270

To better understand the metal-linker isolation system the linker/metal ratio was reduced to 2, where the precursors flux of linker is smaller by an order of magnitude (Table A-1). Figure 5-12 shows surface images of the membranes synthesised with isolated precursors with metal outside the tubular substrates. The crystal sizes are between 3-8 µm and 2-8 µm at metal concentrations of 72 and 288 mM, respectively. The surface images may suggest that when the precursors are isolated the crystals are more evolved at the linker/metal ratio 2 when compared to the ratio of 8 (Figure 5-7), since the smaller linker/metal ratios have less nuclei in the system allowing the growth of each crystal to be sustained for longer. This may imply that the change in precursors

flux affected the rate of evolution of the nuclei in the isolated system. The cross-sectional images suggest similar level of growth between the two substrates at their respective concentrations (Figure A-3).

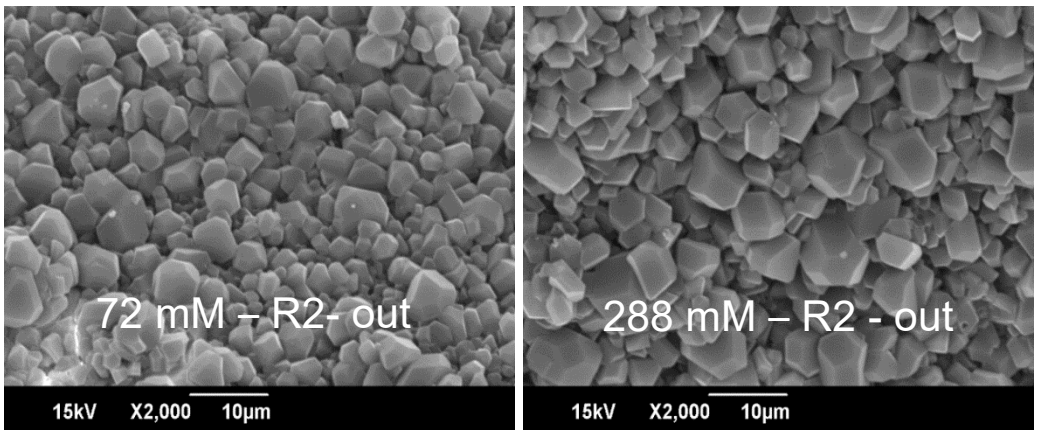


Figure 5- 12: Surface images of membranes synthesised on seeded substrates with isolated pre-cursors (metal outside) using conventional heating at 150 °C for 5 hours with a linker/metal ratio of 2 and metal concentrations of 72 mM and 288 mM.

Figure 5-13 shows the XRD pattern of membrane synthesis with metal solution outside the substrates with linker/metal ratio 2 synthesised at metal concentrations of 72 and 288 mM. The membranes were synthesised at 150 °C for 5 hours using conventional heating with linker/metal ratios of 2. Although the SEM image showed good coverage of substrate surface with micron size crystals, no characteristic peaks was observed at the metal concentration of 72 mM. This is probably due to the selected substrate sample, which may have no growth. The XRD peaks of the 288 mM membrane shows the characteristic peaks of ZIF-8 the peak at 7.36°, suggesting a dense coverage of fully evolved ZIF-8 crystals.

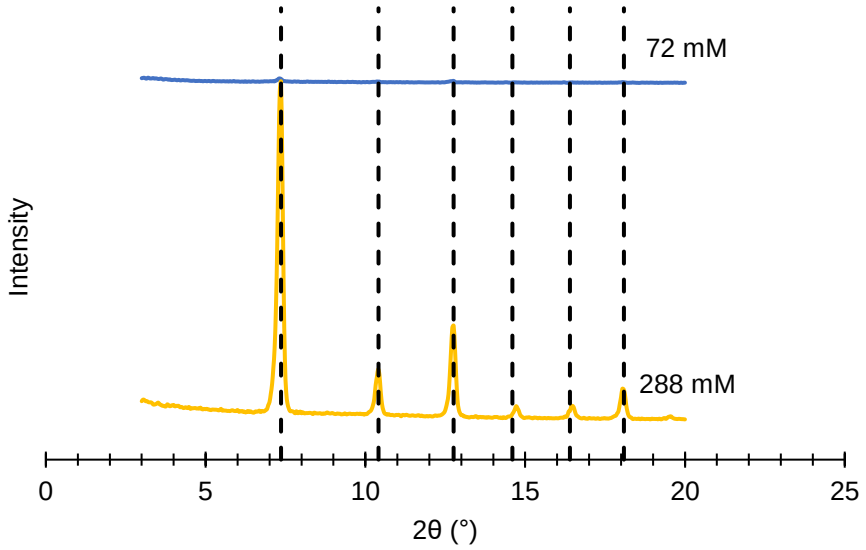


Figure 5- 13: XRD patterns of membranes synthesised on seeded substrates with isolated pre-cursors (metal outside) at 150 °C for 5 hours using linker/metal ratio of 2 and metal concentration of 72 mM and 288 mM. The dashed lines refer to the position of the most prominent characteristic peak of ZIF-8.

To shed light on the structure of membranes synthesised using 72 mM metal concentration, EDX analysis was performed. In contrast to XRD pattern, Figure 5-14 clearly shows the zinc ions on the surface of the substrates that proves the ZIF-8 growth. This may suggest that the effects of Ostwald ripening may have less of an effect on the heterogenous growth of ZIF-8 with isolated precursors when the metal is outside the substrate.

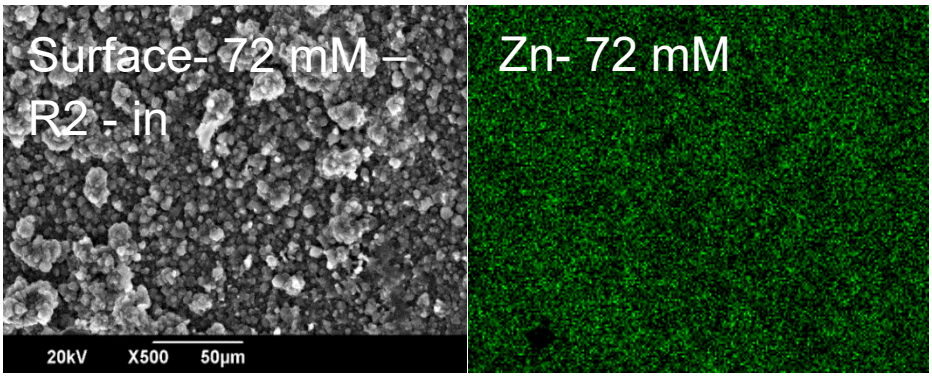


Figure 5- 14: Surface image and EDX analysis of a membrane, showing Zn ions (in green), synthesised on seeded substrates with isolated pre-cursors (metal outside) at 150 °C for 5 hours, linker/metal ratio of 2 and metal concentration of 72 mM.

Figure 5-15 shows surface images of membranes synthesised with isolated precursors (metal inside) at linker/metal ratio of 2, and metal concentrations of 72 and 288 mM. Surface images suggest that when the metal is inside the tubular substrate the crystal sizes are greater, similar to linker/metal ratio 8. The surface images may show that when the metal precursor is inside the substrate the crystal sizes are between 8-114 µm and 19-280 µm at metal concentrations of 72 and 288 mM, respectively. The surface images may imply the heterogenous growth of ZIF-8 with isolated precursors reduced the effects of Ostwald ripening since the growth of crystals across the substrates at their respective concentrations suggest that the smaller crystals remained on the surface of the substrate and were not dissolved to provide nutrients for the more thermodynamically stable rhombic shaped larger crystals (Voorhees, 2002, Venna et al., 2010). The cross sectional images (Figure A-4) support the observed surface growth.

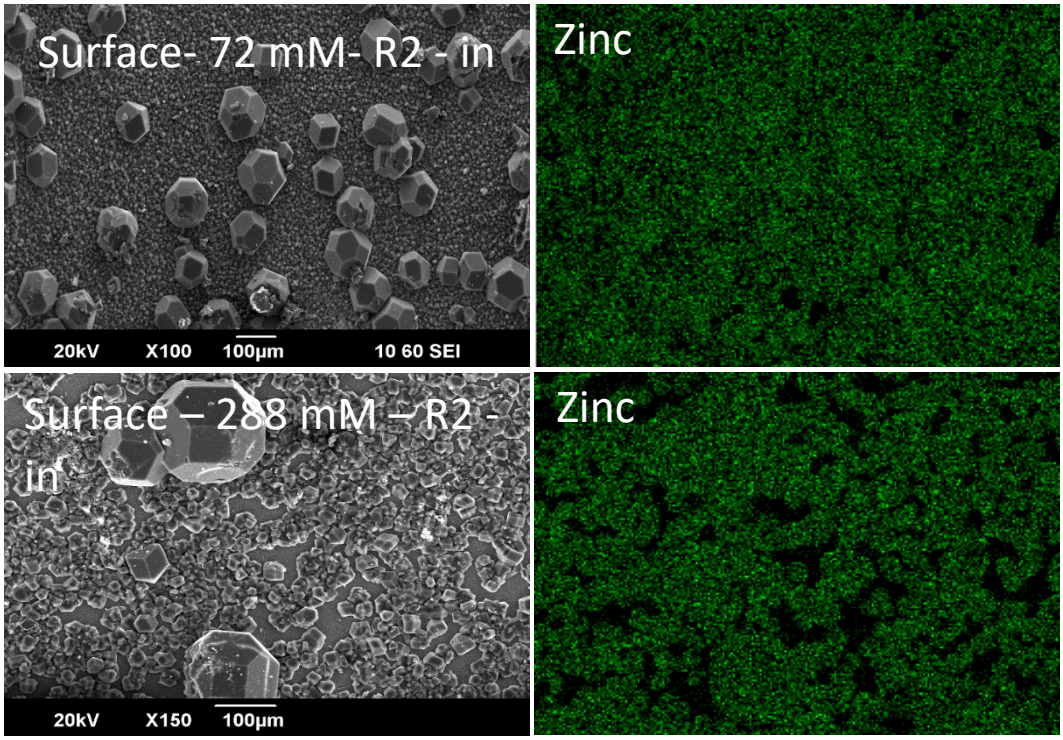


Figure 5- 15: Surface images of membranes synthesised on seeded substrates with isolated precursors (metal inside) at 150 °C for 5 hours, at linker/metal ratio of 2 and metal concentration of 72 mM and 288 mM.

Figure 5-16 shows the XRD patterns of the membranes synthesised with metal inside the substrate, with a linker/metal ratio of 2 and metal concentrations of 72 and 288 mM. The characteristic peaks are present for all membranes synthesised across both concentrations. The membranes synthesised with the linker/metal ratio 8 and 72 mM concentration did not show the peak at 7.36 °, this may suggest that when at the linker/metal ratio of 2 and metal precursor is inside, more evolved ZIF-8 crystals can be obtained. Therefore, it is hypothesised that the ratio of the fluxes contributed to the control of crystal morphology (/membrane microstructure) akin to how in the mixed batch systems smaller linker/metal ratios produced larger crystals, the ratio of precursor fluxes acted as a second parameter in the metal-linker isolation work allowing control over membrane microstructure. In conclusion, in addition to the linker/metal ratio controlling the membrane microstructure in the isolated system, the precursor location controls the structure too. Regarding this hypothesis, the metal-linker isolation system can achieve different microstructures at the same precursor concentrations and ratios depending on precursor locations.

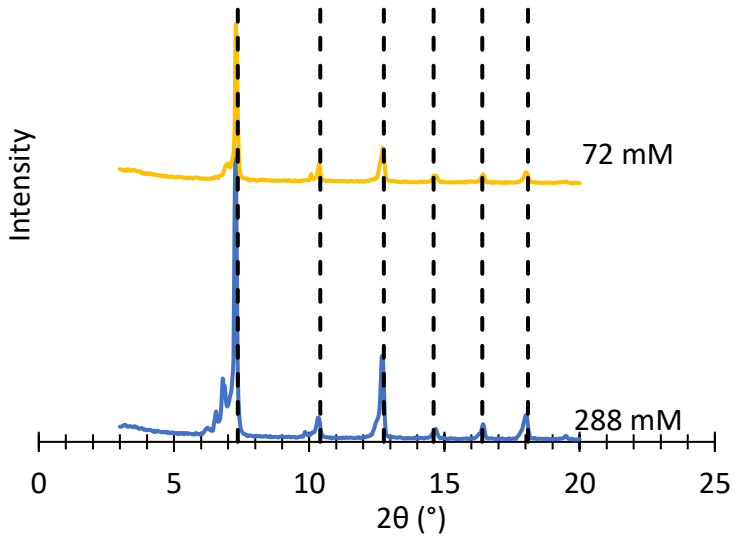


Figure 5- 16: XRD patterns of membranes synthesised on seeded substrates with isolated pre-cursors (metal inside) at 150 °C for 5 hours using linker/metal ratio of 2 and metal concentration of 72 mM and 288 mM. The dashed lines refer to the position of the most prominent characteristic peaks of ZIF-8.

To assess the growth of ZIF-8 in the pores of substrate a two cycle isolated system was studied synthesised at linker/metal ratio 8 and metal concentration of 288 mM (Figure 5-17). The surface image of the two-cycle membrane synthesis may suggest that there was a reduced flux of precursor and the generation of both smaller and larger crystals on the substrate surface. The crystals size was estimated between 13-242 µm, which is in a similar range with the membrane synthesised at linker/metal ratio of 2 (Figure 5-15), implying that the flux of precursors decreased. Therefore, partial growth of ZIF-8 in the pores of the substrate, also because of existing nucleated crystals on the substrate surface obstructing the diffusion of precursors across the substrate (Yao et al., 2011). Another consideration for the metal-linker system could be to introduce a catalyst such as sodium formate (Kwon and Jeong, 2013) to promote deprotonation of the linkers accelerating the reaction leading to a rapid nucleation and fast crystal formation within the vicinity of the substrate surface. However, without a more tailored surface modification a dense and continuous membrane may still fail to be obtained.

Figures 5-17 show the XRD pattern of the membranes synthesised for two cycles with isolated precursors with metal solution inside the substrate with metal concentrations of 288 mM, and linker/metal ratio of 8. The typical characteristic peak of 7.36° representing the evolved rhombic shape of ZIF-8 can be observed that implies fully evolved crystals on the surface of substrate.

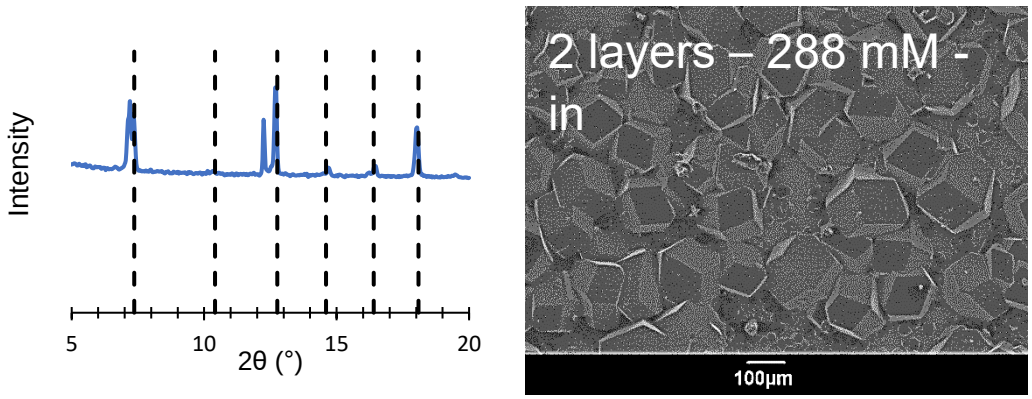


Figure 5- 17: XRD pattern and surface image of a membrane synthesised on seeded substrates with isolated pre-cursors (metal inside) at 150 °C for 5 hours, two cycles, using linker/metal ratio of 8 and metal concentration of 288 mM.

The metal/linker isolation study was investigated further by changing the linker/metal flux to 32 with metal inside the substrate. Figure 5-18 shows the surface images (not of same scale) of membranes synthesised with isolated precursors with metal solution inside the substrate with metal concentrations of 288 mM, and linker/metal ratio of 32. The surface image suggests dense crystal growth. Although the ratio has been increased (and so has the respective flux of linker), the surface images of the metal-linker isolation work suggest crystal sizes are between 19-154 µm, and for the linker/metal ratios of 8, it was 87-134 µm. This may suggest that for metal-linker isolation batch system, the precursor location has a more dominant effect on the rate of nucleation and growth than the linker/metal ratio. Figure 5-18 shows the XRD patterns of the membranes synthesised with metal inside the substrate, with a linker/metal ratio of 32 and metal concentration of 288 mM. The membrane shows all characteristic peaks of ZIF-8 indicating oriented growth.

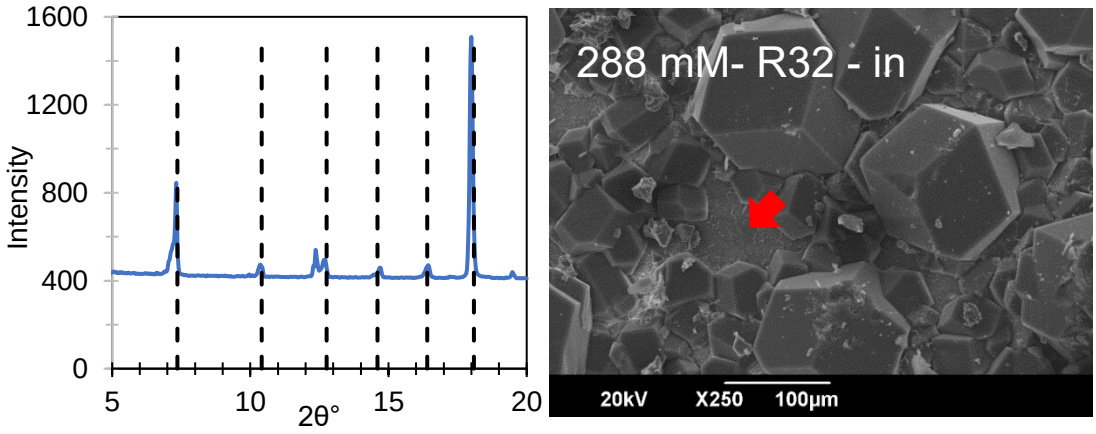


Figure 5- 18: XRD pattern and surface image of a membrane synthesized on seeded substrates with isolated pre-cursors (metal inside) at 150 °C for 5 hours at a linker/metal ratio of 32 and metal concentration of 288 mM. Red arrow highlights region of bare substrate.

Figure 5-19 shows surface image of membranes synthesised from zinc nitrate with isolated precursors (metal inside) at a linker/metal ratio of 8 and metal concentrations 288 mM. The surface images suggest crystal size between 14-46 µm suggesting there are more nuclei in the system when compared to the membrane synthesised using zinc acetate, however, the surface growth is not as dense with the zinc nitrate. This may

indicate that the conjugate base associated with the Zn^{2+} ion effects heterogenous nucleation in the metal-linker isolation system. The metal-linker isolation (irrespective of precursor location) system may imply that the ZIF-8 is a competitive nucleating system i.e. homogenous vs. heterogenous (Maina et al., 2018, Tuninetti et al., 2015, Ruan et al., 2019), since the rate of reaction has increased (while rate of diffusion remains the same) using zinc nitrate whilst an increase in the heterogenous growth of ZIF-8 on the substrate is not reflected, this may suggest a more tailored surface modification is needed for the metal-linker isolation work. Figure 5-19 shows the XRD pattern of the membranes synthesised with isolated precursors with metal solution inside the substrate with metal concentrations 288 mM using zinc nitrate, and linker/metal ratio of 8. The XRD patterns show the typical characteristic peak of 7.36°, 10.41 and 12.76 indicating preferential oriented growth on the substrate.

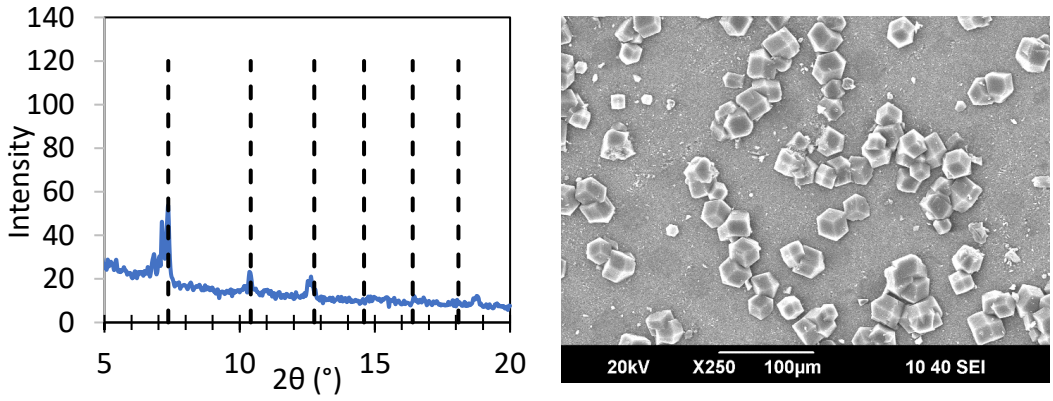


Figure 5- 19: XRD pattern and surface image of a membrane synthesised on seeded substrates using zinc nitrate hexahydrate with isolated pre-cursors (metal inside) at 150 °C for 5 hours, at a linker/metal ratio of 8 and metal concentration of 288 mM.

The experimental work in this chapter indicated that the effect of Ostwald ripening were reduced, achieving growth of new nucleation sites past the ZIF-8 growth phenomena of 60 minutes (Schejn et al., 2014). However, securing a dense and continuous membrane was still challenging supporting the comments made by the literature about the difficulty of synthesising ZIF-8 membranes, particularly when the tubular substrate was used (Tao et al., 2013b, Zhang et al., 2013, Kong et al., 2014). Xie et al. (Xie et al., 2012) reported a similar system to the metal-linker isolation system with their tubular substrates, however, membranes were synthesised on the outer surface of the tubular substrate. Tran et al.(Tran et al., 2020b) adopted a counter diffusion method for

membrane growth, reporting failure when synthesising the membrane inside the lumen of tubular substrate whilst success when growing on the outer surface of the substrate. They suggested that the failure was due to the narrow space, limited mass transfer from solution to substrate surface and differences in surface area between the inner and outer sides of the tubular substrate. The outer, larger surface area can accommodate more sites of nucleation thereby sustaining a dense and packed membrane. Figure 5-20 shows that the lumen of the substrate cannot accommodate the same number of sites of nucleation as the outer surface. An alternative to physical deposition of seeds is silane coupling agents, the concentration of which can be adjusted to optimise the level of density of growth desired, which were highlighted Xie et al. and Tanaka et al. (Xie et al., 2012, Tanaka et al., 2017). In conclusion, the role of concentrations of seeds deposited onto the substrate before membrane synthesis can be further investigated, and the seeds size can be controlled by altering linker/metal ratio (larger ratios generating smaller nuclei). The amounts of seeds deposited can be deciphered by weighing the substrate before and after seeding procedure, and weight change noted.

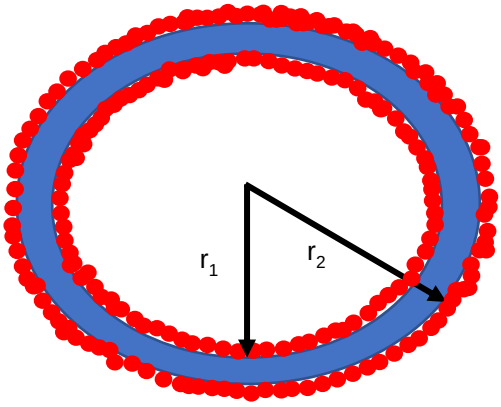


Figure 5- 20: Schematic view of the edge of a tubular substrate with deposited seeds (filled red circles) on the outer and inner sides of the substrate surface, r_1 and r_2 representing inner and outer radius of the tubular substrate.

5.4 Conclusion

In this chapter the heterogenous growth of ZIF-8 onto tubular substrates and the parameters that control the membrane microstructure using isolated precursors were investigated.

The metal-linker isolation results show the reaction zone can be brought to the substrate surface. The reaction system in the isolated system is ongoing, past the first 60 minutes of the ZIF-8 nucleation stage; the crystal size, shape and hence membrane microstructure can be controlled by precursor fluxes when at the same precursor concentration and ratios. Results show that even though the reaction zone was at the substrate surface, more nucleation sites were needed to promote growth on the substrate surface. Table 5-3 summarises the quantitative analysis of surface and cross sectional growth. A higher percentage of surface coverage can be achieved on the substrate surface when the metal precursor is positioned outside the substrate across all concentrations and ratios. However, 100 % surface coverage of ZIF-8 was not achieved. This may suggest that the linker ions could potentially act as some form of surface modifier. In conclusion, this may indicate the linker ions are the limiting reactant in the metal-linker isolation work since more nuclei are generated on the substrate surface when metal is located out of the substrate that is reflected with the smaller crystal sizes obtained when the metal is located outside. Further work is needed on metal-linker isolation system to further evaluate the system, one area of investigation could be the assessment of membrane growth on the outer surface of the tubular substrate.

Table 5- 3: Membrane thickness and surface coverage of membrane synthesised using isolated precursors at their respective precursors' concentrations and ratios.

Metal concentration (mM)	Linker/metal ratio	Seed	Metal precursor location	Surface coverage (%)	Thickness[1] (μm)
72	8	No	Out	84-92	2-3

[1] Thickness values have been estimated from same susbtrate but taken from other regions

288				97-98	74-77
72			In	31-49	2-4
288				76-86	7-19
36			Out	95-99	7-22
72				95-97	8-25
288				95-99	42-65
36			In	96	12-51
72				56-75	6-15
288				91-93	8-21
72	2	Yes	Out	96-99	8-39
288				95	13-46
72			In	84-92	12-26
288				91-96	11-47
288	32			99	22-71
288[1]	8			90-92	10-37
288[2]				41	7-26

[1] Two cycle synthesis
[2] Synthesised from zinc nitrate

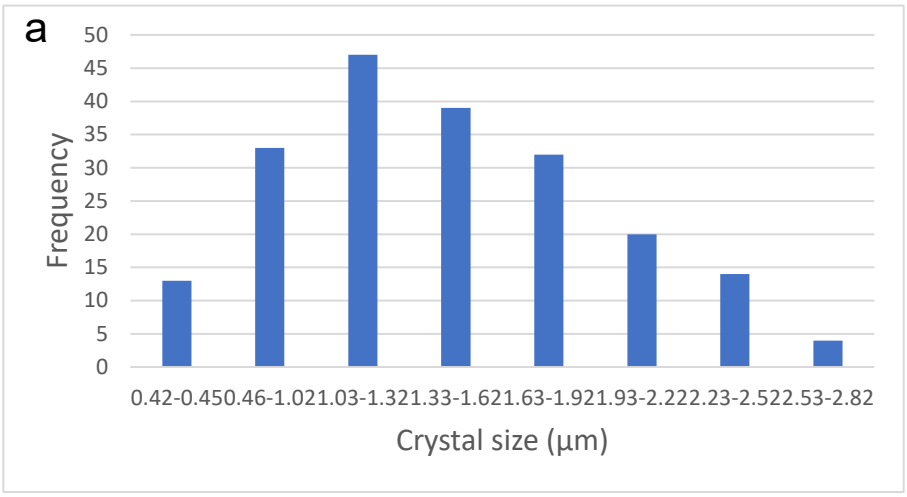
The metal-linker isolation results indicated that the seeding technique employed was a weak form of surface modification due to the detachment and dissolution of the seeds. Therefore, the substrate did not have sufficient sites of nucleation to support a securely attached continuous and dense membrane for gas separation. Applying a surface modification technique (section 2.5.1) that complements the metal-linker isolation batch system conditions (metal salt and substrate geometry), a dense and continuous membrane can be achieved with a measure of repeatability. The literature review has suggested that one form of surface modification that works for one MOF/ZIF type does not necessarily mean success for another type, suggesting that this investigation will be an iterative process.

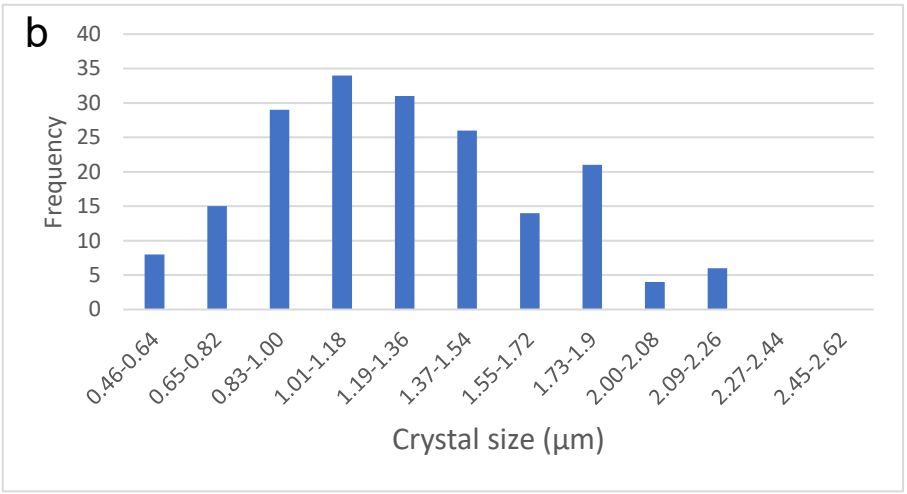
In conclusion, once a tailored surface modification is obtained, the next stage in the metal-linker isolation work will be to use longer tubular substrates, and more than two substrates per reaction vessel.

5.5 Appendix

Table A- 1: Molar fluxes of ZIF-8 precursors at linker/metal ratio 8 at respective precursor location and concentrations.

Precursor being measured and its location	Linker / metal ratio	Concentration of metal precursor (mM)	Flux of the precursor (mol/m^2.s)
Metal in	32, 8 and 2	288	10.0×10^{-8}
Metal in	8 and 2	72	1×10^{-8}
Metal in	8	36	0.35×10^{-8}
Metal out	8 and 2	288	2×10^{-8}
Metal out	8 and 2	72	0.2×10^{-8}
Metal out	8	36	0.075×10^{-8}
Linker in	8	288	270×10^{-8}
Linker in	8	72	29×10^{-8}
Linker in	8	36	9.7×10^{-8}
Linker out	8	288	58×10^{-8}
Linker out	8	72	6×10^{-8}
Linker out	8	36	2.1×10^{-8}
Linker in	2	288	29×10^{-8}
Linker in	2	72	3×10^{-8}
Linker out	2	288	6×10^{-8}
Linker out	2	72	0.7×10^{-8}
Linker out	32	288	530×10^{-8}


a
Frequency
50
45
40
35
30
25
20
15
10
5
0
0.42-0.45
0.46-1.02
1.03-1.32
1.33-1.62
1.63-1.92
1.93-2.22
2.23-2.52
2.53-2.82
Crystal size (µm)


b
Frequency
40
35
30
25
20
15
10
5
0
0.46-0.64
0.65-0.82
0.83-1.00
1.01-1.18
1.19-1.36
1.37-1.54
1.55-1.72
1.73-1.9
2.00-2.08
2.09-2.26
2.27-2.44
2.45-2.62
Crystal size (µm)

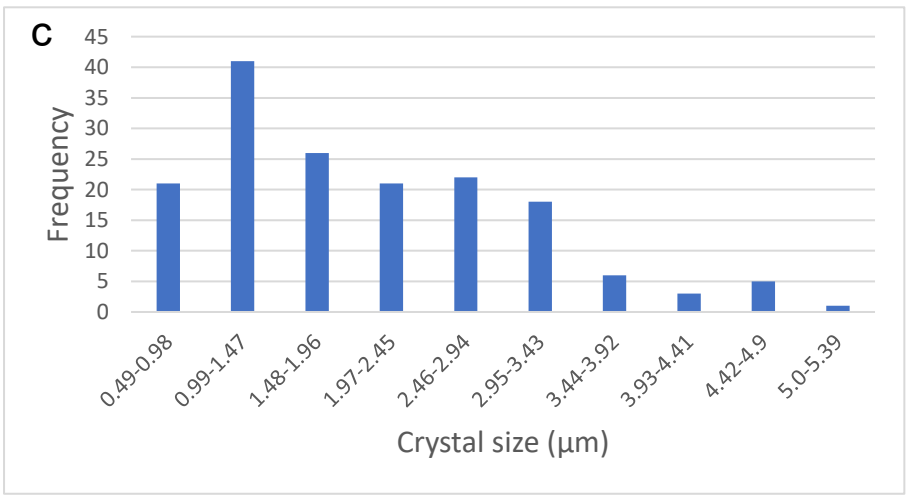

c
Frequency
45
40
35
30
25
20
15
10
5
0
0.49-0.98
0.99-1.47
1.48-1.96
1.97-2.45
2.46-2.94
2.95-3.43
3.44-3.92
3.93-4.41
4.42-4.9
5.0-5.39
Crystal size (µm)

Figure A- 8: Crystal size histograms of crystals on the seeded substrate surface synthesised at linker/metal ratio 8 and metal concentrations 36 (a), 72 (b) and 288 (c) mM with metal solution outside. Membranes synthesised for 5 hours using conventional heating at 150 °C.

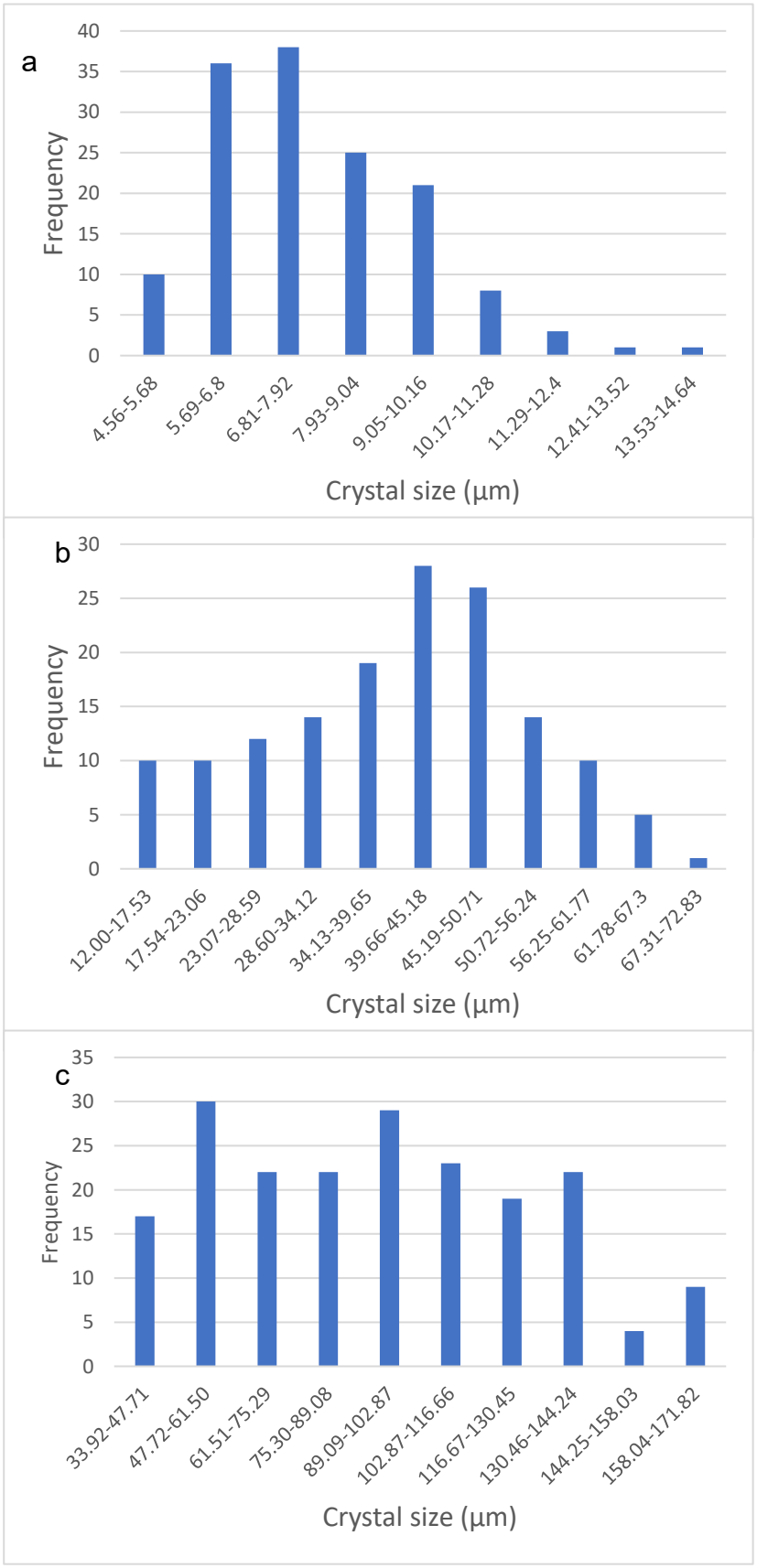


Figure A- 9: Crystal size histograms of crystals on the substrate surface synthesised at linker/metal ratio 8 and metal concentrations 36 (a), 72 (b) and 288 (c) mM with metal solution inside. Membranes synthesised for 5 hours using conventional heating at 150 °C.

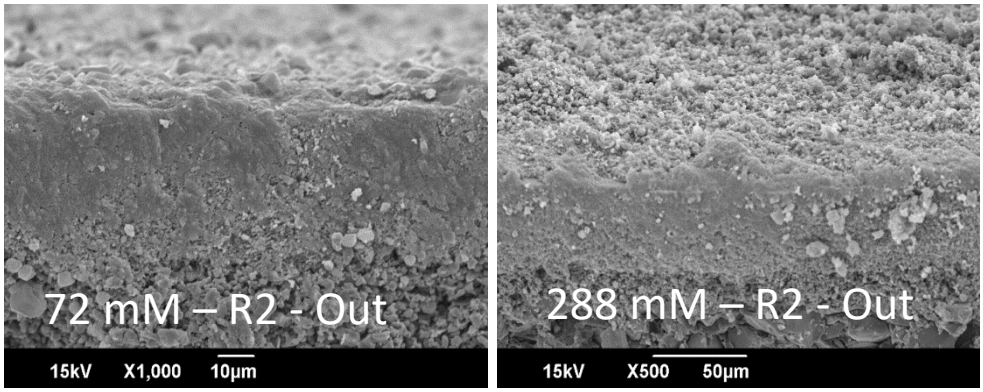


Figure A- 10: Cross sectional images of membranes synthesised on seeded substrates with isolated pre-cursors (metal outside) using conventional heating at 150 °C for 5 hours with a linker/metal ratio of 2 and metal concentrations of 72 mM and 288 mM.

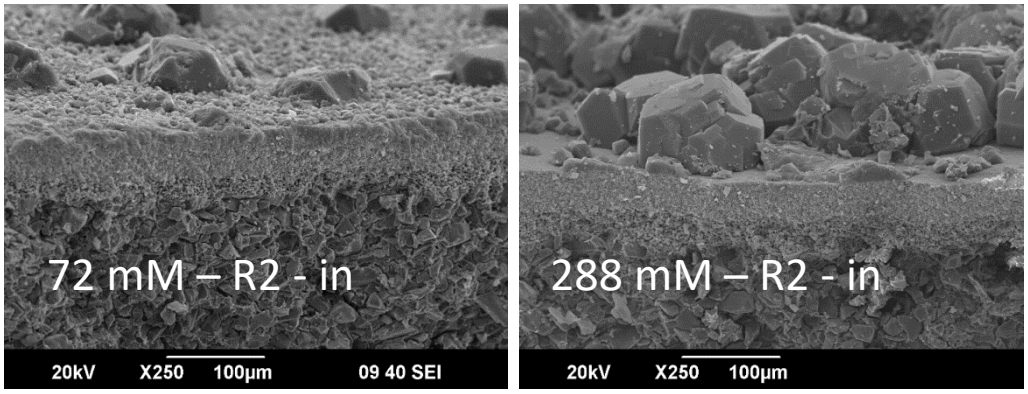


Figure A- 11: Cross sectional images of membranes synthesised on seeded substrates with isolated pre-cursors (metal inside) using conventional heating at 150 °C for 5 hours with a linker/metal ratio of 2 and metal concentrations of 72 mM and 288 mM.

6. Synthesising ZIF-8 onto tubular substrates using microwave heating.

6.1 Introduction

Chapters 4 and 5 discussed the heterogenous growth of ZIF-8 onto tubular substrates using conventional heating at different precursor concentration and ratios. Chapter 5 also saw the introduction of a novel synthesis procedure by studying the kinetics of the formation of ZIF-8 onto the surface of the substrate via metal-linker isolation. This chapter continues with the same concept but investigates how different heating mechanisms, namely microwave heating, impact on the formation and growth of ZIF-8.

Microwave heating delivers heat remotely via the transformation of electromagnetic energy within the reaction medium, and this is on a volumetric basis i.e. there is no heat transfer involved, making it a more efficient method of heating. As well as increased efficiency, microwave heating has a selective heating mechanism because of its specific and localised interaction with the ions of a material, or in the case of a polar solvent, the dipoles of the molecules. Materials are categorised by their dielectric properties, this how well the material can store the electromagnetic energy and then dissipate the energy as heat.

The remote heating without the transference of heat creates a linear heating profile and leads to higher rates of heating, achieving superheating – heating above a solvent boiling point, leading to crystallisation kinetics being accelerated, and synthesis times being significantly reduced. With many microwave processes that involve liquids, this apparent acceleration of kinetics is simply caused by selective, localised heating inside a bulk fluid. The bulk temperature still appears to be relatively low, but there is superheating of some kind of receptor molecule or particle within the bulk fluid. This is a key feature of microwave heating and has often led to the erroneous assumption that microwaves are ‘magic’ (Kappe et al., 2013), whereas it is an artefact of the dielectric properties of different components within a multi-component system. Some fluids are microwave transparent (e.g. non-polar solvents) whereas water is highly microwave absorbing (Dudley et al., 2015).

Literature reports on the synthesis of ZIF-8 membranes using microwave heating with synthesis times between 2-4 hours on unmodified and modified substrates. The microwave chemistry and heterogenous growth of ZIF-8, or for zeolites, has not been discussed before in literature.

This chapter presents a systematic novel study into the investigation of heterogeneous growth of ZIF-8 onto tubular substrates under microwave heating. A reduced temperature of 100 °C and synthesis time of 3 hours is used because of the accelerated heating regime achievable by microwaves. The results were then compared to conventionally heated membranes synthesised at 100 °C for 5 hours.

6.2 Experimental procedures

Membranes were synthesised with metal concentrations of 72 and 288 mM, and linker to metal ratios of 2 and 8. Figure 6-1 shows a schematic of an unplugged tubular substrate in a CEM glass vial (microwave reaction vessel), 2 cm and 6 cm length tubular supports were used for mixed MOF and isolated precursor study, respectively.

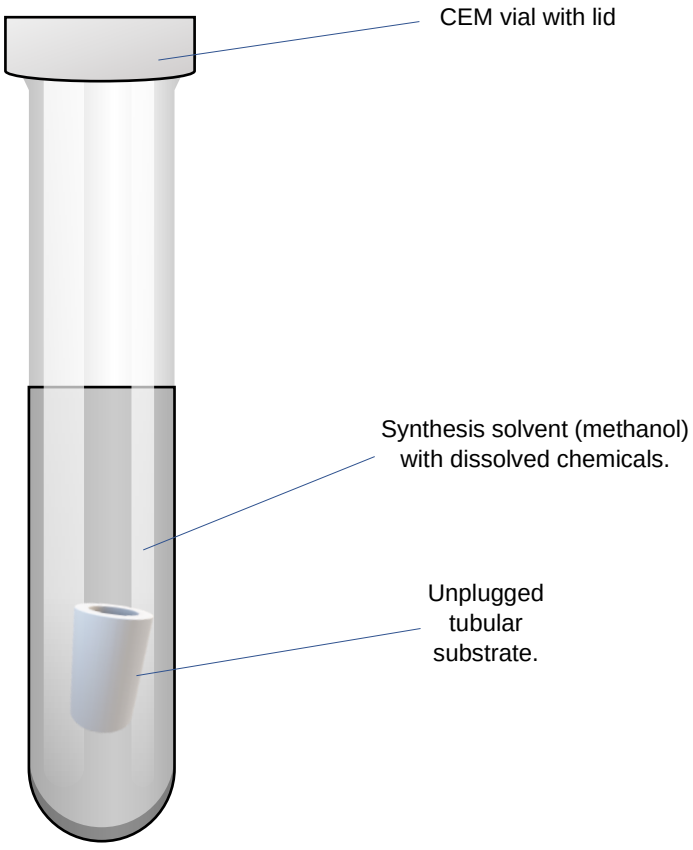


Figure 6- 1: Schematic of unplugged tubular substrate in CEM glass vial (8 ml capacity) with lid and filled with MOF solution (4 ml solvent volume).

The maximum solvent volume for safety reasons during synthesis was 4 and 16 ml for the 8 and 32 ml vials, respectively. This includes any solution in the plugged alumina tube for the metal-linker isolation experiment. For all syntheses, mixed and isolated, substrates were submerged in the solvent as can be seen in the photos in Figure 6-2,

the sealed vials were then inserted into the corresponding attenuator secured in the CEM cavity, indicated with the red arrow (Figure. 6-2d).



Figure 6- 2: Photos of substrates in CEM glass vial with solvent volume of 4 ml and 2 cm alumina substrate in a 8 ml capacity vial (approximate diameter of 20 mm) (a), total solvent volume of 4 ml (2 ml inside plugged substrate) with 6 cm alumina substrate with Teflon plugs in a 8 ml capacity vial (b), solvent volume of 16 ml and 2 cm alumina substrate in a 32 ml capacity vial (approximate diameter of 30 mm) (c), CEM cavity with the selected attenuator (red arrow indicating where vial is inserted) for the 8 ml pressure vial (d) - the “IntelliVent” lid is withdrawn as the microwaves are not engaged.

The metal and linker solutions were synthesised as in the batch synthesis in Chapter 4. For the mixed synthesis, 2 ml of linker solution was added to 2 ml of metal solution dropwise and stirred for 2 mins. The mixed solution was transferred to the CEM glass vial with the seeded substrate in place, which was then sealed with a CEM cap. The sealed vial was placed in the CEM DISCOVER-SP microwave reactor (model number 909155).

For the metal-linker isolation study the tubular substrate was filled with metal or linker solution and plugged with Teflon plugs as instructed in the metal-linker isolation experimental in Chapter 5. The glass vial was then filled with 2 ml of metal or linker solution and the plugged tubular substrate was transferred to the vial and sealed with a CEM cap. The sealed vial was then placed in the microwave reactor and the selected dynamic run was started at 150 W of power. On the PC the synthesis temperature, time and safety parameters were inserted into the microwave reactor as dynamic control with maximum 17 bar (CEM max is 21 bar) pressure. If the pressure exceeded the set maximum the power supply to the reaction chamber would cease so the reaction would be stopped. The heating rate was set to 10 °C min^{-1}, and the cooling rate were set to default setting where the IntelliVent lid would open once the reaction mixture was cooled down to the release point temperature of 50 °C. For each run, once the temperature reached to 100 °C the pressure was monitored for a further 10 minutes. Table 6-1 summarises the experimental conditions of the membranes synthesised in the CEM microwave reactor. Before the reactions, a microwave detector was used to detect any leakage. The probe was slowly moved around the equipment in particular the reaction chamber. If the reading exceeded 5 mW cm^{-2} the microwave generator was turned off. Fluid pressures and temperatures were calculated from National Institute of Standards and Technology fluid database (NIST, 2017).

Table 6- 1: Metal concentration and linker/metal ratio of the isolated membranes synthesis (metal in) and mixed precursor solutions via conventional (5 h) and microwave (3 h) heating at 100 ^{o}C.

Metal concentration (mM)	Linker to metal ratio
288	8
	2
72	8
	2

6.3 Results

6.3.1 Membrane synthesis using mixed precursors with microwave heating.

Figure 6-3 shows the surface images (not of same scale) of the membranes synthesised using microwave heating with metal concentrations of 72 and 288 mM, and linker/metal ratios of 2 and 8. The membranes were synthesised at 100 °C for 1 hour. The surface images of membranes synthesised at the metal concentration of 72 mM and linker/metal ratios of 8 and 2 show some particles on the substrate surface. The particles on the surface do not have the typical ZIF-8 cubic/rhombic morphology suggesting they are seeds that have failed to evolve into ZIF-8 crystals. This may indicate that the seeds may interact weakly with the microwaves. No studies investigate how microwaves interact with full evolved MOF structures – membrane or powder form, or when there is a layer of seeds of MOFs or zeolites acting as sites of nucleation on a substrate surface. It is important also to highlight that the interaction of microwaves between solvent and dissolved species (metal and linker ions) must be experimentally reported (Herrero et al., 2008). Since the dielectric properties (dielectric constant, dielectric loss factor, loss tangent - tan δ) of the reacting volume depend on the number of ions and solvent volume, these dissolved species (and solvent) govern how efficiently microwaves are absorbed, and hence how efficiently heat is generated (Gabriel et al., 1998, Lou et al., 1997, Robinson et al., 2010). It is important to note that the MOF structures response to dielectric heating must be experimentally measured (collect respective dielectric properties) since the dielectric heating mechanism is dependent on the material properties as reported by Laybourn et al. (Laybourn et al., 2016).

Further experimental work is needed to conclude why ZIF-8 seeds have failed to nucleate under microwave heating. A hypothesis is that the seeds failed to nucleate because the seeds relied on heat being transferred via convection from the heat created by the friction of the oscillating ions in the solution. Since the dielectric constant for alumina is 9.8 (Microwaves101, 2020a), suggesting it to be ‘transparent’ to the microwaves. The membrane synthesised at the metal concentration of 288 mM and linker/metal ratio of 2 indicates no growth on the surface of the substrate.

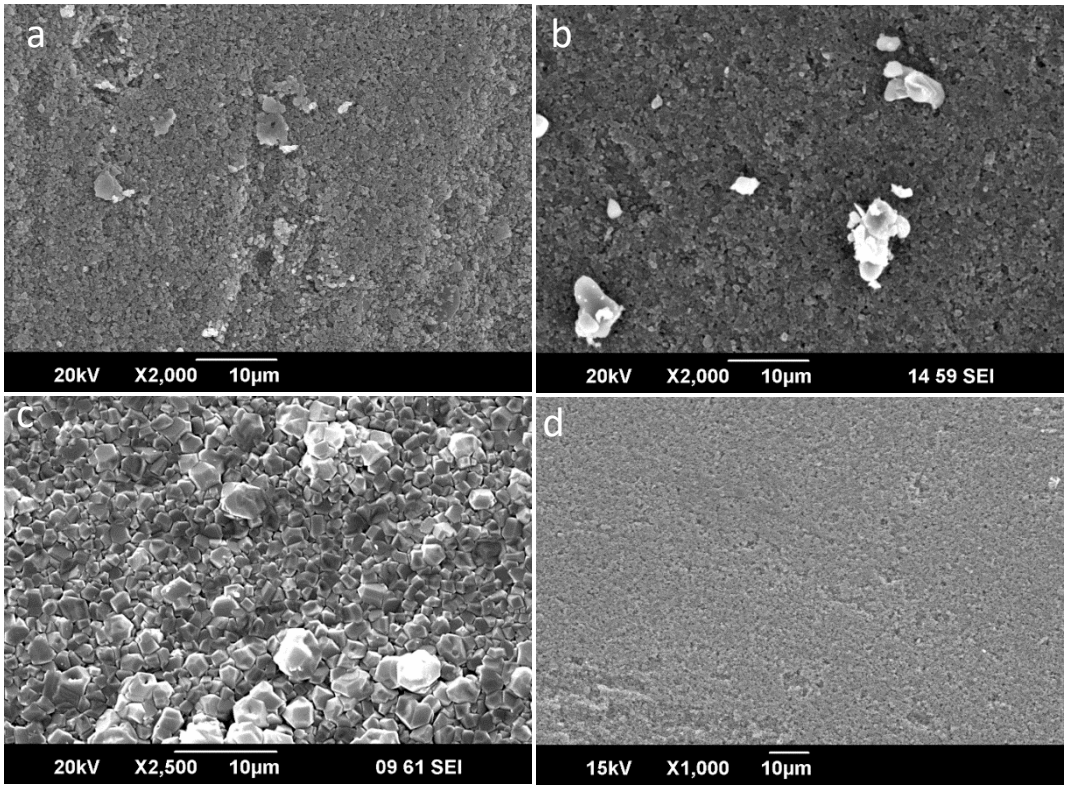


Figure 6- 3: Surface images of seeded membranes synthesised with mixed MOF solutions with metal concentrations of 72 mM at linker/metal ratio of 8 (a) and linker/metal ratio of 2 (b). Surface images of seeded membranes synthesised with mixed MOF solutions with metal concentrations of 288 mM at linker/metal ratio of 8 (c) and linker/metal ratio of 2 (d). Membranes synthesised with microwave heating at 100 °C for 1 hour.

The SEM images of the membrane synthesised at the metal concentration of 288 mM and linker/metal ratio of 8 (Figure. 6-3c) shows a layer of growth that represents the typical cubic and rhombic morphology of ZIF-8. This is an indication of the accelerated heating achieved because of selective heating of the metal ions (‘hot spots’) in the solution. However, the cross sectional image, Figure 6-4, shows no surface growth, indicating that the surface growth observed in Figure. 6-3c is not continuous. This indicates a discrepancy in the growth along the substrate length, suggesting the volumetric heating mechanism was not dominant, rather a combination of both heating mechanisms since growth has been achieved within an hour, since the SEM surface image shows growth fully evolved crystals. However, there are no references available to support the preceding statement about a combination of heating methods since there are no membrane papers (not only MOFs membrane) that integrate the discussion of microwave chemistry and membrane growth. Although Zhu et al. compared their ZIF-8 membranes between microwave and conventional heating and showed that the membrane synthesised under conventional heating (including the

surface modification step) was unsuccessful, no supporting references or hypothesis was included (Zhu et al., 2016).

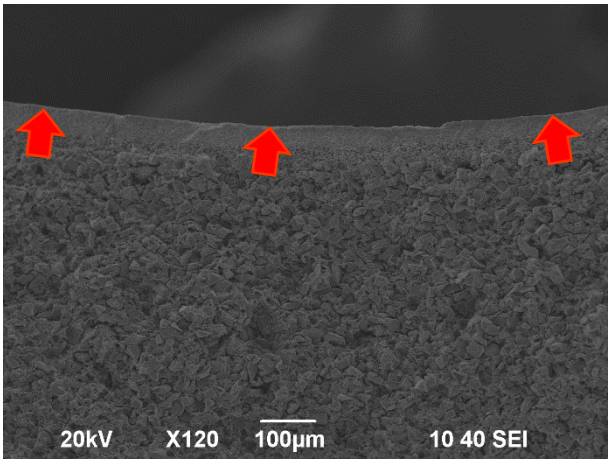


Figure 6- 4: Cross sectional image of membrane synthesised with mixed ZIF-8 solution with metal concentration of 288 mM and linker/metal ratio of 8. Synthesised at 100 °C for 1 hour using microwave heating. Red arrows highlighting the inside of the substrate lining where crystal growth is expected.

Therefore, the crystals are evolved with a range of 0.6-4.2 µm, Figure 6-5. The range is narrow when compared to the conventionally heated membrane crystal size range of 4.5-16.3 µm (Batch chapter), synthesised at the same linker/metal ratio and metal concentration of 8 and 288 mM, respectively. However, the conventional heated membrane was synthesised at higher temperature, longer synthesis time, and with a larger concentration of ions in the reaction vessel (since have volume of 32 ml). As such, drawing a comparison on the size distribution is more difficult. Literature does report on a narrower crystal size distribution of MOFs and zeolites membranes synthesised with microwave heating because of the rapid and accelerated heating mechanism achieved from the dielectric mechanism (Hu et al., 2016, Huang and Yang, 2007). Tsai et al. histograms for ZIF-8 particles synthesised (at linker/metal ratio 8) using microwave heating showed ranges between 26-84 and 17-32 nm at temperatures of -15 and 60 °C, respectively (Tsai and Langner, 2016). Reinforcing the narrower crystal size range achieved with the microwave heating mechanism (Tompsett et al., 2006). This may indicate that the dielectric heating mechanism was not the dominant form of heating on the membrane synthesised with a linker/metal ratio 8 and 288 mM metal concentration. Rather a combination of dielectric heating and convective heat transfer, with the latter being the more dominant mode of heating.

The poor level of heterogenous growth in the microwave system may indicate an increased synthesis time is needed to allow for a more robust heterogenous growth.

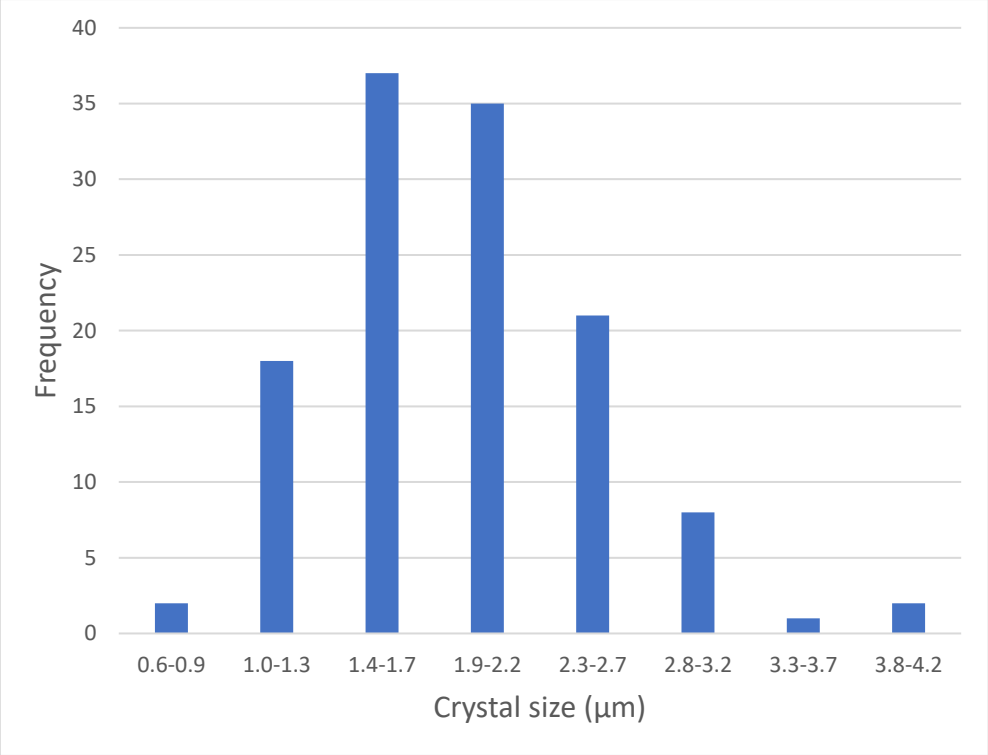


Figure 6- 5: Particle size histograms of crystals on the substrate surface synthesised at linker/metal ratio of 8 and metal concentrations 288 mM synthesised with mixed MOF solution.

Figure 6-6 shows the XRD patterns of the membranes synthesised using microwave heating with metal concentrations of 72 and 288 mM, and linker/metal ratios of 2 and 8. The membranes were synthesised at 100 °C for 1 hour. The XRD patterns supports the SEM images that there is either no crystal or an extremely thin layer of ZIF-8 on the surface of the substrates since none of the characteristic peaks of ZIF-8 are detected.

The XRD pattern of the substrate synthesised at the metal concentration of 288 mM and linker/metal ratio of 8 shows no peaks, indicating the dense growth seen on the surface image is not continuous. A factor to be considered in heterogenous nucleation (growth on substrate) and dielectric heating is that nucleation may be more dominant in the bulk of the solution, homogenous nucleation. This is because the ‘hot spots’ are more receptive to the microwaves than the alumina substrate and deposited seeds. However, to try to better control the accelerated homogenous nucleation, a stepped heating regime is used in this thesis, which has been described in section 5.2.

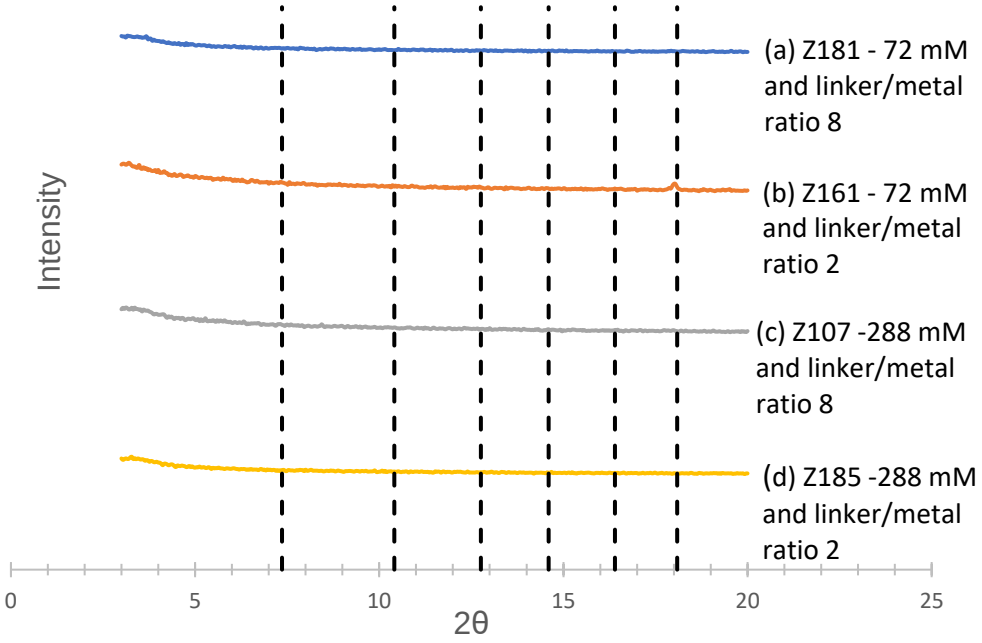


Figure 6- 6: XRD patterns of seeded membranes synthesised with mixed MOF solutions with metal concentration of 72 mM at linker/metal ratio of 8 (a) and linker/metal ratio of 2 (b). Surface images of seeded membranes synthesised with mixed MOF solutions with metal concentrations of 288 mM at linker/metal ratio of 8 (c) and linker/metal ratio of 2 (d). Membranes synthesised with microwave heating at 100 °C for 1 hour. The dashed lines refer to the position of the most prominent characteristic peaks ZIF-8.

Figure 6-7 shows the surface images of the membranes synthesised using microwave and conventional heating at metal concentrations of 72 and 288 mM and linker/metal ratio of 8. The membranes were synthesised at 100 °C for 3 and 5 h via the microwave and conventional heating, respectively. The surface images for both microwave and conventional heating imply sparsely scattered (288 mM-Figure 6-7c, d) or no crystals (72 mM-Fig 6f-7a, b) on the surface of the substrate. The crystals do not reflect the typical cubic/rhombic morphology of ZIF-8 on the substrate. This may imply these are failed nucleated seeds. The lack of surface growth on the microwave heated substrates at the 3 hour synthesis may indicate the detachment and dissolution of potentially weakly attached nucleated ZIF-8 crystals on the substrate surface.

The lack of surface growth on the substrate surface may indicate a more tailored surface modification is needed for the microwave system. Alumina is ‘transparent’ to microwaves so it is possible that some form of receptor (inserted in the tube) might

allow the substrate to make it more receptive to microwaves. Although literature does not explicitly explain the microwave chemistry involved in reactive seeding (Ramu et al., 2018, Sun, 2018). The soaking of the ceramic substrate in the metal solution can deposit the metal ions into the pores of the substrate thereby creating receptors ('hot spots'). These hot spots can then act as receptors to the microwaves (Dudley et al., 2015) thereby heating the alumina substrate directly. When heating the substrate in the linker solution there is a higher chance of ZIF-8 growth on the substrate surface and inside the pores, as opposed to relying on convective heat transfer from the bulk of the solution to heat the substrate. Hence, this is an option for future researchers to deposit receptors into the alumina substrate making it more receptible to the microwaves and heating up.

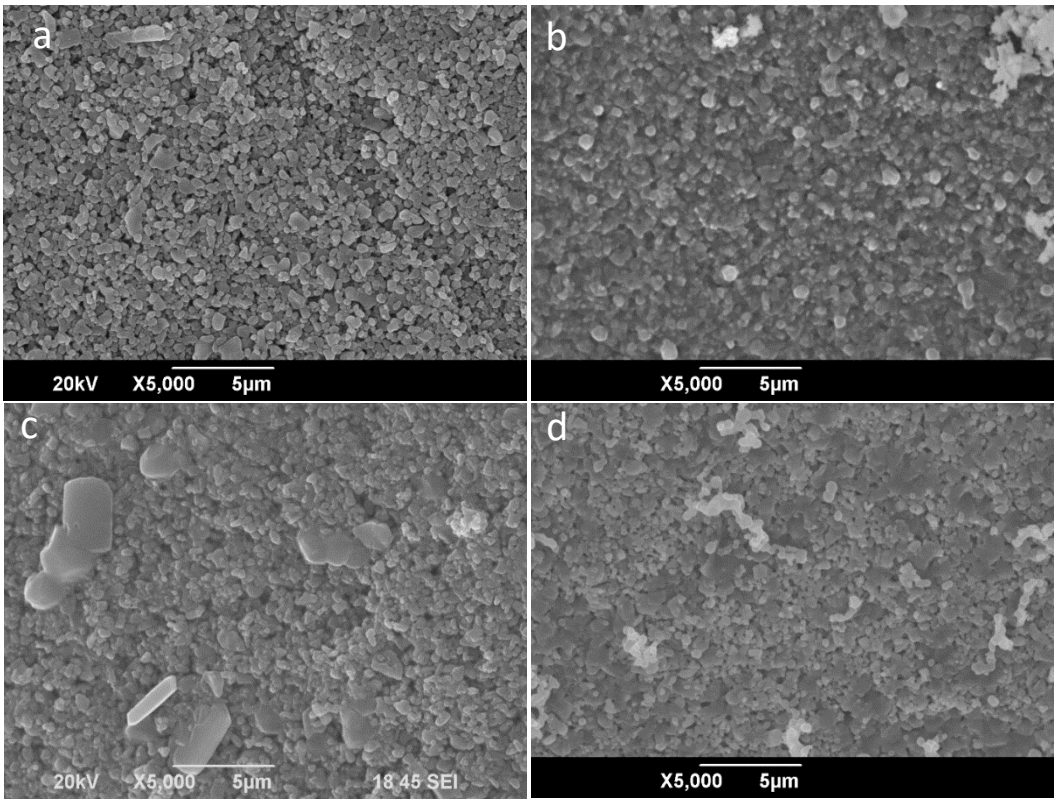


Figure 6- 7: Surface images of seeded membranes synthesised with mixed MOF solutions at linker/metal ratio of 8 and metal concentrations of 72 mM with microwave heating for 3 hours at 100 °C (a) and conventional heating for 5 hours at 100 °C (b). Surface images of seeded membranes synthesised with mixed MOF solutions at linker/metal ratio of 8 and metal concentrations of 288 mM with microwave heating for 3 hours at 100 °C (c) and conventional heating for 5 hours at 100 °C (d).

Figure 6-8 shows the XRD patterns of the membranes synthesised using microwave (100 °C for 3 h) and conventional heating (100 °C for 5 h) at a metal concentration of 72 and 288 mM and linker/metal ratio of 8. The XRD patterns supports the SEM

images that there was either no crystal growth or only a very thin layer of ZIF-8 on the surface of the substrates since none of the characteristic peaks for ZIF-8 were detected, except at the 288 mM concentration. At the concentration of 288 mM, a single peak at 18.09 ° is detected on the substrate samples characterised, for both conventional and microwave heated membranes. This may imply the crystal growth detected on the substrate are orientated with the (222) crystallographic plane facing the detector (Schejn et al., 2014). This may indicate that growth is not continuous on the surface of both the conventional and microwave heated membranes synthesised at the 288 mM concentration, since the SEM images suggest the absence of nucleated seeds.

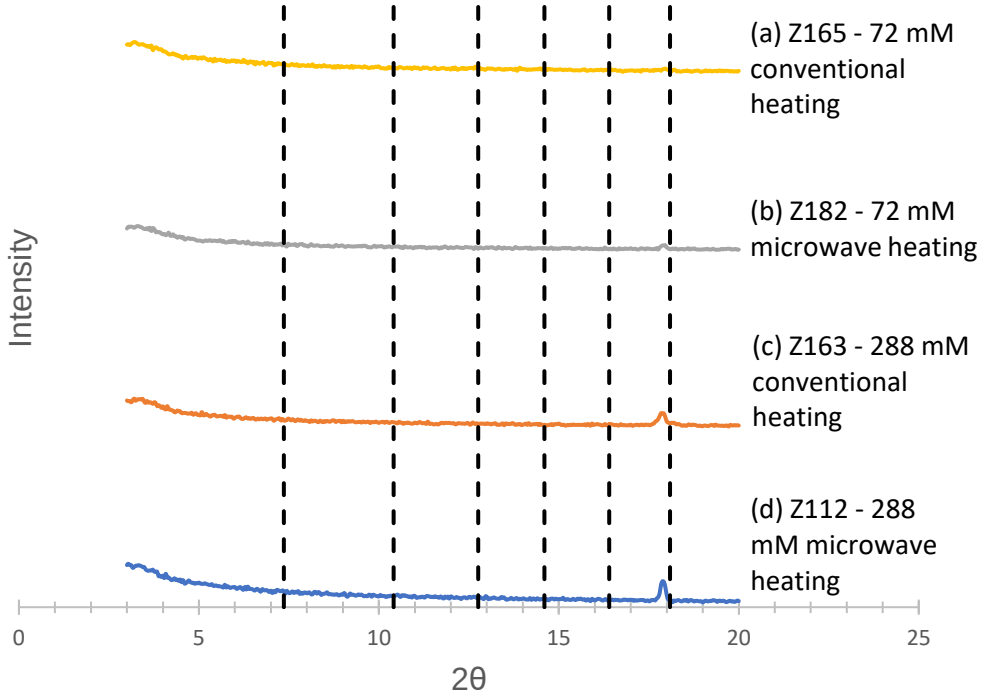


Figure 6- 8: XRD patterns of seeded membranes synthesised with mixed MOF solutions at linker/metal ratio of 8 and metal concentrations of 72 mM using conventional heating (a) and microwave heating (b), and metal concentration of 288 mM using conventional heating (c) and microwave heating (d). Membranes were synthesised at 100 ˚C for 3 and 5 h using microwave and conventional heating, respectively. The dashed lines refer to the position of the most prominent characteristic peaks ZIF-8.

Figure 6-9 shows surface images (not at the same scale) of membranes synthesised using microwave and conventional heating at linker/metal ratio of 2 and metal concentrations of 72 and 288 mM. The membranes were synthesised at 100 °C for 3

and 5 hours for the microwave and conventional heating, respectively. The surface images of the membranes synthesised using microwave heating at 72 mM suggest uneven coverage of ZIF-8 on the substrate. The smaller inset image (Fig 6-9a.) shows the crystals are past the initial cubic morphology and more rhombic, with crystal size range of 0.5-7.0 µm (Figure 6-10b for histogram).

The surface image of the membrane synthesised using conventional heating at 72 mM shows a very thin layer of growth. The inset image (Figure 6-9b) indicates less evolved and more spherical crystals, with a crystal size range of 0.3-1.7 µm (Figure 6-10a for histogram), which suggests that the conventionally heated crystals are still in the metastable state. Reiterating the dielectric heating accelerated heating regime. However, the large range for the crystal size of the microwave heated membrane indicates the heating mechanism was less volumetric leading to a more gradual nucleation rather than an instantaneous nucleation (Khan et al., 2010). This suggests the heating of the reaction mixture was being heated by convective and dielectric heating mechanisms.

The membranes synthesised at 288 mM and linker/metal ratio 2 using microwave suggests no growth (Figure 6-9c), while the conventionally heated (Figure 6-9d) indicates dense growth. This may suggest the densely packed metal ions at 288 mM provide a better rate of heat transfer for the conventionally heated membrane.

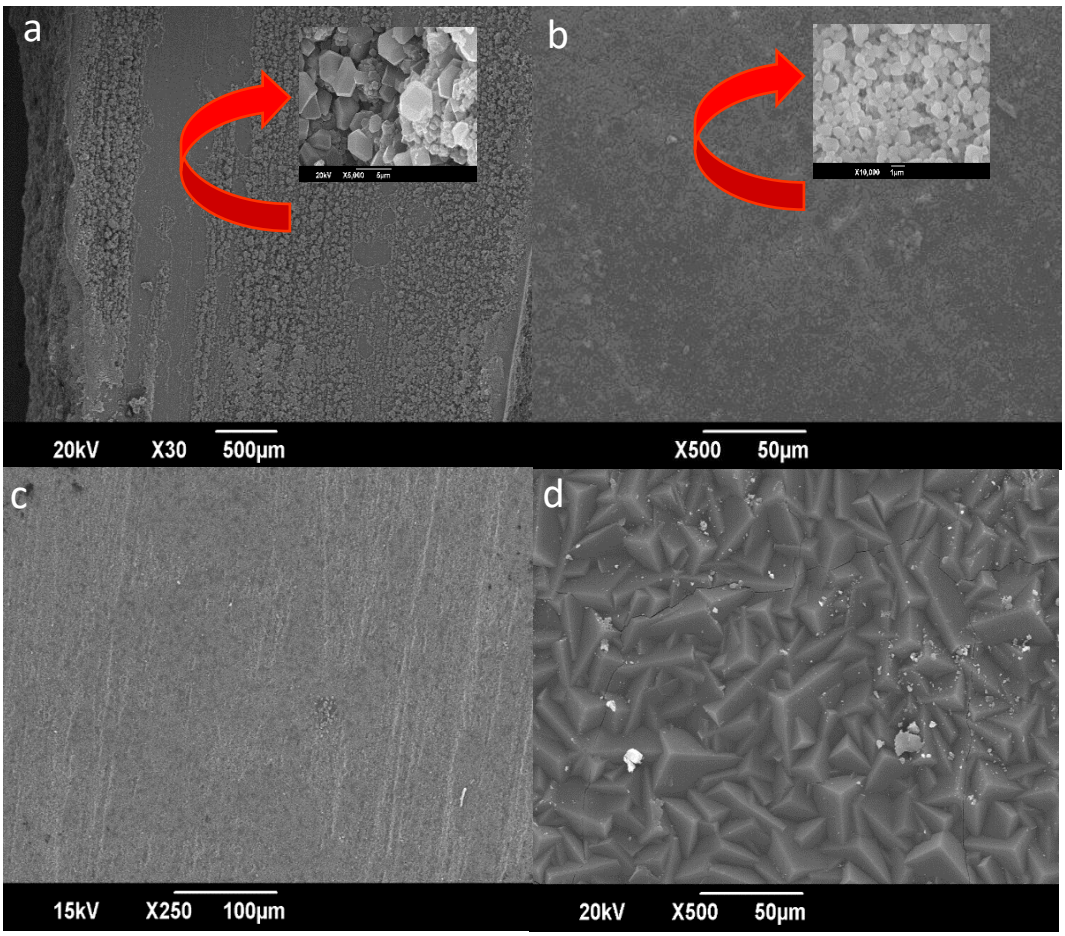


Figure 6- 9: Surface images of seeded membranes synthesised with mixed MOF solutions at linker/metal ratio of 2 and metal concentration of 72 mM via microwave (a) and conventional (b) heating. Surface images of seeded membranes synthesised with mixed MOF solutions with linker/metal ratio of 2 and metal concentration 288 mM via microwave (c) and conventional (d) heating. Membranes synthesised at 100 °C for 3 and 5 hours under microwave and conventional heating, respectively.

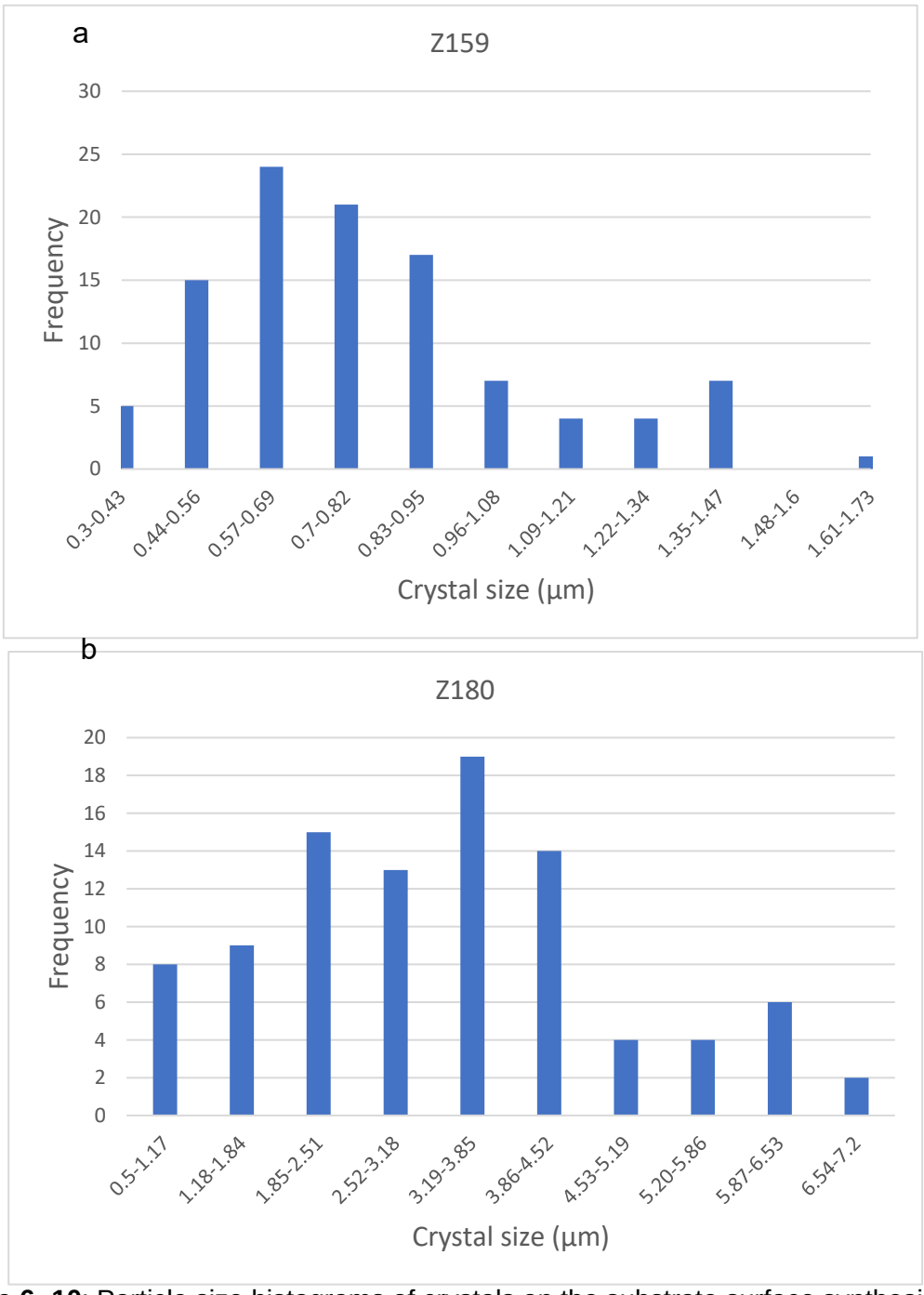


Figure 6- 10: Particle size histograms of crystals on the substrate surface synthesised at linker/metal ratio 2 and metal concentrations 72 mM using conventional (a) and microwave (b) heating. Membranes were synthesised at 100 ^{o}C for 3 and 5 h using microwave and conventional heating, respectively.

Figure 6-11 shows three schematics of solvent volumes (rectangular boxes) containing metal ions (blue circles) and their respective solvation spheres (red dashed circles): Fig. 6-11a and Fig. 6-11b are of dilute and concentrated systems with the same volume

of solvent, respectively, and Fig. 6-11c which has the same number of solvation spheres as Fig. 6-11b whilst in larger solvent volume. It can be seen from Fig. 6-11b the solvation spheres movement is retarded and cannot move with the alternating microwaves, which will lead to a decrement in the dielectric constant, ε' (literature review 2.6), (Laybourn et al., 2016). However, the dielectric loss factor, ε'', in Fig. 6-11b increases due to the high concentration of metal ions ('hot spots') that are now absorbing more microwaves on the surface of the solvent volume than Fig. 6-11a (Dudley et al., 2015, Laybourn et al., 2016). Due to the absorption of microwaves on the surface of the solvent, a 'skin' forms that now prevents the penetration of the microwaves into the remainder of the solvent volume (Sun et al., 2016, Tompsett et al., 2006, Yoo et al., 2009), leading to the remainder of the solvent volume being heated conventionally via convection. Hence, the system is being heated via a combination of microwave and conventional heating mechanisms.

Fig. 6-11c depicts a method by which the formation of the skin can be avoided; the same number of hot spots to Fig. 6-11b are now in an increased solvent volume, and the microwaves can now better penetrate the solvent maximising the volumetric heating mechanism. A similar technique was proposed by Sun et al. They commented on reducing the formation of skin and allowing maximum penetration of microwaves. They recommended mixing activated carbon and high-purity quartz sands that are good absorbers and transparent to microwaves, respectively (Sun et al., 2016). Such microwave chemistry synthesis techniques have not been described in the literature when synthesising membranes under microwave heating.

In conclusion, this suggests a more diluted and a larger solvent volume is needed to allow a better penetration of the microwaves.

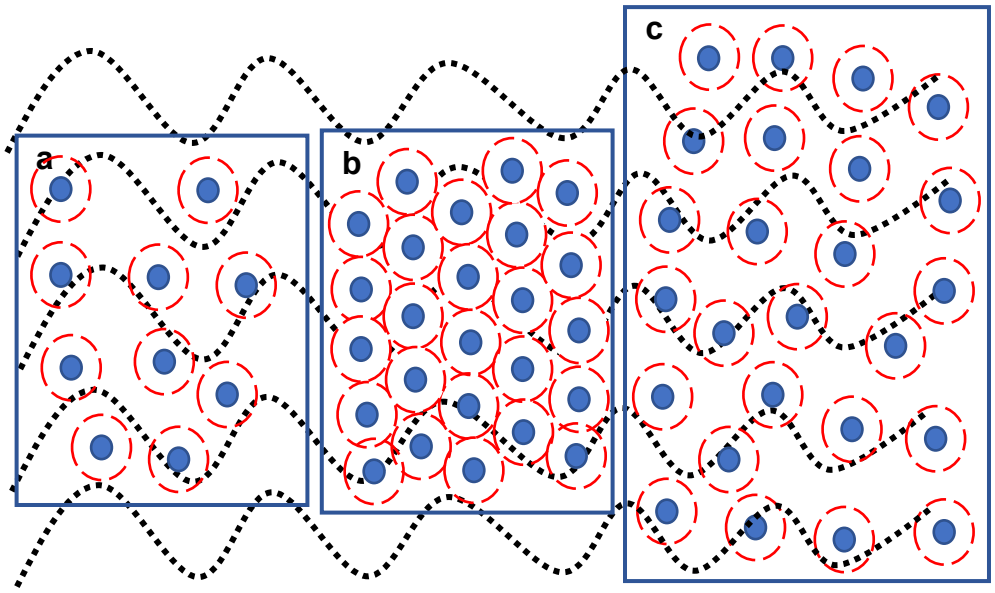


Figure 6- 11: Schematics of metal ions and respective solvation spheres. Diluted (a) and concentrated (b) systems each with different number of ions, and a diluted system with the same number of ions as b now in larger solvent volume (c). The dashed lines represent microwaves.

Figure 6-12 shows the XRD pattern of the membranes synthesised with a linker/metal ratio 2 and metal concentrations of 72 and 288 mM. The XRD pattern of the membrane synthesised using microwave heating at 288 mM suggests a very thin layer or no growth on the substrate surface. The XRD pattern of the membrane synthesised at 72 mM using microwaves shows no characteristic peaks of ZIF-8 implying a very thin layer or no continuous growth on the substrate. The XRD pattern of conventional heated membrane at 72 mM concentration show no characteristic peaks of ZIF-8, suggesting a very thin layer or no growth of ZIF-8. While the XRD pattern of the membrane synthesised using conventional heating at metal concentration of 288 mM, shows all characteristic peaks of ZIF-8, implying the surface growth observed in the SEM to be continuous.

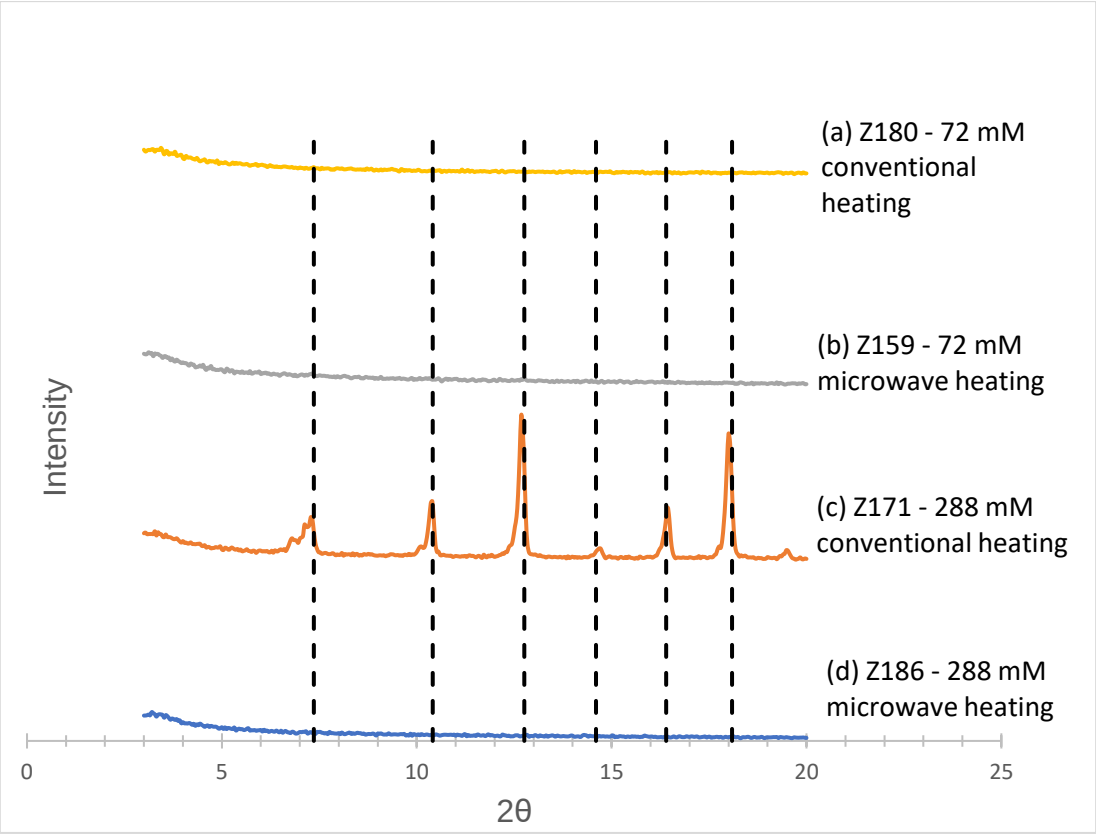


Figure 6- 12: XRD patterns of the seeded membranes synthesised with mixed MOF solutions at linker/metal ratio of 2 with metal concentrations of 72 mM using conventional (a) and microwave (b) heating, and metal concentration of 288 mM using conventional (c) and microwave (d) heating. Membranes were synthesised at 100 ^{o}C for 3 and 5 h using microwave and conventional heating, respectively. The dashed lines refer to the position of the most prominent characteristic peaks ZIF-8.

Table 6-2 summarises solvent volumes and precursor concentrations used in the literature while synthesising ZIF-8 membranes with microwave heating. The table shows that the moles of precursors (linker and metal) used by literature are an order of a magnitude higher than the 4 ml experiments from this study. This may indicate there is not enough precursor in the solution to sustain heterogenous growth of a continuous layer of ZIF-8 onto the substrate. Also, another limiting factor might be the absorption capacity of the system. The amount of solvent used is not absorbing enough power and the heating rate is not able to sustain a more robust heterogenous growth (Robinson et al., 2010). The high precursor concentration used in this study might suggest 'skin' depth issues are created - where the microwave energy cannot penetrate deep enough into the bulk liquid (Meredith, 1998). Higher losses at the surface of the reaction volume may mean less penetration of the electromagnetic waves into the reaction medium and hence the heating mechanism for the bulk fluid is mainly via convection. Equation 6-1 shows the penetration depth (D_p) equation. The

penetration depth equation shows the point at which (in metres) the electric field reaches 37% of its original field and how it can be optimised by the dielectric constant and dielectric loss factor. It should be noted the dielectric parameters must be measured per experiment since it depends on multiple of parameters, the concentration being one, which is discussed in more detail by Laybourn et al. (Laybourn et al., 2016). This was discussed in detail in the literature review (Section 2.6).

$$\boldsymbol{D_p = \frac{\lambda_0}{2\pi\sqrt{2\varepsilon'}} \frac{1}{\sqrt{\left(\left\{1+\left(\frac{\varepsilon''}{\varepsilon'}\right)^2\right\}^{0.5}-1\right)}}}$$ Equation 6- 1 (Thomas-Hillman et al., 2018)

Where D_p is the penetration depth (m), ε' is the dielectric constant, ε'' is the dielectric loss factor, and λ_0 is the free space wavelength of the incident radiation (m).

Table 6- 2: Solvent volumes, moles of precursors used in the synthesis of ZIF-8 membranes using microwave heating from literature and this study.

Reference	Zinc source	Surface modification	Metal concentration (mM)	Solvent volume (ml)	Concentration of metal in system (mM)	Concentration of linker in system (mM)	Linker/metal ratio
Bux et al. 2009	Zinc Chloride	None	99	80	8	12	1.5
Bux et al. 2011	Zinc Chloride	Dip coating	49	80	4	6	1.5
Zhu et al. 2016	Zinc Chloride	APTES	79	220	17	43	2.5
Li Sze Lai. 2016	Zinc Chloride	Solvent evaporation seeding	97	160	16	24	2.5
This study	Zinc Acetate Dihydrate	Physical seeding (rubbing)	288	16	4.6	36.9	8
			72	4	0.3	2.3	8
			288		1.2	9.2	8
			72		0.3	0.6	2
			288		1.2	2.3	2
This study	Zinc nitrate hexahydrate		288		1.2	9.2	8

Figure 6-13 shows the surface and cross-sectional images (scale bar is x5000 and x250 µm for 6-13a and 6-13b, respectively) of membrane synthesised with linker/metal ratio of 8 and metal concentration of 288 mM using microwave heating for 3 hours at 100 °C. A solvent volume of 16 ml was used to try to create a larger absorption capacity while keeping the concentration the same. The surface growth indicates typical cubic and rhombic morphology of ZIF-8. However, identifying individual entities in the intergrowth is difficult. This implies the larger solvent volume has promoted a more robust heterogenous growth when compared to the surface growth of the substrate synthesised using 4 ml (Figure 6-7c) with the same precursor concentration and ratio. Which indicates the increased solvent volume has better accommodated the microwave chemistry because with the larger solvent volume the absorption capacity of the system has now increased, as was reported by Robinson et al. study. Robinson et al. reported that by increasing their MeCN solvent volume (no dissolved species in the solvent) from 1 to 5 ml, power absorption increased from 0.39 to 1.93 W, an approximate five times increase, reflective of the solvent volume increase (dielectric constant of MeCN and methanol 36.5 and 33.6, respectively) (Gregory and Clarke, 2005, Robinson et al., 2010).

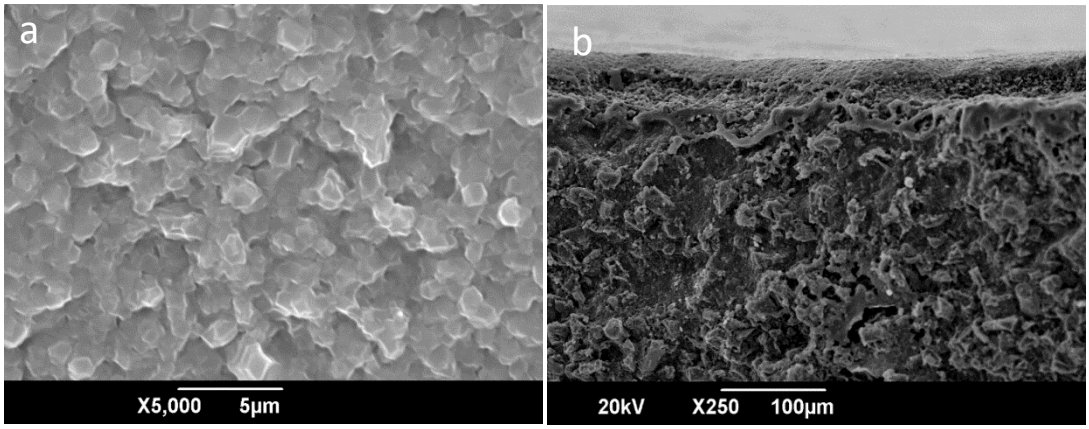


Figure 6- 13: Surface (a) and cross sectional (b) images of seeded membrane synthesised with mixed MOF solution (solvent volume of 16 ml) with linker/metal ratio of 8 and metal concentration of 288 mM using microwave heating at 100 °C for 3 hours.

Figure 6-14 shows the elemental analysis taken from another area of the same membrane synthesised with solvent volume of 16 ml. Although the surface image shows typical cubic and rhombic ZIF-8 growth, the EDX elemental analysis does not show complementary mapping i.e. where there is Zn (Figure 6-14b) the Al map should show those regions as black (Fig 6-14c). This may indicate the growth to be a very thin film where the mapping is detecting both the Zn and Al elements. In conclusion, the

EDX analysis shows that the increased solvent volume has promoted the formation of a continuous thin film.

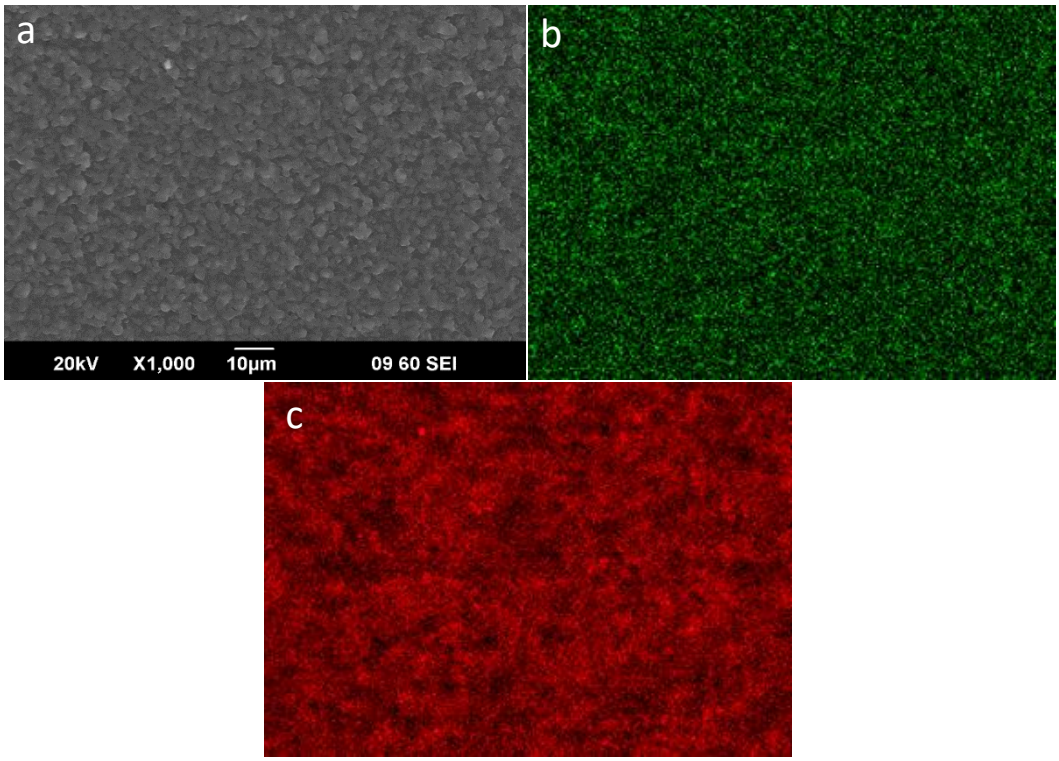


Figure 6- 14: SEM surface image (a) and EDX images of the surface showing Zn in green (b) and Al in red (c) of seeded membrane synthesised with mixed ZIF-8 solution (total solvent volume of 16 ml) with linker/metal ratio of 8 and metal concentration of 288 mM using microwave heating at 100 °C for 3 hours.

Figure 6-15 shows the XRD patterns of the membrane and bulk solution of the synthesis, synthesised using microwave heating for 3 hours at 100 °C with a solvent volume of 16 ml with linker/metal ratio 8 and metal concentration of 288 mM. The XRD pattern shows no characteristic peaks of ZIF-8 indicating a very thin layer or no growth on the substrate surface. The XRD pattern of the bulk solution shows all characteristic peaks of ZIF-8. It is therefore apparent that ZIF-8 is being synthesised in the bulk of the solution but not forming a continuous dense layer on the surface of the substrate. This may suggest that the ZIF-8 is failing to adhere to the substrate. However, is it also possible that any nucleated crystals on the substrate may later detach because of weak interaction, and then later dissolve into the bulk of the solution. Indicating a more tailored surface modification is needed to accommodate the microwave chemistry.

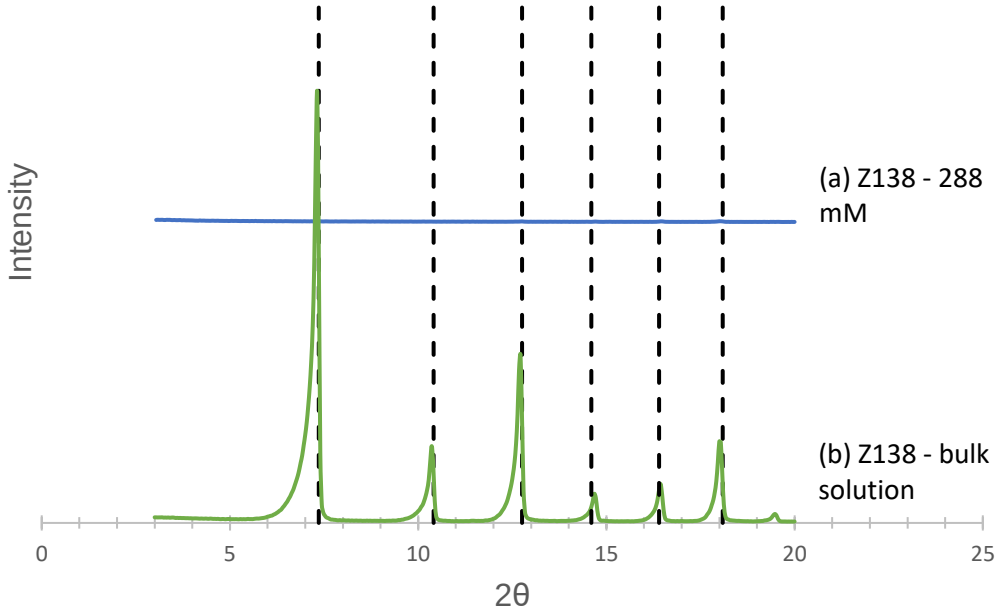


Figure 6- 15: XRD pattern of seeded membrane (a) and of ZIF-8 crystals collected from synthesis solution (b). MOF chemistry of linker/metal ratio of 8 and metal concentration of 288 mM, synthesised using microwave heating at 100 °C for 3 hours. The dashed lines refer to the position of the most prominent characteristic peaks of ZIF-8.

Figure 6-16 shows the surface and cross-sectional images (scale bar is x30 and x5000 µm for 6-16a and 6-16b, respectively) of membrane synthesised with linker/metal ratio of 8 and metal concentration of 36 mM using microwave heating for 3 hours at 100 °C. The surface indicates a small cluster (circled in red) of deposited ZIF-8 crystal. However, the cross-sectional images imply no continuous growth on the substrate. This suggests that metal concentration needs to be reduced further to maximise volumetric heating, and a larger solvent volume is needed to maximise the absorption capacity of the system. The level of power being absorbed at the solvent volumes being used in this study (4-16 ml) may not be enough to accommodate the rapid level of nucleation that is achievable by the microwave system. A higher absorption of power may be needed to achieve a more robust level of heterogenous growth due to the low dielectric heating properties of alumina and deposited seeds. Laybourn et al. studied the effects of absorbed power on MOF formation, where the results showed higher powers with shorter reaction times yielded crystals with a narrow size distribution. The crystals had a well-defined cubic structure, typical of MIL-53(Al) (Laybourn et al., 2017). This may suggest higher absorption of power in the ZIF-8 system may promote a more evolved crystal structure with the narrow crystal size distribution on the substrate. Particularly

when literature use volumes between 80-220 ml for the heterogenous growth of ZIF-8 in their systems (Bux et al., 2011, Bux et al., 2009, Zhu et al., 2016). This finding may imply that a higher rate of absorption of power helps promote a more robust heterogenous nucleation of ZIF-8 in the microwave system.

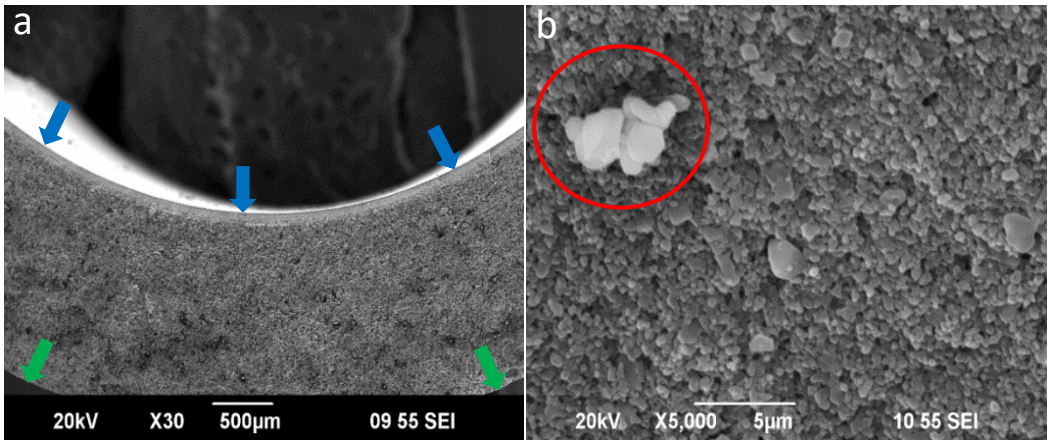


Figure 6- 16: Cross sectional (a) surface (b) images of seeded membrane synthesised with mixed MOF solutions at linker/metal ratio of 8 and metal concentration of 36 mM via microwave (at 100 °C for 3 h). Blue arrows pointing to the inside of the substrate surface and green arrows pointing towards the outside of the substrate.

Figure 6-17 shows the XRD pattern of the membrane synthesised with linker/metal ratio of 8 and metal concentration of 36 mM using microwave heating for 3 hours at 100 °C. The XRD patterns indicates that there was either no crystal or very thin layer of ZIF-8 on the surface of the substrates since none of the characteristic peaks for ZIF-8 were detected. Clearly, a larger and more dilute system is needed. Higher concentrations retard the movement of neighbouring solvation spheres when oscillating, because of the closely packed ions. The close packing leads to a reduction in the dielectric constant whilst the dielectric loss factor increases, due to the close packing providing a better rate of heat transfer. However, because of the close packing, the solvent volume is very good at absorbing microwaves on its surface. Creating the ‘skin’, a barrier to the microwaves, which affects the level of penetration of the microwaves. Resulting in the remainder of the mixture being heated by convection (Laybourn et al., 2016).

The penetration depth of a pure methanol is 1 cm at 2.45 GHz and room temperature (Horikoshi and Serpone, 2013). However, with dissolved species in the solvent and changes in temperature, the penetration depth changes. As ZIF-8 forms over time the dielectric constant and loss factor must be experimentally calculated since is unique to the system being heated. This is due to changes in the system caused by

disappearance of hot spots as ZIF-8 forms, and changes in the pH caused by the deprotonating imidazole releasing protons (Horikoshi and Serpone, 2013, Meredith, 1998, Tompsett et al., 2006).

This is a study that can be investigated for future work to see how the penetration depth effects heterogenous growth of ZIF-8 onto the alumina substrates.

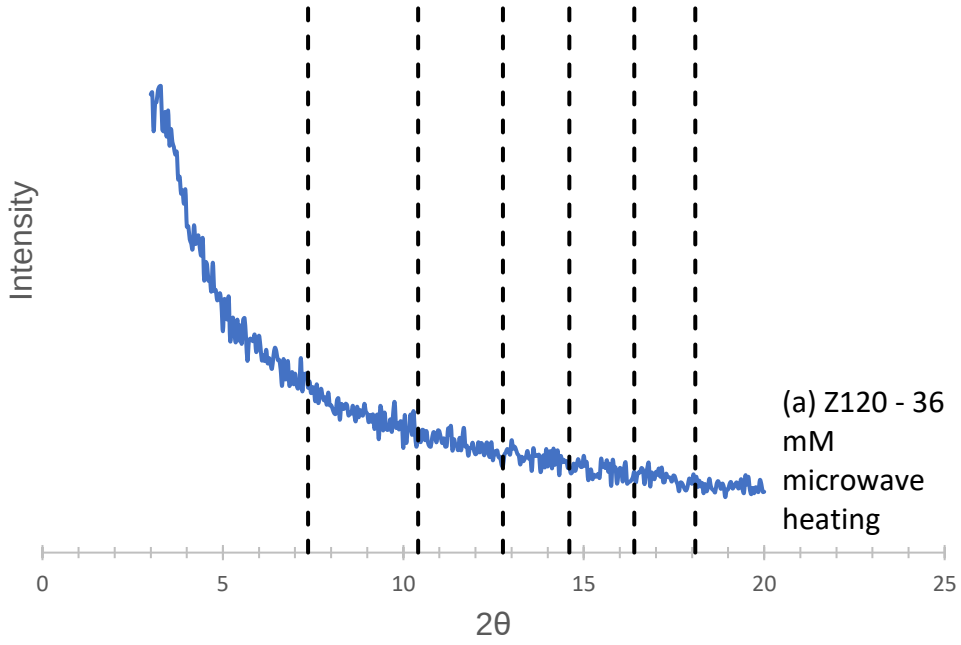


Figure 6- 17: XRD patterns of the seeded membranes synthesised with mixed MOF solutions at linker/metal ratio of 8 with metal concentrations of 36 mM using microwave heating synthesised at 100 ^{o}C for 3 hours. The dashed lines refer to the position of the most prominent characteristic peaks ZIF-8.

Figure 6-18 shows the surface and cross-sectional images (note that the scale bar is different) of membrane synthesised from zinc nitrate hexahydrate with linker/metal ratio of 8 and metal concentration of 288 mM using microwave heating for 3 hours at 100 °C. The surface and cross sectional images may suggest no continuous growth on the substrate. The surface image indicates atypical ZIF-8 growth, suggesting failed nucleated seeds. The lack of surface growth reflects similar findings in the batch chapter that the zinc nitrate delivers a weaker level of heterogenous growth for the batch system as was discussed in Chapter 4.

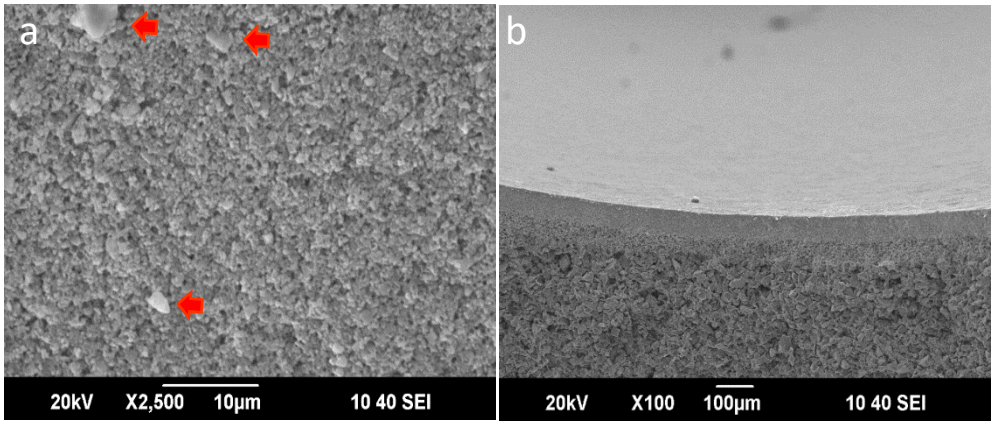


Figure 6- 18: Surface (a) and cross sectional (b) images of seeded membrane synthesised with mixed MOF solution using zinc nitrate hexahydrate at linker/metal ratio of 8 and metal concentration of 288 mM via microwave heating. Synthesised at 100 °C for 3 hours. Red arrows highlighting potentially failed nucleated seeds.

Figure 6-19 shows the XRD pattern of the membrane synthesised from zinc nitrate hexahydrate with linker/metal ratio of 8 and metal concentration of 288 mM using microwave heating for 3 hours at 100 °C. The XRD patterns indicate that there was either no crystal formation or only very thin layer of ZIF-8 on the surface of the substrates since none of the characteristic peaks of ZIF-8 were detected.

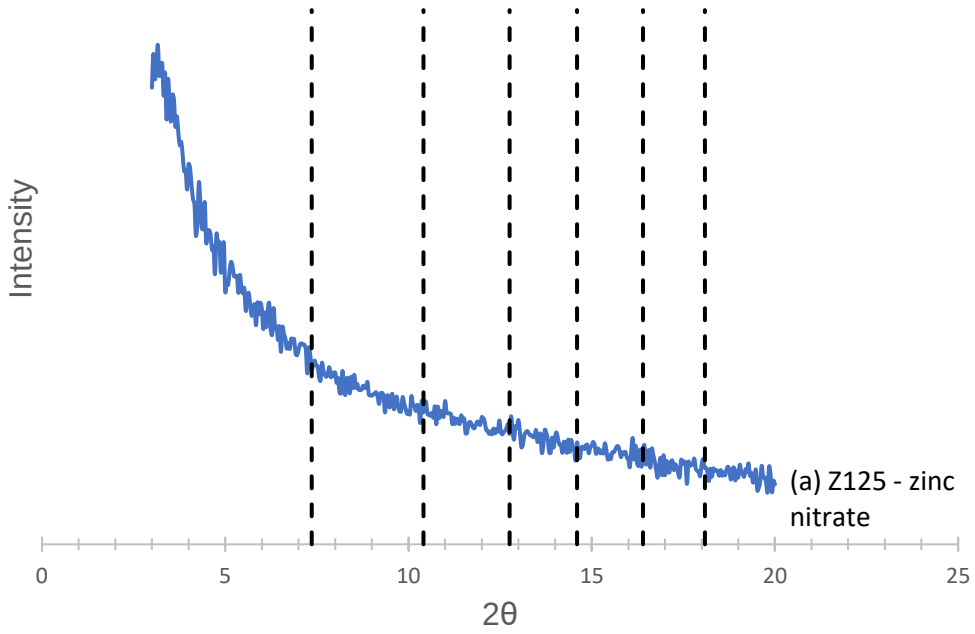


Figure 6- 19: XRD patterns of the seeded membrane synthesised with mixed MOF solutions using zinc nitrate hexahydrate at linker/metal ratio of 8 with metal

concentrations of 288 mM using microwave heating synthesised at 100 °C for 3 hours. The dashed lines refer to the position of the most prominent characteristic peaks ZIF-8.

6.3.2 Membranes synthesis using isolated precursors with microwave heating.

This section investigates formation of ZIF-8 when isolated precursors are heated volumetrically and selectively. The selective heating regime is caused by the dielectric properties' of alumina, Teflon plug, and methanol (without any dissolved species) which are 9.8 (Microwaves101, 2020a), 2.1 (Microwaves101, 2020b), and 33.6 (Hoz et al., 2013), respectively. Because of its low dielectric constant, the alumina and Teflon are considered 'transparent' to microwaves, suggesting a more uniform heating of solutions both inside and outside the substrate. However, as discussed in the previous section, because of the small solvent volume (compared to literature for ZIF-8 membranes) the volumetric heating may not be as efficient. An added advantage of the metal-linker isolation work is the metal ions ('hot spots') can be isolated in the substrate, allowing the maximum penetration of microwaves into the CEM vial. For the microwave heating, all metal-linker isolation work has been done with the metal solution inside the substrate.

The microwave metal-linker isolation results are compared to conventionally heated membranes (metal precursor solution inside) at the same temperature of 100 °C and synthesis time of 5 hours. The conventionally heated membranes had two substrates in the reaction vessel per synthesis with a total solvent volume of 32 ml.

Figure 6-20 shows the surface images (magnification is x2000, x500, x50, and x1000 for 6-20a, 6-20b, 6-20c and 6-20d, respectively) of membranes synthesised with isolated precursors (metal inside the tube) at 100 °C for 1 hour using microwave heating. The membranes were synthesised with linker/metal ratio of 8 and 2, and metal concentrations of 72 and 288 mM. The surface images of the membranes synthesised at the metal concentration of 72 mM shows growth of non-typical cubic/rhombic morphologies. This implies that seeds have failed to nucleate. The surface image of the membrane synthesised with metal concentration of 288 mM and linker/metal ratio of 2 implies no growth. The images of the membranes that were subject to a metal concentration of 288 mM and linker/metal ratio 8 indicate the presence of ZIF-8 crystal with typical rhombic morphology. It is unlikely that the discrepancy in surface growth between the two linker/metal ratios of 2 and 8 at 288 mM is because of the difference in linker concentration. Since literature shows that linker ions in the solution do not significantly alter the dielectric properties, and hence the degree of microwave heating (Laybourn et al., 2016). It is most likely due the weak interaction of microwaves

between the seeds and alumina substrate leading to discrepancy in heterogenous growth between the two ratios at 288 mM.

The nature of the surface growth indicates the chemistry of the reaction system needs to be optimised to achieve a more robust level of superheating to achieve a better rate of heat transfer to the alumina substrate. Although the microwave system in this chapter indicates the seeding is a weak form of surface modification, Zhang et al. commented that seeding is an effective way of reducing synthesis time for its zeolite membranes (Zhang et al., 2016). Zhang et al. also referred to the work of Gascon et al. where synthesis time was reduced from 25 to 2 days by using a seed suspension for the DDR zeolite membrane (Gascon et al., 2008). Bux et al. worked with ZIF-8 membranes reflecting similar findings (Bux et al., 2011, Bux et al., 2009). Bux et al. synthesised continuous ZIF-8 membrane on surface modified flat disks in 2 hours using seeds incorporated into a polymer binder (previous study 4 hours on unmodified flat disk). The synthesis conditions used in the two studies by Bux et al. were the same, except for the precursor concentrations, where metal concentrations of 79 and 49 mM were used for the first and second studies, respectively. Supporting former discussions in this chapter that the decrease in the number of ions in the system promotes a more volumetric heating regime.

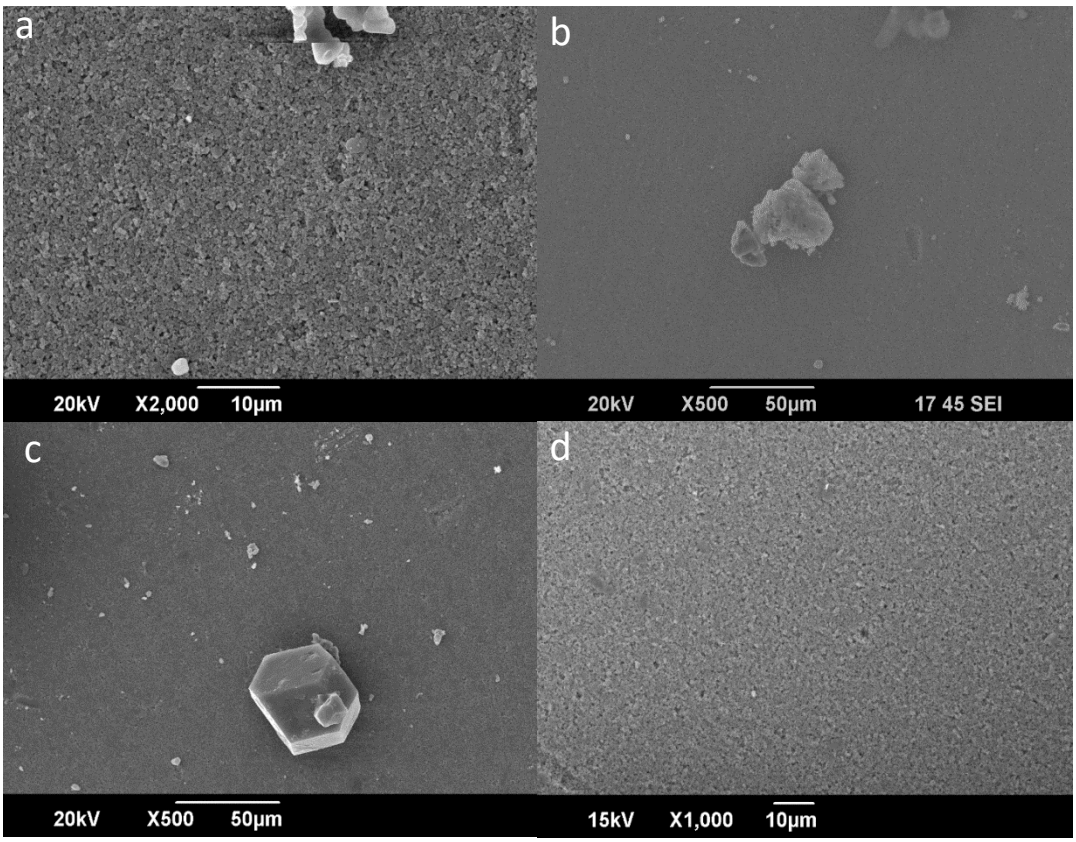


Figure 6- 20: Surface images of seeded membranes synthesised with isolated precursors (metal inside) with metal concentration of 72 mM and linker/metal ratio of 8 (a) and linker/metal ratio of 2 (b). Surface images of seeded membranes synthesised with isolated precursors (metal inside) with metal concentration of 288 mM and linker/metal ratio of 8 (c) and linker/metal ratio of 2 (d). Membranes synthesised at 100 °C for 1 hour using microwave heating.

Figure 6-21 shows the XRD patterns of the membranes synthesised with isolated precursors using microwave heating with metal concentrations of 72 and 288 mM, and linker/metal ratios of 2 and 8. The XRD patterns supports the SEM images that there was either no crystal or very thin layer of ZIF-8 on the surface of the substrates since none of the characteristic peaks of ZIF-8 were detected.

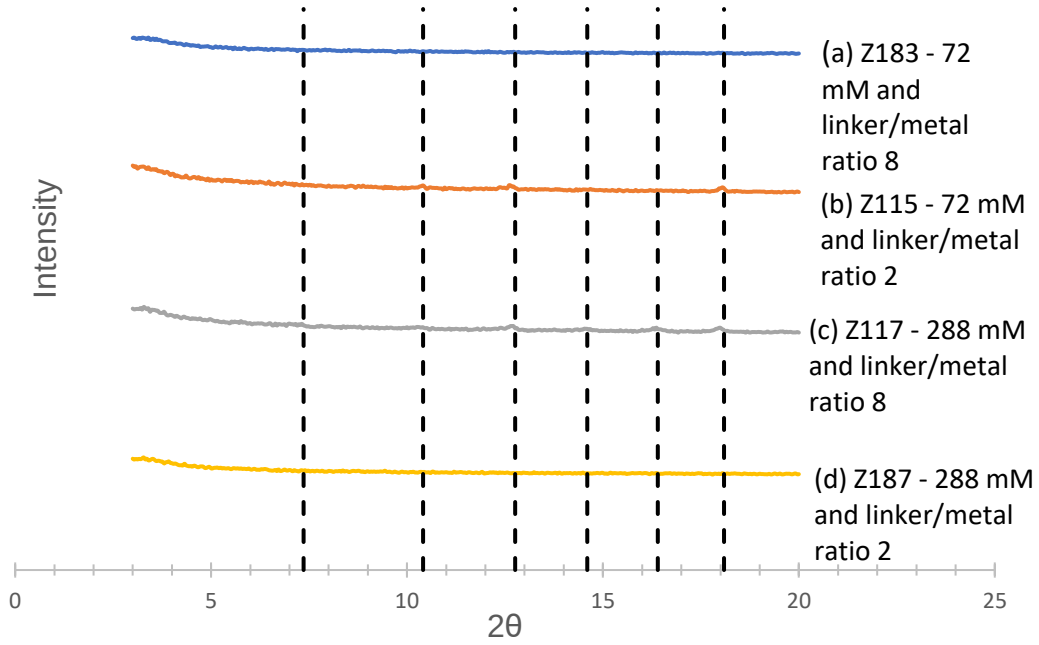


Figure 6- 21: XRD patterns of seeded membranes synthesised with isolated precursors (metal inside) with metal concentration of 72 mM and linker/metal ratio of 8 (a), and linker/metal ratio of 2 (b). Surface images of seeded membranes synthesised with isolated precursors (metal inside) with metal concentration of 288 mM and linker/metal ratio of 8 (c) and linker/metal ratio of 2 (d). Membranes synthesised at 100 °C for 1 hour using microwave heating. The dashed lines refer to the position of the most prominent characteristic peaks ZIF-8.

Figure 6-22 shows the surface images (not at the same magnification) of membranes synthesised with isolated precursors (metal inside the tube) at 100 °C for 5 and 3 h using conventional and microwave heating, respectively. The membranes were synthesised with linker/metal ratio of 8 and metal concentrations of 72 and 288 mM. The conventionally heated membranes surface images indicate no growth at the 72 mM concentration, while the surface images at 288 mM concentration suggest ZIF-8 crystals with typical cubic/rhombic morphology. From the surface growth, the conventionally heated system indicates a more robust level of growth with the more closely packed ions in the 288 mM concentrated system. The surface images of the microwave heated membranes at the 72 mM concentration show typical cubic/rhombic shape with crystal size range of 9.4-49.6 µm (Figure 6-23 for histogram), and non-typical ZIF-8 crystal growth at the 288 mM metal concentration. The non-typical growth at 288 mM concentration may imply failed nucleated seeds. The surface images of the microwave system suggest a more diluted system favours heterogenous nucleation

implying a better penetration of microwaves for heating as was concluded in Section 6.3.1.

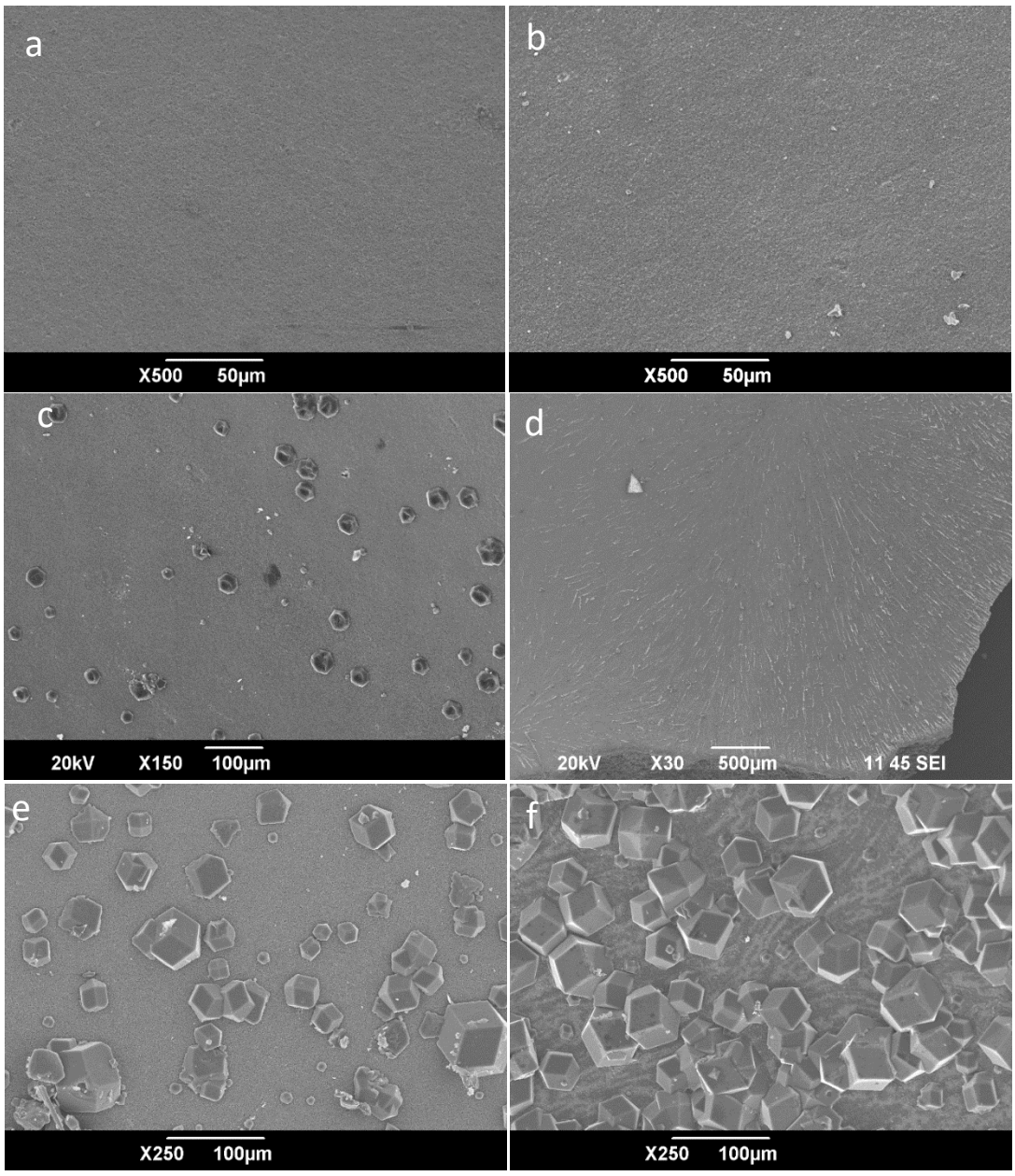


Figure 6- 22: Surface images of seeded membranes synthesised with isolated precursors (metal inside) at linker/metal ratio of 8 and metal concentration of 72 mM at 100 °C using conventional heating for 5 hours (a, b), and microwave heating for 3 hours (c). Surface images of seeded membranes synthesised with isolated precursors (metal inside) with linker/metal ratio of 8 and metal concentration of 288 mM at 100 °C using microwave heating for 3 hours (d) and conventional heating for 5 hours (e, f).



Figure 6- 23: Particle size histogram of crystals on the substrate surface synthesised at linker/metal ratio 8 and metal concentrations 72 mM using microwave heating. Membranes synthesised for 3 hours at 100 °C.

Figure 6-24 shows the XRD patterns of the membranes synthesised with isolated precursors using conventional and microwave heating with linker/metal ratio of 8 and metal concentrations of 72 and 288 mM. As expected, the membranes synthesised under microwave heating at 72 and 288 mM concentration show no peaks suggesting either no or sparse levels of ZIF-8 crystal growth. The membranes synthesised using conventional heating at 72 mM concentration suggest no or sparse ZIF-8 crystal growth. The membrane, Z161A, synthesised at 288 mM concentration under conventional heating may suggest oriented growth with a single peak at 18.09 indicating the crystallographic plane, 222, facing the detector. While Z161B, shows all characteristic peaks of ZIF-8, suggesting crystals formed on the substrate surface to have no preferred orientation. The oriented growth may suggest more densely packed crystals on the membrane sample characterised with XRD.

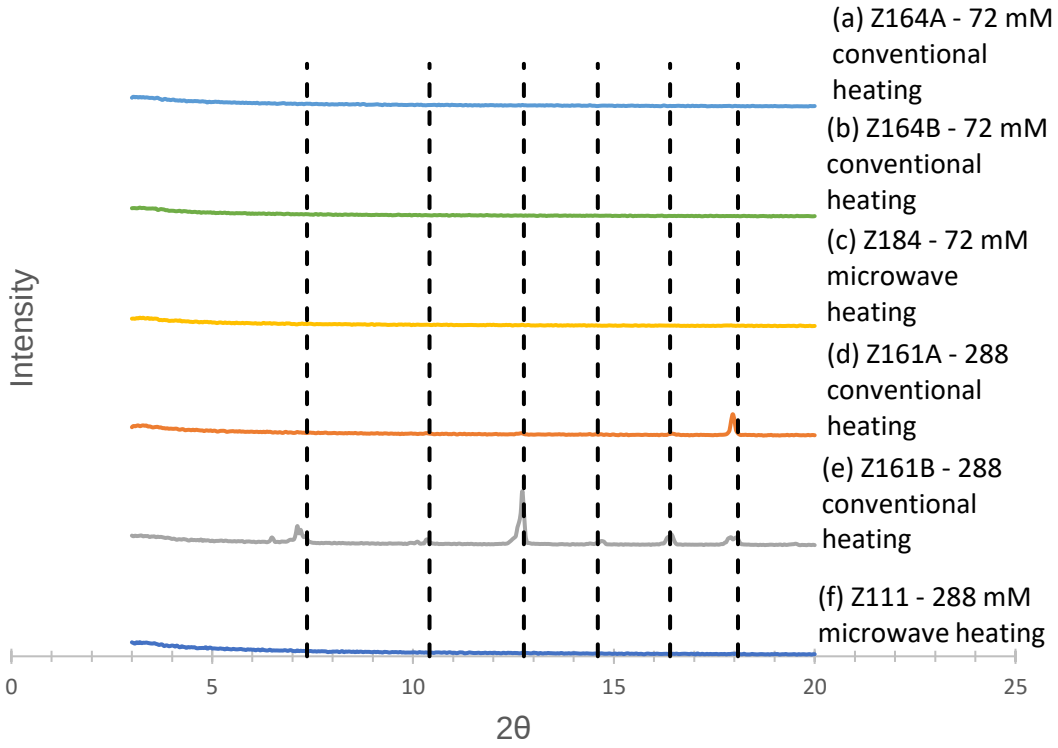


Figure 6- 24: XRD pattern of seeded membranes synthesised with isolated precursors (metal inside) with linker/metal ratio of 8 at metal concentration of 72 mM using conventional heating for 5 hours (a, b) and microwave heating for 3 hours at 100 °C (c), and metal concentration of 288 mM hours using conventional heating for 5 hours (d, e) and microwave heating for 3 hours at 100 °C (f). The dashed lines refer to the position of the most prominent characteristic peaks ZIF-8.

Figure 6-25 shows the surface images (not at same magnification) of the membranes synthesised with isolated precursors (metal precursor present inside the tube) at 100 °C with linker/metal ratio 2 using microwave and conventional heating for 3 and 5 h, respectively. Membranes synthesised using conventional heating at concentrations of 72 mM and 288 mM show evolved ZIF-8 crystals with the typical rhombic morphology. The membrane synthesised using microwave heating at 72 mM indicates crystal growth on the substrate surface, however, there are gaps between the ZIF-8 crystals. While the surface image at the 288 mM concentration under microwave heating appears to show a single spherical crystal deposited on the substrate surface. This implies crystal growth still to be in the metastable state, suggesting convective heat transfer to be the more dominant form of heat transfer in the microwave system at the 288 mM concentration and linker/metal ratio 2. Although the metal-linker isolation system brings the reaction zone to the substrate surface, it reiterates the conclusions made in Section 6.3.1; a larger and more diluted system favours a better penetration of microwaves.

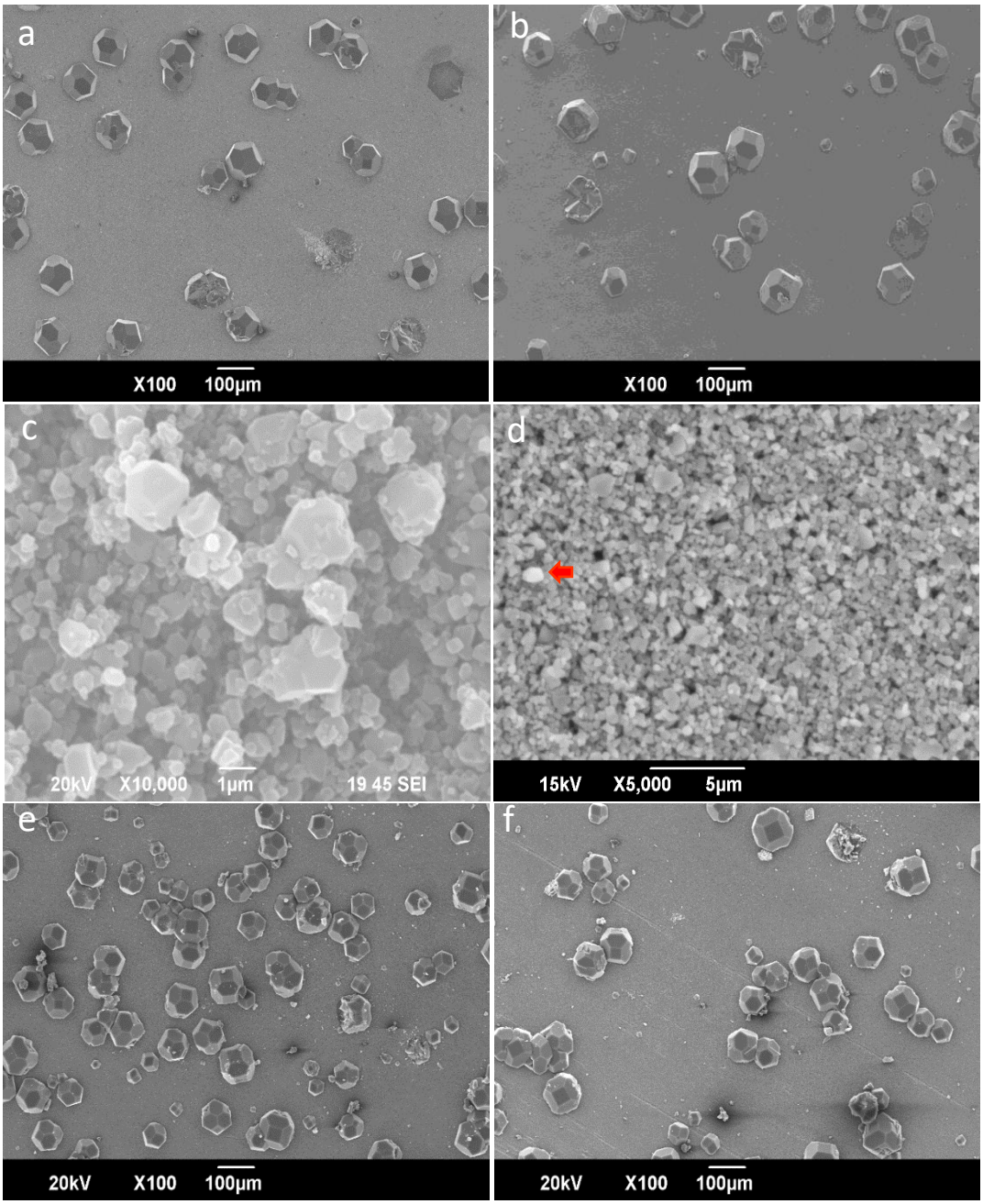


Figure 6- 25: Surface images of seeded membranes synthesised with isolated precursors (metal inside) with linker/metal ratio of 2 at 100 °C and metal concentration of 72 mM using conventional heating for 5 hours (a, b), and microwave heating for 3 hours at 100 °C (c). Surface images of seeded membrane synthesised with isolated precursors (metal inside) with linker/metal ratio of 2 at 100 °C and metal concentration 288 mM using microwave heating for 3 hours (d), and conventional heating for 5 hours (e, f). Red arrows highlighting ZIF-8 crystals.

Surprisingly, a smaller crystal size range of 0.34-1.97 µm (Figure 6-26 for histogram) was obtained for the microwave heated membrane at 72 mM and linker/metal ratio 2, when compared to the microwave system at linker/metal ratio of 8 at the same concentration of 72 mM, 9.4-49.6 µm (Figure 6-23). The smaller ratio normally yields

larger crystal size due to there being fewer metal centres in the system. This may suggest that the reduced concentration of linker ions may have allowed for a better penetration of microwaves into the reacting system leading to smaller crystals with a narrow size distribution. However, the numerical data presented by Laybourn et al. of the linker ion BDC^- (Laybourn et al., 2016), from terephthalic acid indicated linker component themselves only weakly interact with microwaves. This is because the solvation spheres dictate the interaction mechanisms of the linker ions meaning that BDC^- only has minimal effect on the dielectric properties of the overall solution. Hence, the nature of the solvent dictates the behaviour of the linker ions. However, the solvent being used in this thesis has remained the same, methanol. Therefore, this may suggest the heterogenous growth observed at linker/metal ratio 2 and 72 mM metal concentration is a combination of the conventional and microwave heating mechanisms, with microwave component being the more dominant form of heating mechanism in this instance.

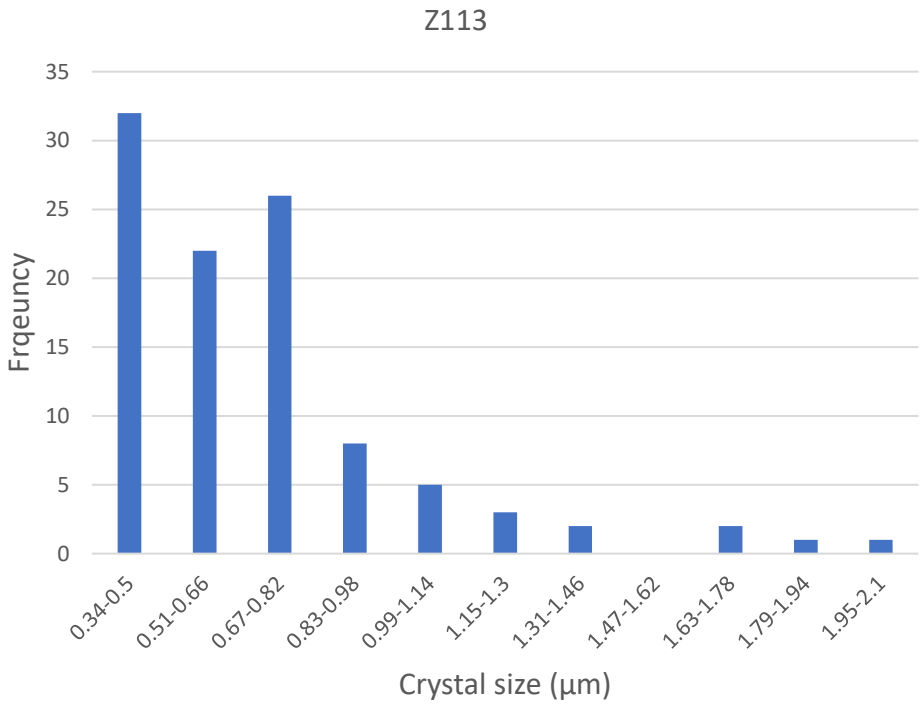


Figure 6- 26: Particle size histogram of crystals on the substrate surface synthesised with isolated precursors (metal inside) at linker/metal ratio 2 and metal concentrations 72 mM microwave heating for 3 hours at 100 °C.

Figure 6-27 shows XRD patterns of the membranes synthesised with isolated precursors (metal inside the tube) at 100 °C with linker/metal ratio 2 using microwave and conventional heating for 3 and 5 hours, respectively. The XRD pattern of the membrane synthesised using microwave heating at 72 mM shows all characteristic

peaks of ZIF-8, indicating crystals on the surface have no preferred orientation. The membrane synthesised at 288 mM using microwave heating suggests little or no crystal growth. For the conventional heated systems, at 72 mM, the XRD patterns of the Z160B membranes shows all characteristic peaks, suggesting growth on the substrate surface to have no preferred orientation. The XRD pattern of Z160A suggests little or no coverage. The XRD patterns of the membranes synthesised at 288 mM using conventional heating shows all the characteristic peaks of ZIF-8, indicating oriented growth.

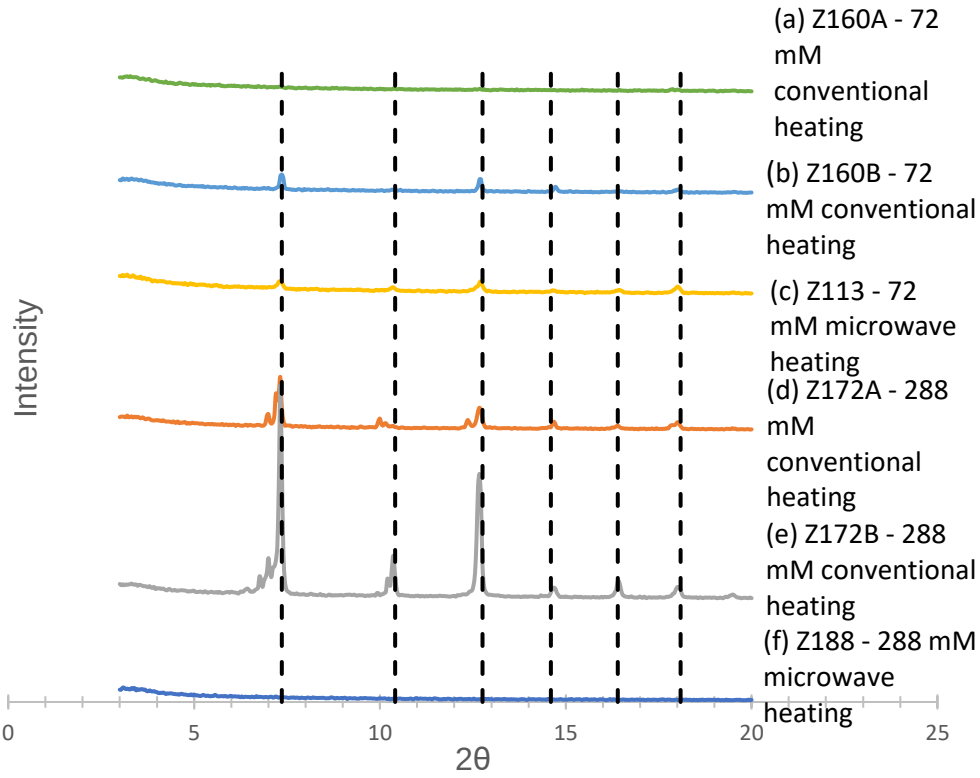


Figure 6- 27: XRD pattern of seeded membranes synthesised with isolated precursors (metal inside) with linker/metal ratio of 2 with metal concentration of 72 mM using conventional heating at 100 °C for 5 hours (a, b) and microwave heating for 3 hours (c). XRD pattern of seeded membranes synthesised with isolated precursors (metal inside) with metal concentration of 288 mM using conventional heating at 100 °C for 5 hours (d, e) and microwave heating for 3 hours (e). The dashed lines refer to the position of the most prominent characteristic peaks of ZIF-8.

Figure 6-28 shows the surface and cross sectional images (magnification is x1000 and x250 for 6-28a and 6-28b, respectively) of the membrane synthesised with microwave heating at 100 °C with isolated precursor, linker/metal ratio of 8 and metal concentrations of 288 mM with total solvent volume of 16 ml. The surface images may suggest crystal growth of typical ZIF-8 rhombic shape with crystal size range of 15-49 µm (Figure 6-29 for histogram). While the growth on the surface image (Figure 6-22d)

of the membrane synthesised at the same precursor concentration and ratio in the isolated system using 4 ml implied failed nucleated seeds. This implies the increased solvent volume has been volumetrically heated. However, the cross-sectional image (Figure 6-27b) shows non-typical ZIF-8 crystal growth. To further study the role of solvent volume in dielectric heating and heterogeneous nucleation of ZIF-8 in the metal-linker isolation system larger solvent volumes are needed, ideally reflecting that used by literature for ZIF-8 membranes, specifically 80-220 ml (Bux et al., 2011, Bux et al., 2009, Zhu et al., 2016).

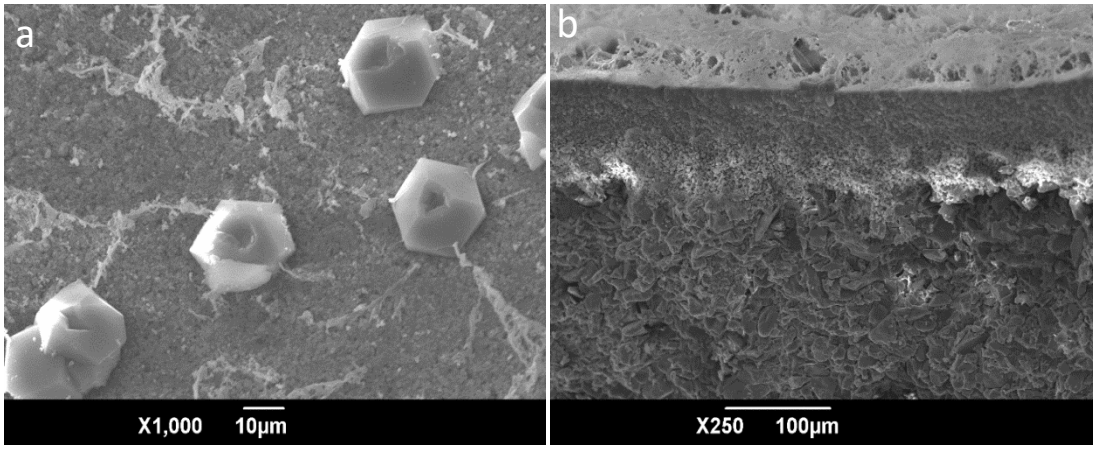


Figure 6- 28: Surface image of seeded membrane synthesised with isolated precursors (metal inside) with metal concentration of 288 mM and linker/metal ratio of 8. Membranes synthesised at 100 °C for 3 hours using microwave heating with total solvent volume of 16 ml.

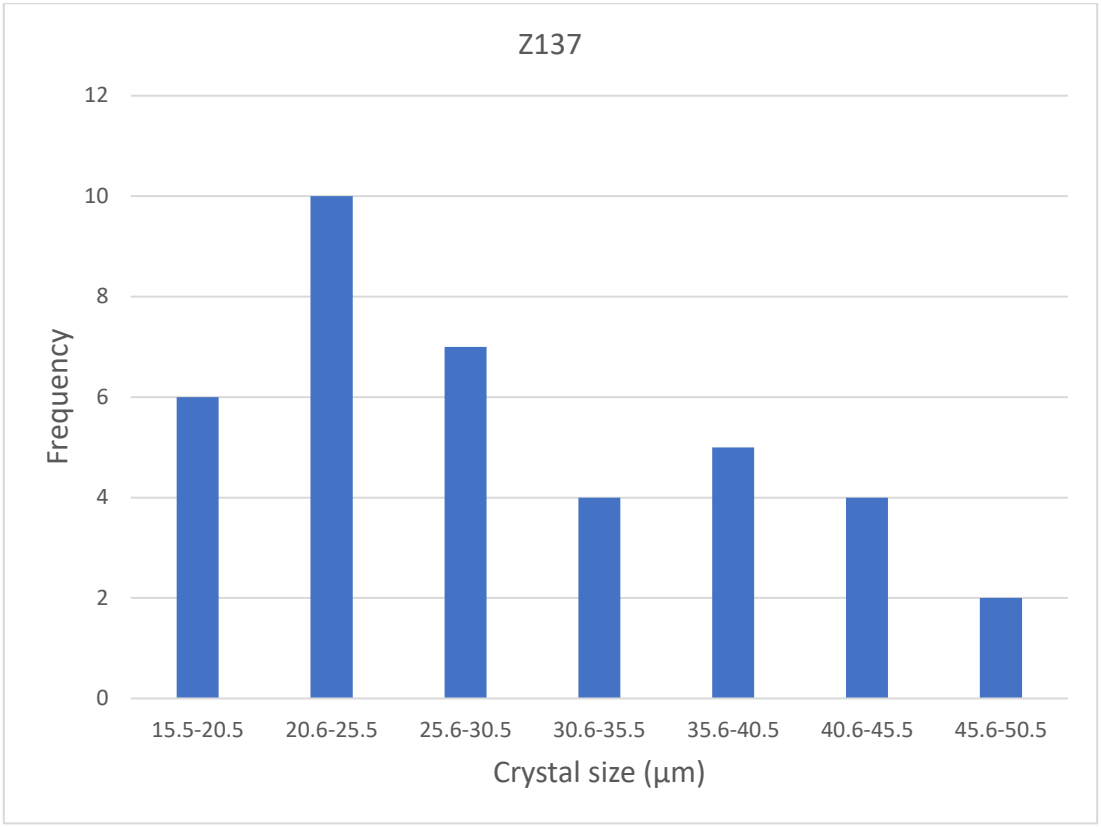


Figure 6- 29: Particle size histogram of crystals on the substrate surface synthesised with isolated precursors (metal inside) at linker/metal ratio 8 and metal concentrations 288 mM using microwave heating with total solvent volume of 16 ml. Membranes synthesised for 3 hours at 100 °C.

Figure 6-30 shows the XRD pattern of the membrane synthesised with microwave heating at 100 °C with isolated precursor, linker/metal ratio of 8 and metal concentrations of 288 mM with total solvent volume of 16 ml. The XRD pattern show all the characteristic peaks of ZIF-8, indicating the crystals showing no preferred orientation. The double and single peaks at 18.09° and 14.00°, respectively, indicate the presence of linker precursor on the surface (Figure 6-31 shows the XRD pattern of precursors). This implies the growth seen from the cross sectional image (Figure 6-28b) to be unreacted linker. This may suggest a higher rate of absorption is needed via increasing solvent volume, to help promote a more robust reaction zone at the substrate boundary in the isolated system.

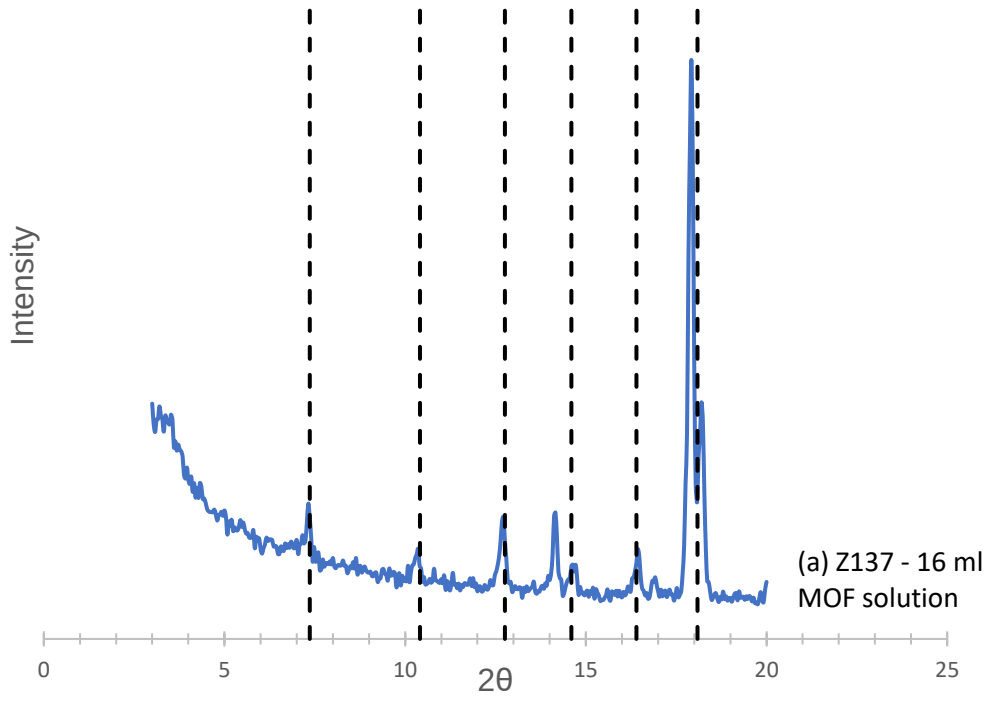


Figure 6- 30: XRD pattern of seeded membranes synthesised with isolated precursors (metal inside) with linker/metal ratio of 8 at metal concentration of 288 mM. Membranes synthesised at 100 °C for 3 hours using microwave heating with total solvent volume of 16 ml. The dashed lines refer to the position of the most prominent characteristic peaks of ZIF-8.

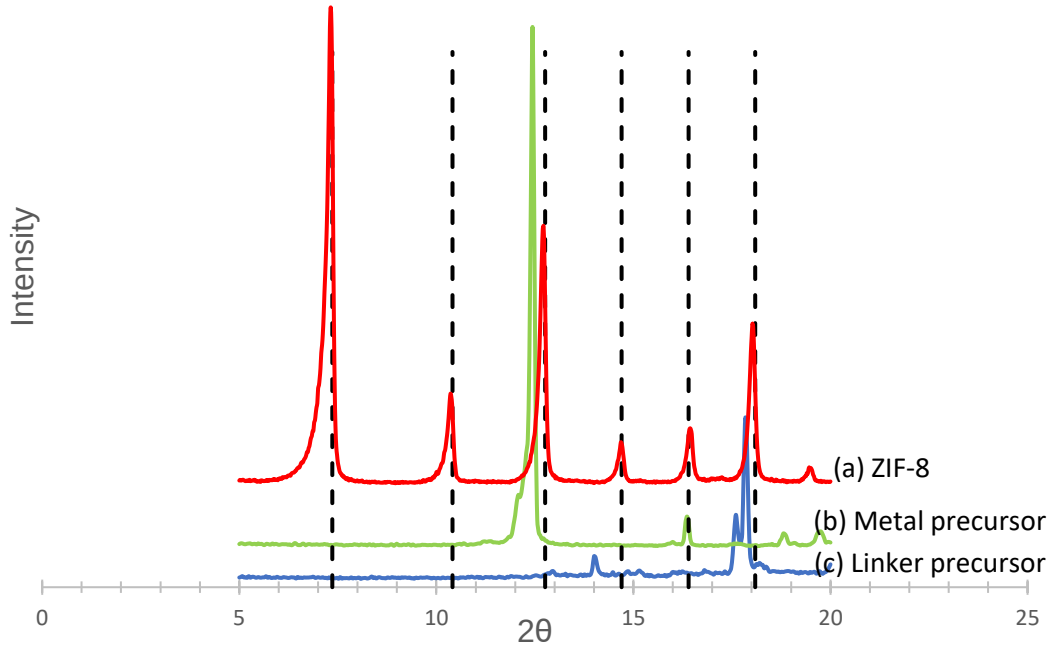


Figure 6- 31: XRD pattern of ZIF-8 seeds synthesised from zinc nitrate hexahydrate and 2-methylimidazole using methanol at 150 °C for 5 hours (a), and the metal precursor zinc acetate dihydrate (b) and the linker precursor 2-methylimidazole (c) used for ZIF-8 membrane synthesis. The dashed lines refer to the position of the most prominent characteristic peaks of ZIF-8.

6.4 Conclusions

This chapter investigated how two different heating mechanisms (microwave and conventional heating) affects the growth of ZIF-8 on a substrate at 100 °C. The impact of microwave heating on heterogenous growth of ZIF-8 onto ceramic substrates was compared to conventional heating. The work was carried out systematically to better understand heterogenous growth of ZIF-8 and microwave chemistry.

Whilst volumetric heating is a more efficient heating mechanism for the bulk fluid (compared to heating through conduction and convection) it can result in selective heating of specific areas to create hotspots. This 'superheating' of selective of individual components during the experiment which can give the appearance of enhanced kinetics because the bulk temperature is comparable to conventional methods whilst exceeding expected levels of conversion/growth.

The heterogenous growth of ZIF-8 onto substrates was achieved within 60 minutes demonstrating that microwave heating has the potential to achieve shorter synthesis times.

Also, the results have suggested that the reaction chemistry needs to be optimised when using a microwave heating system to ensure for a more robust heterogenous growth of ZIF-8. For example, optimising precursor concentration and reaction solvent volume to achieve better dielectric heating and potentially better rate of power absorption is needed. This has not been discussed before in the literature specifically around zeolite and MOF membranes. Table 6-3 quantitatively summarises the surface growth of membranes synthesised using microwave heating. Although some SEM images suggest coverage is > 90 %, their accompanying results (EDX, cross sectional images, or XRD) have suggested the growth is not continuous.

Table 6- 3: Summary of surface coverage of membrane synthesised using microwave heating with their respective precursors concentration and ratios.

Concentration (mM)	Linker/ metal ratio	Mixed or isolated (metal in)	Surface coverage (%)	Synthesis time (hours)	Solvent Volume (ml)	Thickness (um)
72	8	Mixed	-	1	4	-
72	2	Mixed	-	1	4	-
288	8	Mixed	98	1	4	-
288	2	Mixed	-	1	4	-
36	8	Mixed	-	3	4	-
72	8	Mixed	-	3	4	-
288	8	Mixed	-	3	4	-
72	2	Mixed	27-84	3	4	-
288	2	Mixed	-	3	4	-
288	8	Mixed	99-100	3	16	-
72	8	Isolated	-	1	4	-
72	2	Isolated	-	1	4	-
288	8	Isolated	-	1	4	-
288	2	Isolated	-	1	4	-
72	8	Isolated	7-8	3	4	-
288	8	Isolated	-	3	4	-
72	2	Isolated	84-89	3	4	-
288	2	Isolated	-	3	4	-
288	8	Isolated	10-23	3	16	-

In conclusion, the work in this chapter has shown more tailored reaction system is needed to optimise the microwave-assisted growth of MOF membranes. To maximise the absorption capacity of the reaction medium a large and diluted solvent volume is needed to minimise the formation of the ‘skin’, allowing the maximum penetration of microwaves into the reaction mixture and maximising volumetric heating. A more tailored surface modification to accommodate the microwave chemistry, such as metal ions deposited onto the substrate surface that can act as receptors for the microwaves making the substrate less transparent to the microwave energy. Another option is silane coupling agents that can form a chemical bond between the substrate and ZIF-8 structure instead of the physical deposition of ZIF-8 seeds. Hence, by optimising these parameters (surface modification, large and diluted solvent volume), the manufacture of ZIF-8 membranes on a pilot scale using microwave heating can be successful.

For the future, sections 6.3.1 and 6.3.2 lists suggestions and supporting information via references for future experiments that can help promote membrane growth under microwave heating.

7. Dynamic cold spraying of MOFs onto substrates

7.1 Introduction

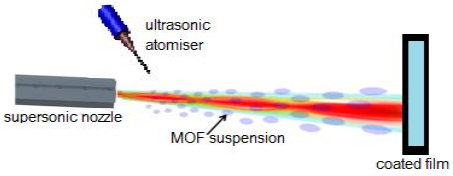


Figure 7- 1: Schematic of MOF suspension injected into high-pressure gas stream.

Cold gas dynamic spraying (CGDS) is an emerging coating deposition method in which particles are injected into a supersonic gas stream that is generated by the expansion of a high-pressure gas stream through a convergent-divergent nozzle. The main advantage is that the particles are not heated during the spray. Therefore, no phase change of the MOFs occurs in the gas stream. Figure 7-1 shows a schematic of the atomisation (break-up) of MOF slurry, coating a substrate whereby the slurry is injected into a heated air stream. The hot air evaporates the carrier solvent off, leaving behind individual MOF particles. If the particles surpass the critical velocity (velocity needed for particle attachment), they will attach to the substrate on impact.

Supersonic CGDS coated rapid deposition of preferentially orientated and non-orientated ZIF-8 films. In addition, a feasibility study of Kim et al. (Kim et al., 2016a) showed an external injection of the MOF suspension in the supersonic gas stream. This technique is ideal for size scaling, and high throughput commercialisation whilst the control of the external injection setup has not been studied before in literature. A fundamental understanding of the relationship between the processing and microstructure properties of the CGDS of MOF films can allow for the maintenance of crystal structure and control over film thickness and uniformity.

Studies have reported on the importance of selecting mechanical parameters for spray work such as air pressure and stand of distance (Arslan et al., 2011, Hurrle et al., 2017), the number of passes (Kim et al., 2014) and angle of injection (C.-J Li, 2003), which is only studied for the spraying of powders. Although these properties are crucial for the deposition of materials onto a substrate, the atomiser's systematic study (slurry and gas stream interaction) and the mechanical setup of the coating process have not been studied before, especially for MOF coatings.

In this chapter, the continuous coating of HKUST-1 films from suspensions onto an flat non-porous alumina substrate was conducted at room temperature since the efficiency of the coating process using MOF slurry in unheated air streams has not been explored to date. During the experiments, the systematic design of the novel atomiser was

investigated. The influence of the angle of injection and airstream pressure on the coatings were explored. The interaction between the unheated compressed air and HKUST-1 suspension were studied by using a high-speed camera, in which the images were taken every millisecond. The effects of the stand of distance (SOD) and number of passes were also reported.

7.2 Experimental procedure

HKUST-1 particles, with an average particle size of 3 microns, in methanol (7 wt%) was used for coating. HKUST-1 was selected due to its availability as suspension from Promethean Particles at the time. In addition, the blue HKUST-1 coating can be immediately seen on the substrate.

Cold gas dynamic spray experiments were conducted using LPCS Dymet 423. Dymet 423 gun was set up on the wheeled stand, then connected to the external compressed air pipeline providing air to the Dymet, and then to the mains – the Dymet was not turned on at this stage.

Figures 7-2 and 7-3 show a photo and schematic of the atomiser setup, respectively. Figure 7-3 show the mechanical parameters that will be varied systematically in the chapter that affect particle velocity and adhesion onto the target substrate. Before the gun was secured to the stand, the nozzle with a silicon connector was attached to the gun. The Dymet gun with the attached bracket and extended arm was then secured onto the wheeled stand. The nozzle from which the MOF suspension was released was then secured to the arm. The syringe pump was connected to the mains and turned on, the syringe filled with suspension was secured to the pump; the desired flow rate was selected. The flexible pipe between the syringe and spray nozzle was securely connected. Before any spray work, the syringe pump was turned to check for a steady stream of suspension to ensure no blockages or intermittent flow.

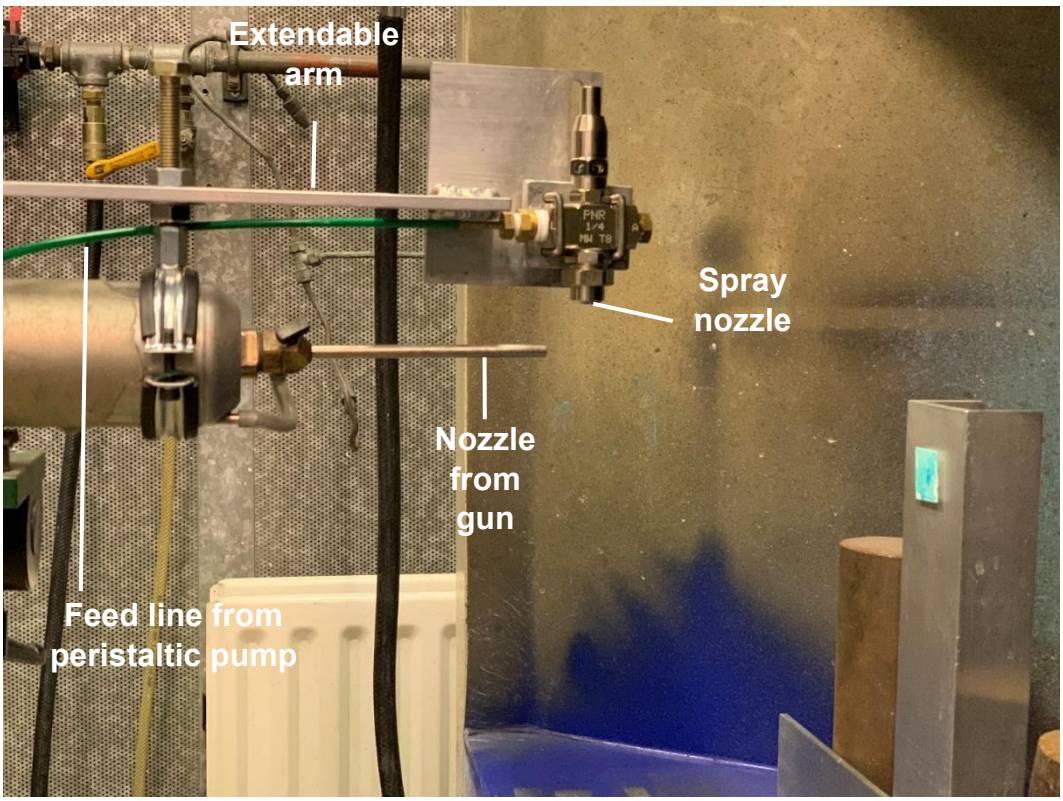


Figure 7- 2: Photo of Dymet gun, extendable arm, suspension feed line feeding into spray nozzle.

The flat alumina substrates were cut into approximate 4 cm^2 and secured to a steel plate. The pressure was selected on the instrument. The Dymet was turned on, and the flow of suspension was started. Once a steady spray of suspension was established, the gun movement was started. When the desired number of passes were completed, gun movement and pump were stopped simultaneously.

Figure 7-3 shows the schematic of the atomiser setup. The substrate was positioned 100 mm below the nozzle exit. The gun was installed on a traversing stage with a movement speed of 20 mm/s in the vertical direction. The experimental work studied the effects of slurry flow rate (25-100 ml/s), d – distance between slurry and gun nozzles (5-30 mm), pressure (2-6 bar) and angle of injection (30-90°) to see the effects on atomisation and surface coverage. The SOD (10-60 cm) and the number of passes (2-6 passes) were also studied to see the effects on surface coverage.

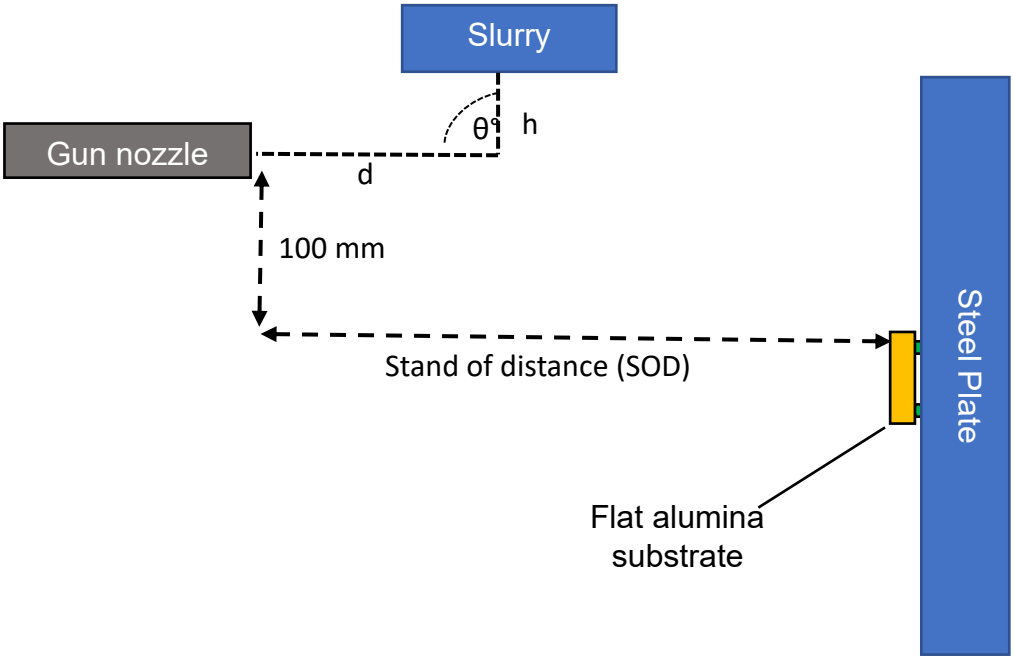


Figure 7- 3: Schematic of the atomiser set up.

The atomiser's design was further optimised by studying the level of penetration of the slurry by varying the parameter, d (Figure 7-3). The high-speed imaging was carried using the Phantom V12 high-speed camera (model VEO 1310). The images had a resolution of 10 px/mm and an exposure time of 1 ms. This allowed the study of the slurry plume's penetration at different points of the air streams from the nozzle. The obtained images were then subtracted using the program ImageJ for further analysis.

7.3 Results

7.3.1 Alumina substrate

Figure 7-4 shows SEM images (not of the same scale) and a photo of an uncoated flat alumina substrate used for coating.

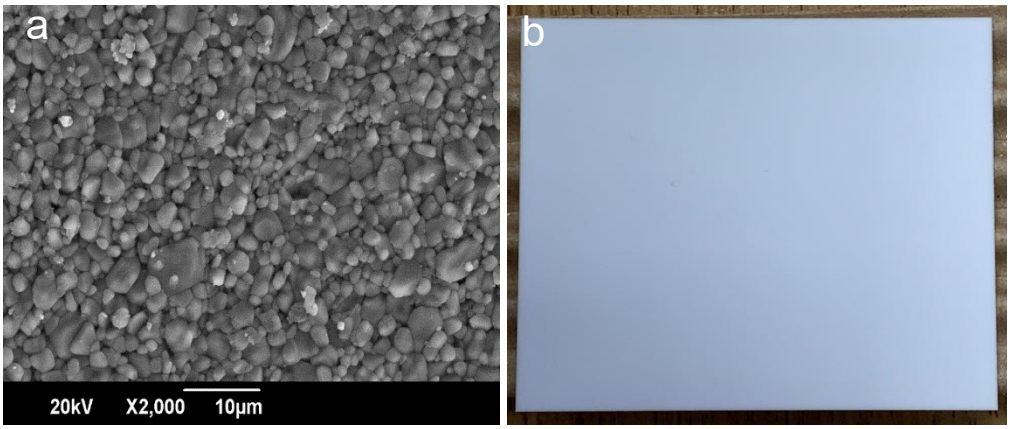


Figure 7- 4: SEM surface images of uncoated flat alumina substrate (a) and uncoated flat alumina photo (b).

7.3.2 Pressure

A suspension flow rate of 0.25 ml/s, SOD of 100 mm, single pass, and 90° angle of injection was used. The gun was positioned 100 mm above sample before traversing, with d and h values of 20 and 10 mm, respectively (Figure 7-3).

Initially, the substrates were coated with the suspension injected from the side where Figure 7-5 shows the photos and SEM surface images (not of the same scale) of prepared samples. The photos and SEM surface images of coated substrates indicate weaker attachment of MOF particles onto the substrate when the suspension is injected from the side of the air stream when compared to releasing from above the air stream (Figure 7-6). Also, experimental observations suggested poor atomisation – a fine spray was not being formed when the suspension was injected from the air stream's side. Following this result, the suspension was injected from above the air stream for all coatings.

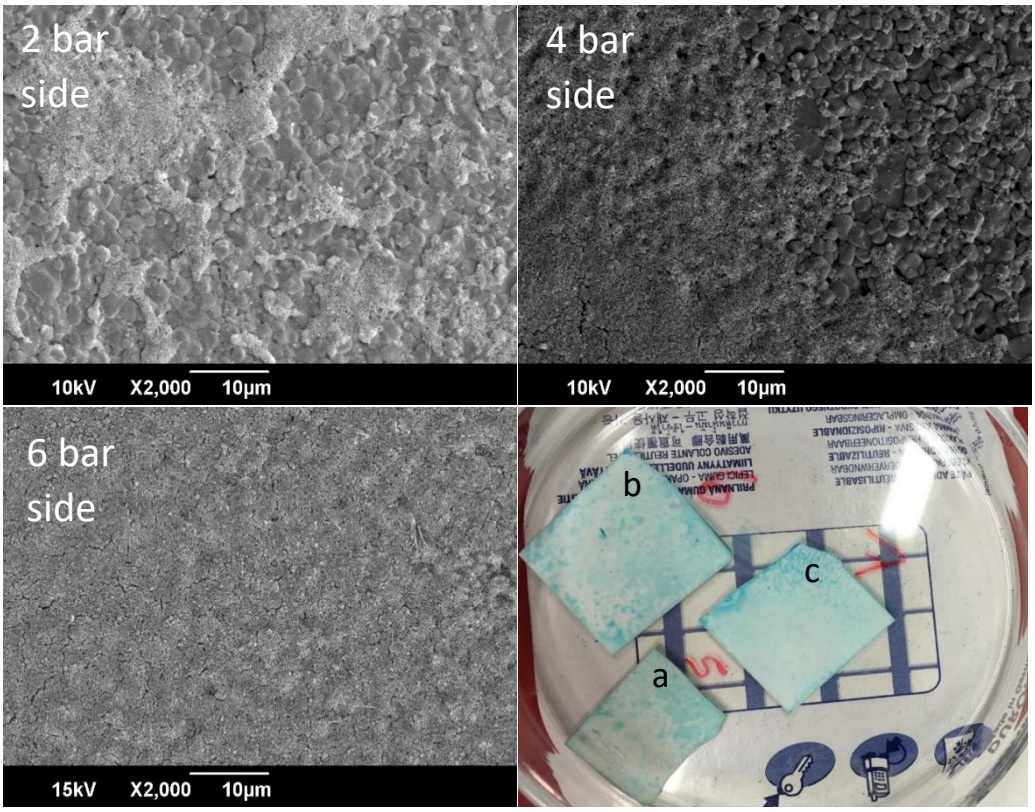


Figure 7- 5: SEM images of substrates synthesised with the suspension released from the side of the airstream at pressures of 2, 4 and 6 bar. Photo of coated substrates of 2 bar (a), 4 bar (b), and 6 bar (c).

Figure 7-6 shows the photos and SEM images (not of the same scale) of flat alumina substrates coated with HKUST-1 at 2, 4 and 6 bars (slurry injected from above air stream). The photos of the substrates show that HKUST-1 attached to the substrate across all pressures. Although there was no uniformity in the coating across all pressures, the best coverage was observed at 2 bar. The SEM surface images may suggest that a continuous coating was achieved at 2 bar. While at 4 and 6 bar, the surface images may imply inhomogeneous coverage in some areas. Results may indicate that the deposited MOF particles were blown off when the pressure was increased.

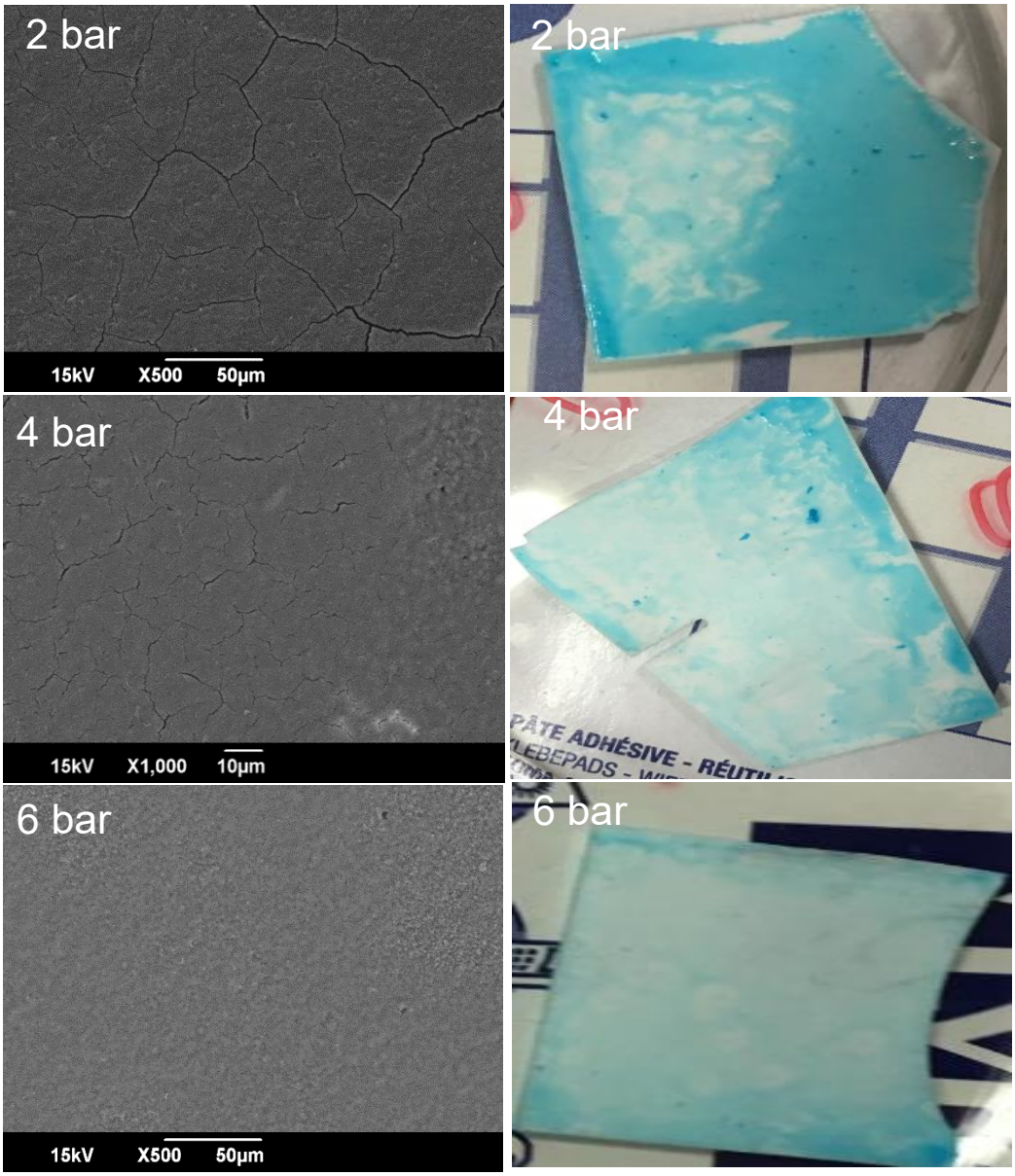


Figure 7- 6: SEM surface images and photos of coated substrate sprayed at 2, 4 and 6 bars pressure. Other synthesis parameters, suspension flow rate of 0.25 ml/s, gun speed of 20 mm/s, SOD of 100 mm, single-pass, angle of injection of 90 °, HKUST suspension with an 7 wt.%, and distance between nozzle and suspension release point 20 mm and height above nozzle 10 mm.

These results suggest some form of binder would aid the secure attachment of the particles as reported by Kim et al. that a nylon binder 6 wt.% was included in the ZIF-8 suspension. However, heated air streams were used in their study, driving off the water before the MOF particles reached the target substrate. In addition, high temperatures (250°C) increased the momentum of MOF particles, promoting better adhesion (Lee et al., 2015, Kim et al., 2016a, Kim et al., 2014). A drawback of using unheated air streams is that there is a combination of solvent and MOF particles, which reach the

substrate surface, leading some MOF particles being washed off at the substrate surface. To help reducing the wash off a higher MOF loading in the slurry with a binder can be used and thus more MOF particles reach the target substrate, and the binder promotes attachment. However, the atomisation level needs to be considered with increased particle loadings as previous study using r-Go flakes reported poor atomisation for loadings ≥25% (Kim et al., 2014). Particle size is also another variable that must be considered, as a previous study with cold spray coating of metallic powders concluded how smaller particle size exhibited higher average particle velocity achieving a more uniform coating (Jodoin et al., 2006).

Figure 7-7 shows the XRD patterns of flat alumina substrates coated with HKUST-1 at 2, 4 and 6 bar. The XRD patterns across all three pressures show all the characteristic peaks of HKUST-1 , indicating the crystalline structures were not amorphised due to framework collapse on impact (Zhou et al., 2018). The peak intensity was decreased with increasing pressure. Although this may be due to the loss of crystallinity (Kim et al., 2016a), it is unlikely as unheated air streams were used. Alternatively, thinner, and not densely packed samples were obtained as the particles were blown off at 4 and 6 bar. Therefore, the pressure of cold spray coating was fixed at 2 bar.

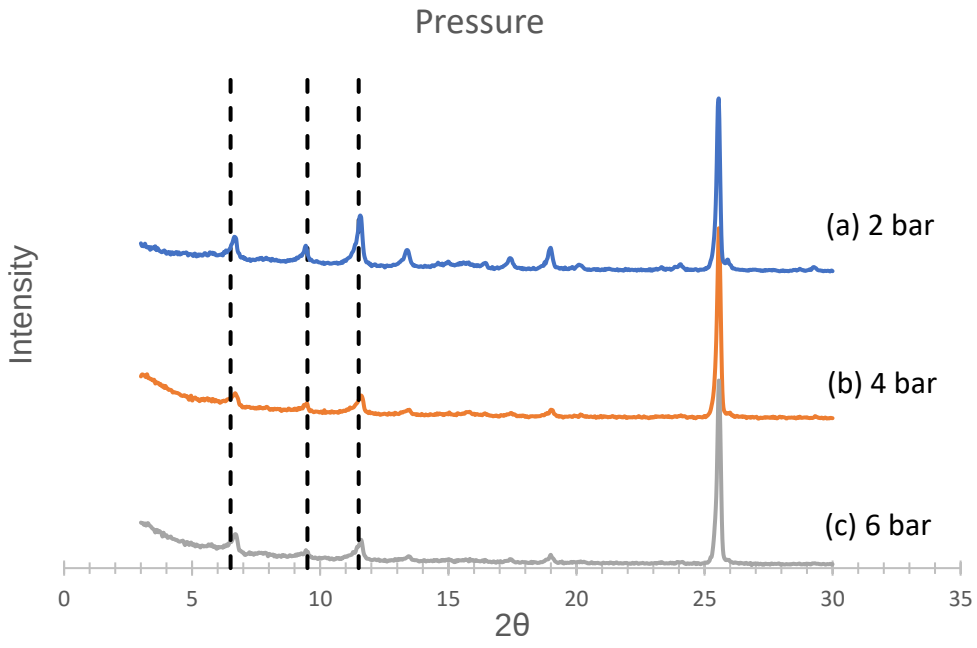


Figure 7- 7: XRD patterns of coated substrate sprayed at 2 (a), 4 (b) and 6 (c) bars pressure. Other synthesis parameters, suspension flow rate of 0.25 ml/s, gun speed of 20 mm/s, SOD of 100 mm, single-pass, angle of injection of 90 °, HKUST suspension

with a 7 wt.%, and distance between nozzle and suspension release point 20 mm and height above nozzle 10 mm. The dashed lines refer to the position of the most prominent characteristic peaks of HKUST-1.

7.3.3 Stand of distance (SOD)

For the study of SOD, a suspension flow rate of 0.25 ml/s, the pressure of 2 bar, single pass, and 90 ° angle of injection was used. The gun was positioned 100 mm above the sample before traversing, with d and h values of 20 and 10 mm, respectively (Figure 7-3).

Figure 7-8 shows the photos and SEM images (not of the same scale) of flat alumina substrates coated with HKUST-1 at the respective SOD. The photos show that with increasing SOD, the homogeneity level (uniform coverage) decreases, with the most uniform coverage achieved at 300 mm. However, the 300 and 600 mm coated substrates' SEM images reveal similar coverage levels between the two samples, indicating MOF particles still successfully deposited onto the substrate securely at 600 mm. However, the 900 mm sample clearly shows bare alumina. These results imply that when the SOD is increased the particles have further to travel further in the unheated air stream and fewer particles reach the target substrate. Therefore, the level of surface coverage is weaker. To date, there are no studies on the design of the atomiser for the MOF coatings. Therefore, the discussion cannot be directly supported by MOF literature. However, Li et al. investigated SOD, using heated air streams (520°C) for dry metal powder coatings. Similarly, they reported that the deposition efficiency decreased with increasing SOD, due to the reduction in gas velocity, carrying the particles as the particles move further away from the nozzle exit (Li et al., 2008b). The particle velocities are affected by the temperature of the air stream; Yin et al. reported increased particle velocities with increased temperatures (Yin et al., 2016), and particle size; Li et al. reported the smaller particles had higher velocities (Li et al., 2008b). Therefore, it is likely that reducing the particle size will increase the chance of a more secure attachment of particles onto the substrate surface. Hence, future experimental work can investigate the optimum particle size, however, below 1 µm would be a good starting point since Kim et al. worked with nanosized ZIF-8 particles (Kim et al., 2016a). In summary, with unheated air streams, the optimum SOD is 300 mm for secure particle attachment.

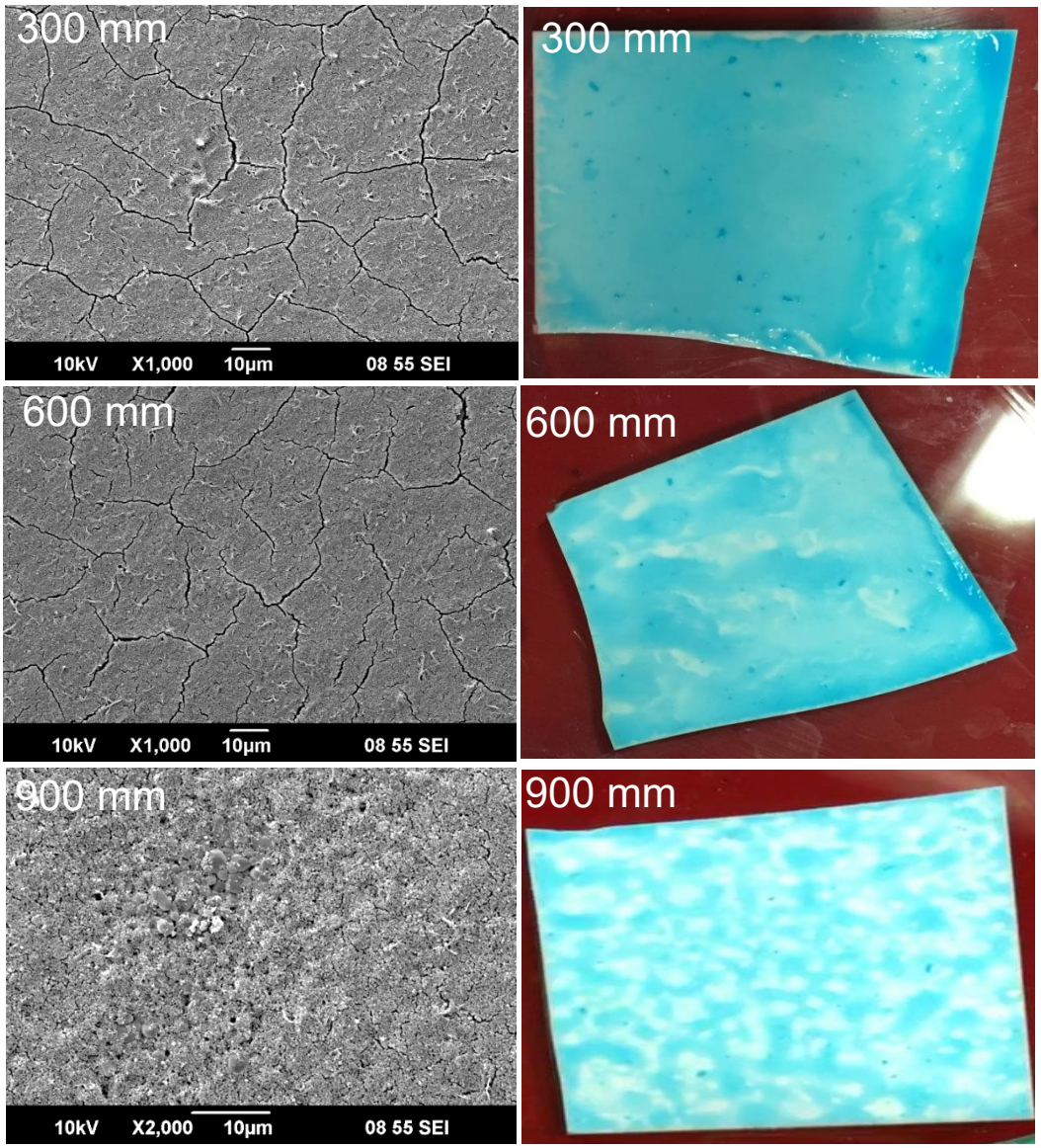


Figure 7- 8: SEM images and photos of coated substrates prepared at SOD of 300 mm, 600 mm, and 900 mm. Prepared with a suspension flow rate of 0.25 ml/s, gun speed 20 mm/s, 2 bar pressure, single-pass, angle of injection of 90 °, HKUST suspension with a 7 wt.% and distance between nozzle and suspension release point 20 mm and height above nozzle 10 mm.

Figure 7-9 shows the XRD patterns of flat alumina substrates coated with HKUST-1 with SOD of 300, 600, 900 mm. The XRD patterns of the substrate coated with SOD of 300- and 600-mm distances show similar peak intensities, and the XRD pattern of the coated substrate at 900 mm suggests less dense coverage of HKUST-1 supporting the SEM images and sample photos. In conclusion, 300 mm is the optimum SOD.

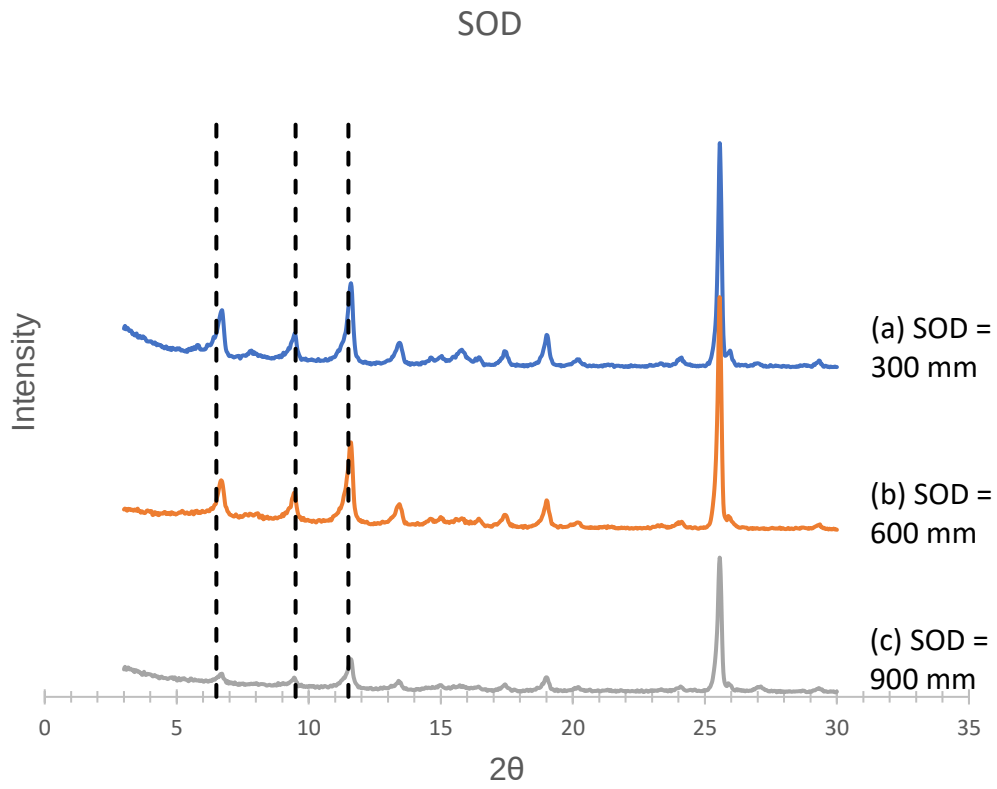


Figure 7- 9: XRD patterns of coated substrate sprayed at SOD of 300 (a), 600 (b) and 900 (c) mm. Other synthesis parameters, suspension flow rate of 0.25 ml/s, gun speed of 20 mm/s, 2 bar pressure, single-pass, angle of injection of 90 °, HKUST suspension with a 7 wt.%, and distance between nozzle and suspension release point 20 mm and height above nozzle 10 mm. The dashed lines refer to the position of the most prominent characteristic peaks of HKUST-1.

7.3.4 Number of Passes

After determining the optimum SOD for the coating of substrates is 300 mm, the optimum number of passes needed for a homogeneous coating was studied. The conditions selected for the number of passes was suspension flow of 0.25 ml/s, air pressure of 2 bar, and 90° angle of injection. The gun was positioned 100 mm above the sample before traversing, with d and h values of 20 and 10 mm, respectively (Figure 6-3).

Figure 7-10 shows the photos and SEM surface images (not of the same scale) of HKUST-1 coated substrates at 2, 4, and 6 passes. The coated substrates' photos prepared at 2 and 6 passes suggest a similar coating of HKUST-1, the substrate prepared with 6 passes suggests a less dense coating. The substrate's SEM surface image prepared with 2 passes may imply a dense and continuous layer of HKUST-1, whilst the substrates prepared with 4 and 6 passes show regions where the substrate

structure is visible. The results support the experimental observation where multiple passes removed deposited particles from the substrate surface.

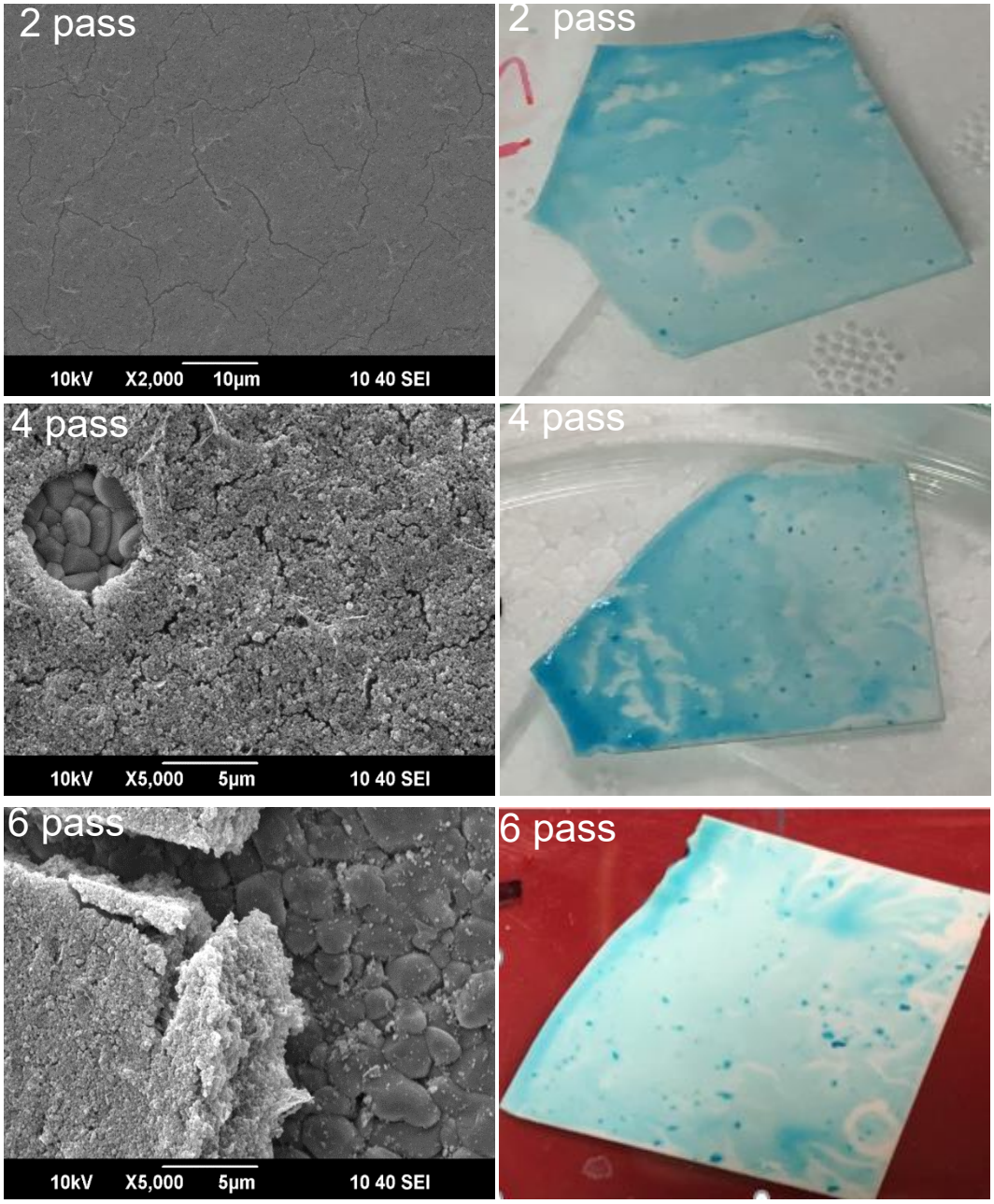


Figure 7- 10: SEM images and photos of coated substrates prepared with 2, 4 and 6 passes. Other synthesis parameters, suspension flow rate of 0.25 ml/s, gun speed 20 mm/s, SOD of 300 mm, angle of injection of 90 °, HKUST suspension with an 7 wt.% and distance between nozzle and suspension release point 20 mm and height above nozzle 10 mm.

These results may imply that the coating of substrates with unheated air streams may not be viable. During each pass a combination of solvent and MOF particles reach the substrate, leading to a wash off of the deposited particles. As discussed in the pressure

effect, the heated air streams not only drive off the solvent particles in the air stream before reaching the target substrate, but also increases the momentum of the particles that helps the particles to achieve the velocity required (critical velocity) for attachment to the target substrate on impact (Gärtner et al., 2006, Dykhuizen and Smith, 1998). Since some particles remain attached to the substrate surface in the coated samples it is evident that some reaches the critical velocity even with unheated air streams. However, Dykhuizen et al. and Gartner et al. highlighted that the deposition efficiency increases with increasing particle velocities when powder samples used (Gärtner et al., 2006, Dykhuizen and Smith, 1998), i.e. the more particles reaching the critical velocity the better the level of deposition efficiency. In conclusion, with unheated air streams, when using two passes, fewer particles were removed from the substrate. Hence, two passes are the optimum number of passes.

Figure 7-11 shows the XRD patterns of flat alumina substrates coated with HKUST-1 with 2, 4 and 6 passes. The XRD patterns of all the coated substrate at the different number of passes indicate the presence of HKUST-1, whilst the peak intensities of the coated substrate at the 4 and 6 passes show more intense peaks, suggesting packed HKUST-1 crystals. However, the SEM surface images suggested the coating was not continuous at the 4 and 6 passes since the alumina substrate was visible. This may imply some form of a binder is needed to help promote a more robust attachment of particles to the substrate to prevent wash off when the subsequent coating is being sprayed onto the substrate. In summary, without a binder, 2 passes are the optimum number of passes for a more uniform coating.

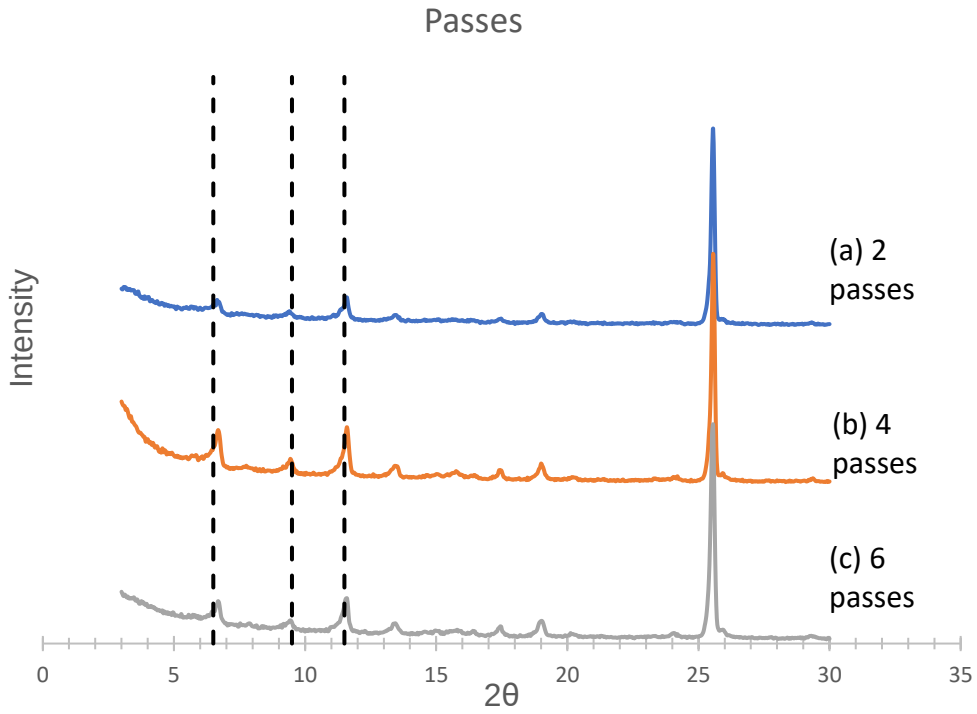


Figure 7- 11: XRD patterns of coated substrate sprayed at 2 (a), 4 (b) and 6 (c) passes. Other synthesis parameters, suspension flow rate of 0.25 ml/s, gun speed of 20 mm/s, 2 bar pressure, 300 mm SOD, angle of injection of 90 °, HKUST suspension with a 7 wt.%, and distance between nozzle and suspension release point 20 mm and height above nozzle 10 mm. The dashed lines refer to the position of the most prominent characteristic peaks of HKUST-1.

7.3.5 Angle of injection

To better design the atomiser, the penetration angle of slurry into the airstream was investigated, the coating of substrates was done at an angle of injection of 30, 50 and 70 °, and then compared to the previous study where the angle of injection was 90 °. The other synthesis parameters have a suspension flow rate of 0.25 ml/s, the pressure of 2 bar, SOD of 300 mm, and 2 passes. The gun was positioned 100 mm above the sample before traversing, with d and h values of 20 and 10 mm, respectively (Figure 7-3).

Figure 7-12 shows the photos and SEM surface images (not of the same scale) of flat alumina substrates coated with HKUST-1 at injection angles of 30, 50 and 70 °. The photos of substrates coated at all injection angles show inhomogeneous coatings of MOF. Photos also show that the HKUST-1 particles are accumulated at the substrate's edge rather than the centre. Although the photos show a similar level of coating on the surface for all the angles, the SEM image of the substrate coated at 30° was not

deposited with a film of HKUST-1 since the bare alumina structure was visible. SEM surface images of the substrate coated at angles of 50° and 70° suggest regions where the support structure is visible between film growth. The results show that increasing the angle of injections increases the momentum transfer between slurry and air streams. This implies that with decreasing angle the liquid column remains compact and reaches the substrate with less vaporisation, hence more solvent reaches the target substrate leading to more wash off. Therefore, the transfer of momentum is smaller when the angle is < 90°. The interaction between feed (powder or slurry) and air stream has not been investigated via cold spray set-up. However, Venturi and Hussain et al. reported that adjusting the angle of the feed stream of 1 wt.% slurry of graphene nanoplatelets from 90 to 75° led to a narrower plume, suggesting a reduced transfer of momentum between the two streams for thermal spray set-up (Venturi and Hussain, 2020).

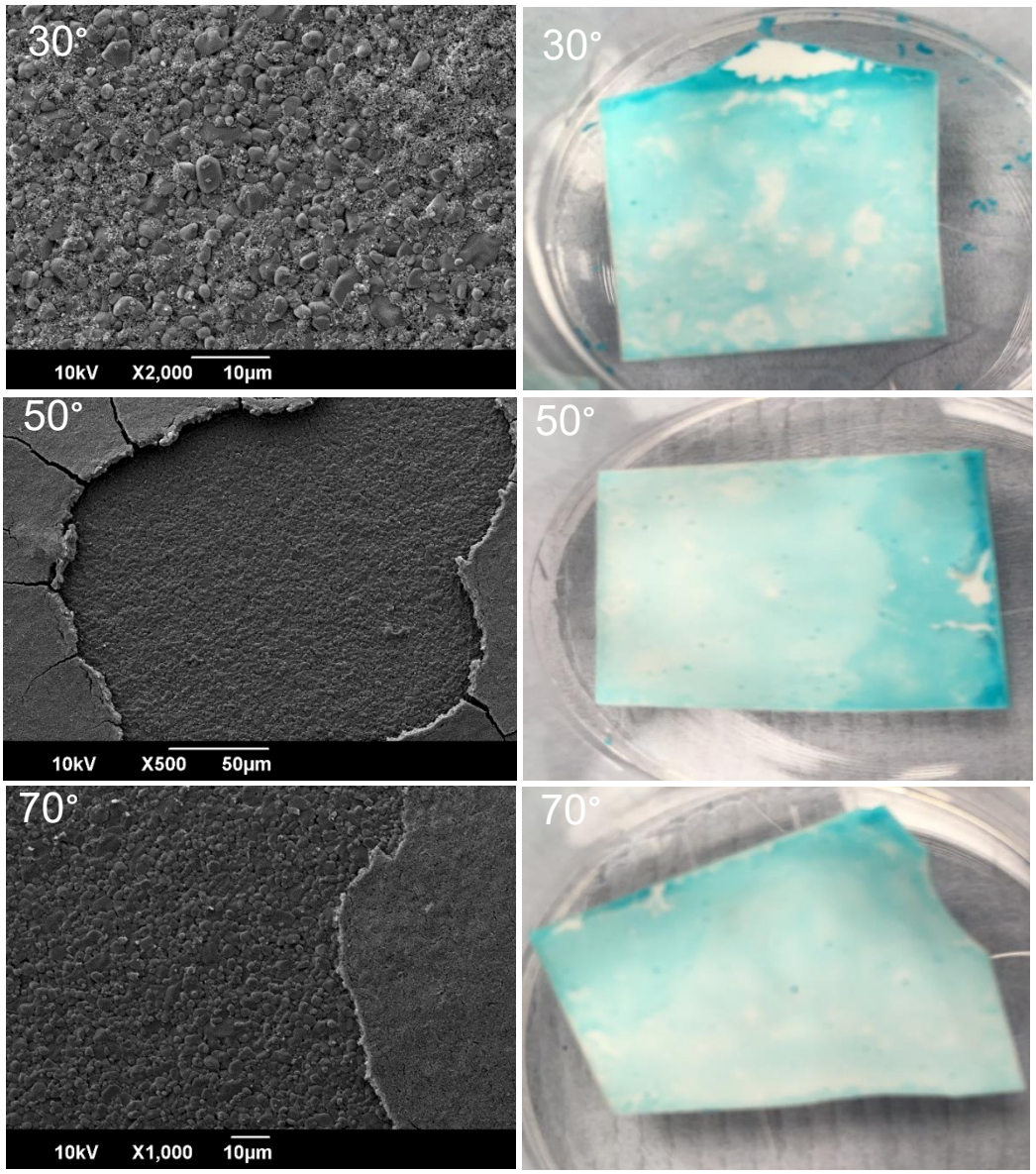


Figure 7- 12: SEM images and photos of coated substrates of samples prepared with an angle of injection of 30 °, 50 °, and 70 °. Other synthesis parameters, suspension flow rate of 0.25 ml/s, gun speed 20 mm/s, SOD of 300 mm, 2 passes, HKUST suspension with a 7 wt.% and distance between nozzle and suspension release point 20 mm and height above nozzle 10 mm.

However, figure 7-13 shows SEM images taken from other areas of the same coated angle of injection substrates and indicates a similar level of coverage between the three injection angles, implying an inhomogeneous coating of HKUST-1. The results showed that the MOF suspension would remain suspended in the air stream that would later deposit onto the substrate when the Dymet gun completed two passes; this was not the case at 90 °. In conclusion, the surface images and results indicate the angle of injection does impact the slurry's atomisation, leading to the variation in particle attachment between the substrates.

In summary, between the angles of 30, 50, 70 and 90 °, the 90 ° angle results (Figures 7-10 and 7-11 for SEM and XRD, respectively) suggest the most robust coating implying that the slurry can be atomised more efficiently when penetrating the airstream at 90 °.

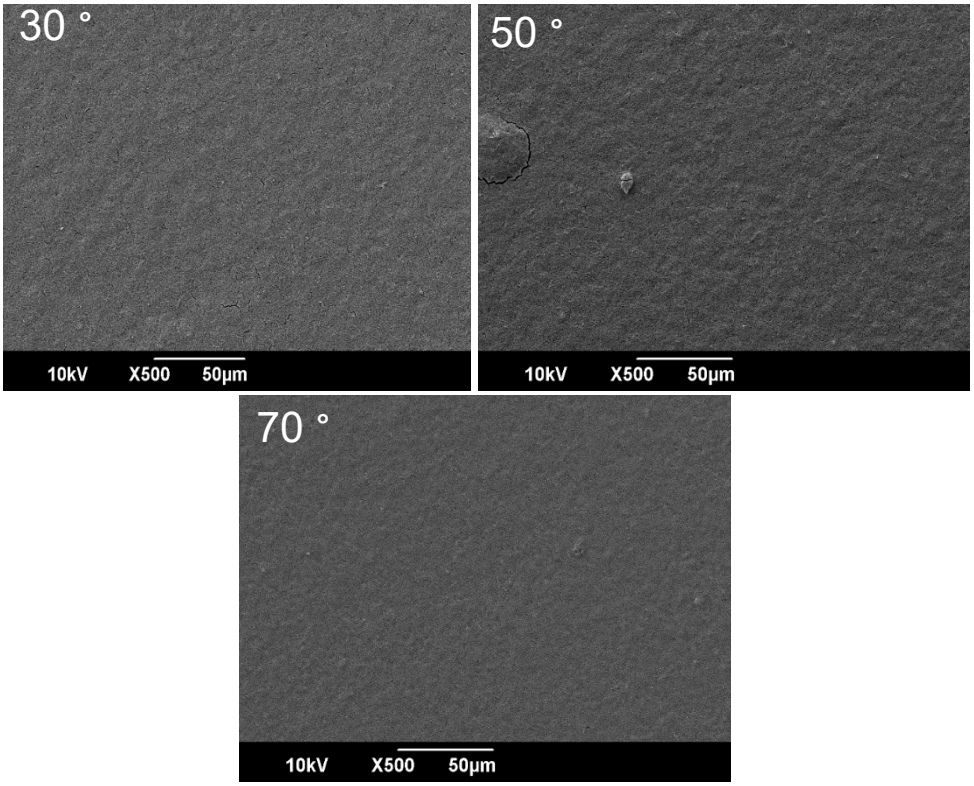


Figure 7- 13: SEM images of samples synthesised with an angle of injection of 30 °, 50 ° and 70 °. Other synthesis parameters, suspension flow rate of 0.25 ml/s, gun speed

20 mm/s, SOD of 300 mm, 2 passes, HKUST suspension with a 7 wt.% and distance between nozzle and suspension release point 20 mm and height above nozzle 10 mm.

Figure 7-14 shows the XRD patterns of flat alumina substrates coated with HKUST-1 with the angle of injections of 30, 50 and 70 °. Although the coating is inhomogeneous, the XRD pattern has detected the deposition across the substrate, reflecting all characteristic peaks of HKUST-1. However, the 30 ° angle sample peaks are not intense, indicating a sparse deposition of crystals. In conclusion, the optimum angle of injection is 90 °.

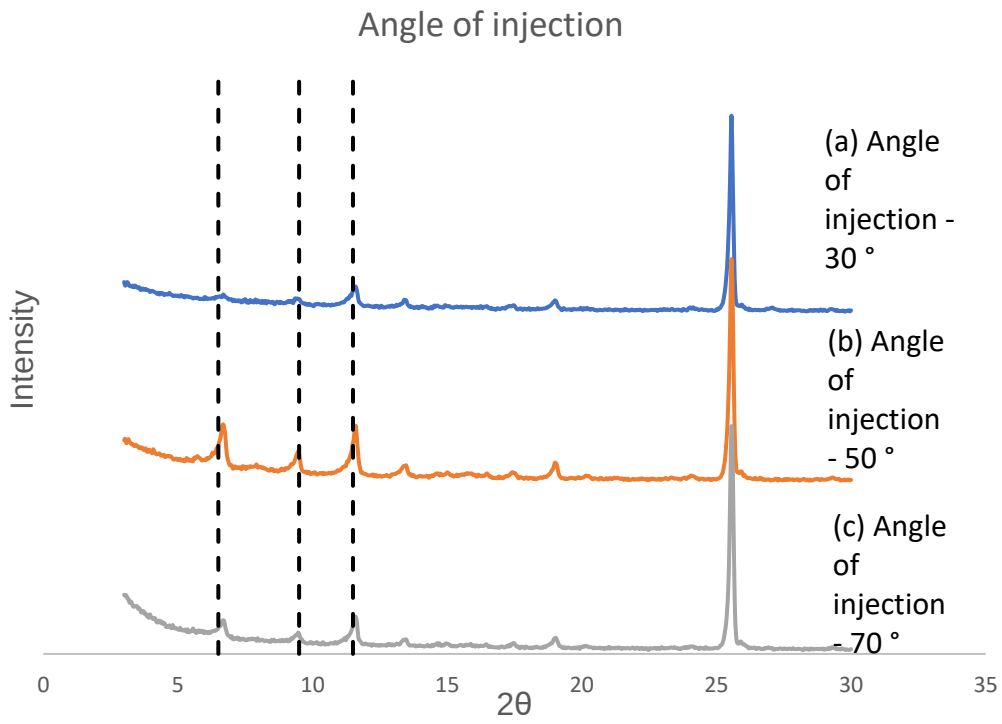


Figure 7- 14: XRD patterns of coated substrate sprayed with an angle of injection of (a) 30, (b) 50 and (c) 70 °. Other synthesis parameters, suspension flow rate of 0.25 ml/s, gun speed of 20 mm/s, 2 bar pressure, 300 mm SOD, 2 passes, HKUST suspension with a 7 wt.%, and distance between nozzle and suspension release point 20 mm and height above nozzle 10 mm. The dashed lines refer to the position of the most prominent characteristic peaks of HKUST-1.

7.3.6 High speed camera

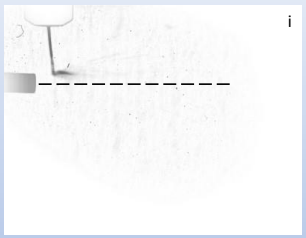
Following the injection study angle, the next step was to maximise the momentum transfer level from the high-speed air to the slurry stream. A high-speed camera was used that took images every millisecond, allowing the study of the level of penetration of the slurry into the air stream. The feed distance, d (Figure 7-3), was varied to study

the effects of the slurry penetration into the air stream to find the optimum flow rate to reach the centre of the air stream to gain maximum momentum transfer, thereby minimising overspray (Moonga and Jen, 2017). Experiments were conducted at 2 bar, with SOD of 300 mm, 2 passes, 90 ° injection angle, and a water flow rate varied between 30-100 ml/min. The gun was positioned 100 mm above the sample before traversing, with h value of 10 mm, and d varied between 5-30 mm (Figure 7-3).

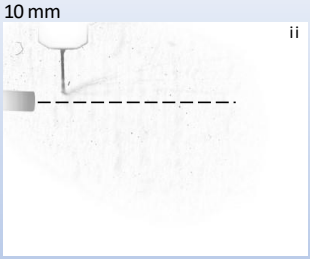
Figure 7-15 shows the subtracted images of water penetration with the airstream at the respective flow rates of 30, 50, 75, and 100 ml/min, at distances of 5, 10, 20, and 30 mm between air nozzle and water release point for each flow rate. The images reveal that at flowrates of 30 and 50 ml/min, the water could not penetrate the air stream's centre for all distances between the air nozzle and water release point. At the flow rate of 100 ml/min, the subtracted images indicate the plume passes through the air stream's centre for all distances. The subtracted images at 75 ml/min show that the plume was pushed away at 5 and 10 mm, and penetrates the stream at 20 and 30 mm. The plume's widening at the distance of 30 mm indicates the plume is carried away down the air stream showing a higher rate of momentum transfer between the air and water streams.

(a) Flowrate = 30 ml/min

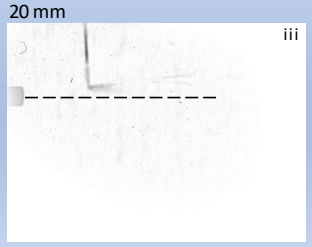
5 mm



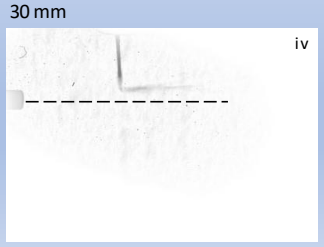
10 mm



20 mm

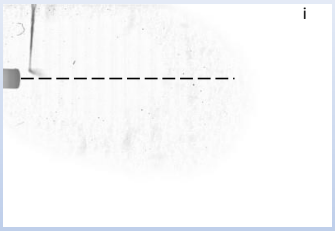


30 mm

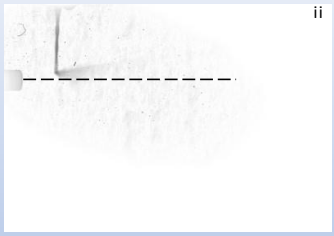


(b) Flowrate = 50 ml/min

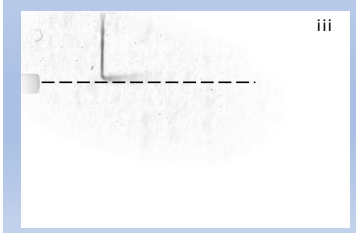
5 mm



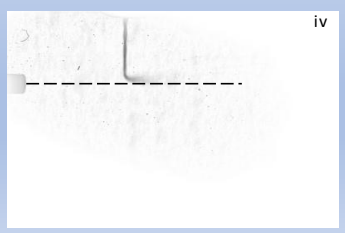
10 mm



20 mm



30 mm



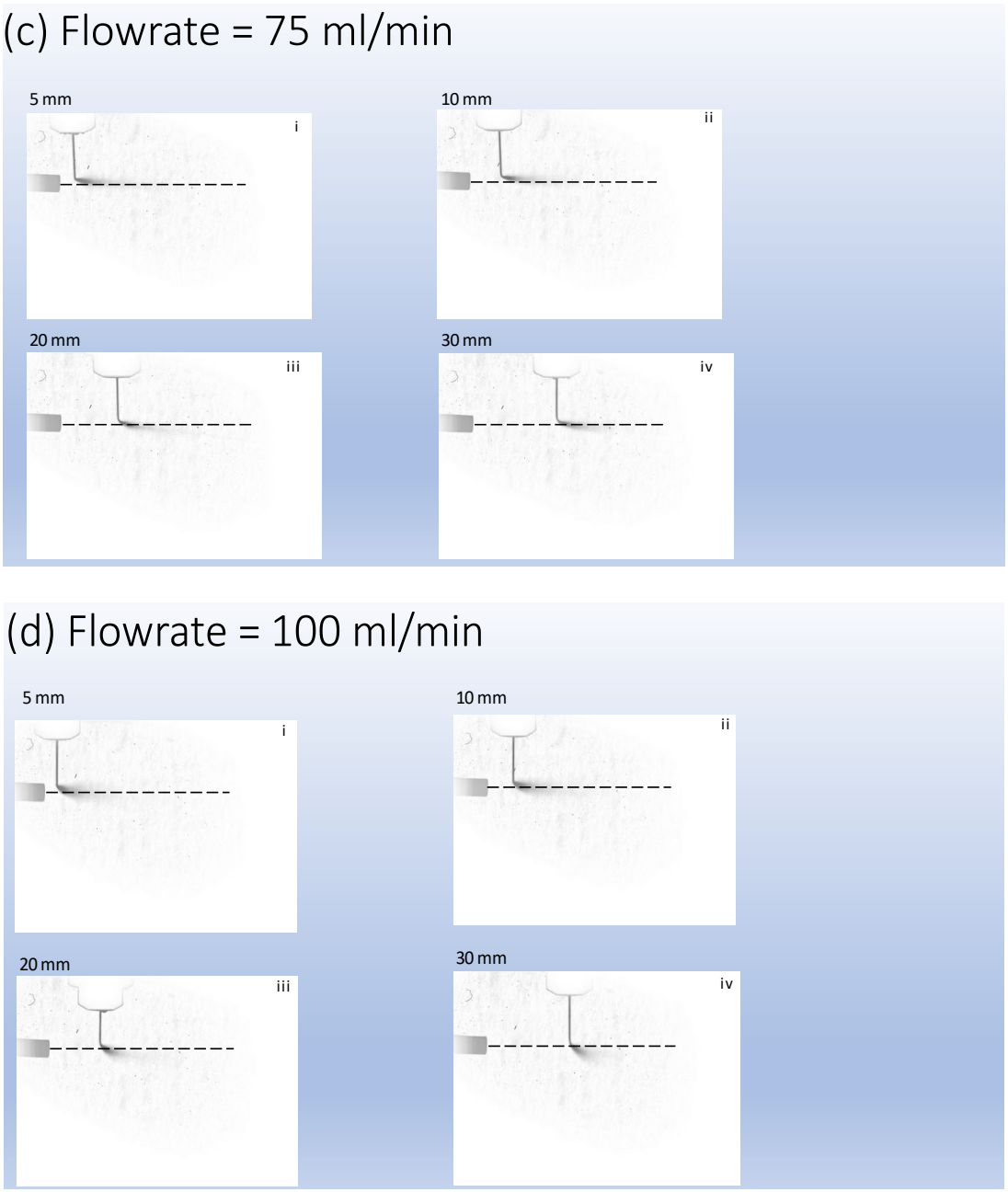


Figure 7- 15: High speed camera images at the flow rates of 30 ml/min (a), 50 ml/min (b), 75 ml/min (c) and 100 ml/min (d). Figures (i), (ii), (iii) and (iv) represent 5, 10, 20 and 30 mm distance between air nozzle and suspension exit, respectively. The angle of injection across all flow rates is 90 °.

Figure 7-16 shows the images of HKUST-1 suspension in methanol (Figure 6-16a) and water with no particles (Figure 6-16b) at a flow rate of 75 ml/min and a 10 mm distance between air nozzle and fluid release point. The images show that the HKUST-1 suspension penetrated the air stream more than water. Although the density is similar between the water and 7 wt% methanol slurry at 1 g/cm^3 and 0.982 g/cm^3, respectively, the results may imply the difference in interaction with the air stream is due to some of

the methanol evaporating leaving behind individual HKUST-1 particles surrounded by the methanol particles creating a denser fluid.

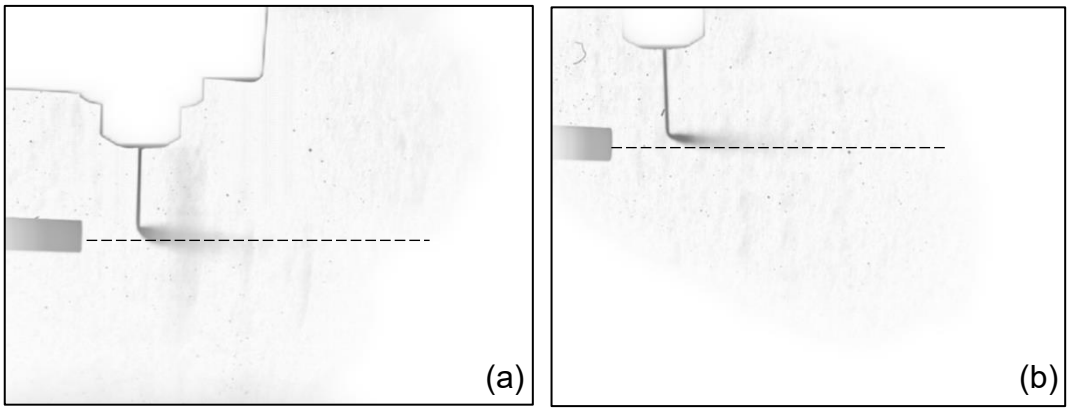


Figure 7- 16: Subtracted images of HKUST-1 suspension at 7 wt.% (a) and water (b). A flow rate of 75 ml/min with 10 mm distance between the air nozzle and suspension release point. The angle of injection of 90 °.

7.4 Conclusions

In the chapter, the cold spray coating method was studied, for the first time, for the preparation preparation of MOF films on flat non-porous alumina substrates, using HKUST-1 suspension in methanol. The successful design of the atomoiser by determining the experimental parameters were presented. Results suggest that the parameters studied for the atomiser's design impact the quality of the MOF coatings on the substrates e.g., surface coverage and homogeneity. The optimum conditions for successful coatings were 2 bar, 300 mm, two passes, and 90 °, respectively.

The results show that the scalable cold spray coating method using MOF suspepsnion under unheated air streams has the potential to be successful. However, the role of MOF amount in suspension and particle size on surface coverage and thickness require further investigation. In addition, heated air streams and a binder in the suspension have potential to promote better adhesion of particles and hence to achieve a more homogenous and secure membrane on the target substrate.

The cold spray work has potential to deliver large scale manufacture of membranes since the operation is continuous. Although it is not possible to see the method to coat the inside of tubular substrate due to the size of the nozzle, the external surface of longer tubular substrates (~ 1m) can be coated. However, this adds additional variables such as rotation speed, to ensure uniform coverage on the surface. Hence the cold spray work requires further work to be conducted for the pilot scale operations.

In conclusion, the cold spray work has contributed membrane manufacturing methods by delivering a novel study for the design of the atomiser, which has not been studied before for MOF suspensions. In addition, with the work focusing on upscaling the coating process using tubular substrates, this is the first coating study of its kind to be moving forward towards the pilot scale using tubular substrates.

8. Gas separation testing

8.1 Introduction

Chapters 4, 5 and 6 discussed the heterogenous growth of ZIF-8 onto tubular substrates at their respective heating mechanisms using different precursor concentrations and ratios and its effects on the membrane microstructure and continuity. This chapter investigates the separation performance of ZIF-8 membranes grown on tubular substrates using conventional heating. The conventionally heated system membranes have only been tested since this was the first system introduced into the PhD, and gas separation testing began almost immediately.

With an ultramicroporous structure on the scale of small gas molecules (Yoo et al., 2009, Liu et al., 2009, Yao and Wang, 2014), surface to volume ratios comparable to MOFs, and similar chemical and thermal stabilities to zeolites (Shah et al., 2011, Venna and Carreon, 2009), ZIFs are ideal structures for the separation of gas mixtures. ZIF-8 being ideal for the separation of CO_2/CH_4 mixture since has pore aperture of 0.34 nm (Li et al., 2015), and since the CO_2 has a quadrupole moment it is preferentially adsorbed onto the ZIF-8 structure because the ZIF-8 has an electrostatic potential distribution (Yahia et al., 2021, Md. Nordin et al., 2015, Novaković et al., 2015) (Lai et al., 2014a). ZIF-8 also demonstrates molecular sieving properties, delivering permeances in the order of CO_2 > CH_4 (Zhu et al., 2016). Zhu et al. reported the selectivity and CO_2 permeance remained unchanged for more than 48 hours at 100°C and 1 bar permeate pressure; making ZIF-8 membrane a good candidate for CO_2 separation and removal.

The aim of this chapter is to investigate the level of continuity of membrane growth, and intercrystalline defects not detectable by XRD and SEM. The membranes were tested at 1 bar pressure and at room temperature. The membranes were tested in the gas separation system using CH_4 and CO_2. The ideal selectivities were calculated by taking the calculated permeances ratios of CO_2 to CH_4.

8.2 Experimental procedure

Figure 8-1 and 8-2 show a photo and flow diagram of the gas separation system, respectively.

The piping, valves, back pressure regulators (BPRs) and membrane housing materials were supplied by Swagelok. Bronkhorst supplied the mass flow controllers (MFM), mass flow meters (MFM), transducer, and software. The gas cylinders were obtained from BOC gases with research grades of N4.5 and N5.0 for CH_4 and CO_2, respectively.

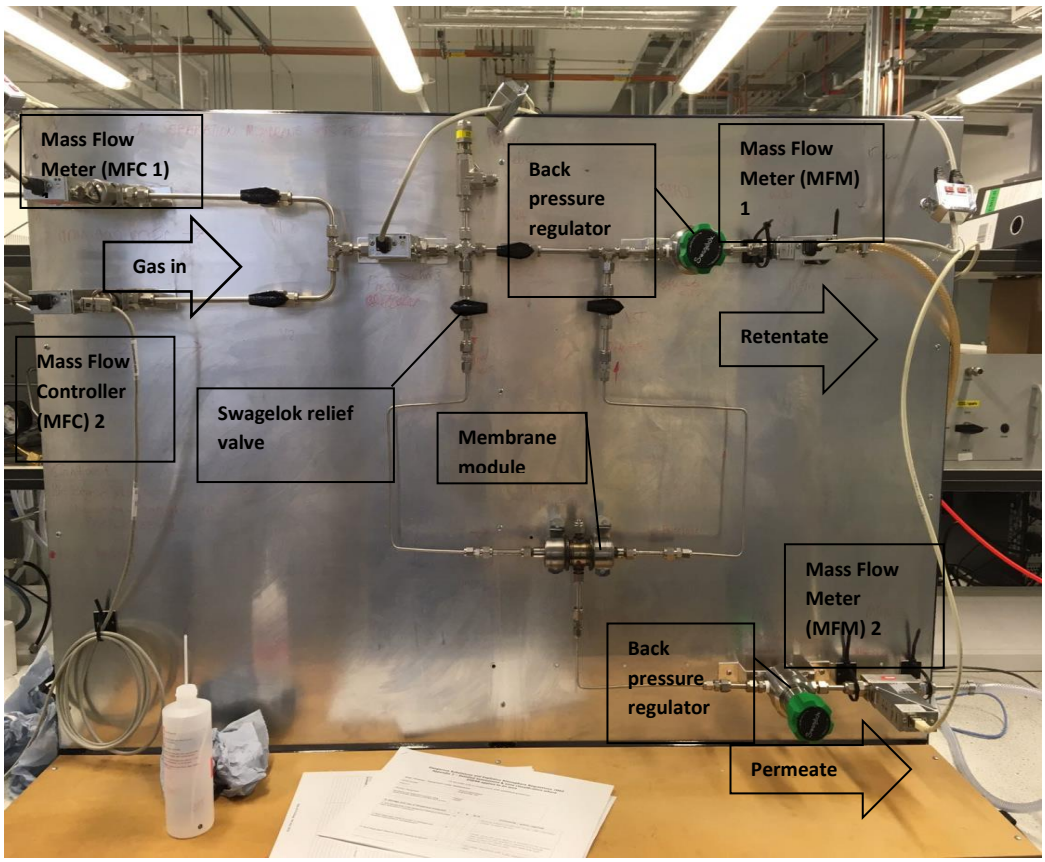


Figure 8- 1: Photo of the gas separation system near to completion.

The membranes were mounted into the membrane module with silicone O-rings positioned at the substrate's glazed end to create an airtight seal. The membrane was secured into the module by tightening the nuts at both ends. The Bronkhorst software was uploaded onto a PC from where the respective flow rates were controlled and pressure monitored. The desired pressure for testing the membranes was set via pressure regulators.

Before performing separation testing, the system was tested for leaks using the leak detecting fluid. If bubbles formed when squirting the fluid onto the pipe joints, the gas supply was turned off and technical support sought from laboratory technicians so the respective joint could be tightened.

When conducting single gas measurements, valves 1, 2, 3, and 5 were kept open while valve 4 remained closed (Fig. 8-2). The respective gas desired flow rate was set on the computer via MFC1 or MFC2. The desired feed pressure was seen in Transducer 1 (on software) by tightening BPR (PR_1). Once the system was at a steady state, the permeance was recorded.

At the end of the session, the values of both MFC1 and MFC2 were set to 0 using the software. Valve 4 was opened, BPR was loosened, and both gas cylinders closed, and Bronkhurst MFC software closed.

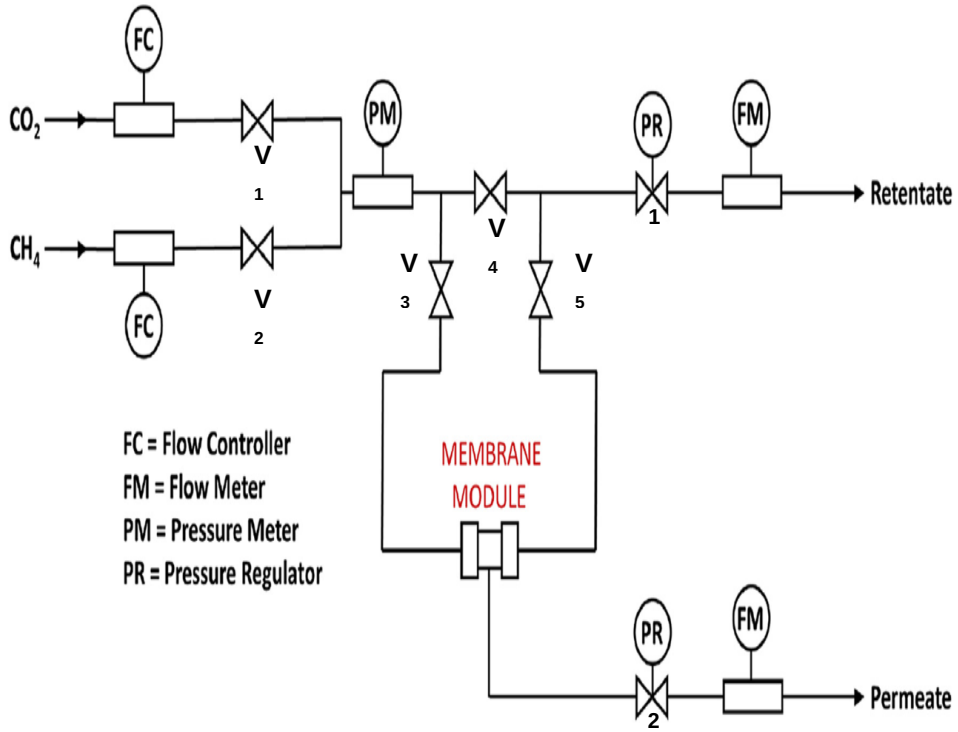


Figure 8- 2: Flow diagram of the gas separation system (Campbell and Tokay, 2017). Reproduced with permission from Campbell and Tokay 2017.

8.3 Results

Table 8-1 summarises the permeances and ideal selectivities of membrane tested in the gas separation system, and single gas permeances of CO_2 and CH_4 from literature. A pressure drop of 1 bar was applied, single gas permeation properties could only be collected for two-cycle synthesis membranes synthesised at linker/metal ratio 8 and metal concentration of 36 mM; Z8-30, Z59A and Z59B. The other tested membranes may have been defected, or there may be no continuous layer of ZIF-8 growth on the substrate, resulting in no pressure drop being created. Table 8-1 also lists unseeded (Z8-47), 10-hour (Z61, Z62) synthesis, and a membrane synthesised at a linker/metal ratio 2 (Z8-32). However, due to the membranes having defects or inhomogeneous growth on the substrate, they failed to hold pressure. Therefore, it is not possible to comment on those synthesis parameters' role in gas separation perform.

Table 8- 1: Permeance and ideal selectivities of seeded membranes synthesised using mixed ZIF-8 solution under conventional heating. Membranes synthesised at linker/metal ratio 8 for 5 hours at 150 °C, washed, dried at 100 °C for 2 hours in the conventional heated oven unless indicated differently in footnotes. Permeance and ideal selectivity of ZIF-8 membranes from literature for the CO_2/CH_4 mixtures are also tabulated.

Code or Author	Synthesis cycles	Metal concentration (mM)	Washing details	Permeance mol/m^2.s.Pa		Ideal selectivity
				CO_2	CH_4	
Z8-44	1	36	Deionised water	-	-	-
Z8-46			Deionised water	-	-	-
Z8-47[6]			Deionised water	-	-	-
Z48[7]			Tap rinse then deionised water rinse	-	-	-
Z8-32[8]			Tap rinse then deionised water rinse	-	-	-
Z8-30	2		Deionised water	9.7×10^{-7}	1.0×10^{-7}	9.7
Z57			Deionised water	-	-	-
Z59A			Deionised water	8.8×10^{-7}	7.5×10^{-7}	1.2
Z59B			Methanol rinse	9.55×10^{-7}	9.6×10^{-7}	1.0

[6] Unseeded substrate
[7] Dried at 25 °C for 24 hours and then at 100 °C for 2 hours.
[8] Linker/metal ratio 2

Z61[9]	1	144	Tap rinse then deionised water rinse	-	-	-
Z53			Deionised water	-	-	-
Z63[10]			Deionised water	-	-	-
Z49[2]			Tap rinse then deionised water rinse	-	-	-
Z62[4]			Tap rinse then deionised water rinse	-	-	-
(Venna and Carreon, 2009)	2	36	Deionised water	2.11×10^{-5}	5.17×10^{-6}	4.1
(Zhu et al., 2016)	2	79	Methanol	0.97×10^{-8}	1.43×10^{-9}	6.8
(Lai et al., 2016c)	1	97	Methanol	1.31×10^{-8}	0.59×10^{-8}	2.2
(Yu et al., 2016)	1	9	Methanol	1.1×10^{-7}	0.6×10^{-7}	1.8
(Hara et al., 2014)	1	400	-	2×10^{-8}	1×10^{-8}	2
(Kong et al., 2015)	1	50	Methanol	8×10^{-8}	3×10^{-8}	2.7
(Tao et al., 2013b)	1	41	Methanol	2×10^{-7}	1.7×10^{-7}	1.2

[9] Synthesised for 10 hours
[10] Soaked in deionized water for 24 hours and then methanol for 24 hours, both washing stages at room temperature.

(Michael C. McCarthy, 2010)	1	31	Methanol	4 x 10^{-8}	1.3 x 10^{-8}	3
(Shah et al., 2013a)	1	101	Methanol	3.5 x 10^{-8}	1.5 x 10^{-8}	2.3
(Tao et al., 2013a)	1	81	Methanol	1.4 x 10^{-7}	0.6 x 10^{-7}	2.3
(Yang et al., 2014)	1	37	Methanol	0.46 x 10^{-7}	0.41 x 10^{-7}	1.12
(Wang et al., 2016)	1	55	Methanol	3 x 10^{-7}	1.5 x 10^{-7}	2
(Bux et al., 2009)	1	99	Methanol	1.33 x 10^{-8}	0.48 x 10^{-8}	2.7
(Tanaka et al., 2014a)	1	25	Methanol	2 x 10^{-7}	0.5 x 10^{-7}	4

Post synthesis activation (Z63, Z59) and drying (Z48) of the membranes was investigated. These investigated the optimal process for removing unreacted species from the pores of the ZIF-8 structure that can obstruct the passage of gas molecules through the pores and drying to investigate the optimum condition to prevent cracks from forming. However, it was not possible to draw a conclusion on the activation studies for those membranes due to them not being able to hold pressure, except for Z59, which will be discussed shortly.

Another investigation was to test membranes synthesised at the same conditions to investigate discrepancies in the batches. None of four single cycle membranes synthesised (each synthesised in separate reaction vessels) at 36 mM metal concentration and linker/metal ratio 8 held pressure. Four two-cycle membranes Z57, Z8-30, Z59A and Z59B, were synthesised at the 36 mM concentration and linker/metal ratio 8. Z57 held no pressure, Z59A and Z59B delivered selectivities of 1.2 and 1.0, respectively. Z8-30 was selective with a selectivity of 9.7, comparing favorably to the reported selectivities in literature. Although Venna and Carreon et al. reported higher permeances than the membranes tested in this thesis, they had a selectivity half of

what Z8-30 delivered. The synthesis methodology between Venna and Carreon et al. and the Z8-30 membrane are the same except for the metal salt used, the Z8-30 and Venna and Carreon et al. membrane have been derived from zinc acetate and zinc nitrate, respectively. Zinc nitrate generates smaller size crystals (Schejn et al., 2014) delivering thinner membranes (Ramu et al., 2018) and zinc acetate generates larger crystals forming thicker membranes (Ramu et al., 2018, Tanaka et al., 2014a). Which reflects the membrane thickness for Z8-30 and Venna and Carreon et al. of 12 and 5 µm, respectively. When comparing permeances of the two-cycle membranes from this thesis a favorable comparison is seen between the tabulated data collected from literature, indicating it is worthwhile to continue to synthesize with zinc acetate for this system since both a high permeance and selectivity is needed for upscaling (Duan et al., 2018).

In conclusion, the gas separation testing data indicates that two-cycle synthesis can achieve a dense and continuous membrane synthesised for 5 hours at 150°C. However, the experiments imply challenges with repeatability when synthesizing ZIF-8 membranes. This has been highlighted in literature, particularly for tubular substrates, such as the limited reactant availability in the lumen of the substrate creates a concentration gradient, and the stacking of particles can restrict access for reactants to substrate surface with no crystal growth (Brown et al., 2014a, Sun et al., 2014, Zhang et al., 2013, Tao et al., 2013b, Tran et al., 2020b). A hypothesis is that the stacking of the particles is more thermodynamically favorable than forming new nuclei on the substrate surface because of the Ostwald ripening affect. The stacking reduces the energy of the system since it reduces the surface area via increasing the size of the existing crystals (section 2.4). In conclusion, the reaction zone needs to be brought to the substrate surface to overcome this difficulty whilst a more tailored surface modification method is needed to provide a more uniform layer of sites of nucleation.

Another contributory factor to the difficulty with the manufacturing of the membrane synthesis in this system could be the detachment of physically deposited seeds and the dissolution of the seeds during membrane synthesis stage (Kong et al., 2015, Zhang et al., 2013). Literature has reported incorporating binders with the seeding steps (Bux et al., 2011) or using the reactive seeding option, ZnO (Kong et al., 2015, Yang et al., 2014, Lee et al., 2019, Wang et al., 2016, Yu et al., 2016, Drobek et al., 2015), or silane coupling agents (Tanaka et al., 2014b, Tanaka et al., 2017, Zhu et al., 2016, Xie et al., 2012), are viable alternatives to seeding. However, the literature review has reported synthesis variables (metal salt, metal concentration, linker/metal ratios, to name a few) that have worked for one system may fail to work for other systems –

including the surface modification stage conditions (section 2.5.1). In conclusion, future work needs to systematically investigate alternative surface modification options and conclude what works for this system.Tubular substrates are ideal for upscaling due to high surface area to volume ratios that reduce module size and cost (Zhang et al., 2013, Li et al., 2020, Tao et al., 2013b). Another advantage of tubular substrates is that the membrane is synthesised on the inner surface of the tubular substrate and thus can be more closely packed avoiding membrane to membrane contact points. This allows for a more scalable fabrication of membranes – tightly packing them together (Brown et al., 2014a). However, because of the narrow space of the inner tube there is a low mass transfer efficiency of reactants from solution to substrate surface leading to an inhomogeneous surface coverage along the length of the substrate (Tran et al., 2020b, Kong et al., 2014, Brown et al., 2014a).

Z59 membranes were synthesised together in the same reaction vessel and studied the solvent's role for the removal of unreacted species from the ZIF-8 structure. Membrane Z59-A and Z59-B were rinsed with water and methanol to remove unreacted species, respectively. Membrane Z59A is selective, with CO_2 permeance greater than CH_4 with an ideal selectivity of 1.2. However, membrane Z59B is not selective because it has a selectivity of 1.0, indicating defects allowing both gas molecules to pass through it. It is unlikely the methanol rinsing would have made a difference to the separation performance due to its weak interaction with the ZIF-8 structure and its small size (Pan et al., 2015). Although water is corrosive towards the ZIF-8 structure, Zhang et al. reported structure breakdown after 4 hours (Zhang et al., 2015). In conclusion, the difference in gas separation performance is likely due to the nature of heterogeneous nucleation during the synthesis stages as opposed to the activation stage, suggesting discrepancies between the two membranes microstructures.

Literature reports ZIF-8 to exhibit molecular sieving properties, with the permeance of $CO_2 > CH_4$ (Zhu et al., 2016). Venna et al. two-cycle synthesis membrane cross-sectional image showed a thickness of 5 µm delivering permeances in the magnitude of 10^{-5} and 10^{-6} for CO_2 and CH_4, respectively (Venna and Carreon, 2009). In comparison, Zhu et al. two-cycle synthesis achieved permeances in the magnitude of 10^{-8} and 10^{-10} for CO_2 and CH_4, respectively, with an approximate thickness of 25 µm (Zhu et al., 2016). The thickness of 12 µm for the two-cycle synthesis membrane from this thesis identified from Fig. 8-3f suggests being a reliable indication of the thickness of the membranes tested in the gas separation system since delivered permeances in the magnitude of 10^{-7}. However, due to the differences in selectivities of the three

membranes, and with the fourth not being able to hold pressure, they indicate discrepancies between the membranes' microstructures. The membranes with selectivities of 1.0 and 1.2 have a relatively poor microstructure since Zhu et al. and Venna et al. reported selectivities of 6.8 and 4.1 for their two-cycle membranes, respectively.

Figure 8-3 shows the cross-sectional images of membranes synthesised in the batch system at the same synthesis conditions as those tested in the gas separation system for characterisation. The membrane tested with the linker/metal ratio of 2 and metal concentration of 36 mM was not synthesised for characterisation. The cross-sectional images of the single-cycle synthesis (Fig. 8-3a-e) indicate there are no densely packed crystals to form a dense and continuous film above the substrate surface. Except for the 10-hour single synthesis cycle at 144 mM concentration, which indicates there is film growth over the cross-section whilst the membrane tested in the separation system failed to hold pressure. That indicates inhomogeneous film growth or defects in the film such as cracks; it may also suggest a discrepancy between the membranes heterogenous growth between batches. However, more batches are needed to make a more robust conclusion. Cross-sectional image (Fig. 8-3f) of the two-cycle synthesis membrane at 36 mM metal concentration and linker/metal ratio 8 suggests densely packed crystals forming a continuous film with an approximate thickness of 12 µm.

The nature of the growth identified in the SEM images provides a reliable indication of the membranes' performance in the separation system, i.e., no continuous growth no pressure difference. However, the suggestion of discrepancies between membrane growth cannot be eliminated. That can be studied further when growing ZIF-8 membranes at the same synthesis conditions on a minimum of 10 substrates synthesised in separate reaction vessels to measure the level of repeatability.

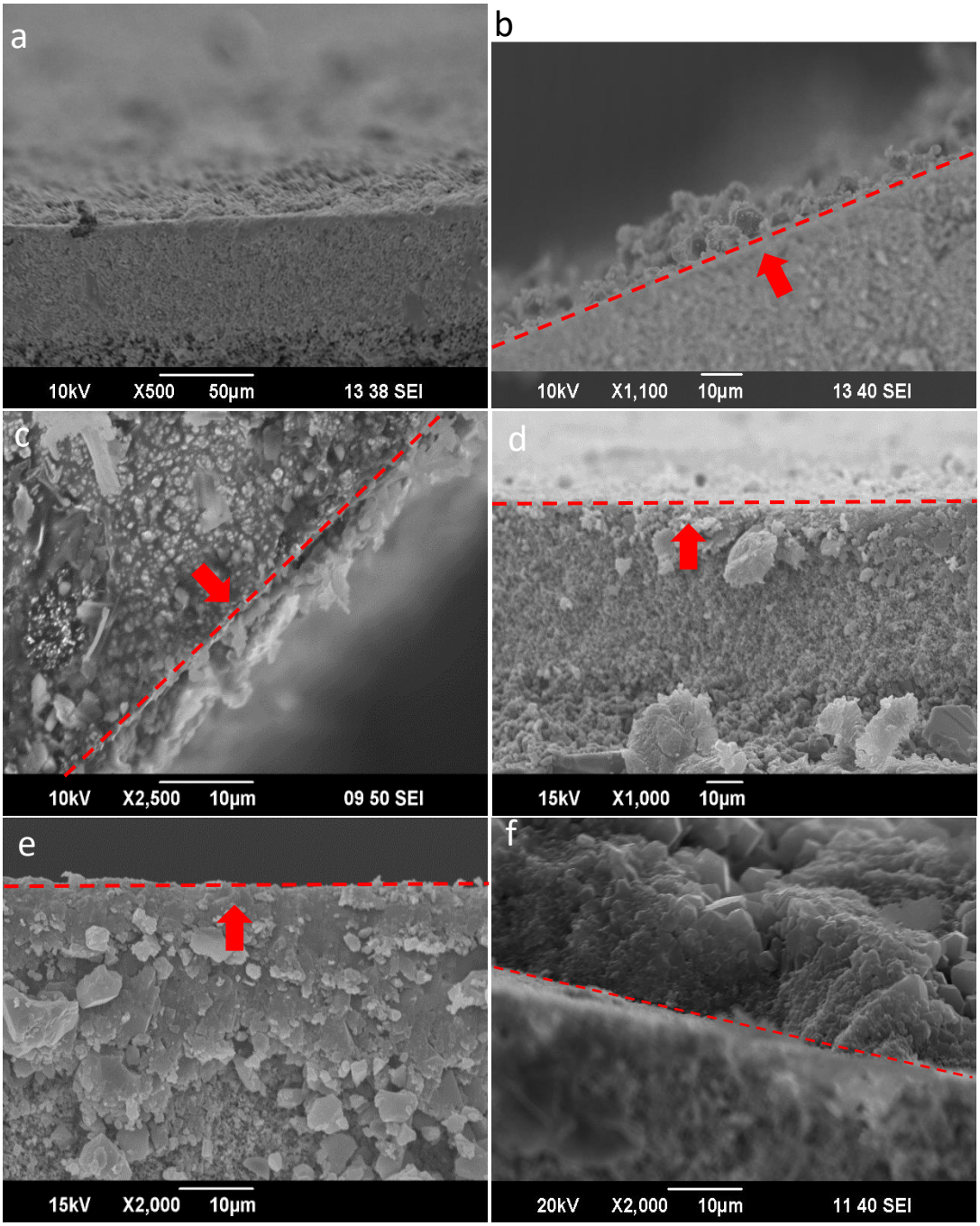


Figure 8- 3: Cross sectional images of membranes synthesised at 150 °C for 5 hours at linker/metal ratio 8 for one cycle at metal concentration of 36 mM on unseeded substrate (a) and seeded substrate (b), and metal concentration 144 mM on seeded substrate (c). Cross sectional image of seeded membranes synthesised at linker/metal ratio 8 at 150 °C for 10 hours at metal concentration of 36 mM (d) and 144 mM (e). Cross sectional image of seeded membrane synthesised at 150 °C for 5 hours at linker/metal ratio 8 and metal concentration of 36 mM for two cycle synthesis. Red arrows and dashed lines highlighting the inside of the substrate lining where crystal growth is expected.

In conclusion, to improve manufacture of the membranes, the precursor's concentration needs to be increased to form dense and continuous membranes in a

single cycle forming more deposited nuclei on the substrate leading to better intergrowth. In addition, an alternative form of surface modification is needed for a more secure attachment of nuclei such as seed suspension with an incorporated binder, since binders have shown to promote particle attachment to substrates (Bux et al., 2011, Kim et al., 2016a), or reactive seeding since the works of Kong et al. showed they manufactured a more securely attached membrane than a membrane synthesised from seeding (Kong et al., 2015). Chemically modifying the substrate with coupling agents such as silane is another viable option since a chemical bond is formed between the substrate and ZIF-8 structure (Tanaka et al., 2014a). In addition to XRD and SEM, when the surface of the substrate is being altered by chemical means (silane coupling agent or ZnO), XPS is ideal since this delivers a quantitative analysis of the chemical distribution and structure composition of the outermost surface of the substrate (Hester et al., 1999, Liu and Kim, 2011). Hence, by measuring the level of homogeneity on the substrate surface the level of success of the adopted surface modification technique can be confirmed and the steps involved in the surface modification can be optimised, thereby improving the overall manufacture of the membranes.

8.4 Conclusions

This chapter investigated the separation performance of membranes synthesised under conventional heating with mixed ZIF-8 precursors. The gas separation testing indicates a select few membranes with continuous growth of ZIF-8 on the substrate surface. However, the ideal selectivity indicates there are defects in the membrane microstructure since they are not selective except for Z8-30 that delivered an ideal selectivity of 9.7. The gas separation testing supported the conclusions drawn from the SEM and XRD results, there are instances where synthesis has produced membranes with no dense and continuous film growth. Which reiterates the difficulty when synthesizing membranes in the lumen of the tubular substrates due to the low mass transfer efficiency. Hence, the way forward for gas separation testing is to use higher precursor concentrations, and a more robust surface modification technique that will complement the membrane synthesis conditions.

In conclusion, the chapter has contributed to the scientific community by demonstrating that the surface modification technique is system specific – this is not commented on by literature. The surface modification technique needs to be systematically investigated to see what works for this system, and optimised by using quantitative analysis, XPS. Hence this optimisation will promote a dense and continuous membranes capable of gas separations.

The gas separation system is crucial since it can allow for a conclusion to be made on stability of the synthesised membrane, and a measure of repeatability of the synthesis method.

9. Conclusions and Future Work

9.1 Conclusions

This thesis aimed to study the heterogenous growth and coating of MOFs onto a substrate using batch and continuous systems, respectively. The thesis introduced robust synthesis methodologies to reach the pilot-scale; for this reason, the focus remained on tubular substrates. There have been limited works on synthesising ZIF-8 membranes where the precursors are isolated, mainly when synthesising on tubular substrates. The microwave reaction chemistry also has not been discussed before when heterogeneously growing ZIF-8 onto substrates. The design of the atomiser when coating MOFs onto substrates has not been investigated before by literature. The thesis conducted a systematic set of experiments in each respective research area to find solutions to the challenges highlighted by literature, leading to novel systems' development. The metal-linker isolation work in the microwave and conventional heated systems and the atomiser's design in the continuous cold spray coating system.

The heterogeneous growth of ZIF-8 using mixed MOF solution under conventional heating showed that the precursors' concentrations and ratios affect heterogeneous growth, with decreasing linker/metal ratio producing larger and more evolved crystals on the surface. The conjugate bases associated with the metal ion, Zn^{2+}, also affects heterogeneous growth and crystal morphology. With zinc acetate delivering a more robust heterogeneous growth, this is because of the intermediate ion, $Zn(CH_3COO)_2$. The intermediate ion creates a delay in the release of the Zn^{2+}, which reduces the rate of homogenous nucleation. Although the synthesis time was increased from 5 to 10 hours for the mixed MOF batch system, the SEM surface images suggested no more nucleation sites were formed (though the crystals were larger and more evolved). They are supporting observations made in literature when synthesising ZIF-8 in the bulk of the solution. There are no more nuclei formed after 60 minutes; instead, existing nuclei evolve and become larger at the expense of the smaller and less evolved nuclei's disappearance.

The metal-linker isolation system shows that the metal and linker location (inside or outside substrate) also affects crystal size and morphology of the ZIF-8 crystals, and the nature of heterogeneous growth onto the substrate surface when at the same linker/metal ratio. The metal-linker isolation system also showed that the precursor's flux, concentration, and linker/metal ratios influence the heterogeneous growth. The conjugate bases associated with the Zn^{2+} controlled the reaction rate, where the NO_3^- base increased the reaction rate (since dissociation increases); however, the SEM and

XRD results implied weak heterogeneous growth. Which may suggest the reaction chemistry and the substrate geometry must accommodate the selected surface modification to promote robust heterogeneous growth since some papers report success in achieving ZIF-8 membranes using zinc acetate while others favour zinc nitrate.

In the microwave chapter, the heterogeneous growth of ZIF-8 with microwave heating indicated that growth could be achieved on the substrate within an hour, though the XRD results suggested it was not continuous since yielded no typical ZIF-8 peaks. The chapter showed that the reaction chemistry must accommodate the dielectric heating mechanisms. Published papers synthesising metal organic framework and zeolite membranes using microwave heating do not discuss the microwave heating properties and heterogeneous growth. This thesis has taken a more fundamental approach and discussed the microwave chemistry effects on heterogeneous nucleation of ZIF-8; this has not been discussed before in literature. The results indicate the reaction chemistry suitable for a conventionally heated system is not ideal for microwave system; in conventional heating, the 288 mM concentration provides a better rate of heat transfer due to the closely packed ions. However, with microwave heating the 288 mM can contribute to the formation of the 'skin' (barrier) forming at the surface of the reaction volume reducing the penetration depth of the microwaves, thereby relying on conventional modes of heat transfer to heat the reaction mixture.

With microwave heating, the closely packed ions reduce the dielectric constant since the solvation spheres retard the ions' movement when they try to oscillate due to the alternating microwaves. Also, the larger solvent volumes in microwave heating allow for a higher power absorption rate, leading to higher heating rates. However to account for these and to better design, the reaction chemistry for heterogeneous growth of ZIF-8, the dielectric properties of the reaction medium needs to be experimentally measured for ZIF-8 since as the hot spots disappear, i.e. as ZIF-8 forms its dielectric properties will change, as will the penetration depth that is a function of the systems pH (system pH decreases as ZIF-8 forms – releasing protons from imidazole).

The cold spray coating of the flat alumina substrates studied the slurry's atomisation and its effect on particle adhesion onto the flat substrates. The results showed that the coating of substrates with unheated air streams delivered the best results with pressure, stand of distance (SOD), number of passes and angle of injection at 2 bar, 300 mm, two passes, and 90 °, respectively.

The thesis reiterated the challenge when heterogeneously growing ZIF-8 onto tubular ceramic substrates. The novel metal-linker isolation indicates the potential to expand this area of work and reach a pilot scale using both heating mechanisms. However, the novel batch system suggests that a more tailored surface modification is needed to achieve dense and continuous growth of ZIF-8 on the substrate surface. The cold spray coating has demonstrated that when optimising the atomisation of the slurry, MOF particles' deposition can be optimised. Heat sensitive MOF/ZIF structures can be deposited using the cold spray technique.

This thesis has advanced the knowledge and understanding of heterogeneous growth and coating of MOFs onto alumina substrates. With further work, the development of the novel ideas presented in this thesis can be commercialised.

9.2 Future work

In this thesis, the novel metal-linker isolation work investigated the formation of ZIF-8 at the substrate surface across both heating mechanisms. The results clearly showed that the precursor location (inside or outside of the substrate) controls the substrate's crystal growth's microstructure. Even though the precursors' first point of contact was at the substrate's pores and the substrate surface, the level of heterogenous growth remained weak, highlighting the challenges of ZIF-8 growth onto substrates. Although cold spray coating work designed the atomiser depositing MOFs onto flat substrates, the results indicated the potential to extend onto tubular substrates. Nevertheless, there still is the potential to upscale both the batch and continuous processes. However, additional work is needed.

9.2.1 Conventionally heated batch system

The manual deposition of seeds onto the substrate surface produced membrane growth failing in the gas separation system. Alternative form of surface modification is needed, chemically modifying the substrates could be a viable alternative to seeding. For the mixed MOF system, chemically modified tubular and flat alumina disks can better understand the mass transfer limitations reported with tubular substrates.

Using longer length tubular substrates and more than two substrates per reaction vessel per synthesis can direct the metal-linker isolation towards the pilot-scale. Reactive seeding in the metal-linker isolation is another viable form of surface modification when synthesising ZIF-8 membranes, the effect of heterogeneous growth can be evaluated based on the respective (metal or linker) precursor location.

9.2.2 Microwave heated batch system

More work needs to be done on understanding the role of microwave chemistry when synthesising membranes. The reaction mixtures dielectric property must be measured to accommodate the microwave chemistry when heterogeneously growing ZIF-8.

Since larger solvent volumes increase power absorption, the solvent volumes can be related to the higher heating rates and assess heterogeneous growth and membrane microstructure by changing the solvent volume.

9.2.3 Cold spray coating

The novel design of the atomiser still requires more work. Investigating the flat target substrate seating angle is important since it affects the depositing particles' impact velocity. When using tubular substrates, the rotating substrate's rpm will impact the coating's homogeneity and thickness, and gun movement speed will also affect particle deposition.

Incorporating a binder into the slurry can promote depositing particles' adhesion onto the target substrate, however, the atomisation of the slurry at the different wt.% must also be studied.

10. References

Aceituno Melgar, V. M., Kim, J. & Othman, M. R. (2015). Zeolitic imidazolate framework membranes for gas separation: A review of synthesis methods and gas separation performance. *Journal of Industrial and Engineering Chemistry,* 28**,** 1-15.

Adatoz, E., Avci, A. K. & Keskin, S. (2015). Opportunities and challenges of MOF-based membranes in gas separations. *Separation and Purification Technology,* 152**,** 207-237.

Aguado, S., Gascón, J., Jansen, J. C. & Kapteijn, F. (2009). Continuous synthesis of NaA zeolite membranes. *Microporous and Mesoporous Materials,* 120**,** 170-176.

Arslan, H. K., Shekhah, O., Wohlgemuth, J., Franzreb, M., Fischer, R. A. & Wöll, C. (2011). High-Throughput Fabrication of Uniform and Homogenous MOF Coatings. *Advanced Functional Materials,* 21**,** 4228-4231.

Australia, M. (2020). *Scanning Electron Microscopy* [Online]. Available: https://myscope.training/#/SEMlevel_2_3 [Accessed 31st December 2020 2020].

Bai, L., Nan, G., Wang, Y., Hu, D., Zeng, G., Zhang, Y., Li, M., Wei, W. & Sun, Y. (2016). Ultrafast microwave synthesis of all-silica DDR zeolite. *Microporous and Mesoporous Materials,* 228**,** 54-58.

Baig, M. A., Patel, F., Alhooshani, K., Muraza, O., Wang, E. N. & Laoui, T. (2015). In-situ aging microwave heating synthesis of LTA zeolite layer on mesoporous TiO2 coated porous alumina support. *Journal of Crystal Growth,* 432**,** 123-128.

Baker, R. (2002). Future directions of membrane gas-separation technology. *Membrane Technology,* 138**,** 5-10.

Baker, R. W. (2012). *Membrane Technology and Applications,* New York, UNITED KINGDOM, John Wiley & Sons, Incorporated.

Baker, R. W. & Lokhandwala, K. (2008). Natural Gas Processing with Membranes: An Overview. *American Chemical Soceity,* 47**,** 2109-2121.

Baker, R. W. & Low, B. T. (2014). Gas Separation Membrane Materials: A Perspective. *Macromolecules,* 47**,** 6999-7013.

Ban, Y., Zhao, M. & Yang, W. (2020). Metal-organic framework-based CO2 capture: From precise material design to high-efficiency membranes. *Frontiers of Chemical Science and Engineering,* 14**,** 188-215.

Bao, Z., Chang, G., Xing, H., Krishna, R., Ren, Q. & Chen, B. (2016). Potential of microporous metal-organic frameworks for separation of hydrocarbon mixtures. *Energy and Environmental Science,* 9**,** 3612-3641.

Bastani, D., Esmaeili, N. & Asadollahi, M. (2013). Polymeric mixed matrix membranes containing zeolites as a filler for gas separation applications: A review. *Journal of Industrial and Engineering Chemistry,* 19**,** 375-393.

Basu, S., Cano-Odena, A. & Vankelecom, I. F. J. (2011). MOF-containing mixed-matrix membranes for CO2/CH4 and CO2/N2 binary gas mixture separations. *Separation and Purification Technology,* 81**,** 31-40.

Bioenergy, I. (2018). United Kingdom - 2018 Update: Bioenergy policies and status of implementation. *Country Reports.*

Brown, A. J., Brunelli, N. A., Eum, K., Rashidi, F., Johnson, J. R., Koros, W. J., Jones, C. W. & Nair, S. (2014a). Interfacial microfluidic processing of metal-organic framework hollow fiber membranes. *Science,* 345**,** 72-75.

Brown, A. J., Brunelli, N. A., Eum, K., Rashidi, F., Johnson, J. R., Koros, W. J., Jones, C. W. & Nair, S. (2014b). Interfacial microfluidic processing of metal-organic framework hollow fiber membranes. *Science,* 345**,** 72.

Butova, V. V., Budnik, A. P., Bulanova, E. A. & Soldatov, A. V. (2016). New microwave-assisted synthesis of ZIF-8. *Mendeleev Communications,* 26**,** 43-44.

Bux, H., Feldhoff, A., Cravillon, J., Wiebcke, M., Li, Y.-S. & Caro, J. (2011). Oriented Zeolitic Imidazolate Framework-8 Membrane with Sharp H2/C3H8 Molecular Sieve Separation. *Chemistry of Materials,* 23**,** 2262-2269.

Bux, H., Liang, F., Li, Y., Cravillon, J., Wiebcke, M. & Caro, J. (2009). Zeolitic Imidazolate Framework Membrane with Molecular Sieving Properties by Microwave-Assisted Solvothermal Synthesis. *American Chemical Soceity,* 131**,** 16000-16001.

C.-J Li, W. Y. L., Y. Y Wang (2003). Effect of Spray Angle on Deposition Characteristics in Cold Spraying. *In:* INTERNATIONAL, A. (ed.) *Plasma.* USA: ASM International.

Campbell, J. & Tokay, B. (2017). Controlling the size and shape of Mg-MOF-74 crystals to optimise film synthesis on alumina substrates. *Microporous and Mesoporous Materials,* 251**,** 190-199.

Caro, A. H. a. J. (2011). Application of Microwave Heating on the Facile Synthesis of Porous Molecular Sieve Membranes. *Advances in Induction and Microwave Heating of Mineral and Organic Materials.*

Caro, J. & Noack, M. (2008). Zeolite membranes – Recent developments and progress. *Microporous and Mesoporous Materials,* 115**,** 215-233.

Caro, J., Noack, M., Kölsch, P. & Schäfer, R. (2000). Zeolite membranes – state of their development and perspective. *Microporous and Mesoporous Materials,* 38**,** 3-24.

Cengel, Y. A. (2006). *Heat and Mass Transfer: A Practical Approach*, McGraw-Hill.

Chae, H. K., Siberio-Pérez, D. Y., Kim, J., Go, Y., Eddaoudi, M., Matzger, A. J., O'Keeffe, M., Yaghi, O. M., Materials, D. & Discovery, G. (2004). A route to high surface area, porosity and inclusion of large molecules in crystals. *Nature,* 427**,** 523-527.

Chen, P.-K., Rosana, M. R., Dudley, G. B. & Stiegman, A. E. (2014). Parameters Affecting the Microwave-Specific Acceleration of a Chemical Reaction. *The Journal of Organic Chemistry,* 79**,** 7425-7436.

Chen, X., Yang, W., Liu, J. & Lin, L. (2005). Synthesis of zeolite NaA membranes with high permeance under microwave radiation on mesoporous-layer-modified macroporous substrates for gas separation. *Journal of Membrane Science,* 255**,** 201-211.

Chen, X. Y., Vinh-Thang, H., Ramirez, A. A., Rodrigue, D. & Kaliaguine, S. (2015). Membrane gas separation technologies for biogas upgrading. *RSC Advances,* 5**,** 24399-24448.

Cheng, Z. L. & Qin, X. X. (2014). Microwave-Assisted Secondary Synthesis of NaA Zeolite Membranes Grown on ZrO2 Substrate. *Applied Mechanics and Materials,* 477-478**,** 1481-1484.

Chew, T. L., Ahmad, A. L. & Bhatia, S. (2011). Ba-SAPO-34 membrane synthesized from microwave heating and its performance for CO2/CH4 gas separation. *Chemical Engineering Journal,* 171**,** 1053-1059.
Chmelik, C., van Baten, J. & Krishna, R. (2012). Hindering effects in diffusion of CO2/CH4 mixtures in ZIF-8 crystals. *Journal of Membrane Science,* 397-398**,** 87-91.
Clark, B. L. D. a. C. M. (2020). *X-ray Powder Diffraction (XRD)* [Online]. Montana State University: Geochemical Instrumentation and Analysis. Available: https://serc.carleton.edu/research_education/geochemsheets/techniques/XRD.html [Accessed 18.05.2020 2020].
Corporation, R. (2020). *X-ray Diffraction* [Online]. Available: https://www.rigaku.com/techniques/x-ray-diffraction-xrd [Accessed 16.05.2020 2020].
Daglar, H. & Keskin, S. (2020). Recent advances, opportunities, and challenges in high-throughput computational screening of MOFs for gas separations. *Coordination Chemistry Reviews,* 422**,** 213470.
Dibenedetto, A. & Aresta, M. (2013). *Inorganic Micro- and Nanomaterials : Synthesis and Characterization,* Berlin/Boston, GERMANY, De Gruyter, Inc.
DoITPoms. (2019). *Loss in dielectrics* [Online]. Available: https://www.doitpoms.ac.uk/tlplib/dielectrics/loss.php [Accessed 25.11.2019 2019].
Drobek, M., Bechelany, M., Vallicari, C., Chaaya, A. A., Charmette, C., Salvador-Levehang, C., Miele, P. & Julbe, A. (2015). An innovativea pproach for the preparation of confined ZIF-8 membranes by conversion of ZnO ALD layers. *journal of Membrane Science,* 475**,** 39-46.
Duan, J., Pan, Y., Liu, G. & Jin, W. (2018). Metal-organic framework adsorbents and membranes for separation applications. *Current Opinion in Chemical Engineering,* 20**,** 122-131.
Dudley, G. B., Richert, R. & Stiegman, A. E. (2015). On the existence of and mechanism for microwave-specific reaction rate enhancement. *Chemical Science,* 6**,** 2144-2152.
Dykhuizen, R. C. & Smith, M. F. (1998). Gas dynamic principles of cold spray. *Journal of Thermal Spray Technology,* 7**,** 205-212.
Eddaoudi, M., Kim, J., Rosi, N., Vodak, D., Wachter, J., Keeffe, M. & Yaghi, O. M. (2002). Systematic Design of Pore Size and Functionality in Isoreticular MOFs and Their Application in Methane Storage. *Science,* 295**,** 469.
Elsevier (1996). *Fundamentals of Inorganic Membrane Science and Technology,* New York.
First, E. L., Hasan, M. M. F. & Floudas, C. A. (2014). Discovery of Novel Zeolites for Natural Gas Purification Through Combined Material Screening and Process Optimization. *American Institute of Chemical Engineers,* 60.
Furukawa, H., Cordova, K. E., O'Keeffe, M. & Yaghi, O. M. (2013). The chemistry and applications of metal-organic frameworks. *Science,* 341.
Gabriel, C., Gabriel, S., H. Grant, E., H. Grant, E., S. J. Halstead, B. & Michael P. Mingos, D. (1998). Dielectric parameters relevant to microwave dielectric heating. *Chemical Society Reviews,* 27**,** 213-224.

Gärtner, F., Stoltenhoff, T., Schmidt, T. & Kreye, H. (2006). The Cold Spray Process and Its Potential for Industrial Applications. *Journal of Thermal Spray Technology,* 15**,** 223-232.
Gascon, J., Blom, W., van Miltenburg, A., Ferreira, A., Berger, R. & Kapteijn, F. (2008). Accelerated synthesis of all-silica DD3R and its performance in the separation of propylene/propane mixtures. *Microporous and Mesoporous Materials,* 115**,** 585-593.
Ge, L., Zhou, W., Du, A. & Zhu, Z. (2012). Porous Polyethersulfone-Supported Zeolitic Imidazolate Framework Membranes for Hydrogen Separation. *The Journal of Physical Chemistry C,* 116**,** 13264-13270.
Goodhew, P. J., Humphreys, J., Beanland, R., Cartwright, L. E., Humphreys, F. J. & Beanland, R. (2000). *Electron Microscopy and Analysis,* London, UNITED STATES, Taylor & Francis Group.
Gregory, A. P. & Clarke, R. N. (2005). Traceable measurements of the static permittivity of dielectric reference liquids over the temperature range 5–50 °C. *Measurement Science and Technology,* 16**,** 1506-1516.
Guo, Y. & Peng, X. (2019). Mass transport through metal organic framework membranes. *Science China Materials,* 62**,** 25-42.
Hägg, M. B., Lindbråthen, A., He, X., Nodeland, S. G. & Cantero, T. (2017). Pilot Demonstration-reporting on CO2 Capture from a Cement Plant Using Hollow Fiber Process. *Energy Procedia,* 114**,** 6150-6165.
Hara, N., Yoshimune, M., Negishi, H., Haraya, K., Hara, S. & Yamaguchi, T. (2014). Diffusive separation of propylene/propane with ZIF-8 membranes. *Journal of Membrane Science,* 450**,** 215223.
Hara, N., Yoshimune, M., Negishi, H., Haraya, K., Hara, S. & Yamaguchi, T. (2015). ZIF-8 membranes prepared at miscible and immiscible liquid–liquid interfaces. *Microporous and Mesoporous Materials,* 206**,** 75-80.
Harker, J. H., Backhurst, J. R., Richardson, J. F. & Coulson, J. M. (2002). *Chemical Engineering Volume 2 : Particle technology and separation processes,* Oxford, UNITED KINGDOM, Elsevier Science & Technology.
Hayes, B. L. (2002). *Microwave Synthesis: Chemistry at the Speed of Light,* USA, CEM Publishing.
He, B. B. (2009). *Two-Dimensional X-Ray Diffraction,* Hoboken, UNITED STATES, John Wiley & Sons, Incorporated.
Herrero, M. A., Kremsner, J. M. & Kappe, C. O. (2008). Nonthermal Microwave Effects Revisited: On the Importance of Internal Temperature Monitoring and Agitation in Microwave Chemistry. *The Journal of Organic Chemistry,* 73**,** 36-47.
Hester, J. F., Banerjee, P. & Mayes, A. M. (1999). Preparation of Protein-Resistant Surfaces on Poly(vinylidene fluoride) Membranes via Surface Segregation. *Macromolecules,* 32**,** 1643-1650.
Hiroyasu Furukawa, K. E. C., Michael O'Keeffe, Omar M. Yaghi (2013). The Chemistry and Applications of Metal-Organic Frameworks. *Science,* 341**,** 974-987.
Horikoshi, S. & Serpone, N. (2013). *Microwaves in Nanoparticle Synthesis : Fundamentals and Applications,* Weinheim, GERMANY, John Wiley & Sons, Incorporated.
Hoz, A. d. l., Loupy, A. & Loupy, A. (2013). *Microwaves in Organic Synthesis,* Weinheim, GERMANY, John Wiley & Sons, Incorporated.

Hu, N., Li, Y., Zhong, S., Wang, B., Zhang, F., Wu, T., Yang, Z., Zhou, R. & Chen, X. (2016). Microwave synthesis of zeolite CHA (chabazite) membranes with high pervaporation performance in absence of organic structure directing agents. *Microporous and Mesoporous Materials,* 228**,** 22-29.

Huang, A. & Yang, W. (2007). Hydrothermal synthesis of NaA zeolite membrane together with microwave heating and conventional heating. *Materials Letters,* 61**,** 5129-5132.

Huang, K., Li, Q., Liu, G., Shen, J., Guan, K. & Jin, W. (2015). A ZIF-71 Hollow Fiber Membrane Fabricated by Contra-Diffusion. *ACS Applied Materials & Interfaces,* 7**,** 16157-16160.

Hurrle, S., Friebe, S., Wohlgemuth, J., Wöll, C., Caro, J. & Heinke, L. (2017). Sprayable, Large-Area Metal–Organic Framework Films and Membranes of Varying Thickness. *Chemistry – A European Journal,* 23**,** 2294-2298.

Ileleji, K. E., Martin, C. & Jones, D. (2015). Chapter 17 - Basics of Energy Production through Anaerobic Digestion of Livestock Manure. *In:* DAHIYA, A. (ed.) *Bioenergy.* Boston: Academic Press.

International Energy Agency, I. (2018). Natural Gas Information 2018. *In:* AGENCY, I. E. (ed.).

International Energy Agency, I. (2020). Outlook for biogas and biomethane: Prospects for organic growth.

Isaeva, V. I., Barkova, M. I., Kustov, L. M., Syrtsova, D. A., Efimova, E. A. & Teplyakov, V. V. (2015). In situ synthesis of novel ZIF-8 membranes on polymeric and inorganic supports. *Journal of Materials Chemistry A,* 3**,** 7469-7476.

James, J. B., Lang, L., Meng, L. & Lin, J. Y. S. (2020). Postsynthetic Modification of ZIF-8 Membranes via Membrane Surface Ligand Exchange for Light Hydrocarbon Gas Separation Enhancement. *ACS Applied Materials & Interfaces,* 12**,** 3893-3902.

Jian, M., Liu, B., Liu, R., Qu, J., Wang, H. & Zhang, X. (2015). Water-based synthesis of zeolitic imidazolate framework-8 with high morphology level at room temperature. *RSC Advances,* 5**,** 48433-48441.

Jodoin, B., Ajdelsztajn, L., Sansoucy, E., Zúñiga, A., Richer, P. & Lavernia, E. J. (2006). Effect of particle size, morphology, and hardness on cold gas dynamic sprayed aluminum alloy coatings. *Surface and Coatings Technology,* 201**,** 3422-3429.

Johnsson, F., Kjarstad, J. & Rootzen, J. (2019). The threat to climate change mitigation posed by the abundance of fossil fuels. *Climate Policy,* 19**,** 258-274.

Kang, Z., Fan, L. & Sun, D. (2017). Recent advances and challenges of metal–organic framework membranes for gas separation. *Journal of Materials Chemistry A,* 5**,** 10073-10091.

Kao, C. M., Ong, S. L., C. Zhang, T., Y. Surampalli, R., Vigneswaran, S., D. Tyagi, R. & Surampalli, R. Y. (2012). *Membrane Technology and Environmental Applications,* Reston, UNITED STATES, American Society of Civil Engineers.

Kappe, C. O., Pieber, B. & Dallinger, D. (2013). Microwave Effects in Organic Synthesis: Myth or Reality? *Angewandte Chemie International Edition,* 52**,** 1088-1094.

Kenarsari, S. D., Yang, D., Jiang, G., Zhang, S., Wang, J., Russell, A. G., Wei , Q. & Fan, M. (2013). Review of recent advances in carbon dioxide separation and capture. *Royal Soceity Chemistry Advances,* 3**,** 22739-22773.

Keskin, S. & Kızılel, S. (2011). Biomedical Applications of Metal Organic Frameworks. *Industrial & Engineering Chemistry Research,* 50**,** 1799-1812.

Khan, N. A., Haque, E. & Jhung, S. H. (2010). Rapid syntheses of a metal–organic framework material Cu3(BTC)2(H2O)3 under microwave: a quantitative analysis of accelerated syntheses. *Physical Chemistry Chemical Physics,* 12**,** 2625-2631.

Kida, K., Fujita, K., Shimada, T., Tanaka, S. & Miyake, Y. (2013a). Layer-by-layer aqueous rapid synthesis of ZIF-8 films on a reactive surface. *Dalton Transactions,* 42**,** 11128-11135.

Kida, K., Okita, M., Fujita, K., Tanaka, S. & Miyake, Y. (2013b). Formation of high crystalline ZIF-8 in an aqueous solution. *CrystEngComm,* 15**,** 1794-1801.

Kim, D.-Y., Joshi, B. N., Lee, J.-G., Lee, J.-H., Lee, J. S., Hwang, Y. K., Chang, J.-S., Al-Deyab, S., Tan, J.-C. & Yoon, S. S. (2016a). Supersonic cold spraying for zeolitic metal–organic framework films. *Chemical Engineering Journal,* 295**,** 49-56.

Kim, D.-Y., Sinha-Ray, S., Park, J.-J., Lee, J.-G., Cha, Y.-H., Bae, S.-H., Ahn, J.-H., Jung, Y. C., Kim, S. M., Yarin, A. L. & Yoon, S. S. (2014). Self-Healing Reduced Graphene Oxide Films by Supersonic Kinetic Spraying. *Advanced Functional Materials,* 24**,** 4986-4995.

Kim, D. Y., Joshi, B. N., Lee, J. G., Lee, J. H., Lee, J. S., Hwang, Y. K., Chang, J. S., Al-Deyab, S., Tan, J. C. & Yoon, S. S. (2016b). Supersonic cold spraying for zeolitic metal-organic framework films. *Chemical Engineering Journal,* 295**,** 49-56.

Kim, S. & Lee, Y. M. (2013). High performance polymer membranes for CO2 separation. *Current Opinion in Chemical Engineering,* 2**,** 238-244.

Kohl, A. L. N., R. B. (1997). *Gas Purification*, Gulf Professional Publishing.

Kong, C., Du, H., Chen, L. & Chen, B. (2017). Nanoscale MOF/organosilica membranes on tubular ceramic substrates for highly selective gas separation. *Energy & Environmental Science,* 10**,** 1812-1819.

Kong, L., Zhang, X., Liu, H. & Qiu, J. (2015). Synthesis of a highly stable ZIF-8 membrane on a macroporous ceramic tube by manual-rubbing ZnO deposition as a multifunctional layer. *Journal of Membrane Science,* 490**,** 354-363.

Kong, L., Zhang, X., Liu, Y., Li, S., Liu, H., Qiu, J. & Yeung, K. L. (2014). In situ fabrication of high-permeance ZIF-8 tubular membranes in a continuous flow system. *Materials Chemistry and Physics,* 148**,** 10-16.

Koros, W. J. & Fleming, G. K. (1993). Membrane-based gas separation. *Journal of Membrane Science,* 83**,** 1-80.

Kosinov, N., Gascon, J., Kapteijn, F. & Hensen, E. J. M. (2016). Recent developments in zeolite membranes for gas separation. *Journal of Membrane Science,* 499**,** 65-79.

Kwon, H. T. & Jeong, H.-K. (2015). Improving propylene/propane separation performance of Zeolitic-Imidazolate framework ZIF-8 Membranes. *Chemical Engineering Science,* 124**,** 20-26.

Kwon, H. T., Jeong, H., Lee, A. S., An, H. S., Lee, T., Jang, E., Leef, J. S. & Choi, J. (2016a). Defect-induced ripening of zeolitic-imidazolate framework ZIF-8 and its implication to vapor-phase membrane synthesis. *Royal Soceity Chemistry,* 52**,** 11669-11672.

Kwon, H. T. & Jeong, H. K. (2013). In situ synthesis of thin zeolitic-imidazolate framework ZIF-8 membranes exhibiting exceptionally high propylene/propane separation. *Journal of the American Chemical Society,* 135**,** 10763-10768.

Kwon, H. T., Jeong, H. K., Lee, A. S., An, H. S., Lee, T., Jang, E., Lee, J. S. & Choi, J. (2016b). Defect-induced ripening of zeolitic-imidazolate framework ZIF-8 and its implication to vapor-phase membrane synthesis. *Chemical Communications,* 52**,** 11669-11672.

Kyo Sung Park, Z. N., Adrien P. Cote, Jae Yong Choi, Rudan Huang, Fernando J. Uribe-Romo*, Hee K. Chae, Michael O'Keeffe and Omar M. Yaghi (2006). Exceptional chemical and thermal stability of zeolitic imidazolate frameworks. *The National Academy of Sciences of the USA,* 103**,** 10186-10191.

Lai, L. S., Yeong, Y. F., Chew, T. L., lau, K. K. & Azmi, M. S. (2016a). CO2 and CH4 gas permeation study via zeolitic imidazolate framework (ZIF)-8 membrane. *Journal of Natural Gas Science and Engineering,* 34**,** 509-519.

Lai, L. S., Yeong, Y. F., Keong Lau, K. & Azmi, M. S. (2014a). Zeolitic Imidazolate Frameworks (ZIF): A Potential Membrane for CO2/CH4 Separation. *Separation Science and Technology,* 49**,** 1490-1508.

Lai, L. S., Yeong, Y. F., Keong Lau, K. & Azmi, M. S. (2014b). Zeolitic Imidazolate Frameworks (ZIF): A Potential Membrane for CO<inf>2</inf>/CH<inf>4</inf> Separation. *Separation Science and Technology (Philadelphia),* 49**,** 1490-1508.

Lai, L. S., Yeong, Y. F., Lau, K. K. & Shariff, A. M. (2016b). Effect of Synthesis Parameters on the Formation of ZIF-8 Under Microwave-assisted Solvothermal. *Procedia Engineering,* 148**,** 35-42.

Lai, L. S., Yeong, Y. F., Lau, K. K. & Shariff, A. M. (2016c). Synthesis of zeolitic imidazolate frameworks (ZIF)-8 membrane and its process optimization study in separation of CO2 from natural gas. *Soceity of Chemical Industry,* 92**,** 420-431.

Lai, Z. (2018). Development of ZIF-8 membranes: opportunities and challenges for commercial applications. *Current Opinion in Chemical Engineering,* 20**,** 78-85.

Laybourn, A., Katrib, J., Ferrari-John, R. S., Morris, C. G., Yang, S., Udoudo, O., Easun, T. L., Dodds, C., Champness, N. R., Kingman, S. W. & Schröder, M. (2017). Metal–organic frameworks in seconds via selective microwave heating. *Journal of Materials Chemistry A,* 5**,** 7333-7338.

Laybourn, A., Katrib, J., Palade, P. A., Easun, T. L., Champness, N. R., Schröder, M. & Kingman, S. W. (2016). Understanding the electromagnetic interaction of metal organic framework reactants in aqueous solution at microwave frequencies. *Physical Chemistry Chemical Physics,* 18**,** 5419-5431.

Lee, J.-G., Kim, D.-Y., Kang, B., Kim, D., Al-Deyab, S. S., James, S. C. & Yoon, S. S. (2015). Thin film metallization by supersonic spraying of copper and

nickel nanoparticles on a silicon substrate. *Computational Materials Science,* 108**,** 114-120.
Lee, J. H., Kim, D., Shin, H., Yoo, S. J., Kwon, H. T. & Kim, J. (2019). Zeolitic imidazolate framework ZIF-8 films by ZnO to ZIF-8 conversion and their usage as seed layers for propylene-selective ZIF-8 membranes. *Journal of Industrial and Engineering Chemistry,* 72**,** 374-379.
Leng, Y. (2013). *Materials Characterization : Introduction to Microscopic and Spectroscopic Methods,* Weinheim, GERMANY, John Wiley & Sons, Incorporated.
Leung, D. Y. C., Caramanna, G. & Maroto-Valer, M. M. (2014). An overview of current status of carbon dioxide capture and storage technologies. *Renewable and Sustainable Energy Reviews,* 39**,** 426-443.
Li, J., Lian, H., Wei, K., Song, E., Pan, Y. & Xing, W. (2020). Synthesis of tubular ZIF-8 membranes for propylene/propane separation under high-pressure. *Journal of Membrane Science,* 595**,** 117503.
Li, J. R., Kuppler, R. J. & Zhou, H. C. (2009). Selective gas adsorption and separation in metal-organic frameworks. *Chemical Society Reviews,* 38**,** 1477-1504.
Li, N. N., Fane, A. G., Ho, W. S. W. & Matsuura, T. (2008a). *Advanced Membrane Technology and Applications,* Hoboken, UNITED STATES, American Institute of Chemical Engineers.
Li, P.-Z., Wang, X.-J. & Zhao, Y. (2019). Click chemistry as a versatile reaction for construction and modification of metal-organic frameworks. *Coordination Chemistry Reviews,* 380**,** 484-518.
Li, S., Falconer, J. L. & Noble, R. D. (2004). SAPO-34 membranes for CO2/CH4 separation. *Journal of Membrane Science,* 241**,** 121-135.
Li, S., Martinek, J. G., Falconer, J. L., Noble, R. D. & Gardner, T. Q. (2005). High-Pressure CO2/CH4 Separation Using SAPO-34 Membranes. *Industrial & Engineering Chemistry Research,* 44**,** 3220-3228.
Li, W., Zhang, Y., Li, Q. & Zhang, G. (2015). Metal−organic framework composite membranes: Synthesis and separation applications. *Chemical Engineering Science,* 135**,** 232-257.
Li, W. Y., Zhang, C., Guo, X. P., Zhang, G., Liao, H. L., Li, C. J. & Coddet, C. (2008b). Effect of standoff distance on coating deposition characteristics in cold spraying. *Materials & Design,* 29**,** 297-304.
Li, X., Liu, Y., Wang, J., Gascon, J., Li, J. & Van der Bruggen, B. (2017). Metal–organic frameworks based membranes for liquid separation. *Chemical Society Reviews,* 46**,** 7124-7144.
Li, Y., Chen, H., Liu, J. & Yang, W. (2006). Microwave synthesis of LTA zeolite membranes without seeding. *Journal of Membrane Science,* 277**,** 230-239.
Li, Y. & Yang, W. (2008). Microwave synthesis of zeolite membranes: A review. *Journal of Membrane Science,* 316**,** 3-17.
Lin, R., Villacorta Hernandez, B., Ge, L. & Zhu, Z. (2018). Metal organic framework based mixed matrix membranes: an overview on filler/polymer interfaces. *Journal of Materials Chemistry A,* 6**,** 293-312.
Linder-Patton, O. M., de Prinse, T. J., Furukawa, S., Bell, S. G., Sumida, K., Doonan, C. J. & Sumby, C. J. (2018). Influence of nanoscale structuralisation on the catalytic performance of ZIF-8: a cautionary surface catalysis study. *CrystEngComm,* 20**,** 4926-4934.

Liu, S. X. & Kim, J.-T. (2011). Characterization of Surface Modification of Polyethersulfone Membrane. *Journal of Adhesion Science and Technology,* 25**,** 193-212.
Liu, Y., Ng, Z., Khan, E. A., Jeong, H.-K., Ching, C.-b. & Lai, Z. (2009). Synthesis of continuous MOF-5 membranes on porous α-alumina substrates. *Microporous and Mesoporous Materials,* 118**,** 296-301.
Lombardi, L. & Francini, G. (2020). Techno-economic and environmental assessment of the main biogas upgrading technologies. *Renewable Energy,* 156**,** 440-458.
Lou, J., Hatton, T. A. & Laibinis, P. E. (1997). Effective Dielectric Properties of Solvent Mixtures at Microwave Frequencies. *The Journal of Physical Chemistry A,* 101**,** 5262-5268.
Lu, G., Farha, O. K., Zhang, W., Huo, F. & Hupp, J. T. (2012). Engineering ZIF-8 Thin Films for Hybrid MOF-Based Devices. *Advanced Materials,* 24**,** 3970-3974.
Madhusoodana, C. D., Das, R. N., Kameshima, Y. & Okada, K. (2006). Preparation of Ceramic Honeycomb Filter Supported Zeolite Membrane Modules by Microwave-Assisted In-Situ Crystallization. *Key Engineering Materials,* 317-318**,** 697-700.
Maina, J. W., Gonzalo, C. P., Merenda, A., Kong, L., Schütz, J. A. & Dumée, L. F. (2018). The growth of high density network of MOF nano-crystals across macroporous metal substrates – Solvothermal synthesis versus rapid thermal deposition. *Applied Surface Science,* 427**,** 401-408.
Marti, A. M., Wickramanayake, W., Dahe, G., Sekizkardes, A., Bank, T. L., Hopkinson, D. P. & Venna, S. R. (2017). Continuous Flow Processing of ZIF-8 Membranes on Polymeric Porous Hollow Fiber Supports for CO2 Capture. *American Chemical Soceity,* 9**,** 5678-5682.
Mazyan, W., Ahmadi, A., Ahmed, H. & Hoorfar, M. (2016). Market and technology assessment of natural gas processing: A review. *Journal of Natural Gas Science and Engineering,* 30**,** 487-514.
Mazzotti, M., Gazzani, M., Milella, F. & Gabrielli, P. (Year) Published. MEMBRANE SEPARATIONS RATE CONTROLLED SEPARATION PROCESSES. 2016.
Md. Nordin, N. A. H., Ismail, A. F., Mustafa, A., Murali, R. S. & Matsuura, T. (2015). Utilizing low ZIF-8 loading for an asymmetric PSf/ZIF-8 mixed matrix membrane for CO2/CH4 separation. *RSC Advances,* 5**,** 30206-30215.
Meredith, R. (1998). *Engineers Handbook of Industrial Microwave Heating,* London, The Institution of Electrical Engineers.
Mestre, S., Gozalbo, A., Lorente-Ayza, M. M. & Sánchez, E. (2019). Low-cost ceramic membranes: A research opportunity for industrial application. *Journal of the European Ceramic Society,* 39**,** 3392-3407.
Michael C. McCarthy, V. V.-G., Gregory V. Barnett and Hae-Kwon Jeong* (2010). Synthesis of Zeolitic Imidazolate Framework Films and Membranes with Controlled Microstructure. *Langmuir,* 18**,** 14636-14641.
Microwaves101. (2020a). *Alumina 99.5%* [Online]. everythingRF. Available: https://www.microwaves101.com/encyclopedias/alumina-99-5 [Accessed 04/01/2020 2020].

Microwaves101. (2020b). *PTFE* [Online]. everythingRF. Available: https://www.microwaves101.com/encyclopedias/ptfe [Accessed 04.01.2020 2020].
Mingos, D. M. P. & Baghurst, D. R. (1991). Tilden Lecture. Applications of microwave dielectric heating effects to synthetic problems in chemistry. *Chemical Society Reviews,* 20**,** 1-47.
Mohshim, D. F., Mukhtar, H. b., Man, Z. & Nasir, R. (2012). Latest Development on Membrane Fabrication for Natural Gas Puriication: A Review. *Journal of Engineering,* 2013.
Mondal, M. K., Balsora, H. K. & Varshney, P. (2012). Progress and trends in CO_2 capture/separation technologies: A review. *Energy,* 46**,** 431-441.
Moonga, K. H. & Jen, T.-C. (2017). *Numerical Analysis of the Cold Gas Dynamic Spray Surface Coating Process*.
Morris, W., Stevens, C. J., Taylor, R. E., Dybowski, C., Yaghi, O. M. & Garcia-Garibay, M. A. (2012). NMR and X-ray Study Revealing the Rigidity of Zeolitic Imidazolate Frameworks. *The Journal of Physical Chemistry C,* 116**,** 13307-13312.
Ng, E.-P., Awala, H., Komaty, S. & Mintova, S. (2019). Microwave-green synthesis of AlPO-n and SAPO-n (n = 5 and 18) nanosized crystals and their assembly in layers. *Microporous and Mesoporous Materials,* 280**,** 256-263.
NIST. (2017). *Thermophysical properties of fluid systems* [Online]. USA: National Insitute of Science and Technology. [Accessed 18.10.2017 2017].
Novaković, S. B., Bogdanović, G. A., Heering, C., Makhloufi, G., Francuski, D. & Janiak, C. (2015). Charge-Density Distribution and Electrostatic Flexibility of ZIF-8 Based on High-Resolution X-ray Diffraction Data and Periodic Calculations. *Inorganic Chemistry,* 54**,** 2660-2670.
Obotey Ezugbe, E. & Rathilal, S. (2020). Membrane Technologies in Wastewater Treatment: A Review. *Membranes,* 10.
Öztürk, Z., Filez, M. & Weckhuysen, B. M. (2017). Decoding Nucleation and Growth of Zeolitic Imidazolate Framework Thin Films with Atomic Force Microscopy and Vibrational Spectroscopy. *Chemistry (Weinheim an der Bergstrasse, Germany),* 23**,** 10915-10924.
Pan, Y., Li, T., Lestari, G. & Lai, Z. (2012). Effective separation of propylene/propane binary mixtures by ZIF-8 membranes. *Journal of Membrane Science,* 390-391**,** 93-98.
Pan, Y., Wei, L., Zhao, Y., Wang, C. & Lai, Z. (2015). Improved ZIF-8 membrane: Effect of activation procedure and determination of diffusivities of light hydrocarbons. *Journal of Membrane Science,* 493**,** 88-96.
Park, K. S., Ni, Z., Côté, A. P., Choi, J. Y., Huang, R., Uribe-Romo, F. J., Chae, H. K., O'Keeffe, M. & Yaghi, O. M. (2006). Exceptional chemical and thermal stability of zeolitic imidazolate frameworks. *Proc Natl Acad Sci U S A,* 103**,** 10186-10191.
Pera-Titus, M., Bausach, M., Llorens, J. & Cunill, F. (2007). Preparation of inner-side tubular zeolite NaA membranes in a continuous flow system. *Separation and Purification Technology,* 59**,** 141-150.

PhotoMetrics. (2020). *Energy Dispersive Spectroscopy (EDS)* [Online]. Available: https://photometrics.net/energy-dispersive-spectroscopy-eds/ [Accessed 31.12.2020 2020].
Pina, M. P., Arruebo, M., Felipe, M., Fleta, F., Bernal, M. P., Coronas, J., Men´endez, M. & Santamar´ıa, J. (2004). A semi-continuous method for the synthesis of NaA zeolite membranes on tubular supports. *Journal of Membrane Science,* 244**,** 141-150.
Poshusta, J. C., Tuan, V. A., Falconer, J. L. & Noble, R. D. (1998). Synthesis and Permeation Properties of SAPO-34 Tubular Membranes. *Industrial & Engineering Chemistry Research,* 37**,** 3924-3929.
Prasetya, N., Himma, N. F., Sutrisna, P. D., Wenten, I. G. & Ladewig, B. P. (2020). A review on emerging organic-containing microporous material membranes for carbon capture and separation. *Chemical Engineering Journal,* 391**,** 123575.
Qian, Q., Asinger, P. A., Lee, M. J., Han, G., Mizrahi Rodriguez, K., Lin, S., Benedetti, F. M., Wu, A. X., Chi, W. S. & Smith, Z. P. (2020). MOF-Based Membranes for Gas Separations. *Chemical Reviews,* 120**,** 8161-8266.
Qiu, S. & Zhu, G. (2009). Molecular engineering for synthesizing novel structures of metal-organic frameworks with multifunctional properties. *Coordination Chemistry Reviews,* 253**,** 2891-2911.
Ramu, G., Lee, M. & Jeong, H. K. (2018). Effects of zinc salts on the microstructure and performance of zeolitic-imidazolate framework ZIF-8 membranes for propylene/propane separation. *Microporous and Mesoporous Materials,* 259**,** 155-162.
Rehman, R. U., Song, Q., Peng, L., Wu, Z. & Gu, X. (2020). A facile coating to intact SAPO-34 membranes for wet CO2/CH4 mixture separation. *Chemical Engineering Research and Design,* 153**,** 37-48.
Rezakazemi, M., Ebadi Amooghin, A., Montazer-Rahmati, M. M., Ismail, A. F. & Matsuura, T. (2014). State-of-the-art membrane based CO2 separation using mixed matrix membranes (MMMs): An overview on current status and future directions. *Progress in Polymer Science,* 39**,** 817-861.
Richards, S. J. & Al Zaili, J. (2020). Contribution of encouraging the future use of biomethane to resolving sustainability and energy security challenges: The case of the UK. *Energy for Sustainable Development,* 55**,** 48-55.
Robeson, L. M. (2008). The upper bound revisited. *Journal of Membrane Science,* 320**,** 390-400.
Robinson, J., Kingman, S., Irvine, D., Licence, P., Smith, A., Dimitrakis, G., Obermayer, D. & Kappe, C. O. (2010). Understanding microwave heating effects in single mode type cavities—theory and experiment. *Physical Chemistry Chemical Physics,* 12**,** 4750-4758.
Ruan, X., Zhang, X., Zhou, Z., Jiang, X., Dai, Y., Yan, X. & He, G. (2019). ZIF-8 heterogeneous nucleation and growth mechanism on Zn(II)-doped polydopamine for composite membrane fabrication. *Separation and Purification Technology,* 214**,** 95-103.
Schejn, A., Balan, L., Falk, V., Aranda, L., Medjahdic, G. & Schneider, R. (2014). Controlling ZIF-8 nano- and microcrystal formation and reactivity through zinc salt variations. *CrystEngComm,* 16**,** 4493-4500.
Shah, M., Kwon, H. T., Tran, V., Sachdeva, S. & Jeong, H. K. (2013a). One step in situ synthesis of supported zeolitic imidazolate framework ZIF-8

membranes: Role of sodium formate. *Microporous and Mesoporous Materials,* 165**,** 63-69.
Shah, M., McCarthy, C. M., Sachdeva, S., Lee, K. A. & Jeong, H.-K. (2011). Current Status of Metal-Organic Framework Membranes for Gas Separations: Promises and Challenges. *American Chemical Soceity,* 51**,** 2179-2199.
Shah, M. N., Gonzalez, M. A., McCarthy, M. C. & Jeong, H. K. (2013b). An unconventional rapid synthesis of high performance metal-organic framework membranes. *Langmuir,* 29**,** 7896-7902.
Shimekit, B. & Mukhtar, H. (2012). Natural Gas Purification Technologies - Major Advances for CO2 Separation and Future Directions.
Smith, R. C. D. F. (1998). Gas dynamic principles of cold spray. *Journal of Thermal Spray Technology,* 7**,** 205-212.
Spigarelli, B. P. & Kawatra, S. K. (2013). Oppurtunities and challenges in carbon dioxide capture. *Journal of CO_2 Utilization,* 1**,** 69-87.
Stern, S. A. (1994). Polymers for gas separations: the next decade. *Journal of Membrane Science,* 94**,** 1-65.
Su, J., Wu, W., Li, Z. & Li, W. (2019). Self-crystallization of uniformly oriented zeolitic imidazolate framework films at air–water interfaces. *Dalton Transactions,* 48**,** 11196-11199.
Sun, J. (2018). Propylene-Selective Thin Zeolitic Imidazolate Framework Membranes on Ceramic Tubes by Microwave Seeding and Solvothermal Secondary Growth. *Crystals,* 8.
Sun, J., Wang, W. & Yue, Q. (2016). Review on Microwave-Matter Interaction Fundamentals and Efficient Microwave-Associated Heating Strategies. *Materials (Basel, Switzerland),* 9**,** 231.
Sun, Y., Zhang, R., Zhao, C., Wang, N., Xiea, Y. & Li, J. R. (2014). Self-modified fabrication of inner skin ZIF-8 tubular membranes by a counter diffusion assisted secondary growth method. *Royal Soceity Chemistry,* 4**,** 33007-33012.
Tanaka, S., Kida, K., Okita, M., Ito, Y. & Miyake, Y. (2012). Size-controlled Synthesis of Zeolitic Imidazolate Framework-8 (ZIF-8) Crystals in an Aqueous System at Room Temperature. *The Chemical Soceity of Japan,* 41**,** 1337-1339.
Tanaka, S., Okubo, K., Kida, K., Sugita, M. & Takewaki, T. (2017). Grain size control of ZIF-8 membranes by seeding-free aqueous synthesis and their performances in propylene/propane separation. *Journal of Membrane Science,* 544**,** 306-311.
Tanaka, S., Shimada, T., Fujita, K., Miyake, Y., Kida, K., Yogo, K., Denayer, J. F. M., Sugita, M. & Takewaki, T. (2014a). Seeding-free aqueous synthesis of zeolitic imidazolate framework-8 membranes: How to trigger preferential heterogeneous nucleation and membrane growth in aqueous rapid reaction solution. *Journal of Membrane Science,* 472**,** 29-38.
Tanaka, S., Shimada, T., Fujita, K., Miyake, Y., Kida, K., Yogo, K., Denayer, J. F. M., Sugita, M. & Takewaki, T. (2014b). Seeding-free aqueous synthesis of zeoliticimidazolate framework-8 membranes: How to trigger preferential heterogeneous nucleation and membrane growth in a queous rapid reaction solution. *Journal of Membrane Science,* 472**,** 29-38.

Tanh Jeazet, H. B., Sorribas, S., Román-Marín, J. M., Zornoza, B., Téllez, C., Coronas, J. & Janiak, C. (2016). Increased Selectivity in CO2/CH4 Separation with Mixed-Matrix Membranes of Polysulfone and Mixed-MOFs MIL-101(Cr) and ZIF-8. *European Journal of Inorganic Chemistry,* 2016**,** 4363-4367.

Tao, K., Cao, L., Lin, Y., Kong, C. & Chen, L. (2013a). A hollow ceramic fiber supported ZIF-8 membrane with enhanced gas separation performance prepared by hot dip-coating seeding. *Journal of Materials Chemistry A,* 1**,** 13046-13049.

Tao, K., Kong, C. & Chen, L. (2013b). High performance ZIF-8 molecular sieve membrane on hollow ceramic fiber via crystallizing-rubbing seed deposition. *Chemical Engineering Journal,* 220**,** 1-5.

Terry, R. D. N. a. P. A. (2004). *Principles of Chemical Separations with Environmental Applications,* Cambridge, United Kingdom, Cambridge University Press.

Thomas-Hillman, I., Laybourn, A., Dodds, C. & Kingman, S. W. (2018). Realising the environmental benefits of metal–organic frameworks: recent advances in microwave synthesis. *Journal of Materials Chemistry A,* 6**,** 11564-11581.

Tompsett, G. A., Conner, W. C. & Yngvesson, K. S. (2006). Microwave Synthesis of Nanoporous Materials. *ChemPhysChem,* 7**,** 296-319.

Torad, N. L., Hu, M., Kamachi, Y., Takai, K., Imura, M., Naito, M. & Yamauchi, Y. (2013). Facile synthesis of nanoporous carbons with controlled particle sizes by direct carbonization of monodispersed ZIF-8 crystals. *Chemical Communications,* 49**,** 2521-2523.

Tran, N. T., Kim, J. & Othman, M. R. (2019). Microporous ZIF-8 membrane prepared from secondary growth for improved propylene permeance and selectivity. *Microporous and Mesoporous Materials,* 285**,** 178-184.

Tran, N. T., Kim, J. & Othman, M. R. (2020a). Microporous ZIF-8 and ZIF-67 membranes grown on mesoporous alumina substrate for selective propylene transport. *Separation and Purification Technology,* 233**,** 116026.

Tran, N. T., Yu, T., Kim, J. & Othman, M. R. (2020b). ZIF-8 tubular membrane for propylene purification: Effect of surface curvature and zinc salts on separation performance. *Separation and Purification Technology,* 251**,** 117354.

Treybal, R. E. (1981). *Mass-Transfer Operation,* Singapore, McGraw-Hill.

Tsai, C.-W. & Langner, E. H. G. (2016). The effect of synthesis temperature on the particle size of nano-ZIF-8. *Microporous and Mesoporous Materials,* 221**,** 8-13.

Tuninetti, J. S., Rafti, M. & Azzaroni, O. (2015). Early stages of ZIF-8 film growth: the enhancement effect of primers exposing sulfonate groups as surface-confined nucleation agents. *RSC Advances,* 5**,** 73958.

Ul-Hamid, A. (2018). *A Beginners' Guide to Scanning Electron Microscopy,* Cham, SWITZERLAND, Springer International Publishing AG.

Uragami, T. (2017). *Science and Technology of Separation Membranes,* New York, UNITED KINGDOM, John Wiley & Sons, Incorporated.

Usman, M., Ahmed, A., Yu, B., Peng, Q., Shen, Y. & Cong, H. (2019). A review of different synthetic approaches of amorphous intrinsic microporous

polymers and their potential applications in membrane-based gases separation. *European Polymer Journal,* 120**,** 109262.
Venna, S. R. & Carreon, M. A. (2009). Highly Permeable Zeolite Imidazolate Framework-8 Membranes for CO_2/CH_4 Separation. *American Chemical Soceity,* 132**,** 76-78.
Venna, S. R., Jasinski, J. B. & Carreon, M. A. (2010). Structural Evolution of Zeolitic Imidazolate Framework-8. *Journal of the American Chemical Society,* 132**,** 18030-18033.
Venna, S. R., Zhu, M., Li, S. & Carreon, M. A. (2014). Knudsen diffusion through ZIF-8 membranes synthesized by secondary seeded growth. *Journal of Porous Materials,* 21**,** 235-240.
Venturi, F. & Hussain, T. (2020). Radial Injection in Suspension High Velocity Oxy-Fuel (S-HVOF) Thermal Spray of Graphene Nanoplatelets for Tribology. *Journal of Thermal Spray Technology,* 29**,** 255-269.
Voorhees, L. R. a. P. W. (2002). *Growth and Coarsening*, Springer, Berlin, Heidelberg.
Wang, M., Bai, L., Li, M., Gao, L., Wang, M., Rao, P. & Zhang, Y. (2019). Ultrafast synthesis of thin all-silica DDR zeolite membranes by microwave heating. *Journal of Membrane Science,* 572**,** 567-579.
Wang, M., Wang, Z., Zhao, S., Wang, J. & Wang, S. (2017a). Recent advances on mixed matrix membranes for CO2 separation. *Chinese Journal of Chemical Engineering,* 25**,** 1581-1597.
Wang, M., Zhao, J., Wang, X., Liu, A. & Gleason, K. K. (2017b). Recent progress on submicron gas-selective polymeric membranes. *Journal of Materials Chemistry A,* 5**,** 8860-8886.
Wang, X., Sun, M., Meng, B., Tan, X., Liu, J., Wang, S. & Liu, S. (2016). Formation of continuous and highly permeable ZIF-8 membranes on porous alumina and zinc oxide hollow fibers. *Chemical Communications,* 52**,** 13448-13451.
Wu, X., Yang, Y., Lu, X. & Wang, Z. (2020). Seeded growth of high-performance ZIF-8 membranes in thick wall autoclaves assisted by modulator. *Journal of Membrane Science,* 613**,** 118518.
Xie, K., Fu, Q., Qiao, G. G. & Webley, P. A. (2019). Recent progress on fabrication methods of polymeric thin film gas separation membranes for CO2 capture. *Journal of Membrane Science,* 572**,** 38-60.
Xie, Z., Yang, J., Wang, J., Bai, J., Yin, H., Yuan, B., Lu, J., Zhang, Y., Zhou, L. & Duan, C. (2012). Deposition of chemically modified [small alpha]-Al2O3 particles for high performance ZIF-8 membrane on a macroporous tube. *Chemical Communications,* 48**,** 5977-5979.
Xing, T., Lou, Y., Bao, Q. & Chen, J. (2014). Surfactant-assisted synthesis of ZIF-8 nanocrystals in aqueous solution via microwave irradiation. *CrystEngComm,* 16**,** 8994-9000.
Xu, X., Cheng, M., Yang, W. & Lin, L. (1998). Synthesis and gas permeation properties of silicalite-1 zeolite membrane. *Science in China Series B: Chemistry,* 41**,** 325.
Xu, X., Yang, W., Liu, J. & Lin, L. (2000). Fast formation of NaA zeolite membrane in the microwave field. *Chinese Science Bulletin,* 45**,** 1179-1181.
Yahia, M., Phan Le, Q. N., Ismail, N., Essalhi, M., Sundman, O., Rahimpour, A., Dal-Cin, M. M. & Tavajohi, N. (2021). Effect of incorporating different ZIF-

8 crystal sizes in the polymer of intrinsic microporosity, PIM-1, for CO2/CH4 separation. *Microporous and Mesoporous Materials,* 312**,** 110761.
Yang, J., Xie, Z., Yin, H., Wang, J., Xu, J., Wang, J., Lu, J., Yin, D. & Zhang, Y. (2014). Simultaneous surface and pore structure modification for growth of ZIF-8 membranes on coarse macroporous tube. *Microporous and Mesoporous Materials,* 198**,** 263-270.
Yao, J., Dong, D., Li, D., He, L., Xu, G. & Wang, H. (2011). Contra-diffusion synthesis of ZIF-8 films on a polymer substrate. *Chemical Communications,* 47**,** 2559-2561.
Yao, J., Li, L., Wong, W., Tan, C., Dong, D. & Wang, H. (2013). Formation of ZIF-8 membranes and crystals in a diluted aqueous solution. *Materials Chemistry and Physics,* 139**,** 1003-1008.
Yao, J. & Wang, H. (2014). Zeolitic imidazolate framework composite membranes and thin films: synthesis and applications. *Chemical Society Reviews,* 43**,** 4470-4493.
Yichang Pan, B. W., Zhiping Lai (2012). Synthesis of ceramic hollow fiber supported zeolitic imidazolate framework-8 (ZIF-8) membranes with high hydrogen permeability. *Journal of Membrane Science,* 421-422**,** 292-298.
Yin, S., Meyer, M., Li, W., Liao, H. & Lupoi, R. (2016). Gas Flow, Particle Acceleration, and Heat Transfer in Cold Spray: A review. *Journal of Thermal Spray Technology,* 25**,** 874-896.
Yoo, Y., Lai, Z. & Jeong, H.-K. (2009). Fabrication of MOF-5 membranes using microwave-induced rapid seeding and solvothermal secondary growth. *Microporous and Mesoporous Materials,* 123**,** 100-106.
Yu, J., Pan, Y., Wang, C. & Lai, Z. (2016). ZIF-8 membranes with improved reproducibility fabricated from sputter-coated ZnO/alumina supports. *Chemical Engineering Science,* 141**,** 119-124.
Zhang, C. & Koros, W. J. (2015). Zeolitic Imidazolate Framework-Enabled Membranes: Challenges and Opportunities. *The Journal of Physical Chemistry Letters,* 6**,** 3841-3849.
Zhang, H., Liu, D., Yao, Y., Zhang, B. & Lin, Y. S. (2015). Stability of ZIF-8 membranes and crystalline powders in water at room temperature. *Journal of Membrane Science,* 485**,** 103-111.
Zhang, J., Li, M., Lin, Y., Liu, C., Liu, X., Bai, L., Hu, D., Zeng, G., Zhang, Y., Wei, W. & Sun, Y. (2016). Synthesis and characterization of all-silica DDR zeolite by microwave heating. *Microporous and Mesoporous Materials,* 219**,** 103-111.
Zhang, J., Tan, Y. & Song, W.-J. (2020). Zeolitic imidazolate frameworks for use in electrochemical and optical chemical sensing and biosensing: a review. *Microchimica Acta,* 187**,** 234.
Zhang, X., Liu, Y., Kong, L., Liu, H., Qiu, J., Han, W., Weng, L.-T., Yeungb, K. L. & Zhud, W. (2013). A simple and scalable method for preparing low-defect ZIF-8 tubular membranes. *Journal of Materials Chemistry,* 1**,** 10635-10638.
Zhou, L., Niu, Z., Jin, X., Tang, L. & Zhu, L. (2018). Effect of Lithium Doping on the Structures and CO2 Adsorption Properties of Metal-Organic Frameworks HKUST-1. *ChemistrySelect,* 3**,** 12865-12870.

Zhu, C., Peng, Y. & Yang, W. (2020). Modification strategies for metal-organic frameworks targeting at membrane-based gas separations. *Green Chemical Engineering*.
Zhu, Y., Liu, Q. & Huang, A. (2016). Microwave synthesis of tubular zeolitic imidazolate framework ZIF-8 membranes for CO2/CH4 separation. *Separation Science and Technology,* 51**,** 883-891.